8-2011

MULTI-LENGTH SCALE MODELING OF THE HIGH-PRESSURE, LARGE-STRAIN, HIGH-STRAIN-RATE RESPONSE OF SODA-LIME GLASS

William Bell
Clemson University, wcbell@gmail.com

MULTI-LENGTH SCALE MODELING OF THE HIGH-PRESSURE, LARGE-STRAIN, HIGH-STRAIN-RATE RESPONSE OF SODA-LIME GLASS

A Dissertation
Presented to
the Graduate School of
Clemson University

In Partial Fulfillment
of the Requirements for the Degree
Doctor of Philosophy
Mechanical Engineering

---

by
William Cameron Bell
August 2011

Accepted by:
Dr. Mica Grujicic, Committee Chair
Dr. Paul F. Joseph
Dr. Rajendra Singh
Dr. Gang Li

ABSTRACT

Development of new transparent armor systems is essential for the protection of the current and future US armed forces, especially in light of the recent military operations The Operation Iraqi Freedom in Iraq and The Operation Enduring Freedom in Afghanistan. These conflicts have introduced a new military theater without a well-defined battle front and new types of threats (e.g. improvised explosive devices, IEDs). Development and modeling of new transparent armor systems for use in numerous applications from vehicle windows to face shields is a current area of thrust aimed at addressing the shortcomings of existing systems in order to better protect US soldiers and align with the military's goal of becoming more mobile, deployable, and sustainable.

This dissertation is focused predominately on the computational modeling of transparent armor materials and structures. Glass remains the dominant constituent in many modern transparent armor systems for a number of performance and manufacturing related reasons and thus is the material of focus in the present work. The present work is concerned with the development and further enhancement of a continuum-level, physically-based, high strain-rate, large-strain, high-pressure mechanical material model for soda-lime (and borosilicate) glass. The model is being developed in attempt to capture the complex stochastic, pre-existing flaw-controlled damage nature of glass under blast and impact conditions and do so in a computationally efficient manner. Numerous finite element simulations were carried out using the computational code ABAQUS/Explicit to assess the utility of the model under physically realistic ballistic loading conditions, including multi-hit impact scenarios. Further enhancements of the glass material model are made with the inclusion of the following: (i) differentiation of the mechanical properties of the so-called *air-side* and *tin-side* of glass plates manufactured using the float glass process; and (ii) a damage tensor to produce an orthotropic macro-cracked material. In

addition a multi-length scale modeling approach for glass is taken to elucidate phenomena at different length scales (e.g. glass irreversible densification, shock response, etc.) with the ultimate objective of enhancing the efficacy of the current continuum-level material model. The irreversible densification of glass under ballistic (shock) loading conditions is investigated at multiple length scales (atomistic-level and continuum-level) in order to understand its effect on the ballistic penetration resistance of glass. The findings related to the material shock response and irreversible densification of glass were subsequently included in the continuum-level glass material model equation of state to further increase its efficacy.

The results from the various test scenarios and modifications to the continuum-level glass material models reveal that: (a) transient non-linear dynamics computational analyses, when utilizing the glass material model, have demonstrated to be a useful tool in understanding the multi-hit ballistic-protection performance of laminated glass/polycarbonate transparent armor systems. The loss of the ballistic-protection performance of the armor caused by a sequence of closely spaced bullet impacts has been observed and the results of these analyses are validated against their experimental counterparts; (b) while it was expected (based on quasi-static mechanical testing result) that orienting the borofloat tin-side as a three-layer laminate strike face would enhance its ballistic protection performance, experimental findings did not support this conjecture. Computational simulations of the laminate impact established the capability of the borosilicate glass material model to capture the prominent experimentally observed damage modes and the measured V50, reconfirming the experimental findings; and (c) a 2-4% (shock strength-dependent) irreversible density increase in glass is capture computationally at multiple lengths scales. Subsequent modifications of the continuum-level material model for glass to include the effect of irreversible-densification resulted in minor improvements in the ballistic-penetration resistance of glass and only for high projectile initial velocities.

DEDICATION

This dissertation was made possible by the unwavering love, encouragement, and support of my mother, Nancy Bell, father, Bill Bell, and my brother, Jonathan Bell, to whom I dedicate this dissertation.

ACKNOWLEDGMENTS

I must express my gratitude to my advisor Dr. Mica Grujicic for his guidance and persistent work ethic that ensured my productivity and completion of this research. His ability to simplify problems to a manageable level in addition to his general engineering insight has been invaluable.

In addition, I would like to thank my advisory committee members Dr. Gang Li, Dr. Paul Joseph, and Dr. Rajendra Singh for the insight into my research and constructive criticism that has undoubtedly enhanced the quality of this work. The assistance provided by the Mechanical Engineering administrative staff should not go unrecognized, as well.

My research group members during my time a Clemson University have also provided assistance that aided in the completion of this research. Their willingness to share knowledge and time has significantly contributed to the timely completion of this work.

Finally, I must thank my family and close friends for their support and encouragement. They have most certainly had a positive impact on my quality of life and the quality of my work.

The material presented in this paper is based on research supported by the U.S. Army/Clemson University Cooperative Agreements W911NF-04-2-0024 and W911NF-06-2-0042 and by an ARC-TARDEC research contract. In addition some material was also supported by the Army Research Office (ARO) research contract entitled “Multi-length Scale Material Model Development for Armor-grade Composites”, Contract Number W911NF-09-1-0513. I am also indebted to Drs. Bryan Cheeseman and Paramel Patel whose contributions and support to this ongoing research have been paramount.

TABLE OF CONTENTS

Page

Page

Page

LIST OF TABLES

LIST OF FIGURES

Figure Page

Figure Page

Figure Page

CHAPTER ONE

INTRODUCTION

1.1 Background

Transparent armor is a vital tool in the protection of individuals and objects of value where transparency is still a requirement. A wide variety of transparent armor applications span the civilian and military sectors where it typically serves as windows in vehicles, corrections facilities, storefronts where valuables are displayed, etc. The predominate driving force for the further development of novel materials and laminate structures for such armor is the United States Military for use in protected vehicles (up-armored HMMWVs, MRAPs, etc.). Despite the numerous advancements in transparent protective materials (e.g. Aluminum Oxinitride, spinel, synthetic sapphire, PMMA), glass currently remains the majority constituent in most transparent armor laminates for numerous economic and manufacturing reasons. Thus, it is obvious that furthering the knowledge of glass response under highly dynamic impact conditions is critical for developing transparent armor of greater impact resistance and mass-efficiency.

Toward that end, new design tools and approaches have been employed to accelerate the advancement of the next generation of glass-based transparent armor laminates. One of the critical tools that is increasingly being employed as an accompaniment to experimental testing is computational modeling. With the advancements in computer hardware and software within the last decade, computational modeling has become a more viable tool to further investigate transparent armor impact scenarios in a more time- and cost-efficient manner (relative to their experimental counterparts). However, despite these advancements, computational codes still depended on high-fidelity material models to account for material response to loading. Consequently, the focus of the present work is placed upon multi-length scale (molecular-

through continuum-level) investigation of glass deformation and damage processes. The predominate phenomena/physical processes (e.g. irreversible densification, shock formation, quasi-static versus dynamic facture, float glass surface condition, etc.) are subsequently accounted for in a continuum-level, physically-based, high-strain rate, large strain, high pressure material model for implementation into commercial finite element codes. Such a model allows for efficient modeling of full-scale, in-situ transparent armor.

1.2 Literature Review

The relevant literature survey for each of the sub-topics covered in the present work is provided in Chapters 2-6.

1.3 Thesis Objective and Outline

The overall objective of the present work was to further develop material models and accompanying computational engineering analyses which may reduce the need for experimental testing and speed up the development of new transparent-armor systems with superior single- and multi-hit ballistic-protection performance. Toward that end, the continuum-level, physically-based, high-strain rate, large strain, high pressure material model under ongoing development in the author's research group is enhanced to include additional phenomena affecting the mechanical response of soda-lime glass under dynamic loading conditions and extended to model additional blast/ballistic loading scenarios. The model in question was reported in a series of three journal publications listed as Refs. [2.3,2.11,2.12] in Section 2.6. The enhancements and extensions of this model are presented in Chapters 2-6.

In Chapter 2, the multi-hit ballistic protection performance of a multi-layer glass was computationally assessed. The continuum-level, finite-element computational simulations are compared to their experimental counterparts from open literature to determine suitability of the

approach taken. In addition the main damage and performance-controlling phenomena in multi-hit impact scenarios are investigated/revealed.

In Chapter 3, the main objective was to investigate experimentally and computationally the effect of *air-side* vs. *tin-side* borofloat strike face when glass-based laminates are subjected to projectile impact. Towards that end it was required to extended the existing glass material model (which is under ongoing development in our research group) to allow for other glass formulations (in particular borosilicate float glass, Borofloat® glass) and is enhanced to account for the effect of microstructural/compositional differences between the so-called air-side and tin-side of plate glass fabricated using a conventional float glass process.

In Chapter 4, molecular-level calculations were carried out to investigate and quantify the irreversible densification process in soda-lime glass at high pressures. Subsequently continuum–level finite element simulations were used to determine if modifications in the equation of state and the strength constitutive laws of the JH2 continuum-material model for soda-lime glass to include the effects of high-pressure irreversible densification significantly alters the mechanical response of glass under ballistic-loading conditions.

In Chapter 5, the irreversible densification of glass under isothermal loading conditions was investigated through molecular-level modeling. Emphasis was placed on capturing and elucidating the molecular-level changes (e.g. Si bond coordination) responsible for the irreversible densification of glass under high pressure loading. In addition, the resulting isothermal axial-stress vs. specific-volume relation from the molecular level simulations was converted to a loading Hugoniot and unloading isentrope to allow for an analytical analysis of the potential ballistic impact performance enhancements that high-pressure, irreversible glass densification may provide.

In Chapter 6, equilibrium and non-equilibrium dynamic molecular-level calculations were carried out in order to investigation the molecular-level mechanical response of glass under shock loading conditions. Of particular interest were changes to the molecular structure of glass under highly dynamic loading conditions associated with shock formation and propagation. It was also desired to directly determine (via purely computational means) the glass shock hugoniot from non-equilibrium molecular-level simulations. Knowledge of the glass hugoniot relationship is critical for further enhancement of the dynamic continuum-level material model for glass which is under ongoing development in the author's research group.

CHAPTER TWO

A COMPUTATIONAL INVESTIGATION OF THE MULTI-HIT BALLISTIC-PROTECTION PERFORMANCE OF LAMINATED TRANSPARENT ARMOR SYSTEMS

2.1 Abstract

Multi-hit ballistic-protection performance of a prototypical laminated glass/polycarbonate transparent armor is investigated using a series of transient non-linear dynamics analyses of armor impact with a sequence of four M2AP full metal jacket (FMJ) armor piercing bullets. All calculations were carried out using ABAQUS/Explicit commercial finite element program [2.1] and the computational results obtained were compared with their experimental counterparts obtained by Dolan [2.2]. The comparison revealed that: (a) the proposed computational procedure can reasonably well account for the observed multi-hit ballistic-protection performance of the laminated transparent armor; (b) the role of prior bullet hits in reducing armor's ballistic-protection performance is clearly revealed; (c) the role of polycarbonate lamina in preventing glass fragments from entering the vehicle interior is clearly demonstrated; and (d) the experimentally observed inability of the transparent armor to defeat 0.50-caliber Fragment Simulating Projectiles (FSPs) is confirmed.

2.2 Introduction

Since the beginning of the military operations The Operation Iraqi Freedom in Iraq and The Operation Enduring Freedom in Afghanistan, protection and safety of the occupants of the U.S. Army ground vehicles has become an issue of critical importance. These vehicles are subjected to increased daily attacks from armed insurgents and threats from improvised explosive devices (IEDs, i.e. bombs constructed and deployed in ways different than those used in conventional military practice). Consequently, the U.S. Army is in a continuing process of

evaluating survivability of its vehicles and their occupants when subjected to such threats and in a constant search for ways to improve occupant-protection capabilities and survivability of the vehicles. Considering the fact that the windows and windshields are usually the most vulnerable and the most targeted areas of the vehicle due to occupant visibility, it is understandable that these areas of the vehicle are given extra consideration.

Most transparent armor systems currently used in the vehicle windows and windshield applications consist of stacked layers of glass and plastic (typically transparent polycarbonate, PC). Adjacent layers are bonded using interlaminate adhesives, most frequently those based on polyurethane, PUR. The outermost layer of the armor that the projectile first impacts (typically referred to as the *strike-face*) is made of glass so that armor can efficiently deform and/or fragment the projectile. In addition, high-hardness of glass provides the necessary resistance to scratch and abrasion which may be caused by windshield wipers, dust, etc. The back layer is typically made of polycarbonate which prevents the broken pieces of glass from entering the vehicle interior. The number of layers in a transparent-armor system, layers' thickness, as well as the total transparent armor thickness vary from one transparent-armor system to another as these systems are optimized with respect to their ability to protect against different types of threats (e.g. lead-core and armor-piercing bullets pose a different threat to the transparent armor than fragments from the IEDs).

It is well-established that increased service temperatures may significantly compromise the ballistic-protection performance of transparent armor. In addition, elevated service temperatures are frequently found to cause delamination of the glass and plastic layers which seriously degrades armor transparency (a critical performance requirement for transparent armor systems). Also lower service temperatures may induce brittleness and cracking into the inter-

laminate adhesive layer giving rise to the losses in both the ballistic protection and transparency of the armor.

As mentioned above, in addition to providing the necessary level of the ballistic protection to the vehicle occupants, transparent armor systems must also possess sufficient optical clarity/transparency. It is obvious that if no clear view of the outside is given to the vehicle occupants, they will not be as capable to out their duties such as drive and operate the vehicle, spot roadside mines, locate insurgent hiding places, etc. Consequently, transparent-armor systems must possess adequate level of optical transparency both in the visible and the infrared ranges of the electromagnetic spectrum. The latter is critical for the vehicle occupants using night-vision goggles.

As discussed above, U.S. Army vehicles used in the current operations face two main threats: (a) attacks by armed insurgents and (b) explosions from the IEDs. The armed insurgents present the so-called *small-arms fire* threats since they are usually equipped with handguns, small caliber rifles, or medium machine guns. The small-arms projectiles come in sizes between 5.58mm and 12.7mm and in different types (e.g. lead-core, armor-piercing rounds, round-nose, hollow point, etc.). The IED threats are more difficult to describe and quantify. Currently, when testing armor's ballistic-protection capability against the IED threats, the so called *Fragment Simulating Projectiles* (FSPs) are typically used. The FSPs are generally in the shape of a right circular solid cylinder, made of steel and were originally introduced to model the fragments generated by exploding artillery shells.

To ensure that its vehicles are combat ready, the U.S. Army requires their regular testing for ballistic-protection performance. Also, new vehicles are being designed with improved protection capabilities. However, the new vehicles must also have significantly reduced weight (to ensure their high mobility, rapid deployment, high fuel efficiency, etc.). Since, the

transparent-armor systems are one of the weakest areas on the vehicle and provide the most inefficient weight-normalized ballistic protection, they present the vehicle designers with significant challenges. Consequently, successful design of the future military ground vehicles entails a complete understanding of the ballistic-protection performance of the competing transparent-armor systems under different threats. In particular, knowledge of the ability of armor to provide multi-hit ballistic protection without significant loss in its optical transparency under different threats is important.

In its current practice for acquiring the transparent armor, the U.S. Army uses the ballistic-performance specifications for commercially-available armor like the ones mandated by the National Institute of Justice Test Standard 0108.01, Table 2.1. The specifications listed in Table 2.1 define, for different threat levels (I, II, II-A, III, III-A and IV), projectiles' type, weight, velocity, barrel length and allowable number of penetrations for a given number of hits per armor test panel. As discussed earlier, current ballistic threats far exceed the ones considered in commercial transparent-armor ballistic-performance specifications. That is, these specifications typically cover only protection requirements against handguns and small-caliber rifle rounds, while the U.S. Army vehicles face threats from a larger range of heavier ammunition. Consequently, the U.S. Army is developing a new transparent-armor purchase document ATPD 2352 which outlines all of the new key requirements for the transparent armor systems, and which will guide future armor acquisition by the Army. In addition to specifying the ballistic-protection requirements with respect to the standard military threats (bullets of various shapes and sizes), the ATPD 2352 also includes the ballistic-performance requirements with respect to the FSPs as well as the optical transparency and environmental durability requirements. The inclusion of the armor-protection requirements against the FSP threats is particularly critical considering the fact that IED-related vehicle occupant deaths are on the rise.

Table 2.1: Ballistic Performance Requirements for Armor as Specified by the National Institute of Justice Test Standard 0108.01

Armor Type	Test Ammunition	Nominal Bullet Mass	Suggested Barrel Length	Required Bullet Velocity	Required Hits Per Armor Test Panel	Permitted Penetrations
I	22LHRV Lead	2.6g 40gr	15 to 16.5 cm 6 to 6.5 in	320±12 m/s 1050±40 ft/s	5	0
	38 Special R N Lead	10.2g 158gr	15 to 16.5 cm 6 to 6.5 in	259±15 m/s 850±50 ft/s		
II-A	357 Magnum JSP	10.2g 158gr	10 to 12 cm 4 to 4.75 in	381±15 m/s 1250±50 ft/s	5	0
	9 mm FMJ	8.0g 124gr	10 to 12 cm 4 to 4.75 in	332±12 m/s 1090±40 ft/s		
II	357 Magnum JSP	10.2g 158gr	15 to 16.5 cm 6 to 6.5 in	425±15 m/s 1395±50 ft/s	5	0
	9 mm FMJ	8.0g 124gr	10 to 12 cm 4 to 4.75 in	358±12 m/s 1175±40 ft/s		
III-A	44 Magnum Lead SWCGC	15.55g 240gr	14 to 16 cm 5.5 to 6.25 in	426±15 m/s 1400±50 ft/s	5	0
	9 mm FMJ	8.0g 124gr	24 to 26 cm 9.5 to 10.25 in	426±15 m/s 1400±50 ft/s		
III	7.62 mm 308 Winchester FMJ	9.7g 150gr	56 cm 22 in	838±15 m/s 2750±50 ft/s	5	0
IV	30-06 AP	10.8g 166gr	56 cm 22 in	868±15 m/s 2850±50 ft/s	1	0

Abbreviations: AP - Armor Piercing; FMJ - Full Metal Jacket; JSP - Jacketed Soft Point; LRHV - Long Rifle High Velocity; RN - Round Nose;SWCGC - Semi-Wadcutter Gas Checked

While most details pertaining to a threat level, the testing procedures and the required test results for transparent-armor systems qualification are classified, a rendition of these specifications was used in the recent work by Dolan [2.2], who carried out a detailed experimental investigation of the ballistic-protection performance of a laminated glass/polycarbonate transparent armor system subjected to a rifle-round multi-hit threat. The work of Dolan clearly revealed numerous experimental challenges and excessive cost associated with experimental investigations of the ballistic-protection performance of complex transparent-armor systems. Consequently, any use of computational engineering analyses which would reduce the need for experimental testing and speed up the development of new transparent-armor systems with superior multi-hit ballistic-protection performance is attractive. In the present work, a series

of transient non-linear dynamic simulations of a prototypical laminated glass/polycarbonate transparent armor system when subjected to a multi-hit threat from the M2AP rifle-fired armor-piercing bullet is carried out in order to examine the utility of such analyses. Towards that end, the computational results are compared with their experimental counterparts obtained in the work of Dolan [2.2].

The organization of the paper is as follows: In Section 2.3.1, a brief overview is provided of the experimental set-up and procedures used and the results obtained in the work of Dolan [2.2] who carried out an assessment of the multi-hit ballistic performance of transparent armor. Details regarding the corresponding transient non-linear dynamics computational analysis as well as regarding the material models used are presented in Section 2.3.2. The main results obtained in the present work are presented and discussed in Section 2.4. The key conclusions resulted from the present work are summarized in Section 2.5.

2.3 Experimental and Computational Procedures

2.3.1 Experimental Investigation

In this section, a brief description is provided of the experimental procedures and the results obtained in the recent ballistic-testing work of Dolan [2.2] which was carried out at the TARDEC Armor Integration Laboratory (TAIL) located in Warren, MI. Within the experimental procedure used, plate-like laminated glass/polycarbonate transparent-armor test panels were mounted vertically in a specially-designed test fixture which ensures consistent and reproducible test-panel clamping conditions. Test-panel dimensions were L × W × T = 304.8mm × 304.8mm × 73mm and each panel consisted of five 10.42mm-thick glass layers and five 4.17mm-thick polycarbonate layers. In accordance with the laminated glass/polycarbonate transparent-armor installation procedures on a vehicle, the glass face of the armor test panels is considered as the

strike face. A 0.3 caliber M2AP armor-piercing rifle-fired bullet rounds were used whose velocity was determined using a customized chronographic system placed in front of the fixtured test panels. Each transparent-armor test panel was impacted with four M2AP rounds and the multi-hit test pattern used is displayed in Figure 2.1. A 0.508mm-thick aluminum foil placed parallel to and 150mm behind the fixtured test panel was used as a witness plate. While during testing of the common opaque armor a thicker witness plate is used to mimic the uniform and skin of a soldier, in the present case a thinner witness plate is used which acts as a surrogate for the soldiers' eye cornea. Hence, any perforation of the witness plate signifies a potential eye injury for the soldiers not wearing any eye protection and is considered as failure (*complete penetration*) of the tested transparent armor system. Any other outcome of the armor testing qualifies as a *partial penetration.*

It is customary to quantify the ballistic-protection performance of the opaque armor with respect to a given threat using V_{50}, i.e. average projectile velocity at which the probability of armor penetration is 50%. When single-hit ballistic performance of the armor is tested, one impact is made into each virgin armor test panel or several well-spaced hits are made into a single virgin armor test panel. Each impact involves the same type of projectile at an increased incident velocity. Each impact is considered to be a separate statistical event and, consequently, V_{50} is obtained by the so-called *six-round limit* procedure in which the average single-hit V_{50} is computed between the three highest velocities at which partial penetrations take place and the three lowest velocities at which complete penetrations take place.

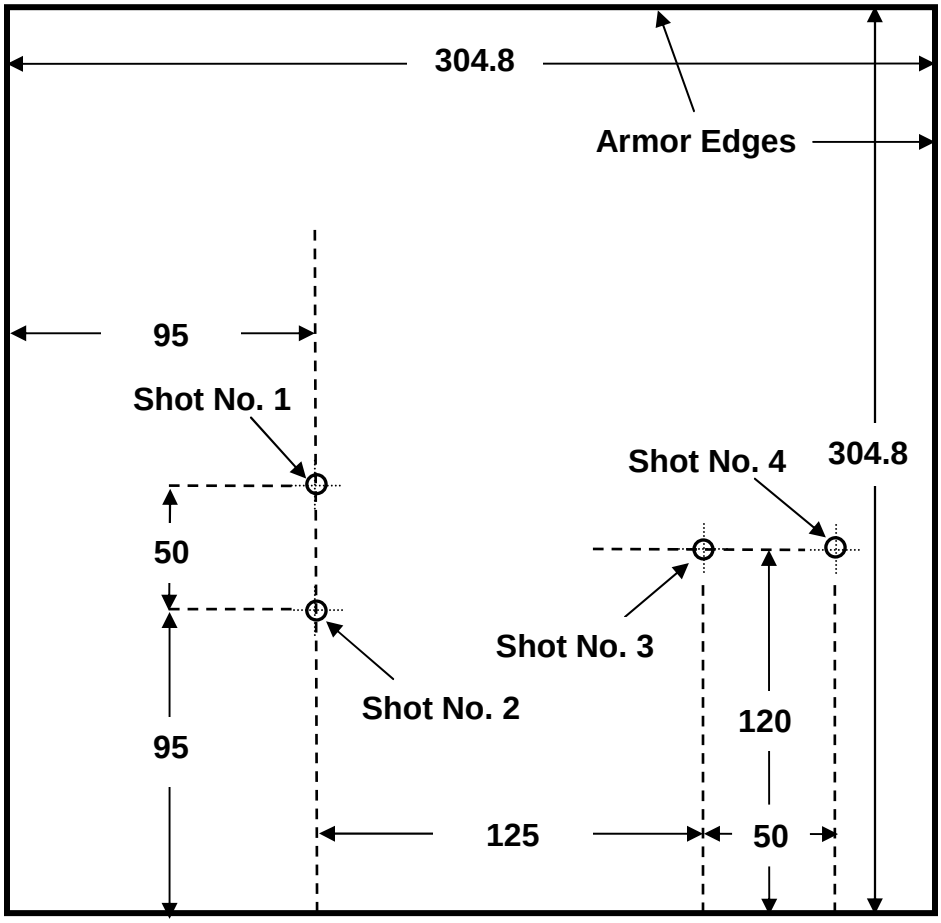

Figure 2.1: Impact locations and firing sequence for the multi-hit ballistic-performance test analyzed in the work of Dolan [2.2] and in the present work. All dimensions are in mm.

When multi-hit ballistic-protection performance of armor is tested, the entire set (four in the present case) of hits associated with a given average projectile velocity are considered as a single statistical event since closely-spaced hits affect ballistic response of the armor. Hence, if any of the four hits results in a complete penetration of the armor, the entire set of four hits is considered to lead to a failure of the armor system. Typically, as the average projectile velocity is increased from the lower values, at which only partial penetrations take place, to the higher values, at which complete penetrations take place, a *zone of mixed results* is encountered. Within this zone, complete penetrations take place at lower projectile velocities and partial penetrations take place at higher projectile velocities. The multi-hit V_{50} is then calculated using only the

armor testing results in the zone of mixed results, i.e. to get the multi-hit V_{50}, the sum of all average projectile velocities in the zone of mixed results is divided by the number of multi-hit tests lying in this zone.

Considering high vulnerability of transparent armor, its ballistic-protection performance is typically not quantified by V_{50} but instead by the highest average velocity of the given projectile at which the probability for complete penetration is 5% or less. To determine this velocity (referred to in the remainder of the manuscript as, V_{05}), and considering the fact that the outcome of each multi-hit test could be either complete penetration or partial penetration, one must use the logistic regression analysis to construct the corresponding logistic regression curve which relates the probability for complete penetration of the armor, P, with the average projectile velocity, v. This curve is defined by the following functional relationship:

$$P = \frac{\exp(\beta_0 + \beta_1 v)}{1 + \exp(\beta_0 + \beta_1 v)} \tag{2.1}$$

where β_0 and β_1 are regression coefficients. To evaluate these coefficients, the average projectile velocities (one for a given set of four hits) are grouped and, within each group, the probability of complete penetration of the armor determined by dividing the number of tests resulting in full penetration by the number of tests in that projectile-velocity group. Once the procedure is completed, Eq. (2.1) is linearized as:

$$\ln\left(\frac{P}{1-P}\right) = \beta_0 + \beta_1 v \tag{2.2}$$

and the coefficients β_0 and β_1 are determined using the standard least-squares based linear-regression (curve-fitting) analysis.

An example of the test results obtained in the experimental work of Dolan [2.2] is displayed in Table 2.2. In Table 2.2, the results of eleven multi-hit ballistic-protection tests each involving four shots with the location and firing sequence in accordance with Figure 2.1, are

displayed. For each test, an average projectile velocity and the observed (partial or complete) penetration mode are specified. The corresponding probability for complete penetration of the armor, *P*, versus the average projectile velocity, *v*, curve obtained using the logistic regression analysis is displayed in Figure 2.2.

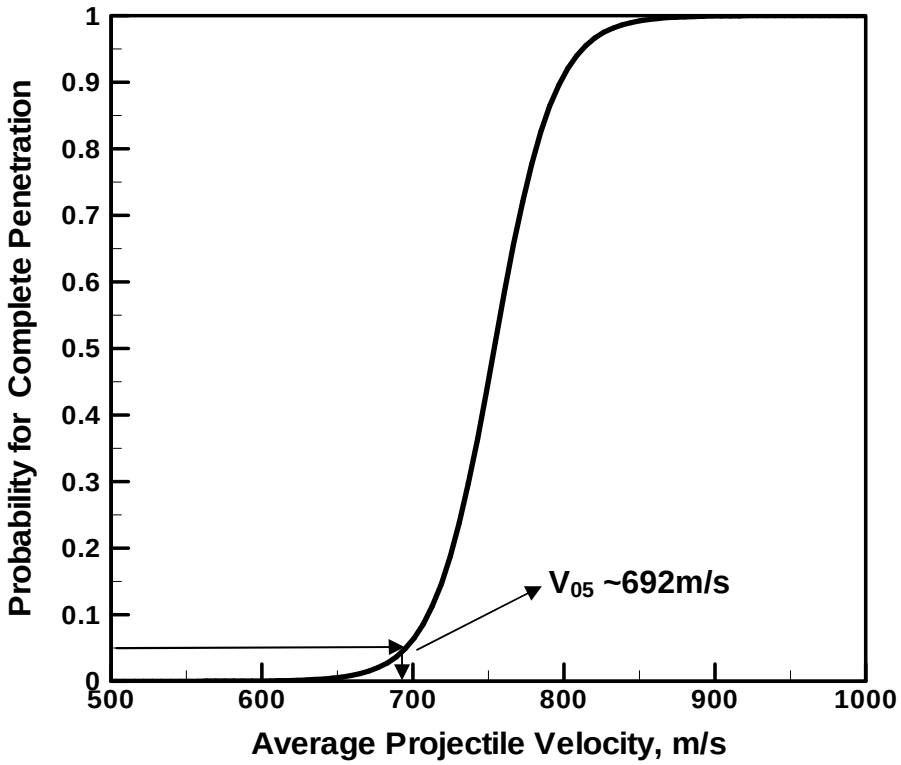

Figure 2.2: The probability for complete penetration of the armor, P, versus the average projectile velocity, v, curve obtained using the logistic regression analysis and the results of Dolan [2.2].

A schematic of the typical results pertaining to a post-mortem analysis of the extent of armor damage around each of the four points of impact at the strike face of the armor obtained in the work of Dolan [2.2] is displayed in Figure 2.3. It is seen that a zone of damage several times larger than the penetration-hole size surrounds each of the four points of impact.

Table 2.2: Experimental Results Obtained by Dolan [2.2] and the Computational Results Obtained in the Present Work Pertaining to the Multi-hit Ballistic Protection Performance of a Laminated Glass/Polycarbonate Transparent-Armor System

Sample Number	Average Projectile Velocity (m/s)	Penetration Type Dolan [2.2]	Penetration Type Present Work
1	592	Partial	Partial
2	640	Partial	Partial
3	682	Partial	Partial
4	713	Complete	Partial
5	779	Partial	Partial
6	804	Complete	Partial
7	807	Complete	Partial
8	815	Partial	Partial
9	847	Complete	Complete
10	858	Complete	Complete
11	893	Complete	Complete

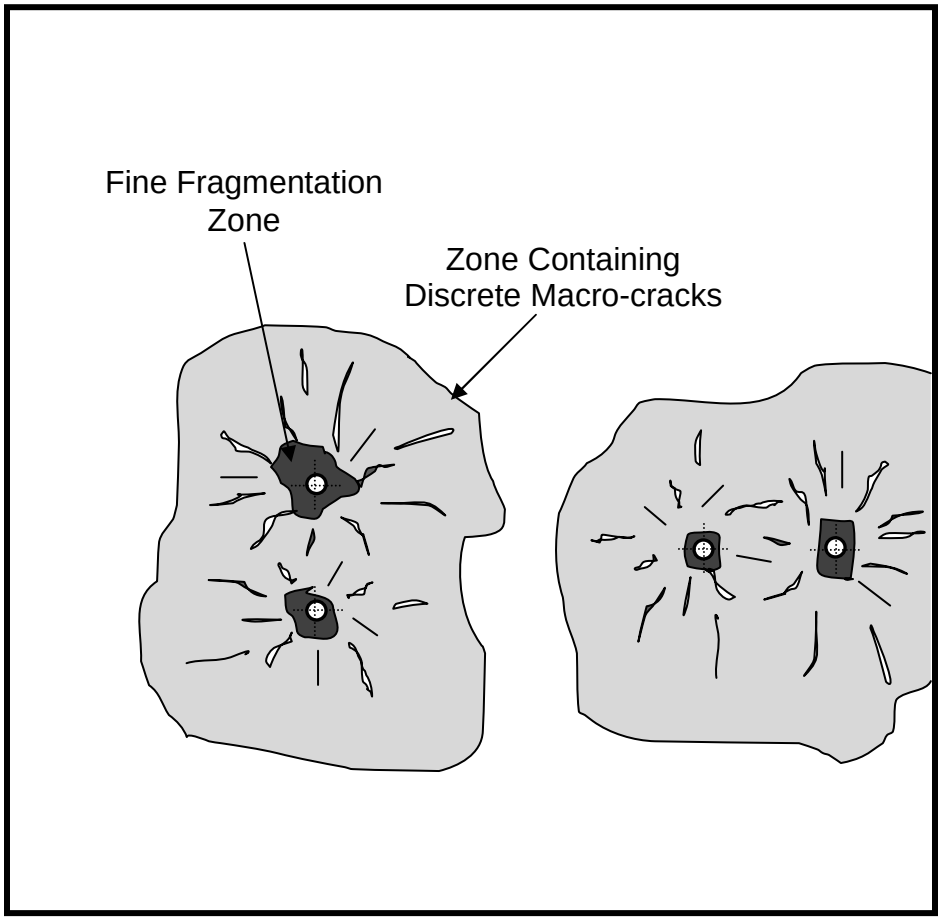

Figure 2.3: A schematic of the typical results pertaining to the damage zone size surrounding each of the four points of impact of the transparent armor as observed in the work of Dolan [2.2] on the strike face of the armor.

2.3.2 Computational Analysis

2.3.2.1 Problem Definition

In this section, a detailed description is provided of the geometrical models for the laminated glass/polycarbonate transparent-armor plates and the 0.3 caliber M2AP armor-piercing rounds and of the computational procedure used in a transient non-linear dynamics analysis of the multi-hit ballistic-performance of transparent armor samples tested experimentally by Dolan [2.2].

A schematic of the transparent-armor square-plate like test sample analyzed is depicted in Figure 2.4(a). It consists of five alternating 10.42mm-thick soda-lime glass laminae and five 4.17mm-thick polycarbonate laminae, making the overall test-sample thickness of 73mm. The in-plane (y-z) dimensions of the sample are 304.8mm by 304.8mm. Both the glass and the polycarbonate laminae are meshed using solid six-node reduced-integration (C3D6R) elements. A finer mesh was used in the region of the armor surrounding the four points of impact where the elements' average edge length was ~ 4mm. Typically there were 8680 elements in a single layer of glass and 4340 elements per layer of polycarbonate. The inter-lamina polyurethane adhesive was not modeled explicitly. Instead, a single layer of six-node cohesive elements (COH3D6) is introduced between the contacting glass and polycarbonate laminae and the tensile and shear strength of polyurethane used to derive the corresponding normal and shear cohesive properties of these elements.

The 0.3 caliber conical pointed-tip M2AP round is 35.6mm long and consists of a 1mm-thick copper jacket and a hard AISI 4340 steel core. The weight of the projectile is ~10.75g. The finite element mesh used to represent the M2AP round is depicted in Figure 2.4(b). The copper jacket and the AISI 4340 steel core are meshed using 4048 and 3220 four-noded tetrahedron (C3D4R) elements, respectively, with an average element edge length of 1mm. The jacket and the core share nodes along their contact surface, i.e. a perfect jacket/core interfacial bonding is assumed.

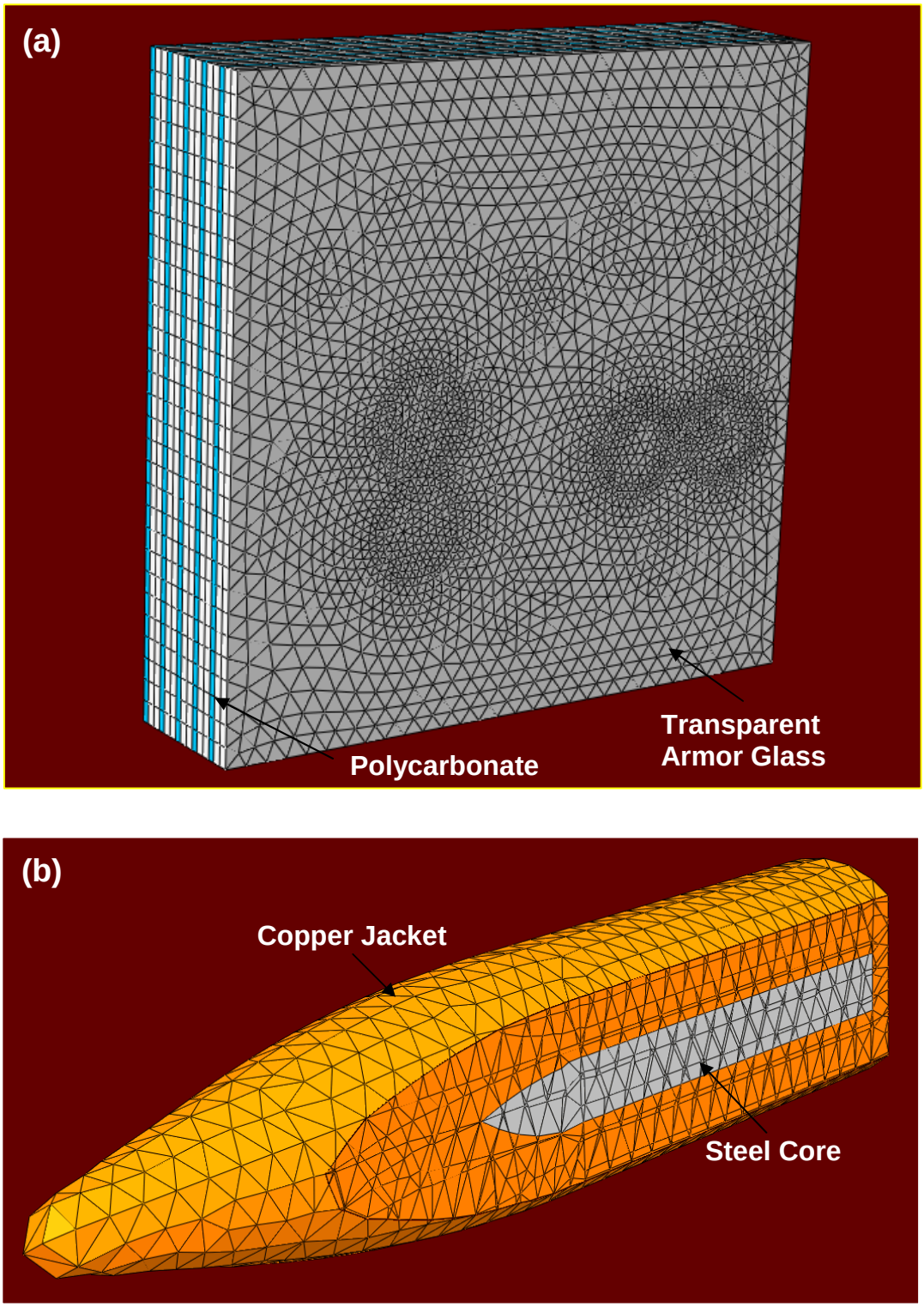

Figure 2.4: Typical finite element meshes used for discretization of: (a) transparent-armor test sample and (b) projectile.

The mesh sizes both for the transparent-armor test-sample and the projectile were varied initially in order to validate that the computational results are not significantly mesh-size dependent.

All the calculations were carried out using ABAQUS/Explicit computer program [2.1]. Built-in material models were used for all materials except for glass which was represented using the material model recently proposed by Grujicic et al. [2.3, 2.10-14]. This model was implemented into a *VUMAT* User Material Subroutine and linked with ABAQUS/Explicit before the model could be used.

Interactions between the projectile and armor were modeled using the *Hard Contact Pair* type of contact algorithm. Within this algorithm, contact pressures between two bodies are not transmitted unless the nodes on the *slave surface* contact the *master surface*. No penetration/over-closure is allowed and there is no limit to the magnitude of the contact pressure that could be transmitted when the surfaces are in contact. Transmission of shear stresses across the contact interfaces is defined in terms of a static, μ_{st}, and a kinematic μ_{kin}, friction coefficient and an upper-bound shear stress limit, τ_{slip} (a maximum value of shear stress which can be transmitted before the contacting surfaces begin to slide).

The impact of the projectile with armor is modeled by assigning an initial (translational) velocity to the projectiles (*the initial condition*). To model sequential impact of the four projectiles, the projectiles were positioned at different distances from the armor and propelled at the same velocities at the same time. The initial velocity of armor was set to zero and, during the impact simulation, the narrow side, top and bottom faces of the target normal to the impacted face was kept at a fixed position (*the boundary conditions*).

To prevent hour-glassing effects which may arise due to the use of reduced-integration elements, a default value of hour-glass stiffness was used. No mass-scaling algorithm was used

to increase the maximum stable time increment. Computational analyses were run on a machine with two 2.33GHz Quad-core Intel Xeon processors with 16GB of RAM. A typical 1ms impactor/target computational analysis would require 5 hours and 30 minutes of (wall-clock) time.

An example of the initial configuration and an intermediate configuration for the finite element model involving four bullets, a laminated transparent-armor panel and a thin-wall witness-plate is displayed in Figures 2.5(a)-(b), respectively.

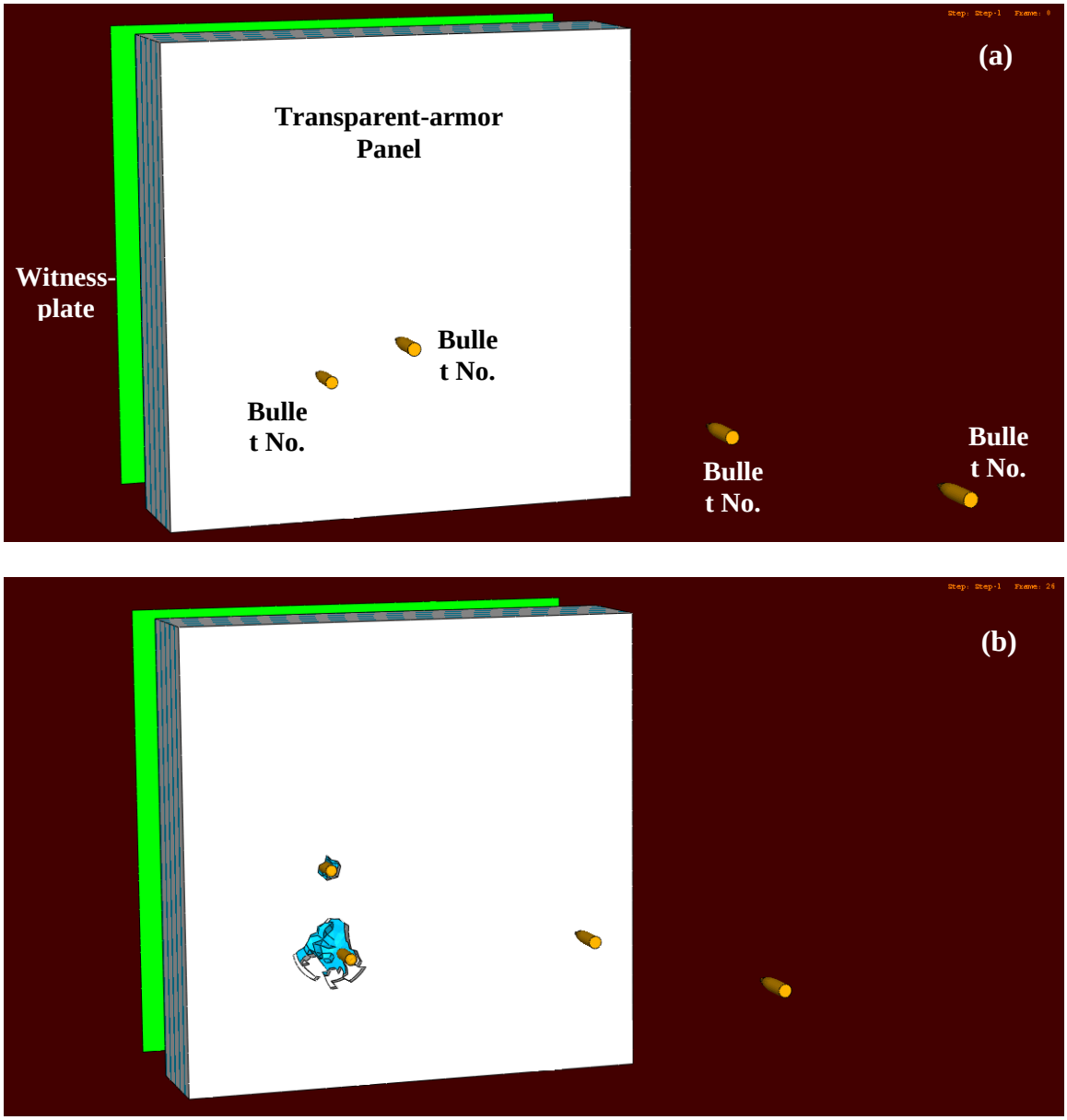

Figure 2.5: An example of: (a) the initial configuration and (b) an intermediate configuration of the projectiles/armor/witness-plate system analyzed in the present work.

2.3.2.2 Material Models

As mentioned in the previous section, the transparent-armor samples consist of three materials: soda-lime glass, polycarbonate and a polyurethane adhesive. Also, the M2AP rounds consist of a copper jacket and an AISI 4340 steel core. Considering the fact that the M2AP round

was used in our recent work [2.4], and that the material models (a linear equation of state, the Johnson-Cook strength model, the Johnson-Cook failure model and an erosion algorithm based on the maximum allowable instantaneous geometrical strain) used for copper and AISI 4340 steel were reviewed in great details in that work, no further discussions of the material models for copper and AISI 4340 steel will be given here. Glass, polycarbonate and polyurethane adhesive on the other hand, are the key material constituents in the laminated transparent armor and material models used to account for their mechanical response under large-strain, high deformation rate, high-pressure conditions encountered during impact with a high-speed projectile are presented in the remainder of this section.

Soda-lime Glass

As mentioned above, mechanical behavior of the soda-lime glass laminae in the armor is represented using our recent model [2.3, 2.10-14]. In the remainder of this subsection, a brief overview of the model is provided.

The model of Grujicic et al. [2.3, 2.10-14] is physically-based and treats glass as a stochastic brittle material whose damage-dominated deformation and ultimate failure are controlled by the pre-existing flaws. To account for the potential role of glass-panel processing and handling, different distributions of flaws are assumed for the surface and bulk regions of the material. The key feature of the model is that it enables glass, depending on the loading conditions, to fail in either a coarse-fragmentation or a fine-fragmentation/comminution mode. The two modes of failure are the result of competition of the following two basic processes:

(a) The growth of newly nucleated cracks which is accompanied by the growth of *shielding zones*, one zone surrounding each crack. Within these zones the pre-existing flaws are shielded from the external field and cannot be activated and converted into cracks. This, in turn, leads to the course-fragmentation mode of failure; and

(b) An increase in the stress-level in the regions surrounding shielding zones of the newly-nucleated cracks which promotes nucleation of additional cracks. The resulting nucleation of multiple cracks causes the cessation of their growth at nearby cracks, a gradual degradation of the material's mechanical properties, and ultimately fine-scale fragmentation.

In the model, the coarse-fragmentation fracture mode is promoted by low-strain rates while high-strain rates lead to the fine-fragmentation mode (comminution). A critical deformation rate is defined which separates the two fracture modes. The model was fully validated by comparing the model-based prediction of a computational analysis of the so-called Edge-on-Impact (EOI) test with the experimental results obtained in the work of Strassburger et al. [2.5].

Finite element implementation of the model is carried out using the following procedure:

(a) When a finite element is failing in the *coarse-fragmentation mode*, a single crack is assumed to extend, at the terminal velocity, through the element. The total time for element failure is obtained by dividing the characteristic element dimension by the terminal crack velocity. Once the element has fractured, it is removed from the model. In other words, multi-axial macro-cracking is not handled explicitly. When an element is undergoing coarse-fragmentation failure, stiffness and strength properties of this element are degraded linearly with the corresponding crack strain from the point of crack initiation to the point of complete traversal of the element by the crack;

(b) When an element has started undergoing *multi-fragmentation damage* due to the formation of multiple cracks, stress-shielding and path-crossing effects initially prevent the nucleation of macro-cracks. However, when the extent of *coherent damage* within a single element reaches a *critical value*, this element is assumed to fracture by micro-crack coalescence and to lose most of its ability to support load. To account for the experimental observations that

the resulting micro-fragments remain confined by the surrounding non-fractured material and can support compressive and shear loads, the elements that failed in the multi-fragmentation mode are not removed from the model. Instead, they are retained and assigned small residual normal and shear stiffness values; and

(c) When an element is experiencing *multiple-fragmentation damage*, the extent of damage, *D*, is governed by a damage evolution equation and the degradation of the corresponding stiffness and stress properties of the material are governed by the appropriate damage-dependent stiffness and strength relations.

Thus, the key components of the soda-lime glass model proposed by Grujicic et al. [2.3, 2.10-14] are: (i) the Weibull-type surface and bulk flaw distribution parameters; (ii) a coarse-fragmentation/fine-fragmentation threshold stress rate; (iii) a damage evolution equation; and (iv) damage-induced stiffness and strength degradation equations. To couple the model with the ABAQUS/Explicit computer program [2.1], it had to be implemented into a *VUMAT* User Material Subroutine.

Polycarbonate

While polycarbonate in its rubbery/leathery state above the glass transition temperature and under low strain-rate loading conditions can have considerable ductility and a quite complex mechanical response, the same material when subjected to high strain rates behaves essentially as a rate-independent isotropic linear elastic and rate-dependent isotropic ideal plastic material with plastic strain-controlled failure [2.9]. Since in the present work, polycarbonate laminae were subjected to high deformation rates, this simple material model for polycarbonate was used. A list of material model parameters for the polycarbonate is given in Table 2.3.

Table 2.3: Rate-independent Isotropic Linear Elastic, Rate-dependent Isotropic Ideal Plastic and Plastic Strain-based Failure Material Model Parameters for Polycarbonate [2.9].

Parameter	Units	Value	Strain Rate (s^{-1})
Young's Modulus	GPa	2.5	N/A
Poisson's Ratio	N/A	0.24	N/A
Yield Strength	MPa	45	400
Yield Strength	MPa	50	1700
Yield Strength	MPa	70	2200
Failure Plastic Strain	N/A	2.0	N/A

Polyurethane Adhesive

The polyurethane adhesive used to bond adjacent glass and polycarbonate laminae is not modeled as a conventional structural hyper-elastic material. Instead this material was modeled in the present work using the *cohesive zone framework* originally proposed by Needleman [2.6]. The cohesive zone is assumed to have a negligible thickness when compared with other characteristic lengths of the problem, such as the glass/polycarbonate lamina thickness and the characteristic lengths associated with the stress/strain gradients. The mechanical behavior of the cohesive zone is characterized by a traction–displacement relation, which is introduced through the definition of an *interfacial potential, ψ.* The perfectly bonded glass/polycarbonate interface is assumed to be in a stable equilibrium, in which case the potential ψ has a minimum and all tractions vanish. For any other configuration, the value of the potential is taken to depend only on the normal, U_n, and tangential displacements discontinuities (jumps), U_t, across the interface. The interface potential of the following form initially proposed by Socrate [2.7] is used in the present study:

$$\psi(U_n, U_t) = \left\{ \{-e\sigma_{\max}\delta_n + \frac{1}{2}\tau_{\max}\delta_t \log\left[\cosh\left(2\frac{U_t}{\delta_t}\right)\right]\right\}\left[e^{-\frac{U_n}{\delta_n}}\left(1+\frac{U_n}{\delta_n}\right)\right] \qquad (2.3)$$

where the parameters $\sigma_{\max}$ and $\tau_{\max}$ are, respectively, the normal and tangential interfacial (cohesion) strengths, and δ_n and δ_t are the corresponding characteristic interface (separation/ sliding) lengths. Differentiation of Eq. (2.3) with respect to U_n and U_t yields the following expressions for the normal and tangential interfacial tractions:

$$F_n(U_n,U_t)=\left\{e\sigma_{\max}-\frac{1}{2}\tau_{\max}\frac{\delta_t}{\delta_n}\log\left[\cosh\left(2\frac{U_t}{\delta_t}\right)\right]\right\}\left[\frac{U_n}{\delta_n}e^{-\frac{U_n}{\delta_n}}\right] \tag{2.4}$$

$$F_t(U_n,U_t)=\left[\tau_{\max}\tanh\left(2\frac{U_t}{\delta_t}\right)\right]\left[e^{-\frac{U_n}{\delta_n}}\left(1+\frac{U_n}{\delta_n}\right)\right] \tag{2.5}$$

Graphical representations of the two functions defined by Eqs. (2.4) and (2.5) are given in Figures 2.6(a)-(b), respectively. If F_n given by Eq. (2.4), is expressed for the case of purely normal interface decohesion, and the F_t for the case of pure sliding, one obtains:

$$F_n(U_n,U_t=0)=F_n^o(U_n)=e\sigma_{\max}\left(\frac{U_n}{\delta_n}e^{-\frac{U_n}{\delta_n}}\right) \tag{2.6}$$

$$F_t(U_n=0,U_t)=F_t^o(U_t)=\tau_{\max}\tanh\left(2\frac{U_t}{\delta_t}\right) \tag{2.7}$$

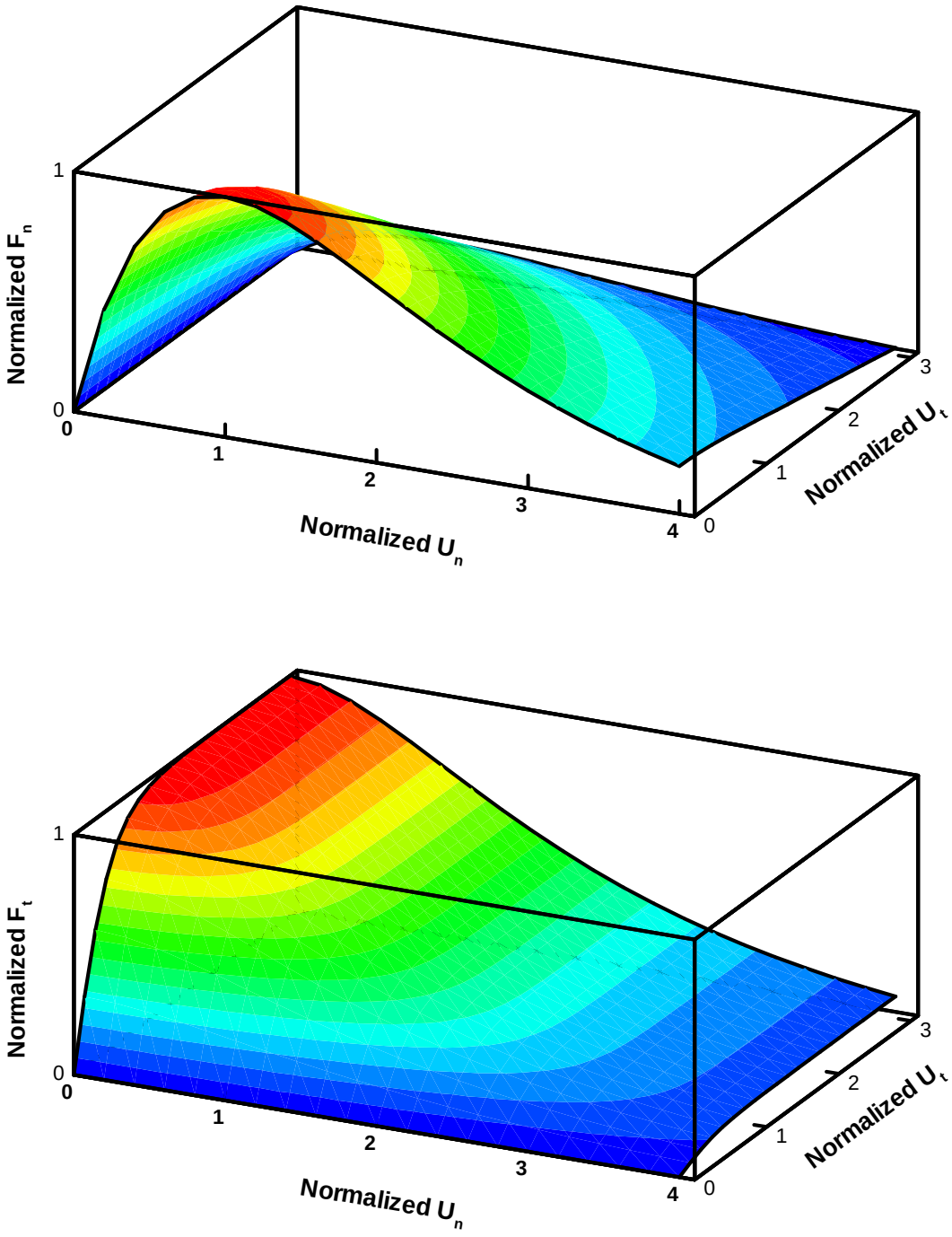

Figure 2.6: Normalized normal, Fn, and tangential components, Ft, of the traction per unit interface area, as a function of the normalized normal, U_n, and normalized tangential, U_t, components of the interface displacements.

An inspection of Eqs. (2.6) and (2.7) shows that the glass/polycarbonate interface behavior is characterized by four parameters: $\sigma_{\max}, \delta_n, \tau_{\max}$ and δ_t; where $\sigma_{\max}$ is the peak normal traction for purely-normal interface decohesion (i.e. the normal decohesion strength); δ_n is the normal interface separation which corresponds to this peak traction; $\tau_{\max}$ is an asymptotic shear traction for interface sliding (i.e. the shear decohesion strength); and δ_t is a characteristic length in pure sliding, which corresponds to a shear traction 1% lower than $\tau_{\max}$, i.e. $F_t^o(\delta_t) \approx 0.99\,\tau_{\max}$. For the case of polyurethane bonded glass/polycarbonate interfaces, these four parameters were determined in our previous work [2.8].

2.4 Results and Discussion

In Section II.2, a detailed description was provided regarding the transient non-linear dynamics finite element analyses of the multi-hit ballistic protection tests of a prototypical laminated transparent-armor system. In the present section, the main results of the multi-hit ballistic protection computational analyses are presented and discussed.

2.4.1 Multi-hit Ballistic Performance of the Transparent Armor System

To validate the present multi-hit ballistic performance computational analyses, the analyses were carried out at the same initial velocities of the M2AP full metal jacket (FMJ) armor piercing bullets as those used in the work of Dolan [2.2], Table 2.2. The results of these analyses are listed in the last column of Table 2.2. It is seen that, for the most part, the experimental and the computational results are in full agreement. However, the computational analyses carried out did not reveal the presence of the zone of mixed results. One possible explanation for this apparent discrepancy is the fact that the same initial population of pre-existing flaws was assumed in all the computational analyses carried out in the present work. In the experimental work of

Dolan [2.2], on the other hand, each multi-hit ballistic-protection test was carried out using a different laminated transparent-armor panel. Due to the statistical nature of the size and potency of pre-existing flaws, each of the test panels used in the work of Dolan [2.2] is expected to have contained different populations of the flaws. Our preliminary investigation has shown that the zone of the mixed results could be obtained if different initial populations of the flaws are taken in the analyses of ballistic-protection performance of the transparent-armor test panels at different projectile velocities. However, to fully account for the effect of variations in the initial population of the pre-existing flaws, a more rigorous statistical procedure should be employed to analyze the obtained computational results. Such an analysis was beyond the scope of the present work.

2.4.2 Temporal Evolution of the Bullets' Velocity

In order to better understand the multi-hit ballistic-protection performance of the transparent armor samples studied in the present work, temporal evolution of the velocity for each of the four M2AP full metal jacket (FMJ) armor piercing bullets are recorded and analyzed. An example of the results pertaining to the temporal evolution of the velocities of the four projectiles in the case of the initial bullet velocity of 682 m/s (the highest velocity at which partial penetration of the armor was observed in the work of Dolan [2.2]) is displayed in Figure 2.7 (a). For each of the four bullets, an 'X' is used to denote the moment when the bullet first makes contact with the armor, while a ' ● is used to denote the instant of bullet arrest. To quantify the multi-hit ballistic performance of the armor in this (partial-penetration case), the time periods between the bullet/armor first contact and the bullet arrest is recorded for all four bullets as follows: bullet 1, 35μs; bullet 2, 320μs; bullet 3, 37μs; and bullet 4, 39μs. These results clearly revealed that the ability of the armor to defeat the projectile is compromised by the prior impact of the armor by the projectile(s). In addition, the effect of higher local levels of failure strength (associated with the current population of flaws) and the proximity of the lateral confinement

induced by the clamped edges of the test panels is also revealed. Consequently, it takes the (undamaged) armor 35μs to stop the first bullet while the same armor after suffering damage due to the impacts of bullets 1-3 takes 39μs to stop the fourth bullet. On the other hand, higher levels of failure strength and the proximity of the right clamped edge to the impact locations of bullets 3 and 4 limits the extent of damage in the armor and, consequently it takes the armor only a slightly longer time to defeat bullet 4 than bullet 3 (39μs vs. 37μs). Also, it is clear that since the damage region produced by the impact of bullets 1 and 2 did not extend to the region of impact of the bullets 3 and 4, the times it takes the armor to stop bullets 1,3 and 4 are quite comparable.

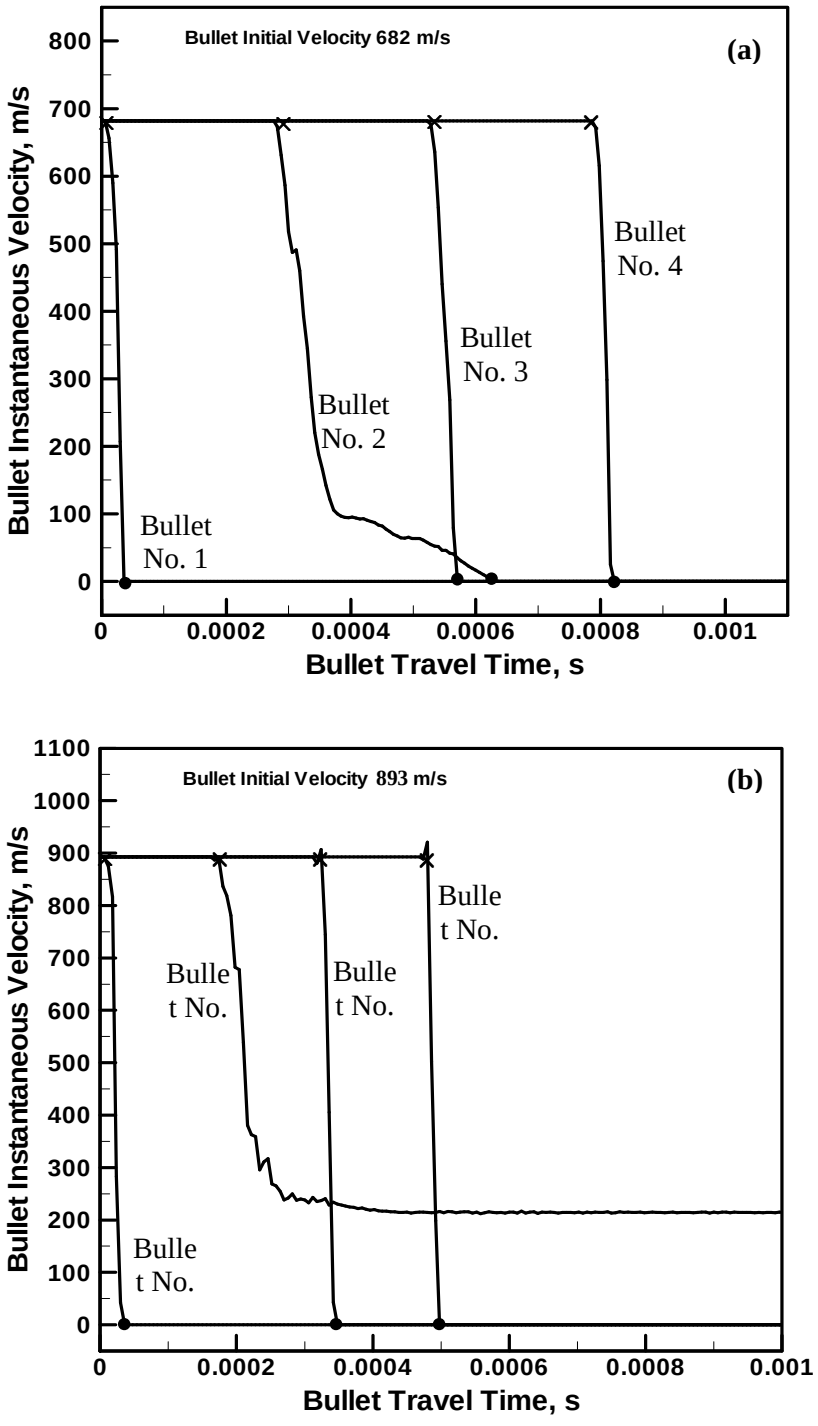

Figure 2.7: Temporal evolutions of the velocity of four M2AP projectiles during their impact with the laminated transparent-armor system for the initial projectile velocities of: (a) 682 m/s; and (b) 893 m/s.

An example of the results pertaining to the temporal evolution of the velocities of the four projectiles in the case of the initial bullet velocity of 893 m/s (the highest bullet velocity used in the work of Dolan [2.2]) is displayed in Figure 2.7 (b). For each of the four bullets, an 'X' is used to denote the moment when the bullet first makes contact with the armor, while a ' • is used to denote the instant of bullet arrest (where applicable). To quantify the multi-hit ballistic performance of the armor in this case the time periods between the bullet/armor first contact and the bullet arrest (where applicable) or the bullet's exit velocity (where applicable) were recorded for all four bullets as follows: bullet 1, 40μs; bullet 2, 247.2m/s; bullet 3, 41.5μs; and bullet 4, 43μs. The results displayed in Figure 2.7 (b) clearly show the effect of the multi-hit scenario on the ballistic performance of the transparent armor. Specifically:

(a) While bullet 1 is fully stopped after 40μs, bullet 2 fully penetrates the armor with a residual velocity of 247.2 m/s;

(b) Since the impact location of bullet 3 is farther away from those of bullets 1 and 2 and the damage induced by bullets 1 and 2 did not extend to the impact location of bullet 3, the armor is successful in stopping bullet 3 and the time to stop bullet 3 is comparable to that for bullet 1.

(c) Since the impact location of bullet 3 is in the vicinity of the right clamped edge of the armor test panel, the resulting damage is apparently not large and wide spread to significantly affect the time to stop bullet 4.

2.4.3 Spatial Distribution of Armor Damage

In order to further reveal details regarding the multi-hit ballistic-protection performance of the transparent armor test-panels studied in the present work, the final spatial distribution of damage in different glass and polycarbonate laminae are recorded and analyzed. An example of the results pertaining to the final spatial distribution of damage within different laminae of the

transparent-armor system in the case of the initial bullet velocity of 682 m/s (the highest velocity at which partial penetration of the armor is observed in the work of Dolan [2.2]) is displayed in Figures 2.8(a)-(e). In Figures 2.8(a)-(e), five lamina-pairs (each consisting of a glass lamina and the adjacent polycarbonate lamina) are displayed. To improve clarity, glass laminae are assigned a white color while the polycarbonate laminae are assigned a cyan color. In Figure 2.8(a), the glass lamina corresponds to the transparent-armor strike face, while in Figure 2.8(e), the polycarbonate lamina corresponds to the armor back-face. An inspection of the results displayed in Figures 2.8(a)-(e) reveals that:

(a) While the polycarbonate laminae suffer a highly localized damage with a size of the damage region only slightly exceeding the cross-sectional area of the bullet(s), the extent of damage in glass panels is widely spread;

(b) In addition to the damage regions surrounding the points of impact of the four bullets, damage in glass laminae in the regions adjacent to the clamped edges of the test panels are also observed. These peripheral regions of damage are mainly caused by the tensile stress waves reflected off the panel edges and by a higher population of the flaws in the glass laminae at and near their lateral faces;

(c) The role of prior bullet impact(s) in reducing the ballistic protection performance of the transparent-armor and the role of the lateral confinement of the test panels on increasing the ballistic performance can be seen by examining the extent of penetration of the armor by the four bullets. The results of this examination are fully consistent with those displayed in Figure 2.8(a). For example, while bullet 1 manages to penetrate only the top-most glass lamina, the tip of bullet 2 is arrested within the third polycarbonate lamina; and

(d) When analyzing the results displayed in Figures 2.8(a)-(e), it should be recalled that the material model for glass used in the present work eliminates the finite elements which contain

discrete (coarse-fragment) cracks. In other words, glass panel regions containing macro cracks which are commonly observed during testing of the ballistic performance of transparent-armor are removed from the model in the present finite-element formulation. In sharp contrast, finite elements undergoing structural damage due to nucleation of numerous sub-micron cracks are retained in the model. In this way, regions of the glass laminae fractured in the coarse-fragmentation regime and those undergoing a fine-fragmentation failure could be distinguished.

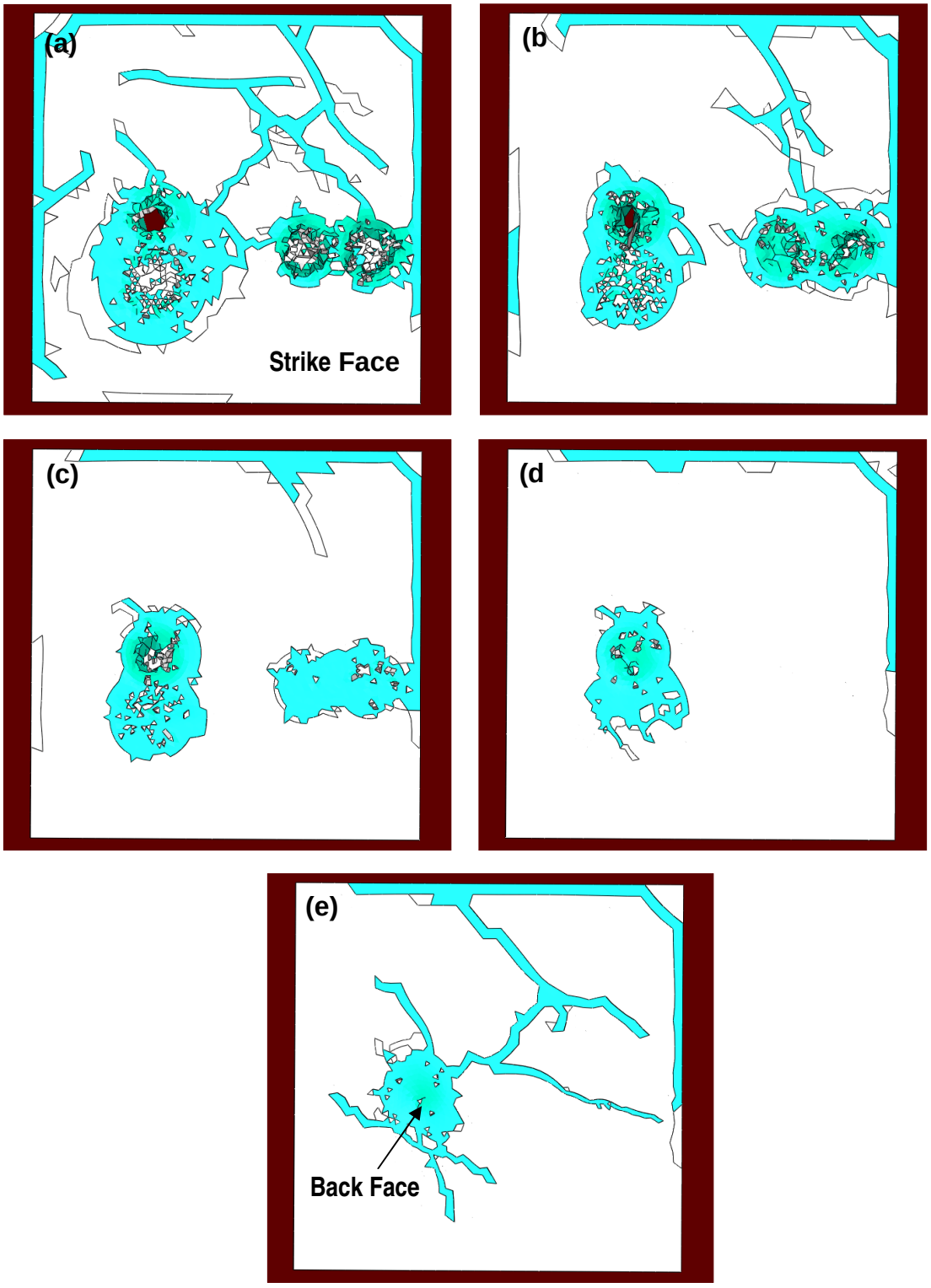

Figure 2.8: Spatial distribution of damage and failure in different glass-polycarbonate lamina pairs for the case of initial projectiles' velocity of 682m/s.

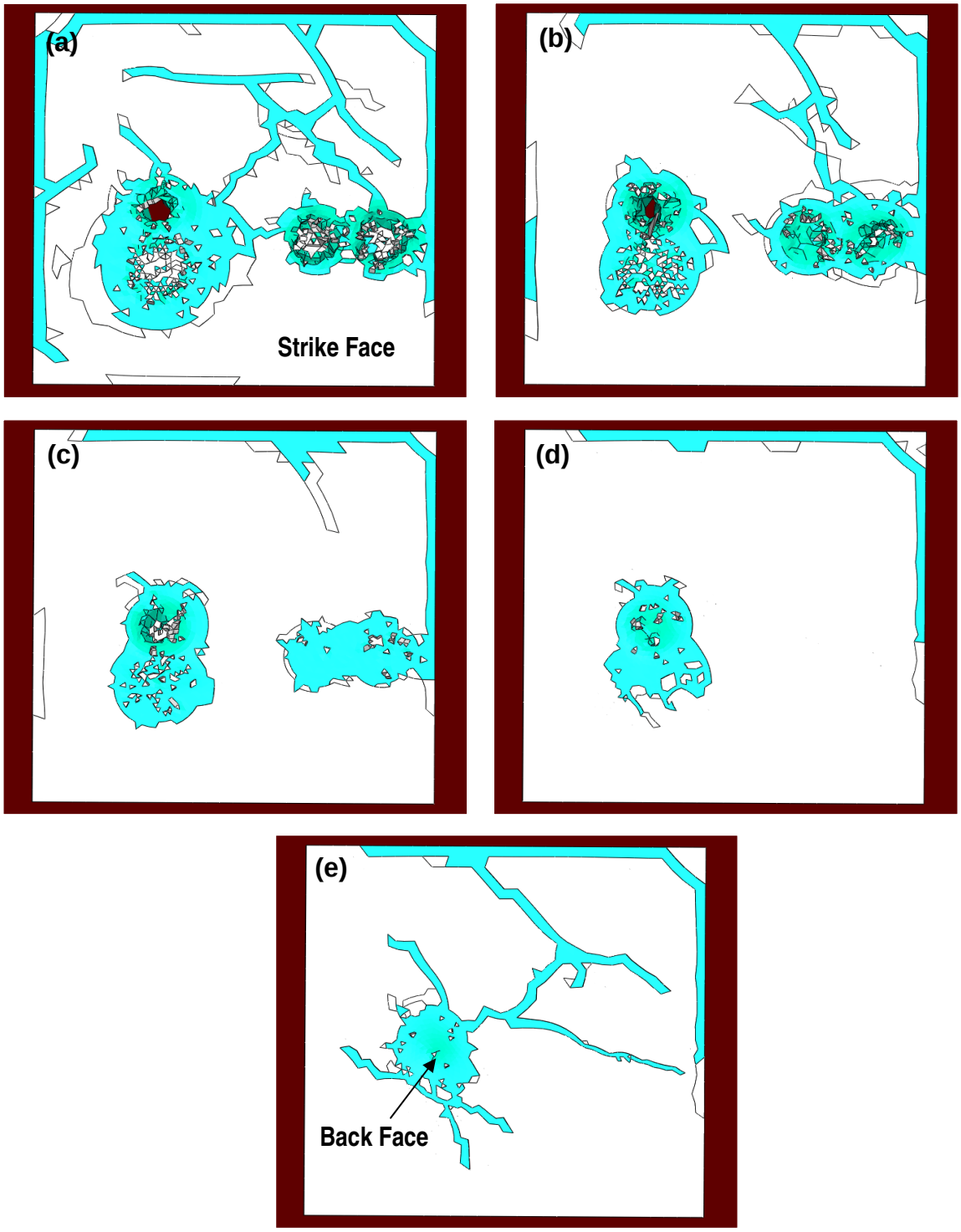

Figure 2.9: Spatial distribution of damage and failure in different glass-polycarbonate lamina pairs for the case of initial projectiles' velocity of 893m/s.

An example of the results pertaining to the final spatial distribution of damage within different laminae of the transparent-armor system in the case of the initial bullet velocity of 893 m/s (the highest bullet velocity used in the work of Dolan [2.2]) is displayed in Figures 2.9(a)-(e). The results displayed in Figures 2.9(a)-(e) are quite similar to their corresponding counterparts displayed in Figures 2.8(a)-(e) except that the extent of damage is somewhat more wide spread and for the fact that bullet 2 fully penetrates the test armor panel.

2.4.4 The Role of Polycarbonate Laminae

As explained earlier, the main role of polycarbonate laminae is to gather the glass fragments and prevent them from entering the interior of the vehicle. Under the standard transient non-linear dynamics analysis conditions used in the present work, this role of the polycarbonate laminae could not be readily revealed (primarily due to the fact that glass-fragments/polycarbonate-laminae interactions were taking place in the interior of the transparent-armor panel). To reveal this role of the polycarbonate laminae, a few analyses were carried out under no-interaction conditions between the glass fragments and the polycarbonate laminae. An example of the results obtained in these analyses is displayed in Figure 2.10. While under the standard transient non-linear dynamics analysis conditions used in the present work no glass fragments were observed past the back face of the armor, such fragments are clearly seen in Figure 2.10. Thus, the present computational approach is capable of accounting for the role of polycarbonate laminae in gathering the glass fragments.

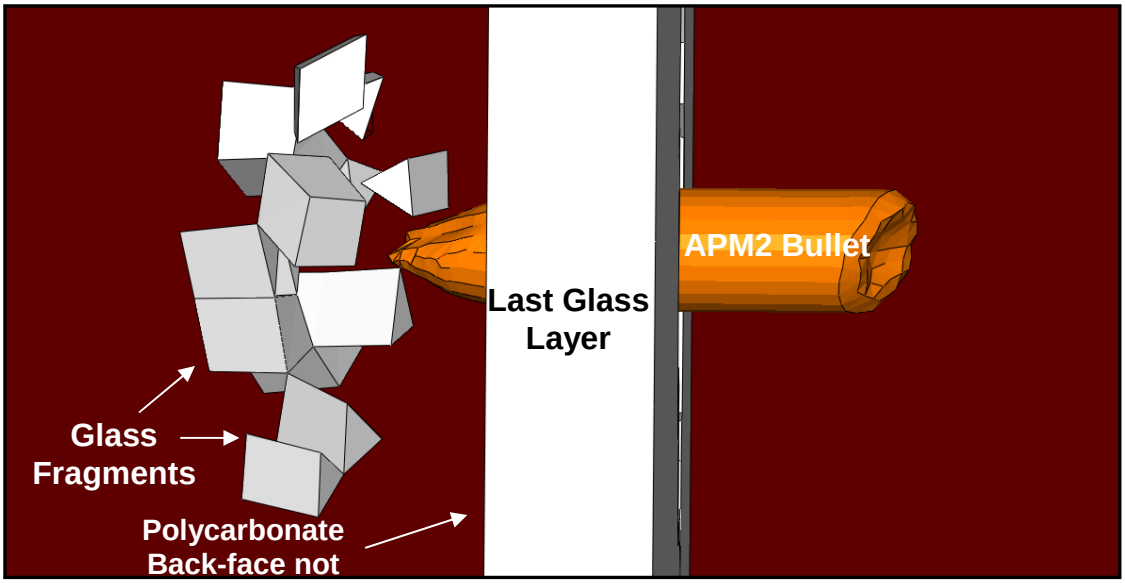

Figure 2.10: When interactions between the glass fragments and the polycarbonate laminae are suppressed, glass fragments can enter the interior of the vehicle.

2.4.5 Transparent-armor Ballistic-protection Resistance with Respect to the FSPs

In the initial stage of his experimental investigation, Dolan [2.2] carried out a couple of tests dealing with the ballistic-protection performance of the transparent-armor with respect to the 0.50 caliber right circular cylinder steel FSPs. It was found that even at the fragment velocities as low as 592m/s, the transparent-armor test panels were *over-matched* by the FSPs. To further validate the computational procedure used in the present work, few computational analyses dealing with the impact of a 0.50 caliber right circular cylinder steel FSP and the transparent-armor test panel were carried out. The results (not shown for brevity) obtained revealed that indeed the test panels were not able to stop a single FSP at the fragment velocity of 592m/s. This finding provides additional evidence for physical soundness of the computational method and material models used in the present work.

2.4.6 Future Work

The comparison between the multi-hit ballistic-protection performance computational results and their experimental counterparts obtained in the work of Dolan [2.2] for a prototypical laminated glass/polycarbonate transparent-armor system revealed that the computational analyses and the material models used can quite realistically account for the field-test observations. Given this fact, our ongoing work is aimed at extending the present investigation into the area of design optimization in order to examine how the design parameters such as the number of glass and polycarbonate laminae, the laminae thicknesses and the grades of these materials and the bonding strength of the polyurethane adhesive can be selected to further enhance the multi-hit ballistic protection performance of transparent armor.

2.5 Summary and Conclusions

Based on the computational analyses of the multi-hit ballistic-protection performance of laminated transparent-armor test panels, the following main summary remarks and conclusions can be drawn:

1. When properly constructed, transient non-linear dynamics computational analyses can be a useful tool in understanding the multi-hit ballistic-protection performance of laminated glass/polycarbonate transparent armor systems.

2. These analyses can clearly reveal and quantify the extent of loss of the ballistic-protection performance of the armor caused by a sequence of closely spaced bullet impacts.

3. Through a proper definition of the multi-hit bullet/armor problem and the careful selection of the material models, a reasonably good agreement was obtained between the computational results obtained in the present work and their experimental counterparts obtained by Dolan [2.2].

4. The role of polycarbonate laminae in gathering the glass fragments and preventing them from entering the vehicle interior has also been revealed using the present computational analysis.

5. The experimentally observed lack of the ballistic protection resistance of the transparent-armor test panels with respect to the 0.50 caliber FSPs is also confirmed computationally.

2.6 References

2.1 ABAQUS version 6.7, User Documentation, Dessault Systems, 2007.

2.2 Dolan, A. M., *Ballistic Transparent Armor Testing Using a Multi-hit Rifle Pattern*, Bachelors' Thesis, Kettering University, December 2007.

2.3 M. Grujicic, B. Pandurangan, N. Coutris, B. A. Cheeseman, C. Fountzoulas, P. Patel and E. Strassburger, *A Ballistic Material Model for Starphire®*, a Soda-Lime Transparent-Armor Glass, Materials Science and Engineering-A, 491, 1-2, 2008, 397-411.

2.4 M. Grujicic, B. Pandurangan, U. Zecevic, K. L. Koudela and B. A. Cheeseman, *Ballistic Performance of Alumina/ S-2 Glass-Reinforced Polymer-Matrix Composite Hybrid Lightweight Armor Against Armor Piercing (AP) and Non-AP Projectiles*, Multidiscipline Modeling in Materials and Structures, 3, 2007, 287-312.

2.5 E. Strassburger, P. Patel, J. W. McCauley, C. Kovalchick, K. T. Ramesh and D. W. Templeton, *High-Speed transmission Shadowgraphic and Dynamic Photoelasticity Study of Stress Wave and Impact Damage Propagation in Transparent Materials and Laminates Using The Edge-on Impact Method*, Proceedings of the 23rd International Symposium on Ballistics, Spain, April 2007.

2.6 A. Needleman, *A Continuum Model for Void Nucleation by Inclusion Debonding*, J. Appl. Mech., 54, 1987, 525-531.

2.7 S. Socrate, *Mechanics of Microvoid Nucleation and Growth in High-strength Metastable Austenitic Steels*, PhD thesis, Massachusetts Institute of Technology, 1995.

2.8 M. Grujicic, V. Sellappan, B. Pandurangan, G. Li, N. Seyr, M. Erdmann and J. Holzleitner, *Computational Analysis of Injection-Molding Residual-Stress Development in Direct-*

Adhesion Polymer-to-Metal Hybrid Body-In-White Components, Materials Processing Technology, 203, 1-3, 2008, 19-36.

2.9 T. Bjerke, Z. Li and J. Lambros, *Role of Plasticity in Heat Generation during High Rate Deformation and Fracture of Polycarbonate*, International Journal of Plasticity, 18, 2002, 549-567.

2.10 M. Grujicic, B. Pandurangan, W. C. Bell, N. Coutris, B. A. Cheeseman, C. Fountzoulas and P. Patel, *An Improved Mechanical Material Model for Ballistic Soda-Lime Glass*, Journal of Materials Engineering and Performance, 18, 8, 2009, 1012-1028.

2.11 M. Grujicic, B. Pandurangan, N. Coutris, B. A. Cheeseman, C. Fountzoulas and P. Patel, *A Simple Ballistic Material Model for Soda-Lime Glass, International Journal of Impact Engineering*, 36, 2009, 386-401.

2.12 M. Grujicic, W. C. Bell, B. Pandurangan, B. A. Cheeseman, C. Fountzoulas, P. Patel, *The Effect of High-pressure Densification on Ballistic-penetration Resistance of Soda lime Glass, Journal of Materials Design and Applications*, submitted for publication, 2011.

2.13 M. Grujicic, W. C. Bell, P. S. Glomski, B. Pandurangan, B. A. Cheeseman, C. Fountzoulas, P. Patel, *Multi-Length Scale Modeling of High-Pressure Induced Phase Transformations in Soda-Lime Glass*, Journal of Materials Engineering and Performance, DOI: 10.1007/s11665-010-9774-2, 2010.

2.14 M. Grujicic, W. C. Bell, B. Pandurangan, B. A. Cheeseman, C. Fountzoulas, P. Patel, *Molecular-Level Simulations of Shock Generation and Propagation in Soda-lime Glass*, Journal of Materials Science, submitted for publication, 2011.

CHAPTER THREE

A DYNAMIC MATERIAL MODEL FOR BOROFLOAT® WHICH ACCOUNTS FOR THE MICROSTRUCTURAL/COMPOSITIONAL DIFFERENCES BETWEEN THE TIN AND AIR PLATE-GLASS SURFACES

3.1 Abstract

Our recently developed continuum-level, physically-based, high strain-rate, large-strain, high-pressure mechanical material model for soda-lime glass has been enhanced to include differences in the flaw-size population between the so-called *air-side* and the so called *tin-side* of float glass plates, and adapted for use in the case of borosilicate glass. The model was structured in such a way that it is suitable for direct incorporation, as a material user-subroutine, into standard commercial transient non-linear dynamics finite-element based software packages. The model was parameterized using various open-literature sources. The experimental portion of the work, which consisted of 28 projectile impacts onto glass/polyurethane/polycarbonate-based test laminates, was intended to allow for quantification of the effect of air- vs. tin-side borofloat strike surface when incorporated into a multi-layer, multi-functional test laminate. Experimental findings indicated the lack of a significant difference in the impact resistance of air- vs. tin-side test laminate strike surfaces. Subsequent to these findings computational simulations were carried out in order to establish if the proposed borofloat material model could capture the prominent experimentally observed damage modes and the measured V50, reconfirming the experimental findings. In general, a good agreement was found between the computational and the experimental results.

3.2 Introduction

Impact-resistant glass is a material (or more often a system of materials) designed to be optically transparent while providing the necessary level of protection against high-rate loading (e.g. those associated with storm winds, blasts, high-speed fragments and projectiles, etc.). This class of materials is used in such diverse applications as storm windows, automobile windshields, bullet-resistant windows, protective visors for non-combat usage (e.g. riot control or explosive ordinance disposal) or as transparent-armor systems (to protect on-board instruments/sensors from fragments and debris, and to protect vehicle occupants from terrorist actions or other hostile events). The continued push for advancement in the development and application of impact-resistant glass is chiefly the result of the ever-increasing need of the military for more mass-efficient transparent materials. This need is associated with continuing escalations in the number and variety of threats and the desire of the military to become more mobile, deployable, and sustainable.

Traditionally, protective transparent structures (or systems) used in military applications are constructed of monolithic glass or transparent-elastomer inter-layered glass laminates. Among the new transparent-armor materials and technologies available today, the following have received the most attention: crystalline ceramics (e.g. aluminum-oxinitride spinel, AlON [3]), new transparent polymer materials (e.g. transparent nylon [4]), and new interlayer technologies (e.g. polyurethane bonding layers [3]), and new laminate designs (e.g. [5]). Due to the large-size and complex-shapes of most protective transparent structures in military applications, the structures are still predominantly glass-based. In other words, while ever increasing demands for reductions in weight and for improvements in impact-resistance of protective transparent structures are calling for increased use of the aforementioned new transparent materials and advanced structures, glass (as well as glass ceramics) continues to remain the material of choice

(especially in military ground-vehicle applications). The main reasons for the continued use of glass as the dominate transparent armor constituent material are: (a) compositional modifications, chemical strengthening, and controlled crystallization have demonstrated to be capable of significantly improving the impact resistance of glass [5]; and (b) glass windshields and windows can also be produced in large sizes with curved geometries, and can be fabricated to provide an incremental improvement in impact resistance at an incremental cost.

The development of new glass-based protective transparent structures with improved mass-normalized impact resistance typically includes extensive experimental test programs. Such experimental test programs are critical for ensuring the utility and effectiveness of the protective transparent structures. However, the use of experimental test programs is generally expensive, time-consuming and involves destructive testing. While the role of experimental test programs remains critical, they are increasingly being complemented by the corresponding computation-based engineering analyses and simulations. Knowledge of the constituent transparent-materials' response under high-deformation rate/high-pressure loading conditions, as described by the corresponding material model, is one of the key components in such analyses greatly affecting their utility and fidelity. In addition, it is imperative to understand the individual and combined effects of the constituent material layers in multi-layer protective transparent structures. The main objective of the present work is to help advance the use of these computational engineering analyses and simulations in protective transparent structure design applications by further developing the physically-based material model for soda-lime ballistic glass (developed in Refs. [1,2]). Specifically the new rendition of the glass material model is extended to other glass formulations (in particular to the borosilicate float glass, Borofloat® glass) and enhanced to account for the effect of microstructural/ compositional differences between the so-called air-side and the so-called tin-side of plate glass fabricated using a conventional float glass process. It

should be noted that borosilicate glass was investigated experimentally and computationally in the present work not in the form of monolithic, single-constituent test structures, but rather as a lamina in a borosilicate/polyurethane/ polycarbonate test laminate (a basic laminated transparent armor repeat unit). The main reason for this approach is that the contribution of a lamina to the laminate performance is affected not only by the material response of the lamina in question (the local effect), but also by the interactions of this lamina with the surrounding laminae/structures (the system-level effect).

It is well established that the ability of glass (as is also the case with the majority of brittle materials) to support external loading is controlled by size and morphology distribution of pre-existing flaws and that this ability is considerably lower in the case of externally applied tensile/bending loads [6,7]. Consequently the observed strength of glass is typically found to be only a minor fraction of its theoretical strength. While flaws are present throughout the entire volume of a glass structure (e.g. plate glass), it is generally recognized that a flaw distribution of higher number-density and increased potency is associated with the structure surfaces [6,7]. Consequently, when plate glass is subjected to bending, (typically mode I) cracks nucleate at pre-existing flaws on the plate-glass surface which are subject to tensile-loads. Nucleated cracks continue to propagate through the plate-glass thickness (and along its surface) as the loading is increased and will ultimately lead to complete plate fracture. The resulting measured flexural-strength values are typically found to be only around one percent of the theoretical material strength of glass (ca. 15-30GPa) [8]. In sharp contrast, tensile strengths as high as 5GPa have been achieved in glass fibers fabricated under tightly controlled laboratory conditions. This finding has been attributed to the near pristine fiber-surface finish.

As mentioned above, brittle failure in glass (as well as in the majority of brittle ceramics) is the result of nucleation (on pre-existing flaws) and propagation of the cracks. These processes

are accompanied by local and global stress attenuation/ relaxation and structure failure/fragmentation [6,7]. Finite element analyses have been extensively used over the last couple decades to elucidate the underlying mechanisms and quantify the impact resistance of protective transparent structures under high-velocity impact and penetration conditions. In these analyses, most of the effort was typically devoted to modeling the complicated post-damage initiation response of ceramic materials (i.e., the mechanical/structural response of these materials to impact loads in the presence of cracks). In general, all the existing brittle-fracture models reported in the literature, can be categorized as being either: (a) continuum based [9-12] or (b) being of a discrete nature [13]. Since a detailed overview of these two groups of brittle-fracture material models was provided in our previous work [1,2], only a brief description of these is provided below. Within the continuum-based approaches, glass is treated as a linear elastic material whose stiffness coefficients can degrade as a result of a cracking-induced damage within the material. Damage, itself, is treated as a continuum quantity which is obtained by homogenizing crack-laden material into an elastically equivalent crack-free continuum material with degraded stiffness. While within the continuum-based models cracks are considered implicitly via their effect on the material stiffness, within the discrete models for brittle fracture cracks (as well their nucleation, propagation and coalescence processes) are treated explicitly. In other words, instead of smearing-out/homogenizing cracks into a crack-free material, cracks are recognized as discrete entities which locally disrupt the continuity in displacement/stress fields and lead to local stress-concentration effects.

Numerous experimental investigations carried out over the last 30 years (e.g. [14-17]) have clearly established that distinct differences exist in the mechanical behavior of the tin-side and air-side surface of plate glass fabricated using a conventional float glass process. These differences are predominantly manifested in the flaw-size populations, indentation/micro-

hardness, and tensile/flexural strengths between the two plate glass surfaces. Furthermore, it is well established that these differences are a consequence of different chemo-thermo-mechanical histories of the two surfaces resulting from the float-glass fabrication processes. These different processing histories are believed to either change the surface flaw population and/or chemically alter the surface layer of glass (mainly through ion-exchange with the tin bath). To better understand the origin of these differences, a brief overview of the conventional float glass manufacturing process is provided in Section II.1.

While common transparent armor structures are made of cost-effective soda-lime glass, the subject material of the present investigation is borosilicate glass. When this material is fabricated in the form of plate glass using the conventional float glass process, it is commonly referred to as Borofloat®. The predominant reason for focusing on borofloat is that this material has approximately 10 percent lower mass-density than the comparable soda-lime-based glass (e.g. Starphire®).

The organization of the paper is as follows: in Sections II.1 and II.2 brief overviews are, respectively, provided of the float glass fabrication process and of the past experimental efforts aimed at highlighting and clarifying the differences in the mechanical properties of the tin-side and air-side surfaces and their subsequent effects on the overall impact resistance of glass-based protective transparent structures. In Sections III.1 and III.2 brief summaries are, respectively, presented of our recent continuum-level physically-based material model for soda-lime glass [1,2] and of the proposed modifications/up-grades to this model to include the effects of tin- vs. air-side microstructural/compositional differences and to reflect the borosilicate nature of the subject material. Details regarding the experimental and computational procedures used to generate the data needed for validation of the upgraded borofloat material model are discussed in Sections IV.1 and IV.2, respectively. The main results obtained in the present work are presented and

discussed in Section V. The key conclusions resulting from the present work are summarized in Section VI.

3.3 Float Glass Fabrication and mechanical testing

3.3.1 Float Glass Fabrication

3.3.1.1 Fabrication Process

Float glass is made using the Pilkington [18] process utilizing silica sand, boric acid, soda ash, limestone, with additional batch materials and other refining agents. These batch/constituent materials are mixed and subsequently combined with cullet (crushed glass) as they are fed into the melting zone of a multi-zone glass fabrication furnace. Within the melting zone of the furnace, preheated air and jets of natural gas are combined and combusted to create a torch-like flame producing temperatures of about 1300-1500°C, melting the pre-mixed materials in minutes. Upon complete melting, the molten glass enters the next furnace zone to begin the so-called *fining process* during which the gas bubbles within the molten glass (common byproducts of the glass melting process) are allowed to escape into the furnace atmosphere. After several hours of fining, the glass then flows into the *forming chamber* onto a molten tin bath at approximately 1100°C. To ensure uniform spreading of the molten glass onto the molten-tin bath (which can have lateral dimensions as large as 3-4 meters) refractory guides are used to control the flow trajectory, while a canal gate is used to control the flow rate. Tin is chosen as the molten-glass float medium due to its relatively high density (which ensures that the glass remains buoyant), a low melting temperature (in order to lower manufacturing power consumption), immiscibility with molten glass (to minimize chemical contamination of the glass), and high cohesion (to minimize wetting of and adhesion to the tin-side as it solidifies). As the molten glass flows down the length of the forming chamber it begins to cool creating a continuous ribbon of semi-solid

material. To prevent the oxidation of tin and the formation of tin oxide (dross) which tends to adhere to glass, the forming chamber atmosphere is typically made up of nitrogen and hydrogen. Heating elements above the glass (which allow for strict temperature control of the glass face exposed to the forming chamber atmosphere, the glass air-side) and motor-driven stretching sprockets (which dig in to the molten glass at the ribbon edges) allow for precise control of the ribbon thickness.

As the glass exits the forming chamber, it has achieved its final thickness. Next the glass ribbon enters the so-called *lehr chamber* where it is cooled from an entrance temperature of 600°C down to 200°C at its exit. The rate of cooling is closely controlled in order to obtain the desired residual stress distribution through the ribbon thickness. Final cooling to room temperature is carried out on the open-air roller-type conveyer using an array of fans. During this time the quality of the fabricated float-glass ribbon is inspected by a number of instruments to determine uniformity of thickness and the potential presence of surface flaws/imperfections. Once fully hard, the continuous glass ribbon is sectioned into discrete plates of predetermined dimensions. The sectioning process is typically carried out by scoring the ribbon surface with CNC carbide rollers and snapping the scored ribbon. The glass plates then continue along the main-line conveyers (while still having their tin-side in contact with the rollers) to a production-line inspection station where they are visually examined for surface or edge defects/imperfections. Before the glass plates are stacked for packing and shipping, they are dusted with a fine powder that acts as a separation medium.

3.3.1.2 Microstructure and Flaw Content of As-fabricated Float Glass

Under most applications of plate glass the flaw content (particularly the one on the plate glass surfaces) is not high enough to significantly affect the functional performance of the glass structure. However, under extreme loading conditions, such as those encountered in the case of

blast or high-velocity projectile impact, fabrication/handling-induced flaws can profoundly affect the impact resistance of plate glass. Based on the description of the float glass process given above and various microstructural investigations of glass (e.g. [14-17]) it is clearly established that there are at least three main sources of flaws on the tin-side of plate glass: (a) flaws induced through mechanical contact with conveyer rollers during the advancement of the glass ribbon and discrete glass plates along the production line. Conveyer roller damage is readily apparent (visible) when the glass ribbon exits the lehr and begins the final cooling stage as it is still soft and the rollers leave visible imprints at the ribbon edges. These ribbon edges are later removed through the use of a longitudinal scoring/breaking process similar to the one described above; (b) flaws associated with tin-oxide particulates adhering to the tin side surface. These tin-oxide particulates are made visible through the use of an ultraviolet radiation lamp which selectively illuminates the tin-oxide structure. In fact, this is the common procedure for identifying the tin-side in as-fabricated plate glass; and (c) flaws induced by tensile stresses associated with thermal gradients present within regions adjacent to the glass-ribbon/tin-bath interface.

In addition to the aforementioned changes in the flaw population on the plate glass tin-side, it has also been demonstrated that tin can diffuse into glass via an ion-exchange process with silicon. A typical diffusion distance can be as large as 50μm [19]. Within the glass, tin tends to integrate into silicate network as either SnO or SnO_2. As a result, the number of non-bridging oxygen atoms in glass is reduced leading to a decrease in the thermal expansion coefficient and an increase in the elastic modulus of the tin-enriched plate glass surface-layer. It is generally expected that these microstructural/compositional changes present at the plate glass tin-side may also affect impact strength of the glass-based protective transparent structures.

As far as the air-side of the plate glass is concerned, its flaw population is going to be mainly dominated by the attendant thermal gradients experienced by the glass ribbon during the float glass manufacturing process.

3.3.2 Mechanical Tests Used to Reveal Tin- vs. Air-side Differences

An open literature review carried out as part of the present work revealed that a great amount of research effort has been put forth in recent decades in order to experimentally characterize the mechanical response of float glass under various loading conditions and to highlight/quantify micro-structure/property differences between the air-side and tin-side. The review also revealed that the most commonly utilized tests are the bi-axial flexure test (used to reveal the characteristic strength of the plate glass back face that is subjected to tension) and indentation tests (based on the use of different indenter geometries, e.g spherical and diamond tip, used to determine the critical indentation loads at the onset of various damage modes, e.g. Hertzian ring, radial, cone, or median cracks and material surface build-up surrounding the indentation). In addition, the following tests have also been employed: (a) *Klosky bar-type test*, a high-rate flexural test used to reveal strain-rate dependency of the material mechanical response; (b) *dilatometry*, used to determine the coefficient of thermal expansion; (c) *sonic resonance*, used to determine the material local, elastic modulus; (d) *dynamic fatigue tests*, used to quantify the effect of moisture on the strain-rate dependency of glass strength; and (e) *fractography*, used to determine the pre-existing surface-flaw geometry and dimensions.

The literature review carried out in the present work revealed the following main experimental findings regarding the (microstructural/property) differences and similarities between the air-side and the tin-side:

(a) The air-side characteristic flexural strength (one of the failure probability Weibull-distribution parameters) is typically greater by a factor between 1.2 and 2.0 relative to that of the tin-side, Refs. [15-17];

(b) The average air-side flaw size is generally smaller by a factor of 1.5 to 2.0 relative to its tin-side counterpart, Refs. [16,17]. This finding is clearly consistent with that made in (a) and can be attributed to damage induced by mechanical contact of the glass ribbon tin-side with the conveyer rollers;

(c) Both the air-side and the tin-side of borofloat plate glass show a positive stress rate dependence of their characteristic strength and the two dependences are quite comparable, Ref. [17];

(d) The air-side Weibull modulus (the second Weibull-distribution parameter) is in general smaller by a factor of 1/3-1/2 relative to the tin-side, Ref. [16]. This finding and the one stated in (a) indicate that the air-side flaw distribution is broader (associated with a smaller value of the Weibull modulus) and shifted toward higher strength levels in the air-side case. Also, this finding suggests that mechanical contact between the tin-side and the conveyer rollers results not only in more potent (larger) flaws but also in a narrower distribution of flaw-size, while on the air-side flaw generation is a more random process which yields a broader flaw-size distribution;

(e) The tin-side elastic modulus is typically ca. 15 percent higher than its air-side counterpart; Ref. [19]. As stated earlier, this finding can be attributed to the fact that, at the tin-side, SnO and SnO_2 are incorporated into the silicate network resulting in a reduced fraction of non-bridging oxygen atoms and result in an increase in the overall network connectivity;

(f) The tin-side coefficient of thermal expansion is typically lower by about 20 percent as compared with its air-side counterpart; Ref. [19]. This finding can be explained using the same argument as that presented in (e); and

(g) The tin-side indenter critical load associated with the nucleation of Hertzian ring cracks (the first type of cracks to form during a spherical-indenter indentation test) is on average 15 percent higher than its air-side counterpart, Ref. [15]. This finding appears to be related to one given in (e) which indicated a higher compliance of the air-side surface layer.

3.4 Glass material model [1,2] – Overview and extension

3.4.1 A Brief Overview of the Soda-lime Glass Material Model [1,2]

3.4.1.1 Physical Foundation of the Model

The soda-lime glass material model developed in our previous work [1,2] was an attempt to account for the fact that the mechanical response of soda-lime glass is drastically different under low deformation-rate (i.e. quasi-static) and high deformation-rate (i.e. impact) loading conditions (e.g. [3,4]). Under quasi-static loading conditions, glass typically fails by the propagation of a single or a couple of discrete cracks and only a few fragments are created after complete fracture. In sharp contrast, under dynamic loading conditions, glass tends to undergo substantial damage (resulting from the formation of a large number of micron and submicron-size cracks) and tends to undergo comminution (i.e. forms a large number of sub-millimeter size fragments). In both cases, however, the failure is believed to be controlled by pre-existing flaws which, when subjected to sufficiently large (tensile or shear) stresses, can become cracks. A brief overview of the two failure regimes (i.e. the quasi-static coarse-fragmentation regime and the dynamic comminution regime) is presented below while a more quantitative discussion of the same can be found in Refs. [1,2].

The occurrence of the two fracture regimes is believed to be the result of the competition between two internal processes accompanying loading of glass: (a) crack formation at the pre-existing flaws and crack growth. The nucleation of cracks is accompanied by the formation of so-

called "*shielding*" zones, i.e. the zones surrounding the cracks within which the stresses are highly relaxed and the probability for nucleation of additional cracks is very small; and (b) the increase in stress level due to continued loading which promotes the formation of additional cracks (at less potent pre-existing flaws). Since the crack formation process is typically associated with mechanical instability (i.e. once a crack is nucleated it continues to grow at a terminal velocity until it reaches the free surface or another crack), low loading rates tend to promote the coarse fragmentation fracture regime. In other words, once a crack or a couple of cracks are formed, they can extend over the entire structure before the stress at other flaws has reached a high enough level to form additional cracks. Conversely, high loading rates promote the formation of a large number of cracks, i.e. the critical stress level for crack nucleation is reached at many pre-existing flaws before the previously-nucleated cracks have a chance to extend far enough and shield these flaws from the externally applied stress.

3.4.1.2 Simplifying Assumptions and Basic Components of the Model

The following are the key simplifying assumptions and basic components of the model developed in Refs. [1,2]:

(a) The distribution of pre-existing flaws throughout the material was assumed to follow the Weibull-type distribution with different distribution parameters being used for the surface/near-surface regions and the bulk region of glass target plate;

(b) Both the nucleation of micro-cracks (which leads to comminution) and macro-cracks (which leads to coarse fragmentation) were postulated to be governed by the same maximum principal normal stress-based damage (mode I cracking) initiation criterion;

(c) It was further assumed that it is the loading/stress rate at the moment of crack nucleation which determines if a crack will remain a single macro-crack within the given finite element resulting in the coarse-fragmentation failure mode of the element or the crack will be

accompanied by the formation of many additional micro-cracks leading to progressive damage and ultimate fine-fragmentation failure of the element. To separate these two regimes of fracture within the bulk and the surface regions, competition between the coarse-fragmentation and the fine-fragmentation modes was analyzed under constant stress-rate loading conditions. This procedure yielded separate values for the critical stress-rate associated with this transition for the bulk and surface regions, respectively. At stress rates below the critical value, a single crack fracture regime was assumed while at stress rates above it a multiple-crack regime was adopted;

(d) When a material element begins to fail via the single-crack mode, the (single) crack nucleated within that element (in accordance with the aforementioned stress-based damage-initiation criterion) was assumed to extend at the terminal velocity. Further growth of the crack is governed by a fracture toughness-based crack growth criterion. This is accomplished as follows: (i) adjacent failed elements aligned in a particular direction are used to define the associated crack length in that direction; (ii) for an element located at a crack tip, the mode-I stress intensity factor K_I is calculated by multiplying its maximum principal stress with a factor $\sqrt{\pi a}$, where a is the crack half-length; and (iii) then, crack extension occurs by failure of an element described in (ii) when the following condition is satisfied: $K_I > K_{IC}$, where K_{IC} is the material mode-I critical stress intensity factor.

(e) When an element is undergoing fracture via the growth of the single-crack, stiffness and strength properties of this element were assumed to degrade linearly with the corresponding crack strain from the point of crack initiation to the point of complete traversal of the element by the crack;

(f) Once an element has started undergoing ("coherent") damage due to the formation of multiple cracks, stress-shielding and path-crossing effects prevent, initially, the nucleation of macro-cracks. However, when the extent of coherent damage within a single element reaches a

(stress-rate invariant) critical value, this element was assumed to fracture by micro-crack coalescence and to lose most of its ability to support load. To account for the experimental observations that the resulting micro-fragments are typically confined by the surrounding non-fractured material and can support compressive and shear loads, failed elements are assigned small residual levels of shear modulus and strength; and

(g) When an element is subjected to coherent damage, the extent of damage was taken to be governed by a damage evolution equation and the extents of degradation of the corresponding stiffness and strength properties of the material were assumed to be governed by the appropriate damage-dependent stiffness and strength material constitutive relations.

3.4.2 Modification and Enhancement of the Model [1,2]

The soda-lime glass material model developed in our prior work [1,2] was, for the most part, retained in its original formulation, and only the modifications/ enhancements listed below were made. Since, detailed accounts of the mathematical formulation of the soda-lime glass model and the procedure employed for its parameterization can be found in Refs. [1,2], these details will not be presented here:

(a) In order to apply the original model to borofloat various structural (e.g. density), mechanical (e.g. stiffness, critical stress intensity factor, critical level of coherent damage at which crack coalescence takes place, etc.), and flaw-size distribution (e.g. the characteristic strength, and the Weibull modulus) parameters were re-evaluated using various open literature sources [e.g. 15,16]. A summary of the material model parameters is provided in Table 3.1. The reader is referred to Refs. [1,2] for the explanation of the symbols appearing in Table 3.1.

(b) To take into account the aforementioned effect of flaw-size distribution differences between the air-side and the tin-side, different values of two-parameter Weibull distribution parameters are assigned to the corresponding plate glass surface-material layers; a total of three

(one bulk and two surface) failure probability distributions are now considered. A list of the associated Weibull distribution parameters is provided in Table 3.1.

(c) Using the procedure outlined in Refs. [1,2], he critical stress rate at which a transition in the fracture mode between the quasi-static coarse-fragmentation regime and the dynamic comminution regime takes place was evaluated as: (a) 3.9MPa/μs for the bulk material, (b) 7.9MPa/μs for the air-side surface material, and (c) 9.5MPa/μs for the tin-side surface material.

(d) While, in the previous rendition of the model [1,2] formation of isolated cracks was allowed to take place only within the bulk portion of the plate glass, in the present model such cracks are allowed to also nucleate at the plate glass surfaces. The reason that formation of surface macro-cracks was neglected in our previous work was that the material model was primarily used in edge-on impact analyses of glass plates in which these cracks are found to be predominantly located within the bulk [3,4]. In the present work, on the other hand, macro cracks were allowed to nucleate at plate glass surfaces in order to comply with numerous experimental investigations which revealed that, during frontal impact, cracks can nucleate both at the strike face (e.g. concentric ring cracks, radial cracks, etc.) as well as at the back face (e.g. radial cracks).

(e) In our previous model, discrete cracking of an element was assumed to result in an isotropic damage, i.e. a *cracked* element was assumed to remain isotropic (although with a substantially degraded elastic modulus). In the present work, this simplification as not implemented and instead discrete cracking is assumed to produce an orthotropic degraded material. In other words, the associated damage was no longer represented using a single scalar damage variable, but rather a second order damage tensor.

Table 3.1: Material model parameters for borosilicate glass used in the present work

Property	Symbol	Value	Unit
Density	ρ	2230	kg/m^3
Mean Fracture Toughness	K_{IC}	0.75	MPa·m$^{1/2}$
Air-side Surface			
Young's Modulus	E	63.0	GPa
Poisson's Ratio	ν	0.18	-
Weibull Modulus	m	6.7	-
Mean Static Fracture Strength	$\sigma_{f,static}$	130.6	MPa
Effective Surface	Z_{eff}	1599	mm^2
Tin-side Surface			
Young's Modulus	E	69.3	GPa
Poisson's Ratio	ν	0.18	-
Weibull Modulus	m	4.0	-
Mean Static Fracture Strength	$\sigma_{f,static}$	111.9e6	MPa
Effective Surface	Z_{eff}	1599	mm^2
Bulk Material			
Young's Modulus	E	63.0	GPa
Poisson's Ratio	ν	0.18	-
Weibull Modulus	m	30.0	-
Mean Static Fracture Strength	$\sigma_{f,static}$	250.0	MPa
Effective Volume	Z_{eff}	1.0e5	mm^3

3.5 Experimental and Computational Procedures

3.5.1 Experimental Procedure

The experimental procedure used in the present work employed the impact of a stainless steel projectile onto a transparent target laminate consisting of a borofloat plate adhesively bonded to a polycarbonate backing plate of equal lateral dimensions. The experiment was originally intended to be carried out using only 5.53mm- (0.218in) diameter ball bearing (BB) projectiles (designation: SS 440C), but they proved unable to penetrate the transparent target laminate and therefore these projectiles were complemented with more massive 5.51mm-

diameter, 5.51mm-height right circular cylinders (RCC, designation: SS 440C) and with steel fragment simulating projectiles (FSP) in the shape of a RCC with a flat-nosed chisel tip with dimensions of 5.46mm-diameter and 6.40mm-height. Each laminated test panel had a square shape with a nominal edge length of 101.6mm (4in). The thickness of the glass plate strike face was either 3.175mm (1/8in) or 6.35mm (1/4in), and in each case the glass plate was bonded using a 2.5mm (1/10in) polyurethane (PU) adhesive interlayer to a 3.175mm (1/8in) polycarbonate backing plate. A total of 32 transparent laminates were tested, where an equal number of test laminates had their outward-facing surface as the borofloat plate tin-side and air-side. The test matrix is displayed in Table 3.2.

Table 3.2: Experimental test matrix indicating the number of single-shot tests for different configurations of three-lamina transparent armor structures employed in the present work

	Air-Side Impact	Tin-Side Impact
3.175mm Borosilicate Glass 2.54mm Polyurethane 3.175mm Polycarbonate	15(1)	9(2)
6.35mm Borosilicate Glass 2.54mm Polyurethane 3.175mm Polycarbonate	2(3)	2(4)

(1) - In 5 tests ball bearing, and in 10 tests RCC projectiles were used
(2) - In 2 tests ball bearing, and in 7 tests RCC projectiles were used
(3) - In 1 test an RCC and in 1 test an FSP projectile was used
(4) - In 2 tests RCC projectiles were used

The experimental test setup consisted of the following main components, Figure 3.1: (a) a gas gun capable of charge pressures up to 10.69MPa (1550psi) with a 22 caliber rifled barrel; (b) a ring-shaped lamp housing 8 halogen bulbs; (c) a square-frame mounting fixture (used for securing the 101.6mm (4in) square test target) which is bolted at each of the four corners to the test-setup safety enclosure; (d) the (aforementioned) polycarbonate safety enclosure that houses the back-light ring lamp and the mounting fixture; and (e) two high-frame-rate video cameras

(Photron FASTCAM SA1.1 model 675K-M1) with a maximum frame-rate of 675,000 frames/sec (a frame rate of 300,000 frames/sec was used in the present analysis).

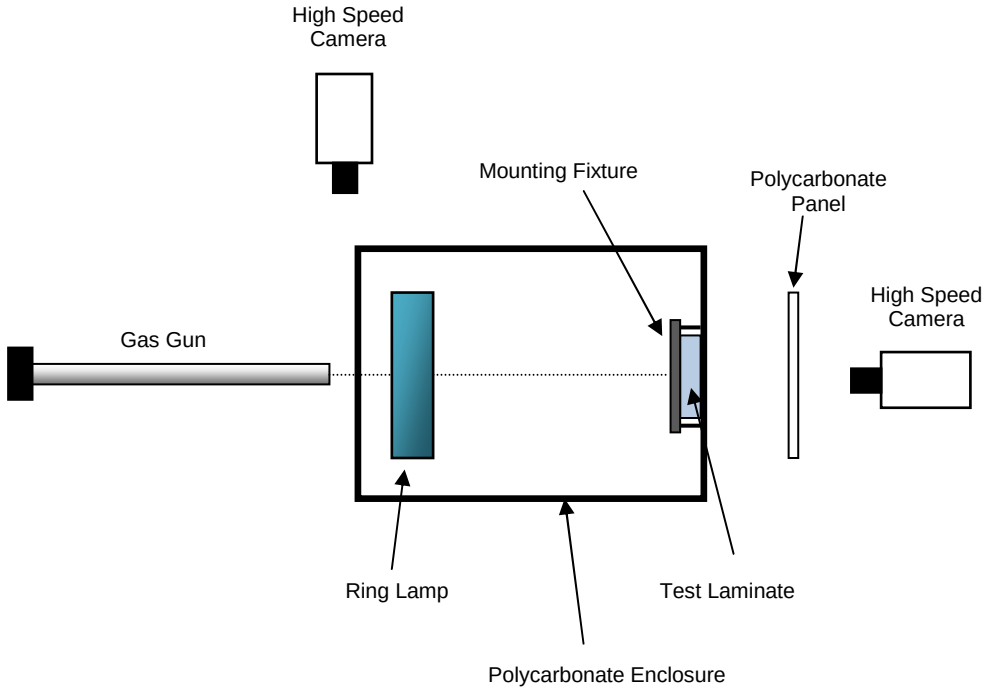

Figure 3.1: Gas gun experimental setup for impact resistance testing

The employed test procedure typically involves the following steps: (a) the transparent test laminate is secured within the safety enclosure using the mounting fixture; (b) while ensuring that the ring-lamp is powered on, a thin-paper light filter with a small hole for the projectile is placed on the strike face of the target in order to help diffuse the light from the ring lamp; (c) the gas gun barrel is loaded with an projectile by first removing the barrel plug/holding clamp, hand-placing the projectile into the barrel, and then replacing the barrel-loading plug and its clamp; (d) the desired gas gun charge pressure is achieved by exposing, via a manual twist valve, the gas gun pressure vessel to a large-capacity high-pressure carbon dioxide cylinder while monitoring the gas gun pressure gauge and then shutting the valve at the desired pressure level; (e) the gas gun is then remotely fired by an electronic switch that activates the solenoid valve which allows

the pressurized gas to instantaneously enter the gun barrel; (f) the projectile is accelerated down the barrel length by the expanding gas and exits the barrel (at a velocity of a few hundred m/s) into the polycarbonate safety enclosure; and (g) the projectile continues along its trajectory through the center of the ring lamp and impacts the target.

Within the test procedure described above, the following measurements are typically carried out: (a) a high speed camera aligned perpendicular to the projectile trajectory is used to track/capture the advancement of the projectile after leaving the gun barrel. The frame capture from this camera is subsequently imported into an image processing software to determine the projectile velocity; and (b) the second camera, aligned directly along the projectile trajectory and located behind the target, is used to capture the temporal evolution of the target/projectile material deformation, damage, and fracture. The frame capture from the second camera is also imported into the image processing software to determine the propagation velocity of discrete macro-cracks as well as the propagation velocity of the dark-region/coherent damage front within the glass plate.

The experimental procedure described above was also used to determine the so-called *V50*, i.e. the velocity at which the projectile has a 50 percent chance of fully penetrating the test laminate. Towards that end, the so-called *walk-up* procedure was employed. Within this procedure the projectile velocity was incrementally increased until further increases in the projectiles' velocity continue to result in laminate full penetration. Then, V50 is defined as an arithmetic mean of the lowest velocity at which full penetration is observed and the highest velocity at which penetration is incomplete.

3.5.2 Computational Procedure

In this section, a brief description is provided regarding the construction of the geometrical and mesh models for the laminated glass/polycarbonate-based test panels and the

stainless steel projectiles, as well as the computational procedure used to simulate the projectile initial frontal impact and subsequent penetration of the laminated test panels as carried out experimentally as part of the present work.

Geometrical model: The first step in the present computational investigation included the development of geometrical models for the transparent laminated test panels and the projectiles with geometrical dimensions, constituent materials, and lamination sequences identical to their experimental counterparts described in the previous section. Since only the case of a normal impact was considered in the present work, advantage is taken of the inherent symmetry of the geometrical model, i.e. only one quarter of the model is analyzed.

Meshed model: Typically the transparent laminated test panels were meshed using 105,000 first-order eight-node reduced integration cuboidal elements with a nominal edge length dimension of 0.6mm. On the other hand, projectiles were in general meshed using 230 first-order eight-node reduced integration cuboidal elements with an average edge length of 0.55mm. An Example of the typical meshed model used in the present work is displayed in Figure 3.2. The mesh size was varied initially in order to validate that the results are not significantly mesh-size dependent. To prevent hour-glassing effects which may arise due to the use of reduced-integration elements, a default value of hour-glass stiffness was used.

Materials: To construct the transparent laminated test panels, three materials (borofloat, polyurethane, and polycarbonate) were used, while the various projectiles were constructed from their respective stainless steel grades. Borofloat was modeled using the material model developed in the present work, while the material models for polyurethane, polycarbonate, and the stainless steels used can be found in our previous work [20].

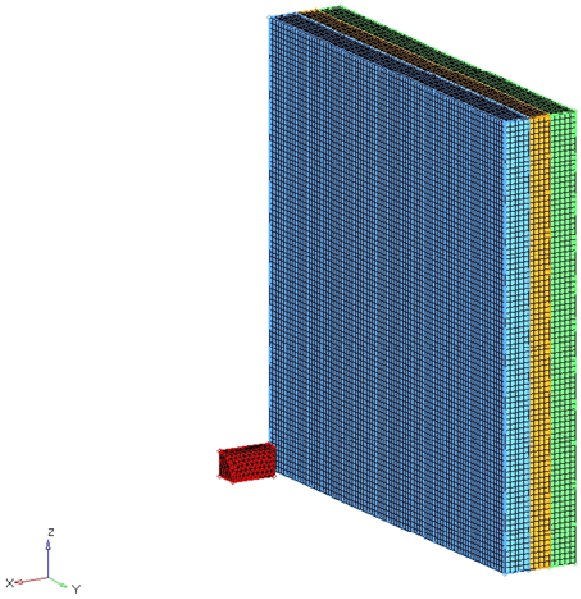

Figure 3.2: An example of the finite element mesh used in the one-quarter model of the polyurethane-bonded glass/polycarbonate transparent test laminate.

Contact interactions: Interactions between the projectile and the target as well as between different fragments of the target are modeled using the "*Hard Contact Pair*" type of contact algorithm. Within this algorithm, contact pressures between two bodies are not transmitted unless the nodes on the "*slave surface*" contact the "*master surface*". No penetration/over closure is allowed and there is no limit to the magnitude of the contact pressure that could be transmitted when the surfaces are in contact. Transmission of shear stresses across the contact interfaces is defined in terms of a static, μ_{st}, and a kinematic μ_{kin}, friction coefficient and an upper-bound shear stress limit, τ_{slip} (a maximum value of shear stress which can be transmitted before the contacting surfaces begin to slide).

Initial and boundary conditions: The impact of the projectile with the target is modeled by assigning an initial (translational) velocity to the projectile ("*the initial condition*"). The initial velocity of the target was set to zero and, during the impact simulation, the laminated test panel

faces that were framed between the mounting fixture and the polycarbonate safety enclosure were kept at a fixed position ("*the boundary conditions*").

Solver and material-model implementation: All the calculations were carried out using ABAQUS/Explicit computer program [21]. The new material model for borosilicate glass was implemented into a *VUMAT* User Material Subroutine and linked with ABAQUS/Explicit.

Computational Cost: No mass-scaling algorithm was used to increase the maximum stable time increment. Computational analyses were run on a machine with dual 2.83GHz quad-core Intel Xeon processors with 8GB of RAM. It should be noted that due to the non-local nature of the glass material model used (that is, calculation of the stress intensity factor within a given element/integration point requires knowledge of the material status for the sounding elements/material points), each calculation could be carried out only using a single computational core of the machine. On the other hand, multiple simulations could be run simultaneously. A typical 150μs projectile/target computational analysis would require ca. 30 minutes (wall-clock time).

3.6 Results and Discussion

3.6.1 Experimental Results

3.6.1.1 Damage Mode Characterization

A selection of the typical high speed photography results obtained in the present work is displayed in Figure 3.3 and Figures A.1 to A.7 (note that the latter seven Figures have been placed in Appendix A due to their similarity to Figure 3.3 and to save space in this chapter). In each of these figures, shadow graphs corresponding to the post impact times of 0μs, 6.6μs, 13.3μs, 36.6μs and 83.3μs in addition to a post mortem shadowgraph are presented. These times correspond roughly to the ones associated with the occurrence of the main damage evolution events (e.g.

initiation of discrete/macro cracks at the edge of the small coherent damage zone occurs at ca. 6.6μs). The odd-numbered figures are associated with air-side impacts, while the even are their tin-side impact counterparts. Figures 3.3 and A.1 are associated with the use of ball bearing projectiles while the remaining 6 figures utilize the RCC projectile. Figures 3.3 and A.1-A.5 are associated with the thinner 3.175mm-thick borofloat glass strike face, while Figures A.6 and A.7 are associated with the thicker 6.35mm-thick borofloat glass strike face. While the results displayed in Figures A.2/3 and A.4/5 are associated with the same projectile type and glass lamina thickness, the projectile initial velocity was lower (493m/s) in the former and higher (540-596m/s) in the latter case.

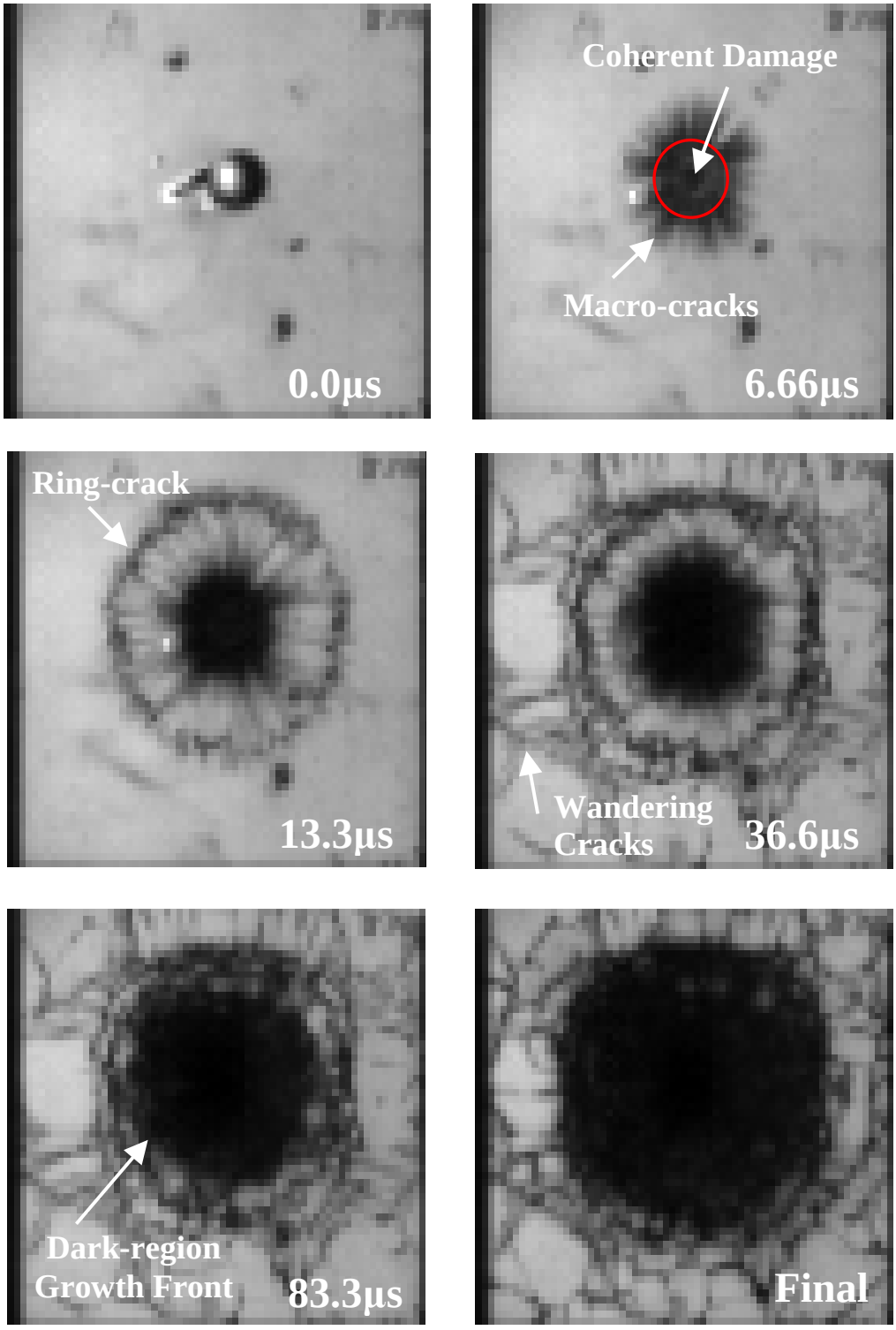

Figure 3.3: Temporal evolution of damage in a 3.18mm-thick borofloat glass plate bonded to a 3.18mm-thick polycarbonate plate using a 2.54mm-thick polyurethane interlayer. Projectile: 5.53mm-diameter steel BB, Velocity = 487m/s, Strike -face = air-side

Careful examination of the results displayed in Figures 3.3 and A.1-A.7 revealed that basically the same damage modes and the same general sequence of damage evolution occurs in all 8 impact cases. Hence, the results displayed in these figures could be jointly described as follows:

(a) the 0μs frame corresponds to the moment of projectile impact onto the glass laminate which is identified by the appearance of a relatively bright spot (when contrasted with the gray colored, undamaged surrounding material) at the location of impact;

(b) the 6.66μs frame is characterized by the clear appearance of: (i) a circular, dark-colored coherent-damage zone. This zone contains a high density of light-scattering micro-cracks and thus appears as a contiguous dark region. The radius of this region is roughly twice the radius of the projectile; and (ii) numerous, discrete, equally-spaced, linear radial macro-cracks emanating from the edge of the coherent damage region. The formation of radial cracks is typically an indication of the development of large tensile hoop stresses. These stresses are most likely the result of glass lamina material radial motion accompanying the projectile penetration into the target. As the material is displaced radially outward, it undergoes circumferential stretching (since the circumference increases with the radial distance from the point of impact). For clarity, the coherent region and the discrete cracks (as well as the other pertinent damage entities discuss below) are labeled in Figure 3.3;

(c) the predominant event in the 13.3μs frame is the formation of a ring crack which connects the cracks fronts of all the outward propagating radial cracks. The formation of the ring crack can be understood in the following way: (i) a combination of the central circular damage region and the adjacent radial cracks results in the formation of an array of radially oriented cantilever beams; (ii) the dynamic load transferred from the projectile to the glass lamina produces target flexion and accompanying large bending moments at the end of the beams which

coincide with the radial crack fronts; (iii) when the associated radial tensile/bending stress becomes equal to the local material strength, failure occurs forming a segment of the ring crack. This process is repeated circumferentially until the ring crack is completed. Meanwhile, relatively slow growth of the central coherent damage zone is observed;

(d) the 36.6μs frame is characterized by appearance of numerous, discrete, randomly distributed, wandering (with an overall outward radial trajectory) macro-cracks emanating from the ring crack outer face. The complex morphology and trajectory of these cracks appears to be related to a highly complex loading in this region resulting from the reflection (at the framed edges and ring-crack outer face) and interaction of various compression and decompression stress waves. As in the 13.3μs frame, relatively slow growth of the central contiguous damage zone is observed;

(e) the 83.3μs frame is characterized by two main observations: (i) low-rate random nucleation of discrete wandering macro-cracks throughout the non-coherent damage region. This process is again related to the associated complex transient stress state; and (ii) extension of the dark-colored (contiguous) region front to the ring crack interface. Post mortem examination revealed that while initially this extension was predominately attributed to the evolution of coherent damage, at later post-impact times the growth of this region was dominated by progression of decohesion and damage at the glass/ polyurethane interface; and

(f) the final state of damage is fairly similar to that observed in the 83.3μs frame except that the extents of macro-crack nucleation/growth and glass/polyurethane decohesion/damage are somewhat greater.

Table 3.3: Experimental test conditions for the 28 test shots carried out on the transparent armor laminate structures

Test #	Strike Face	Projectile	Impact Velocity (m/s)	Impact Coords. (mm,mm)(1)
3.18mm-thick Glass				
1	Air	BB	468	
2	Tin	BB	470	1.3,4.5
3	Air	BB	487	1.8,4.5
4	Air	BB	490	
5	Air	BB	525	
6	Tin	BB	N/A	
7	Air	BB	N/A	
8	Air	RCC	391	
9	Tin	RCC	451	
10	Tin	RCC	473	
11	Air	RCC	480	
12	Air	RCC	480	
13	Tin	RCC	490	
14	Tin	RCC	493	1.6,3.0
15	Air	RCC	493	5.8,4.7
16	Air	RCC	500	
17	Air	RCC	505	
18	Tin	RCC	521	
19	Air	RCC	526	
20	Air	RCC	540	3.8,4.0
21	Tin	RCC	540	
22	Air	RCC	547	
23	Tin	RCC	596	0.9,3.9
24	Air	RCC	N/A	
6.35mm-thick Glass				
25	Tin	RCC	380	
26	Tin	RCC	540	3.1,8.3
27	Air	RCC	532	2.6,5.7
28	Air	FSP	550	

(1) - 0,0 corresponds to the center of the glass plate.

3.6.1.2 Evolution Kinetics and Spatial Distribution of Damage

To facilitate the analysis of the quantitative results, a summary of the experimental test conditions is provided in Table 3.3. This is followed by Table 3.4 in which a summary is provided of the main post-impact quantities measured and the associated values obtained in the present work.

Table 3.4: Experimental results of 28 test shots relative to penetration and damage evolution/distribution

Test #	Penetration Status(1)	Residual Velocity (m/s)	Dark-region Growth Rate (m/s)	Final Dark-region Diameter (mm)	Macro-crack Speed (m/s)
3.18mm-thick Glass					
1A	PP	0			
2T	PP	0	142	68	2120
3A	PP	0	143	69	2240
4A	PP	0			
5A	PP	0			
6T	PP	0			
7A	PP	0			
8A	PP	-17			
9T	PP*	0			
10T	PP	-9			
11A	CP	0			
12A	CP	0			
13T	PP	-5			
14T	CP	197	141	78	2151
15A	PP*	0	148	87	2129
16A	PP*	0			
17A	CP	106			
18T	CP	0			
19A	CP	0			
20A	PP*	-3	145	83	2196
21T	CP	0			
22A	CP	N/A			
23T	CP	250	145	72	2117
24A	CP	N/A			
6.35mm-thick Glass					
25	PP	-14			
26	PP*	-12	135	85	2282
27	PP*	-12	141	86	2120
28	PP*	-12			

* - projectile yawed at time of impact

(1) - PP=partial penetration; CP=complete penetration

The data in Table 3.3 documents the execution of the projectile velocity step-up procedure employed in the present work totaling 28 test shots under various conditions. The first 7 test shots (test #s 1-7) were carried out using the ball bearing projectile impacting the 3.175mm-thick borofloat strike-faced targets under the following conditions: (a) 5 air-side shots were

conducted within a projectile initial velocity range of 468m/s to 525m/s; and (b) 2 tin-side shots were conducted with a single recorded velocity of 470m/s and a subsequent errant velocity recording. It should be noted that any field containing the N/A symbol (such as this errant velocity recording) indicates a malfunction in some step of the test procedure; in this case the side-mounted camera was not trigged by the hand-operated switch. After seven shots it was realized that the ball bearing project was not able to perforate the target at the maximum pressure of the gas gun and the more massive RCC projectile was employed as a substitute. The subsequent 17 shots (test #s 8 to 24) were carried out using the RCC projectile impacting the 3.175mm-thick borofloat strike-faced targets under the following conditions: (a) 10 air-side shots were conducted within a projectile initial velocity range of 391m/s to 547m/s and 1 errant initial velocity recording; and (b) 7 tin-side shots were conducted within a projectile initial velocity range of 451m/s to 596m/s. The final 4 shots (test #s 25 to 28) utilized the 6.35mm-thick borofloat strike faced targets under the following conditions: (a) two air-side shots using the RCC projectile for the first and the FSP projectile for the second where the initial velocities were 532m/s and 550m/s, respectively; and (b) two tin-side shots both utilizing the RCC projectile with impact velocities of 380m/s and 540m/s. It should be noted that the FSP projectile was used on the last shot of the experiment when it was realized that the RCC was unable to perforate the thicker of the two targets, however the FSP also proved to be incapable of target perforation. Table 3.3 also contains quantitative information regarding the impact coordinates of the projectile which quantify the degree to which a given shot was off-center. The same 8 test shots (test #s 2, 3, 14, 15, 20, 23, 26 and 27) from the previous section were investigated and found to be off-center (horizontally and or vertically) within a ca. 1-5% range of the total target width.

The main post-impact quantities measured for the experiment including penetration-status and accompanying residual velocities, dark-colored region growth rate and its final

diameter, and radial macro-crack growth rate are recorded in Table 3.4. The first set of results that were measured for all test shots are related to the target perforation where the results are as follows: (a) zero of the seven test impacts utilizing the ball bearing projectile lead to target perforation and hence are labeled as partial penetration (PP); (b) six of the ten air-side 3.175mm-thick glass strike face test shots yielded complete penetrations (CP) with target-exit residual velocities within a range of 0m/s to 106m/s (with two errant residual velocity recordings). It should be noted that a complete penetration is characterized by some amount of the projectile penetrating past the target back face (it is considered a partial penetration otherwise), thus it is possible to have a complete penetration with a residual velocity of 0m/s if the RCC is stopped partially exiting the structure; (c) four of the seven tin-side 3.175mm-thick glass strike face test shots resulted in complete penetrations with target-exit residual velocities within a range of 0m/s to 250m/s; and (d) zero of the four 6.3mm-thick glass strike face test shots resulted in complete penetrations.

The remaining results displayed in Table 3.4 were measured for the same 8 representative test shots (test #s 2, 3, 14, 15, 20, 23, 26 and 27) as the ones displayed in Figures 3.3 and A.1-A.7. The first measurements pertain to the propagation speed of the dark-region damage front where the main findings are as follows: (a) all measured propagation speeds fell within a range of 135m/s to 148m/s (a ~7 percent difference); (b) there appears to be no discernable pattern in these velocities based on any of the following: projectile-type, target strike face, impact velocity, target-penetration status or glass strike face thickness. The corresponding results for the final diameter of the same dark-region damage zone can be summarized as: (a) the 8 measurements fell within a range of 68mm to 86mm (~25 percent difference); (b) the smallest two damage zones were associated with the two ball bearing projectile test shots at 68mm and 69mm; (c) of the remaining six test shots that utilized the RCC projectile, the two smallest damage zones (78mm and 72mm)

were associated with complete penetration and high exit velocities while the other 4 were all associated with partial penetrations or projectile yaw (i.e. the RCC longitudinal axis was not parallel with the strike face surface normal); and (d) there appear to be no further discernable patterns in these damage zone diameters based on any of the following: borofloat strike face, impact velocity or glass lamina thickness. The final results quantified in Table 3.4 are concerned with the macro-crack propagation speed where the main findings are the following: (a) all measured macro-crack propagation speeds fell within a range of 2117m/s to 2282m/s (a ~5 percent difference); and (b) there, again, appears to be no discernable pattern in these speeds based on any of the following: projectile-type, borofloat strike face, impact velocity, target-penetration status or glass lamina thickness.

3.6.1.3 Determination of V50

It should be recalled that the main objective of the present work was to examine the effect of the air-side vs. tin-side strike face orientation on the penetration resistance of the borofloat plate glass within a three-layer transparent armor structure. The results displayed in Figures 3.3 and A.1-A.7 and Tables 3.3 and 3.4 and discussed in the previous two sections did not reveal any evidence of the effect of borofloat strike face selection on the nature and the kinetics of the prominent deformation/damage processes. In this section, an attempt is made to establish if this selection has an effect on the laminate penetration resistance as quantified by the V50. The first step towards determining the V50 was to use the results displayed in Table 3.4 to construct the corresponding projectile residual velocity vs. projectile initial velocity plots for the air-side and tin-side oriented borofloat strike faces. Since the results associated with the ball bearing projectiles did not result in target penetration, they were not included. For the same reason, the results for the thicker borofloat laminates were also not considered. Thus, for the air-side case, results associated with test shots 7, 8, 11, 12, 15, 16, 17, 19, 20 and 22 were used, while for the

tin-side case the results associated with test shots 9, 10, 13, 14, 18, 21, and 23 were used. It should be noted that while computing the V50 values given above, the zero residual velocity CP results from Table 3.4 are treated as “no penetration cases”. The resulting projectile residual velocity vs. projectile impact velocity data scatter plots are shown in Figure 3.4. The results displayed in this figure are used to determine the V50 as the arithmetic mean of the lowest projectile initial velocity at which full penetration occurs and the highest projectile initial velocity at which no penetration occurs. This procedure yields V50s of 515m/s and 516.5m/s for the air-side and the tin-side oriented strike faces, respectively. This finding suggests that borofloat strike face orientation selection does not have a statically significant effect on the transparent armor laminate penetration resistance.

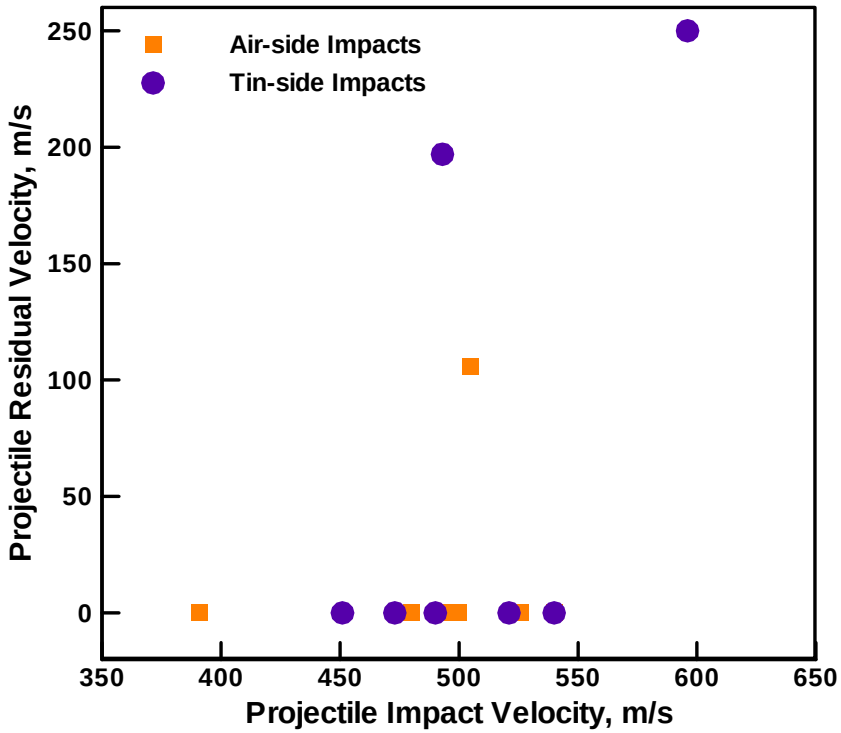

Figure 3.4: Projectile residual velocity vs. projectile initial velocity plot used to determine the air-side and tin-side strike faced target V50s.

3.6.2 Computational Results

Since the experimental results presented in the previous section suggested no statistically-significant effect of borofloat strike face orientation on either the deformation/ damage response of the borosilicate lamina or the penetration resistance of the three-layer laminate, the main objective of the computational analysis was to: (a) reconfirm that borofloat strike face orientation has no first-order effect; and (b) establish if the prominent experimentally observed damage modes and the measured V50 could be reproduced by the employed numerical analysis. For brevity, only ballistic impact scenarios associated with the RCC projectile and the 3.175mm-thick borofloat strike face laminates are considered in the remainder of this section.

3.6.2.1 The Effect of Borofloat Strike face Orientation

A comprehensive post-processing analysis of the computational results could not establish that air-side vs. tin-side strike face orientation plays a statistically significant role on the ballistic response of the transparent laminate studied in the present work. Hence, no distinction will be made between the air-side and tin-side oriented strike faces in the remainder of this section.

3.6.2.2 Damage Mode Characterization

The experimental results reported in the previous section identify the following main damage modes within the borofloat lamina: (a) comminution/coherent damage; (b) radially oriented discrete macro-cracks; (c) ring-cracking; and (d) borofloat/polyurethane interfacial damage. The computational results below confirm the ability of the present computational approach to correctly predict the occurrence of these damage modes.

The computational results displayed in Figure 3.5(a) show a top view of the quarter-model borofloat strike face laminate at the post impact time of 8.0μs. In order to reveal the

damage in the region underneath the projectile, the projectile is not displayed. For the same reason, the material having undergone complete coherent damage is not shown. Two of the previously identified damage modes (i.e coherent damage and radial macro-cracking) are evident in this figure. The coherent damage region is identified by the light-blue, green, and yellow elements corresponding to various degrees of coherent damage with the fully damaged material being removed from the display, while the macro-cracked material is displayed in red.

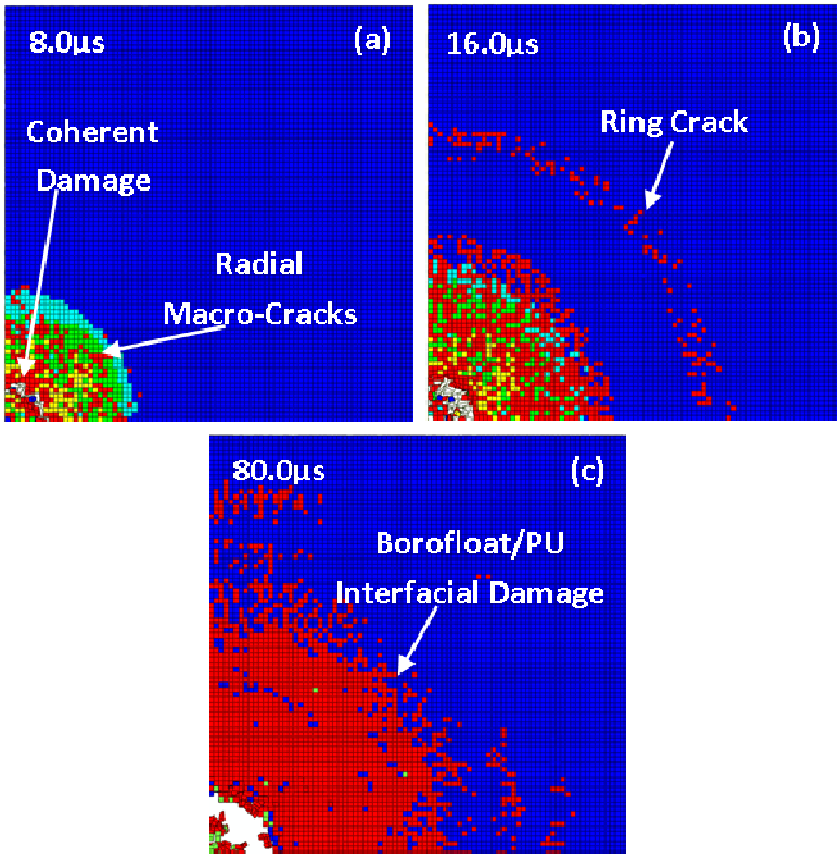

Figure 3.5: Temporal evolution of damage resulting from the computational simulation of ballistic impact onto a 3.175mm-thick borofloat glass plate bonded to a 3.18mm-thick polycarbonate plate using a 2.54mm-thick polyurethane interlayer. Projectile: 5.51mm by 5.51mm steel RCC, Velocity = 510m/s, Strike face = air-side

The computational results displayed in Figure 3.5(b) depict a top view of the quarter-model borofloat strike face laminate at the post impact time of 16.0µs. Examination of this figure

reveals that in addition to the aforementioned coherent and radial macro-crack modes of damage, a third mode (i.e. ring-cracking) has appeared.

The computational results obtained at later post-impact times revealed the onset of the fourth damage mode, i.e. borofloat/polyurethane interfacial damage. To show this damage mode, a bottom view of the quarter-model borofloat strike face laminate at the post impact time of 80.0μs is displayed in Figure 3.5(c). It should be noted that in this figure, the polycarbonate and polyurethane laminae (in addition to the projectile) are not displayed.

3.6.2.3 Evolution Kinetics and Spatial Distribution of Damage

It should be recalled that the experimental results presented in the previous section yielded quantitative information regarding the dark-region growth rate and its final size and the radial macro-crack propagation speed. It should also be recalled that the growth kinetics of the dark region was initially dominated by evolution of coherent damage and at later post-impact times was dominated by the borofloat/polyurethane interfacial damage progression. By subjecting the computational results to a post-process quantitative analysis, the following values were obtained for the damage-kinetics parameters: (a) dark-region growth rate 160m/s; (b) dark-region final diameter 80- 90mm; and (c) radial macro-crack propagation speed 2410m/s. The results are thought to be within reasonable agreement with their experimental counterparts reported in the previous section.

3.6.2.4 Determination of V50

By employing the same V50-determination procedure described in the Section IV.1, the computational equivalent of this quantity was found to be within a 510 to 540m/s range. This finding suggests that the present computational model/analysis procedure can reasonably well predict the penetration resistance of the three-layer transparent armor laminate.

3.6.3 General Discussion

At the onset of the research, it was expected that orienting the borofloat tin-side as the strike face would improve the impact resistance performance of a glass based transparent armor. This expectation was based on the observation that when testing individual glass plates that tin-side projectile impacts lead to ca. 3-5 percent higher V50 values when compared to air-side impacts (i.e. enhanced ballistic protection performance) [23]. However, such an increase in the ballistic protection performance was perceptible in neither the experimental nor computational components of the present work. This does not mean that ballistic performance enhancement cannot be achieved by borofloat tin-side strike face selective orientation, but instead highlights the lack of such a response in the specific transparent laminate system and test conditions examined here.

Multiple contributions may have led to the nearly equivalent impact performance of the air-side and tin-side strike faced borofloat transparent armor laminates. It is thought that the incorporation of borofloat into a laminate system has tempered/concealed the impact performance enhancement of the tin-side strike faced borofloat lamina (the local effect) by additional system level effects. One effect is simply that with additional (polyurethane and polycarbonate) laminae, the impact performance enhancements of the transparent laminate obtained by optimizing a single (borofloat) lamina may be made insignificant, especially if that lamina is not the majority constituent (as is in the present case). Preliminary computational investigations in our ongoing work have indeed indicated that increasing the borofloat lamina relative thickness may lead to the occurrence of superior tin-side strike face ballistic protection performance of a three-layer transparent armor laminate. An additional system-level effect that is currently being investigated is the borofloat/polyurethane interface decohesion (which is believed to be the source of the dark-

region growth) to determine the degree to which this interaction contributes to the overall performance.

3.7 Summary and Conclusions

Based on experimental and computational analyses of the air-side vs. tin-side borosilicate strike faced transparent armor laminate carried out in the present work, the following main summary remarks and conclusions can be drawn:

(1) Twenty-eight experimental test shots were carried out using three different projectiles and two thickness of borofloat glass with varying strike face (air-side and tin-side) orientations in a glass/polyurethane/polycarbonate transparent armor laminate.

(2) Examination of the experimental results revealed no measurable difference between the air-side and tin-side strike face ballistic protection performance with respect to the character and kinetics of the main damage modes and the laminate penetration resistance (as quantified by the projectile critical velocity, V50).

(3) Computational modeling of three-layer transparent armor laminate impacts employing the enhanced glass material model were carried out which reconfirmed the lack of air-side vs. tin-side strike face ballistic protection performance.

(4) Reasonable agreement with the experimental results proved that the enhanced borofloat material model is capable of capturing the main experimentally-identified glass damage modes (and their evolution) in addition to the laminate V50.

(5) It is postulated and early work indicates that a thicker borofloat strike face lamina will reveal a ballistic impact-performance enhancement when the borofloat tin-side is oriented as the laminate strike face.

3.8 References

3.1 M. Grujicic, B. Pandurangan, N. Coutris, B. A. Cheeseman, C. Fountzoulas, P. Patel and E. Strassburger, *A Simple Ballistic Material Model for Soda-Lime Glass*, International Journal of Impact Engineering, 36, 2009, 386-401.

3.2 M. Grujicic, B. Pandurangan, W. C. Bell, N. Coutris, B. A. Cheeseman, C. Fountzoulas and P. Patel, *An Improved Mechanical Material Model for Ballistic Soda-Lime Glass*, Journal of Materials Engineering and Performance, accepted for publication, 18, 8, 2009, 1012-1028.

3.3 E. Strassburger, P. Patel, J. W. McCauley, C. Kovalchick, K. T. Ramesh and D. W. Templeton, *High-Speed transmission Shadowgraphic and Dynamic Photoelasticity Study of Stress Wave and Impact Damage Propagation in Transparent Materials and Laminates Using The Edge-on Impact Method*, Proceedings of the 23rd International Symposium on Ballistics, Spain, April 2007.

3.4 E. Strassburger, P. Patel, W. McCauley and D. W. Templeton, *Visualization of Wave Propagation and Impact Damage in a Polycrystalline Transparent Ceramic- AlON*, Proceedings of the 22nd International Symposium on Ballistics, November 2005, Vancouver, Canada.

3.5 AMPTIAC Quarterly: *Army Materials Research*: *Transforming Land Combat Through New Technologies*, 8, 4, 2004.

3.6 C. Denoual and F. Hild, *Dynamic Fragmentation of Brittle Solids: A Multi-scale Model*, European Journal of Mechanics of Solids A, 21, 2002, 105-120.

3.7 F. Hild, C. Denoual, P. Forquin and X. Brajer, *On the Probabilistic and Deterministic Transition Involved in a Fragmentation Process of Brittle Materials*, Computers and Structures, 81, 2003, 1241-1253.

3.8 L. Zijlstra and A.J. Burggraaf, *Fracture Phenomena and Strength Properties of Chemically and Physically Strengthened Glass*, Journal of Non-crystalline Solids, 1, 1, 1986, 49-68.

3.9 Nghiem, *PhD thesis*, University of Paris 6, France, 1998.

3.10 M. Yazdchi, S. Valliappan and W. Zhang, *A Continuum Model for Dynamic Damage Evolution of Anisotropic Brittle Materials*, International Journal of Numerical Methods in Engineering, 39, 1996, 1555-1583.

3.11 H. D. Espinosa, P. D. Zavattieri and S. K. Dwivedi, *A Finite Deformation Continuum/Discrete Model for the Description of Fragmentation and Damage in Brittle Materials*, Journal of Mechanics and Physics of Solids, 46, 10, 1998, 1909-1942.

3.12 P. D. Zavattieri and H. D. Espinosa, *Grain Level Analysis of Crack Initiation and Propagation in Brittle Solids*, Acta Materialia, 49, 2001, 4291-4311.

3.13 G. T. Camacho and M. Ortiz, *Computational Modeling of Impact Damage in Brittle Materials*, International Journal of Solids and Structures, 33, 20-22, 1996, 2899-2938.

3.14 V. R. Howes, *Surface Resistance to Damage of the 'Tin Side' and the 'Air Side' of Commercially Produced Thermally Toughened and Untoughened Float Glass*, Journal of the American Ceramic Society, 56, 11, 1978, 1049-1060.

3.15 A. Wereszczak, K. E. Johanns, T. P. Kirkland, C. E. Anderson, Jr., T. Behner, P. Patel and D. W. Templeton, *Strength and Contact Damage Responses in a Soda-lime-silicate and a Borosilicate*, The 25th Army Science Conference, Orlando, Florida, November 2006.

3.16 M. H. Krohn, J. R. Hellmann, D. L. Shelleman and C. R. Pantano, *Biaxial Flexure Strength and Dynamic Fatigue of Soda-Lime-Silica Float Glass*, Journal of the American Ceramic Society, 85, 7, 2002, 1777-1782.

3.17 X. Nie, W. W. Chen, A. A. Wereszczak and D. W. Templeton, *Effect of Loading Rate and Surface Conditions on the Flexural Strength of Borosilicate Glass*, Journal of the American Ceramic Society, 92, 6, 2009, 1287-1295.

3.18 L.A.B. Pilkington, *The float glass process*, Proceedings of the Royal Society of London, Series A, Mathematical and Physical Science, 314, 1969.

3.19 M. H. Krohn, J. R. Hellmann, B. Mahieu and C. R. Pantano, *Effect of tin-oxide on the Physical Properties of Soda-lime-silica Glass*, Journal of Non-Crystalline Solids, 351, 2005, 455-465.

3.20 M. Grujicic, B. Pandurangan, W. C. Bell, N. Coutris, *A Computational Investigation of the Multi-Hit Ballistic-Protection Performance of Laminated Glass-Polycarbonate Transparent Armor Systems*, Journal of Materials Engineering and Performance, submitted for publication, April 2011.

3.21 ABAQUS version 6.9, User Documentation, Dessault Systems, 2009.

3.22 M. Grujicic, B. Pandurangan, N. Coutris, B. A. Cheeseman, C. Fountzoulas, P. Patel and E. Strassburger, *A Ballistic Material Model for Starphire®, a Soda-Lime Transparent-Armor Glass*, Materials Science and Engineering-A, 491, 2008, 397-411.

3.23 B. Cheeseman, personal communication, July 2009.

CHAPTER FOUR

THE EFFECT OF HIGH-PRESSURE DENSIFICATION ON BALLISTIC-PENETRATION RESISTANCE OF SODA-LIME GLASS

4.1 Abstract

Molecular-level modeling and simulations of the high-pressure volumetric response and irreversible densification of a prototypical soda-lime glass are first employed. The molecular-simulation results obtained were next used to modify the pressure vs. *degree-of-compression* (the negative of volumetric strain) and yield strength vs. pressure relations in order to account for the effects of irreversible densification. These relations are next used to upgrade the Equation of State and the strength constitutive laws of an existing material model for glass. This was followed by a set of transient non-linear dynamics calculations of the transverse impact of a glass test plate with a solid right-circular cylindrical steel projectile. The results obtained show that irreversible densification can provide only a minor improvement in the ballistic resistance of glass and only in the case of high-velocity (ca. 1000m/s) projectiles. Furthermore, it was demonstrated that if through modifications in glass chemistry and microstructure, the key irreversible compaction parameters can be adjusted, significant improvements in the glass ballistic resistance can be attained and over a relatively wide range of projectile velocities.

4.2 Introduction

A public domain literature review carried out as part of the present work revealed that several different materials and design strategies are currently being used in transparent ballistic-impact resistant vehicle structures (e.g. windshields, door windows, viewports, etc.). Among the most recently introduced transparent materials and technologies, the following have received the most attention: transparent crystalline ceramics (e.g. aluminum-oxinitride spinel, AlON, sapphire

[4.1]), new transparent polymer materials (e.g. transparent nylon [4.2]), and new interlayer technologies (e.g. polyurethane bonding layers [4.3]), and new laminate structure designs [e.g. 4.4]. Despite the clear benefits offered by these materials and technologies (e.g. transparent ceramics offer a very attractive combination of high stiffness and high hardness levels, highly ductile transparent polymers provide superior fragment containing capabilities, etc.), ballistic glass remains an important constituent material in a majority of transparent impact resistant structures used today. Among the main reasons for the wide-scale use of glass, the following three are most frequently cited: (a) glass-structure fabrication technologies enable the production of curved, large surface-area, transparent structures with thickness approaching several inches; (b) relatively low material and manufacturing costs; and (c) compositional modifications, chemical strengthening, and controlled crystallization have demonstrated to be capable of significantly improving the ballistic properties of glass [e.g. 4.2].

The development of new glass-based transparent impact resistant structures aimed at reducing the vulnerability of protected vehicle occupants and on-board instrumentation to various threats typically includes extensive prototyping and laboratory/field testing. These prototyping/testing programs are critical for ensuring the utility and effectiveness of the transparent impact resistant structures. However, the use of prototyping/testing programs is generally expensive, time-consuming and involves destructive test procedures. While the role of prototyping/testing programs remains critical, they are increasingly being complemented by the corresponding computation-based modeling and simulation efforts. However, the availability of realistic physically-based material models describing deformation/fracture response of ballistic glass under high-deformation-rate/high-pressure loading conditions is one of the key requirements for attaining a high level of utility and fidelity of these computation-based modeling and simulation approaches. Therefore, one of the main objectives of the present work is to

further advance the application of computational modeling/simulation-based engineering approaches of transparent impact-resistant structures via improvements in the accuracy of the existing ballistic-glass material models.

A comprehensive literature review carried out as part of the present work revealed that the mechanical behavior of glass is modeled predominantly using three distinct approaches: (a) molecular-modeling methods; (b) continuum-material approximations, and (c) models based on explicit crack representation. A brief overview and the main findings for each of these three approaches are given in the remainder of this section.

4.2.1 Molecular-level Material Modeling

The first molecular-level computational investigation of glass reported in open literature can be traced back to the 1976 work of Woodcock et al [4.5]. Since that time, major advances in computer technology and the introduction of high-fidelity quantum mechanics based force-fields (inter-atomic potentials) have allowed for more accurate computational modeling of glass elastic constants, strength, chemical and thermal diffusivities, surface energies, etc. Of interest to the present work, a great number of researchers have investigated, using molecular modeling techniques, the propensity of various types of glass (of different chemistries and microstructures) to undergo irreversible (permanent) densification when subjected to high hydrostatic pressures on the order of 10GPa [e.g. 4.6-8]. The emphasis in these investigations was placed on elucidating the main atomic-level mechanisms and processes (e.g. increased coordination number, often referred to as *coordination defects*, creation of new metastable chemical bonds, etc.) associated with high pressure irreversible densification of glass. In the present work, on the other hand, molecular-modeling investigations of high-pressure irreversible densification of glass will be carried out in order to assess its effect on the continuum-level pressure vs. degree-of-compression (the negative of volumetric strain) relation, also known as the Equation of State (EOS). In

addition, the ability of glass densification to act as a potent energy absorbing process, and thus, as a glass-toughening mechanism is investigated.

4.2.2 Continuum-level Material Modeling

Within the continuum-level glass models [e.g. 4.9-15], glass is treated as a continuum material whose stiffness and strength properties may become degraded by nucleation, growth, and coalescence of cracks. The fundamental assumption in these models is that the elastic-stiffness and strength degradations are the result of inelastic deformation caused by micron and sub-micron size cracks, and that this degradation can be quantified using a so-called *"damage tensor"* whose evolution during loading can be formulated using generalized Griffith-type crack initiation and propagation criteria for brittle materials. In addition, some continuum models account for the interactions between the cracks, their coalescence, friction between fragments, competition between micro-cracking leading to fine-scale fragmentation of glass and macro-cracking giving rise to coarse fragmentation, etc. In addition to the physically-based continuum-material models for glass mentioned above, the Johnson Holmquist 2 (commonly referred to as the JH2 model, [4.16]) is often used to model the behavior of glass under high-loading rate conditions. Despite its phenomenological nature, the JH2 model has been found to often provide a reasonably good account for glass response under these loading conditions. For this reason, the JH2 model will be used in the present work for coupling with the molecular modeling approaches mentioned above. Specifically, the polynomial EOS used to account for the hydrostatic/volumetric response of glass within the JH2 model will be modified to include pressure vs. degree-of-compression results which will be obtained using the aforementioned molecular modeling procedure. In addition, molecular-level results pertaining to irreversible densification-induced strengthening will be used to modify the JH2 strength constitutive law.

4.2.3 Explicit Crack Representation Material Models

Within this material-modeling framework, glass is treated as a linear elastic material, and its fracture is considered to take place via nucleation, propagation and coalescence of discrete (rather than smeared-out/homogenized) cracks during impact [e.g. 4.17]. In other words, while within the continuum modeling framework the stiffness/strength-degrading effect of smeared-out cracks is included only implicitly, in the explicit crack representation material models cracks are considered as discrete entities and their effect on material stiffness/strength is accounted for explicitly. When the latter-type of glass models are implemented into a finite element computational framework, crack nucleation and propagation are handled by duplicating nodes at the crack tip/front. Adaptive re-meshing is used to provide a rich enough set of possible fracture paths around the crack tip. As a crack grows, forces at newly cracked (free) surfaces are brought to zero in accordance with the Griffith criterion to account for crack growth induced unloading. This enables explicit modeling of the crack coalescence process which can lead to fragment formation. The major disadvantages of the discrete models are that they are extremely computationally expensive and become intractable as the number of cracks increases. That is, in order to capture all possible crack nucleating sites, meshes with micron-size element are ultimately required. Hence, despite the fact that inclusion of high-pressure densification effects may also be beneficial to the discrete glass models, due to their prohibitively high computational costs they will not be considered in the present work.

As demonstrated above, molecular-level, continuum-level and discrete modeling are maturing areas of glass research which are capable of revealing complex intrinsic mechanisms and phenomena associated with deformation and fracture in glass. However, these modeling approaches are typically concerned only with the effect of the observed processes/mechanisms on the behavior of glass at their respective length scales and practically no reports were found where

the knowledge about glass behavior at one length scale was used to improve glass models at other length scale(s). Therefore, the main objectives of the present work are: (a) to investigate and quantify (using molecular-level modeling and simulation techniques) the irreversible densification process in soda-lime glass at high pressures; (b) to determine if modifications in the EOS and the strength constitutive law of the JH2 continuum-material model for soda-lime glass to include the effects of high-pressure irreversible densification obtained in (a) significantly alters the mechanical response of glass under ballistic-loading conditions; and (c) to carry out a preliminary assessment of high-pressure irreversible densification as an energy-absorbing/strength-enhancing mechanism in glass. Toward that end, molecular-level calculations are carried out first to quantify the basic pressure vs. degree-of-compression relation in glass at high-pressure as this material undergoes irreversible densification. Also, molecular-level simple shear tests were carried out to assess the extent of irreversible-densification induced strengthening. The results obtained are next used to modify the JH2 EOS and strength constitutive law for glass. Then, a series of transient non-linear dynamics analyses of transverse impact of a glass test-panel with a solid right-circular cylinder Fragment Simulating Projectile (FSP) is carried out to examine: (a) the extent of change in the temporal and spatial distribution of deformation and damage and (b) the resulting change in ballistic-penetration resistance brought about by the aforementioned modifications in the glass material model.

The organization of the paper is as follows: A discussion of the inter-atomic force field potentials, computational cell, and the computational method used in the molecular-level simulations are all presented in Section 4.3. Then a brief overview of the JH2 continuum-material model for glass is provided in Section 4.4. The main results obtained in the present work (including the definition of a FSP transverse-impact problem for a glass test-panel) are presented

and discussed in Section 4.5, while the key conclusions resulting from the present study are summarized in Section 4.6.

4.3 Molecular-level Modeling of Glass

At the molecular level, soda-lime glass is treated as a discrete material consisting of: (a) silicon (Si) and oxygen (O) atoms mutually bonded via a single covalent bond and forming a connected, non-structured/amorphous network of silica (SiO_4^{4-}) tetrahedra; (b) oxygen anions (O^{2-}) attached as terminal functional-groups to the fragmented silica tetrahedra network; and (c) sodium cations (Na^{+}) dispersed between fragmented silica tetrahedra networks and ionically bonded to the oxygen anions. To fully account for the bonding and non-bonding types of interactions between the atoms/ions listed above one must define the respective interaction-potential functions (commonly referred to as the force-fields), as well as the associated atomic-polar and ionic charges.

While glass is an amorphous material and does not possess any long-range regularity in its atomic/molecular structure, modeling of bulk behavior of glass is typically done at the molecular level by assuming the existence of a larger unit cell. Repetition of this cell in the three orthogonal directions (the process also known as application of the *periodic boundary conditions*) results in the formation of an infinitely-large bulk-type material.

Molecular-modeling simulations typically rely on one of the following two techniques: (a) molecular statics, the technique within which the potential energy of the molecular structure in question is minimized with respect to the position of the constituent and ions in the unit cell as well as with respect to the size and shape of the unit cell; and (b) molecular dynamics, a technique within which the Newton's equations of motion are solved for all interacting atoms an ions in the system as a function of time and the appropriate ensemble averages are used to assess/quantify various molecular-level material properties.

The discussion presented above indicates that the three main components of a molecular-level model which must be defined are: (a) the force-fields; (b) the initial unit cell size and shape as well as the initial positions of atoms and ions within it; and (c) the computational procedure to be employed. A brief description of these three components used in the present molecular-level investigation of soda-lime glass behavior under high pressures is presented in the remainder of this section.

4.3.1 Force-fields

While accurate simulations of a system of interacting particles (i.e. atoms or ions) generally entail the application of quantum mechanical techniques, such techniques are computationally quite expensive and are usually feasible only in systems containing up to a few hundreds of interacting particles. In addition, the main goal of simulations of the systems containing a large number of particles is generally to obtain the systems' bulk properties which are primarily controlled by the location of atomic nuclei and the knowledge of the electronic structure, provided by the quantum mechanics techniques, is not critical. Under these circumstances, a good insight into the behavior of a system can be obtained if a reasonable, physically-based approximation of the potential (force-field) in which atomic nuclei move is available. Such a force-field can be used to generate a set of system configurations which are statistically consistent with a fully quantum-mechanical description.

As stated above, a crucial point in the molecular-level simulations of multi-particle systems is the choice of the force-fields which describe, in an approximate manner, the potential energy hyper-surface on which the atomic nuclei move. In other words, the knowledge of force-fields enables determination of the potential energy of a system in a given configuration. In general, the potential energy of a system of interacting particles can be expressed as a sum of the

valence (or bond), $\boldsymbol{E_{valence}}$, cross-term, $\boldsymbol{E_{cross\text{-}term}}$, and non-bond, $\boldsymbol{E_{non\text{-}bond}}$, interaction energies as:

$$E_{total} = E_{valence} + E_{cross-term} + E_{non-bond} \tag{4.1}$$

The valence energy generally includes a bond stretching term, $\boldsymbol{E_{bond}}$, a two-bond angle term, $\boldsymbol{E_{angle}}$, a dihedral bond-torsion term, $\boldsymbol{E_{torsion}}$, an inversion (or an out-of-plane interaction) term, $\boldsymbol{E_{oop}}$, and a Urey-Bradlay term (which involves interactions between two particles bonded to a common particle), $\boldsymbol{E_{UB}}$, as:

$$E_{valence} = E_{bond} + E_{angle} + E_{torsion} + E_{oop} + E_{UB} \tag{4.2}$$

A schematic explanation of the first four types of valence atomic interactions is given in Figure 4.1.

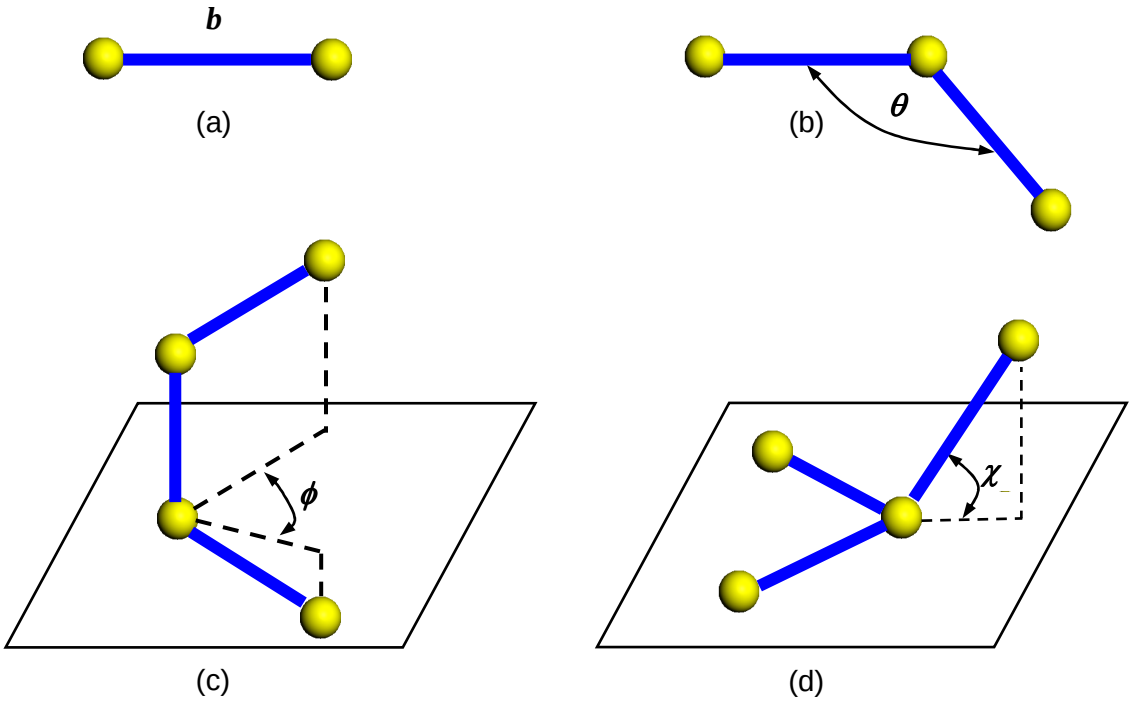

Figure 4.1: A schematic of the: (a) stretch; (b) angle; (c) torsion; and (d) inversion valence atomic interactions.

The cross-term interacting energy, $E_{cross\text{-}term}$, accounts for the effects such as bond length and angle changes caused by the surrounding atoms and generally includes: stretch-stretch

interactions between two adjacent bonds, $E_{bond\text{-}bond}$, stretch-bend interactions between a two-bond angle and one of its bonds, $E_{bond\text{-}angle}$, bend-bend interactions between two valence angles associated with a common vertex particle, $E_{angle\text{-}angle}$, stretch-torsion interactions between a dihedral angle and one of its end bonds, $E_{end\_bond\text{-}torsion}$, stretch-torsion interactions between a dihedral angle and its middle bond, $E_{middle\_bond\text{-}torsion}$, bend-torsion interactions between a dihedral angle and one of its valence angles, $E_{angle\text{-}torsion}$, and bend-bend-torsion interactions between a dihedral angle and its two valence angles, $E_{angle\text{-}angle\text{-}torsion}$, terms as:

$$E_{cross-term} = E_{bond-bond} + E_{angle-angle} + E_{bond-angle} + E_{end\_bond-torsion} + E_{middle\_bond-torsion} + E_{angle-torsion} + E_{angle-angle-torsion} \quad (4.3)$$

The non-bond interaction term, $E_{non\text{-}bond}$, accounts for the interactions between non-bonded particles and includes the van der Waals energy, E_{vdW}, the Coulomb electrostatic energy, $E_{Coulomb}$, and the hydrogen bond energy, $E_{H\text{-}bond}$, as:

$$E_{non-bond} = E_{vdW} + E_{Coulomb} + E_{H-bond} \quad (4.4)$$

Particle interactions in the soda-lime glass system under investigation are modeled using COMPASS (Condensed-phased Optimized Molecular Potential for Atomistic Simulation Studies), the first *ab initio* force-field that enables an accurate and simultaneous prediction of various gas-phase and condensed-phase properties of organic and inorganic materials [4.18,4.19]. The COMPASS force-field uses the following expression for various components of the potential energy:

$$E_{bond} = \sum_{b}\left[K_2(b-b_0)^2 + K_3(b-b_0)^3 + K_4(b-b_0)^4\right] \quad (4.5)$$

$$E_{angle} = \sum_{\theta}\left[H_2(\theta-\theta_0)^2 + H_3(\theta-\theta_0)^3 + H_4(\theta-\theta_0)^4\right] \quad (4.6)$$

$$E_{torsion} = \sum_{\phi}\left[V_1\left[1-\cos\left(\phi-\phi_1^0\right)\right] + V_2\left[1-\cos\left(2\phi-\phi_2^0\right)\right] + V_3\left[1-\cos\left(3\phi-\phi_3^0\right)\right]\right] \quad (4.7)$$

$$E_{oop} = \sum_{x} K_x \chi^2 \tag{4.8}$$

$$E_{bond-bond} = \sum_{b} \sum_{b'} F_{bb'}(b - b_0)(b' - b_0') \tag{4.9}$$

$$E_{angle-angle} = \sum_{\theta} \sum_{\theta'} F_{\theta\theta'}(\theta - \theta_0)(\theta' - \theta_0') \tag{4.10}$$

$$E_{bond-angle} = \sum_{b} \sum_{\theta} F_{b\theta}(b - b_0)(\theta - \theta_0) \tag{4.11}$$

$$E_{end\_bond-torsion} = \sum_{b} \sum_{\phi} F_{b\phi}(b - b_0)[V_1 \cos\phi + V_2 \cos 2\phi + V_3 \cos 3\phi] \tag{4.12}$$

$$E_{middle\_bond-torsion} = \sum_{b'} \sum_{\phi} F_{b'\phi}(b' - b_0')[F_1 \cos\phi + F_2 \cos 2\phi + F_3 \cos 3\phi] \tag{4.13}$$

$$E_{angle-torsion} = \sum_{\theta} \sum_{\phi} F_{\theta\phi}(\theta - \theta_0)[V_1 \cos\phi + V_2 \cos 2\phi + V_3 \cos 3\phi] \tag{4.14}$$

$$E_{angle-angle-torsion} = \sum_{\phi} \sum_{\theta} \sum_{\theta'} K_{\phi\theta\theta'} \cos\phi(\theta - \theta_0)(\theta' - \theta_0') \tag{4.15}$$

$$E_{Coulomb} = \sum_{i>j} \frac{q_i q_j}{\varepsilon r_{ij}} \tag{4.16}$$

$$E_{vdW} = \sum_{i>j} \left[\frac{A_{ij}}{r_{ij}^9} - \frac{B_{ij}}{r_{ij}^6} \right] \tag{4.17}$$

where b and b' are the bond lengths, θ the two-bond angle, ϕ the dihedral torsion angle, χ the out of plane angle, q the atomic charge, ε the dielectric constant, r_{ij} the *i-j* atomic separation distance. b_0, K_i (i=2-4), θ_0, H_i (i=2-4), ϕ_i^0 (i=1-3), V_i (i=1-3), $F_{bb'}$, b'_0, $F_{\theta\theta'}$, θ'_0, $F_{b\theta}$, $F_{b\phi}$, $F_{b'\phi}$, F_i (i=1-3), $F_{\theta\phi}$, $K_{\phi\theta\theta'}$, A_{ij}, and B_{ij} are the material-system dependent parameters implemented into Discover [4.20], the atomic simulation program used in the present work.

4.3.2 Computational Cell

In the molecular-level modeling portion of the work, a 2916 particle computational cell was created with a chemical composition of $(Na_2O)_{0.15}$ $(SiO_2)_{0.85}$. The molecular-level unit cell was constructed with a cubic geometry having a uniform edge-length of 3.347nm. An amorphous cell of sodium silicate glass was thus created with a density of 2.613g/cm^3. The three edges (*a*, *b* and *c*) of the cell were aligned respectively with the three coordinate axes (*x*, *y* and *z*). To create a bulk-material environment for the particles, periodic boundary conditions were applied to all six faces of the unit cell.

To create the initial particle configuration in the unit cell, the Visualizer [4.21] from Accelrys was first used to construct a short silica-chain fragment. The fragment was then *grown* by a duplicate-and-attach process using the same program. The resulting silica network was next used within the Amorphous Cell program [4.22] from Accelrys to randomly populate the computational cell while ensuring that the target material density of 2.613g/cm^3 was attained. Lastly, sodium cations were added to obtain an electrically neutral system of particles. An example of a typical molecular-level topology within a single unit cell is displayed in Figure 4.2. When creating the computational cell for the subject material (soda-lime glass in the present case), one should try to answer the question as to how representative is the computational cell of the material in question. Typically, the size of the computational cell, i.e., the number of the constituent atoms analyzed is a compromise between the available computer resources (CPU time, primarily) and a desire to maximize the size of the computational model. The reason that the computational-model size should be maximized is that the effect of the periodic boundary conditions which artificially introduce configurational-order into an amorphous/disordered solid should be minimized. To qualify the computational cell used in the present work, few simulations are carried out using a computational cell with a doubled edge length. Since no statistically

significant differences in the key results were seen for the two choices of the unit cell, it is concluded that the computational cell used is adequate.

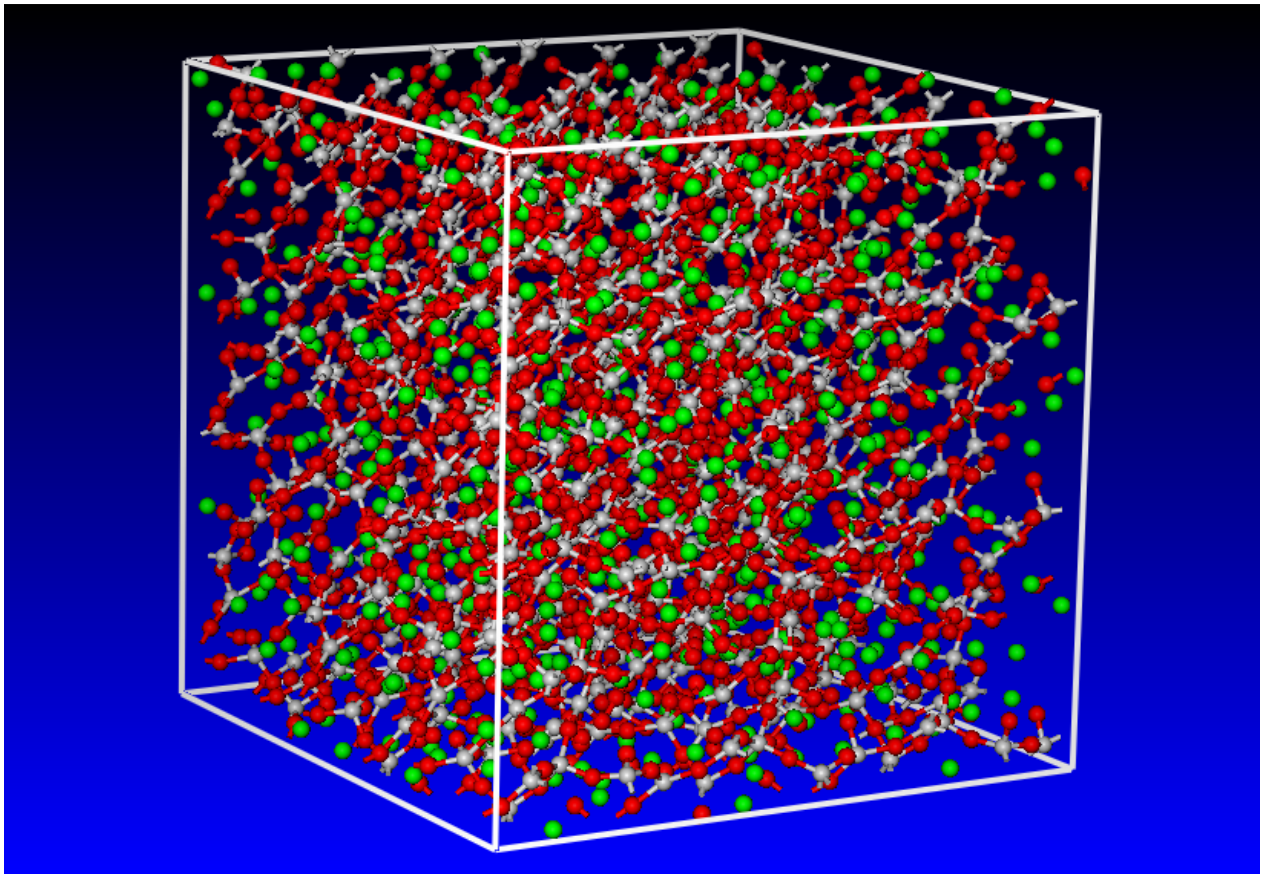

Figure 4.2: The computational unit cell for soda-lime glass molecular-level simulations used in the present work.

4.3.3 Computational Method

High-pressure irreversible densification of glass was studied using a conventional *NPT* dynamics method within the Discover program [4.20] from Accelrys, where *N* (the number of particles), *P* (pressure), and *T* (temperature) are the system variables that are held constant or ramped in a controlled manner during compression-simulation runs. The equations of motion were integrated using the velocity Verlet algorithm with a time step of 1.0fs. To comply with typical ballistic-impact loading conditions, pressure was ramped linearly at a rate of 0.3GPa/ps.

Pressure ramping was accomplished by 3GPa discrete increments in pressure followed by 10.0ps equilibration times at a given pressure level. Temperature, on the other hand was held constant at a value of 300K using a Nosé Thermostat [4.23].

At the end of equilibration at each pressure level, the average material density was computed from the corresponding pair-correlation functions. This procedure yielded the sought pressure vs. degree-of-compression relation for the pressurization portion of a loading cycle. To determine the corresponding pressure vs. degree-of-compression relation during the depressurization portion of a loading cycle, pressure was decreased in a similar manner as discussed above. Differences in the pressure vs. degree-of-compression relations for the pressurization and depressurization portions of the loading cycle are then used to quantify the extent of high-pressure irreversible densification of glass.

As will be explained later in more detail, irreversible-densification can affect the ballistic-penetration of glass not only via increased density but also through the associated changes in the material strength. Too assess the extent of densification-induced strengthening, molecular-level simple-shear tests were carried out. These tests were conducted through the use of a Discover input file which was written in a Basic Tool Command Language (BTCL). This enabled the use of a scripting engine that provides very precise control of simulation runs, e.g. a cell deformation to be carried out in small steps each followed by energy minimization. The minimization portion of the molecular-level simple shear tests was carried out using a combination of three (Steepest Descent, Conjugate Gradient, and Newton's) potential-energy minimization algorithms within Discover [4.20]. These algorithms are automatically activated/ deactivated as the molecular-level configuration approaches its energy minimum (i.e. the Steepest Descent method is activated at the beginning of the energy-minimization procedure, while the Newton's method is utilized in the last stages of the simulation).

4.4 JH2 Continuum-material Model

To completely define a continuum-level material dynamic model, the relationships between the flow variables (pressure, mass-density, energy-density, temperature, etc.) must be specified. These relations typically involve: (a) an EOS; (b) a strength equation; (c) a failure equation and (d) an erosion equation. These equations arise from the fact that, in general, the total stress tensor can be decomposed into a sum of a hydrostatic stress (pressure) tensor (which causes a change in the volume/density of the material) and a deviatoric stress tensor (which is responsible for the shape change of the material). An EOS then is used to define the corresponding functional relationship between pressure, mass density (degree-of-compression) and internal energy density (temperature). Likewise, a strength relation is used to define the appropriate equivalent plastic strain, equivalent plastic strain rate, and temperature dependencies of the materials yield strength. This relation, in conjunction with the appropriate yield-criterion and flow-rule relations, is used to compute the deviatoric part of stress under elastic-plastic loading conditions. In addition, a material model generally includes a failure criterion (i.e. an equation describing the hydrostatic or deviatoric stress and/or strain condition(s) which, when met, causes the material to fracture and lose its ability to support, abruptly in the case of brittle materials or gradually in the case of ductile materials, normal and shear stresses). Such a failure criterion in combination with the corresponding material-property degradation and the flow-rule relations governs the evolution of stress during failure. The erosion equation is generally intended for eliminating numerical difficulties arising from highly distorted Lagrange cells. Nevertheless, the erosion equation is often used to provide additional material failure mechanisms especially in materials with limited ductility.

To summarize, the EOS along with the strength and failure equations (as well as with the equations governing the onset of plastic deformation and failure and the plasticity and failure

induced material flow) enable assessment of the evolution of the complete stress tensor during a transient non-linear dynamics analysis. Such an assessment is needed in order to solve the governing (mass, momentum and energy) conservation equations. It is important to note that separate evaluations of the pressure and the deviatoric stress enable inclusion of the nonlinear effects in the EOS. Generally these effects are shock related but, in the present work, they will be, at least partly, attributed to the phenomenon of high-pressure irreversible densification.

In the present work, glass was modeled using the JH2 brittle-material model [4.25,4.26]. The JH2 model is a phenomenological model which postulates the existence of two terminal glass states: (a) an intact material; and (b) a failed material. The two material states are weighted by a single scalar variable called damage, *D*, whose evolution is governed by an inelastic (plasticity-like deformation model). The JH2 model includes a polynomial-type EOS, a strength model (based on the von Mises yield criterion, normality flow rule and a pressure and strain-rate hardening constitutive relation), a progressive failure model, and an instantaneous geometric strain-based erosion criterion. The values of all the JH2 material-model parameters for soda-lime float glass are available in the ANSYS/Autodyn materials library [4.24]. Further details of the JH2 model for brittle materials are provided in the remainder of this section.

4.4.1 Polynomial Equation of State

Within the JH2 polynomial EOS, the effect of internal-energy density is neglected and the pressure vs. degree-of-compression in a damage-free material is defined as:

$$P = K_1\mu + K_2\mu^2 + K_3\mu^3, \quad \mu > 0 \quad (\textit{hydrostatic compression}) \tag{4.18}$$

and

$$P = K_1\mu, \quad \mu < 0 \quad (\textit{hydrostatic tension}) \tag{4.19}$$

where degree-of-compression is $\mu = (\rho/\rho_0 - 1)$ and ρ is the current density, while ρ_0 (the reference density), K_1 (the bulk modulus), K_2 and K_3 are material specific constants.

After glass has begun to accumulate damage (i.e. when the extent of damage is no longer zero, $D>0$), Eq. (4.18) has to be upgraded to include the effect of bulking. Bulking is a phenomenon associated with the fact that fragments of fractured materials are not generally fully conformable and, consequently fractured material is associated with a larger volume (a lower density at a constant pressure) than the damage-free material. The bulking modified polynomial EOS is then given by [4.24]:

$$P = K_1\mu + K_2\mu^2 + K_3\mu^3 + \Delta P, \quad \mu > 0 \tag{4.20}$$

where the bulking-induced pressure increment, ΔP, is determined from energy considerations and varies from zero at $D=0$ to ΔP_{max} at $D=1.0$. Assuming that a fraction of the internal elastic energy decrease (due to decrease in deviatoric stresses in the material) is converted to an increase in potential internal energy, the bulking induced pressure increment ΔP at a time $t+\Delta t$ can be represented in terms of ΔP at the time t as:

$$\Delta P(t+\Delta t) = -K\mu(t+\Delta t) + \sqrt{(K_1\mu(t+\Delta t) + \Delta P(t))^2 + 2\beta K_1 \Delta U} \tag{4.21}$$

where ΔU is the decrease in deviatoric elastic energy due to damage induced yield-strength reduction and β is the fraction of the deviatoric elastic energy converted to hydrostatic potential/elastic energy. The decrease in deviatoric elastic energy is given by:

$$\Delta U = U_t - U_{t+\Delta t} \tag{4.22}$$

where

$$U_t = \frac{\sigma_t^2}{6G} \tag{4.23}$$

The parameters σ_t and G appearing in Eq. (4.23) are the actual yield strength and the damage-free shear modulus of the glass material, respectively.

4.4.2 Strength Model

Within the JH2 strength model [4.25,4.26], the normalized yield strength is defined as a damage-weighted rule of mixtures of the corresponding damage-free and fractured yield strengths as:

$$\sigma^* = \sigma_i^* - D(\sigma_i^* - \sigma_f^*) \tag{4.24}$$

where subscripts ***i*** and ***f*** are used to denote intact and fractured material states and the superscript * indicates that the corresponding yield strength is normalized by the Hugoniot Elastic Limit (HEL) (uni-axial stress) yield strength, i.e.:

$$\sigma^* = \frac{\sigma}{\sigma_{HEL}} \tag{4.25}$$

The normalized yield strengths σ_i^* and σ_f^* are also defined in the same manner as σ^*. The normalized (pressure and strain rate dependent, ideal-plastic) yield strength of the damage-free material, σ_i^*, and the fractured material, σ_f^*, are respectively given by:

$$\sigma_i^* = A(P^* + T^*)^N (1 + C\ln \dot{\varepsilon}^*) \tag{4.26}$$

$$\sigma_f^* = B(P^*)^M (1 + C\ln \dot{\varepsilon}^*) \tag{4.27}$$

where *A*, *B*, *C*, *M*, *N* and σ_{HEL} appearing in Eqs. (4.25)-(4.27) are all material specific constants while P^* and T^* are respectively defined as:

$$P^* = \frac{P}{P_{HEL}} \tag{4.28}$$

and

$$T^* = \frac{T}{P_{HEL}} \tag{4.29}$$

where P and T are the actual pressure and the maximum hydrostatic tensile pressure that the glass material can withstand, respectively, and P_{HEL} is the pressure at the Hugoniot Elastic Limit. A schematic of the JH2 strength model in the normalized yield strength vs. normalized pressure plane is displayed in Figure 4.3.

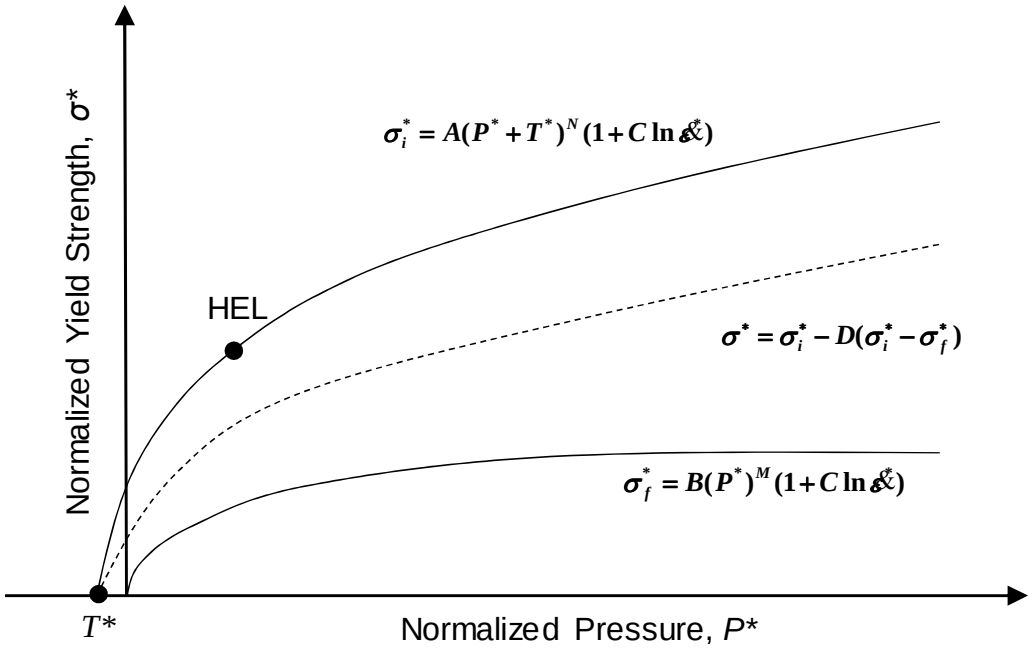

Figure 4.3: A schematic of the JH2 strength model in the normalized yield strength, σ*, vs. normalized pressure, P*, plane.

As shown in Ref. [4.26] P_{HEL} and σ_{HEL} are related to the (uni-directional shockwave-based) uniaxial-strain compressive strength, HEL, as: $HEL = P_{HEL} + \frac{2}{3}\sigma_{HEL}$. Since both P_{HEL} and σ_{HEL} are dependent on the compression ratio at the HEL, both of these parameters can be determined from HEL. Finally, the dimensionless material strain rate, $\dot{\varepsilon}^*$, appearing in Eqs. (4.28) and (4.29) is defined as:

$$\dot{\varepsilon}^{*} = \frac{\dot{\varepsilon}}{\dot{\varepsilon}_0} \tag{4.30}$$

where $\dot{\varepsilon}$ is the actual strain rate and $\dot{\varepsilon}_0$ is the reference strain rate (typically set to 1.0 s^{-1}).

4.4.3 Failure Model

Within the JH2 failure model [4.25,4.26], the evolution/accumulation of damage is defined as:

$$D = \sum \frac{\Delta \varepsilon_p}{\varepsilon_p^f} \tag{4.31}$$

where $\Delta\varepsilon_p$ is the increment in equivalent plastic strain with an increment in loading and the failure strain ε_p^f is a pressure dependent equivalent fracture strain which is defined as:

$$\varepsilon_p^f = D_1 (P^* + T^*)^{D2} \tag{4.32}$$

where D_1 and D_2 are material specific constants.

Within the JH2 failure model, fracture occurs when either damage reaches a critical value of 1.0 or when negative pressure reaches a value of T. Fracture material has no ability to support any negative pressure, while its ability to support shear is defined by Eq. (4.27).

4.4.4 Erosion Model

Within the finite-element computational framework, numerical difficulties may arise from excessive distortion of the elements. To overcome these difficulties an erosion algorithm is employed, which, at a predefined level of strain, removes the excessively distorted elements while transferring the momentum associated with the removed nodes to the remaining nodes. Following our prior work [4.27-30], the erosion criterion is defined by prescribing a critical value for the instantaneous geometrical equivalent strain.

4.5 Results and Discussion

4.5.1 Molecular-level Analysis of High-pressure Densification of Glass

In this section, a brief summary of the molecular-level calculations of glass response to high pressure is provided. While this portion of the work yielded numerous results, only the ones directly related to the potential role of high-pressure irreversible densification in improving impact/penetration resistance of glass are presented and discussed in greater detail. Other results are discussed only qualitatively.

4.5.1.1 Molecular-level Topology

A detailed examination of the molecular-level topology after subjecting the unit-cell to high pressures revealed distinct differences depending on whether the maximum pressure was below or above ca. 4GPa.

Pressures below ~4GPa

Molecular modeling of glass pressurization/depressurization revealed that when glass is exposed to pressures not exceeding ca. 4GPa, no detectable irreversible changes generally take place in its molecular topology. Closer examination of the atomic structure at different pressure levels between 0GPa and 4GPa revealed:

(a) The presence of *active regions* within which atoms may occasionally undergo large displacements/jumps (ca. 0.1nm). These atomic displacements (the results not shown for brevity) were found to involve coordinated motion of at least a dozen atoms and to be accompanied by abrupt changes in the average potential energy;

(b) In most cases, atomic rearrangement described in (a) appears to be associated with low-frequency transition of the active regions between two distinct *equilibrium* states (of comparable potential energy). These findings are in complete agreement with those found by

Trachenko and Dove [4.7] who termed this phenomenon as Double Well Potential (DWP) and the associated low-frequency transition/vibrational mode as the *floppy mode*; and

(c) While pressurization up to 4GPa did not yield any permanent changes in the molecular topology, the locations of the active regions were found to change with pressure. That is, the regions active at one pressure level may become inactive at another pressure level while, at the same time other previously inactive regions would become active.

Pressures above ~4GPa

When the computational cell is subjected to pressure exceeding ca. 4GPa and subsequently depressurized to zero pressure, permanent changes in the glass molecular topology were normally observed. These molecular topology changes were accompanied by a permanent density increase on the order of 3–7%. An example of typical results obtained in this portion of the work is given in Figures 4.4(a)-(d), where oxygen atoms/anions are displayed in red and silicon atoms are shown in gray (as well green, pink and yellow highlighting), while sodium cations are omitted for clarity. To aid in visualization/interpretation of the topological changes experienced by glass during high pressure loading/unloading cycles, only a 30-40 atom exemplary region of computational cell was monitored in Figures 4.4(a)-(d). The molecular level topologies displayed in these figures pertain respectively to: (a) high-pressure state, Figure 4.4(a); (b) high pressure state after a prolonged (20ps) relaxation period, Figure 4.4(b); (c) ambient pressure state resulting from depressurization of state (a), Figure 4.4(c); and (d) ambient pressure state resulting from depressurization of state (b), Figure 4.4(d). It should be noted that the results displayed in Figure 4.4(c) are essentially identical to those in the initial configuration prior to loading. A closer examination of the molecular-level topology results displayed in these figures revealed that:

(a) Pressurization alters not only molecular-level topology, but also changes the bonding structure and increases the average coordination number (of mainly Si atoms). This can be seen by comparing the results displayed in Figures 4.4(a) and (c). It should be noted here, that the results displayed in Figure 4.4(c) are used in place of the initial molecular-level topology results. In these figures, it is seen that silicon atoms labeled *A* and *B* change their fourfold coordination to fivefold coordination upon pressurization.

(b) As implied earlier, if the depressurization is carried out without allowing the material to relax at high pressures, the molecular level configuration obtained at the ambient pressure is effectively identical to the initial configuration, Figure 4.4(c). Thus, in the resultant ambient-pressure configuration, most silicon atoms regain their fourfold coordination;

(c) Increased duration of the exposure of glass to high pressure, results in continued changes in the molecular-level topology and bond structure. This can be seen by comparing the results displayed in Figures 4.4(a) and (b). These figures show that relaxation of glass leads to the *C*-label silicon atom acquiring a fivefold coordination while, at the same time smaller size Si-O rings are being formed. For example, a twofold ring is formed involving the *A* and *C* silicon atoms, while a threefold ring involving the *C*, *D* and *E*-labeled Si atoms also appears, Figure 4.4(b). These changes in the molecular-level topology of glass are a manifestation of its relaxation to a material state that is energetically-preferred at high pressures; and

(d) Upon depressurization of glass which was relaxed at high pressures, some changes in the molecular-level topology and the bonding structure are observed. However, the initial material state is not restored. That is, the material has undergone permanent changes in its molecular level topology, bond structure, and density. This can be seen by comparing results displayed in Figures 4.4(c) and (d). These figures show that while *A*- and *B*-label silicon atoms regain their fourfold coordination upon depressurization to ambient pressure, the *C*-labeled

silicon atom retains its fivefold coordination, Figures 4.4(b) and (d). Thus, the average coordination number of silicon atoms in the relaxed-then-depressurized state, Figure 4.4(d), is higher than that in the initial configuration, Figure 4.4(c). Furthermore, while the aforementioned twofold Si-O ring was broken upon depressurization, the threefold ring involving the *C*, *D* and *E*-labeled silicon atoms survived this process. In addition, a new fourfold ring involving the Si atoms labeled *F*, *G*, *H* and *I* was formed. The threefold and fourfold rings were not present in the initial molecular-level configuration, Figure 4.4(c).

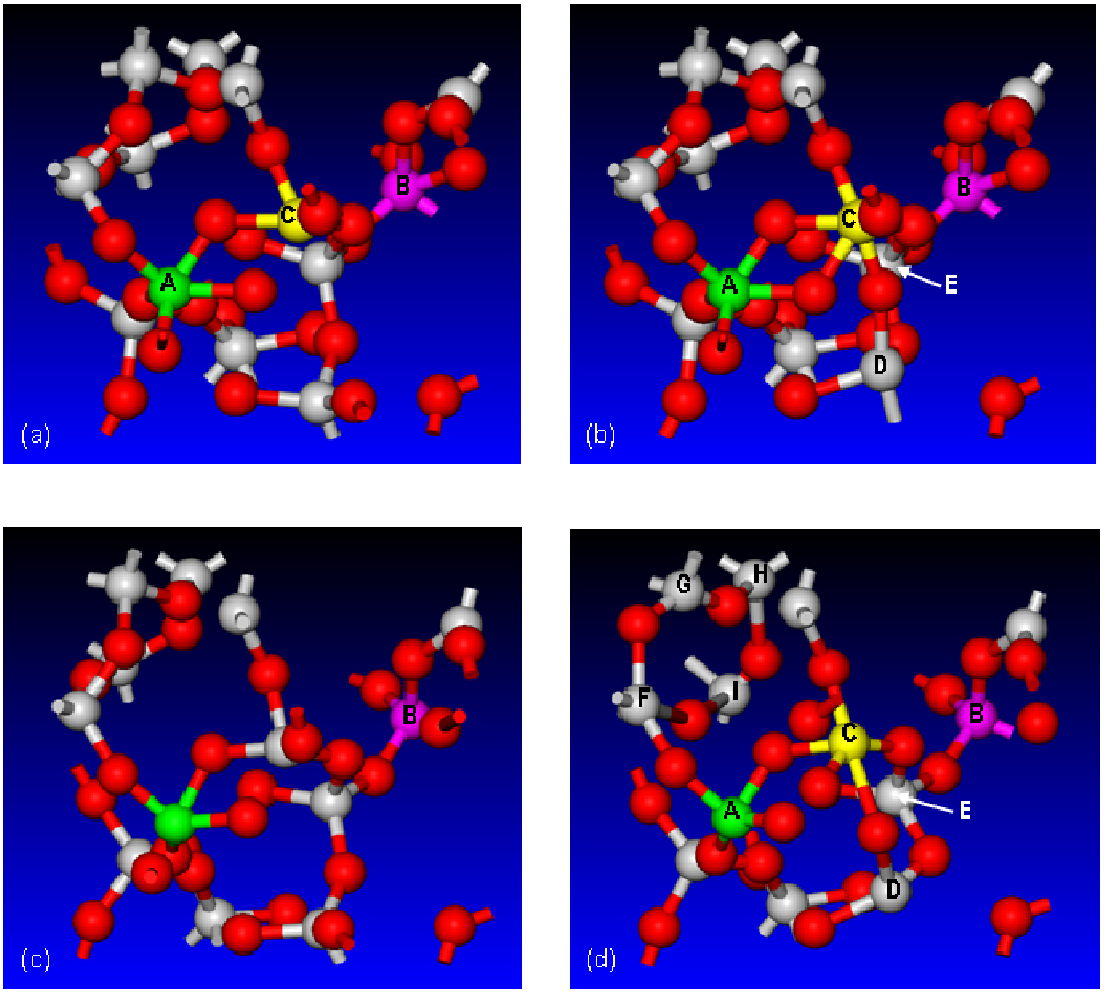

Figure 4.4: The molecular level topologies pertaining to: (a) high-pressure state; (b) high pressure state after a prolonged (20ps) relaxation period; (c) ambient pressure state resulting from depressurization of state (a); and (d) ambient pressure state resulting from depressurization of state (b).

4.5.1.2 Pressure vs. Degree-of-compression Relation

An example of the typical pressure, P vs. degree-of-compression, μ results obtained in the present molecular-level analysis of high-pressure irreversible densification of glass is displayed in Figure 4.5. The results in Figure 4.5 show four loading pressurization/ depressurization cycles. The first cycle does not result in any irreversible densification of glass since the maximum pressure attained is not high enough. The second and third cycles yield irreversible densification and reveal that this process is associated with a nearly constant ca. 4GPa pressure level. During the last cycle, irreversible densification is completed so that glass behaves as a perfectly elastic material when subjected to any further loading.

To summarize, the examination of the results displayed in Figure 4.5 revealed the following three important findings: (a) irreversible densification begins at a pressure level of ~4GPa and proceeds to full densification at a nominally constant pressure; (b) irreversible densification is associated with a density increase of ca. 5%; and (c) the average rate of change of pressure with density (which scales with the material bulk modulus) is not significantly different (and will be assumed equal) in the pre- and post-densification glass states.

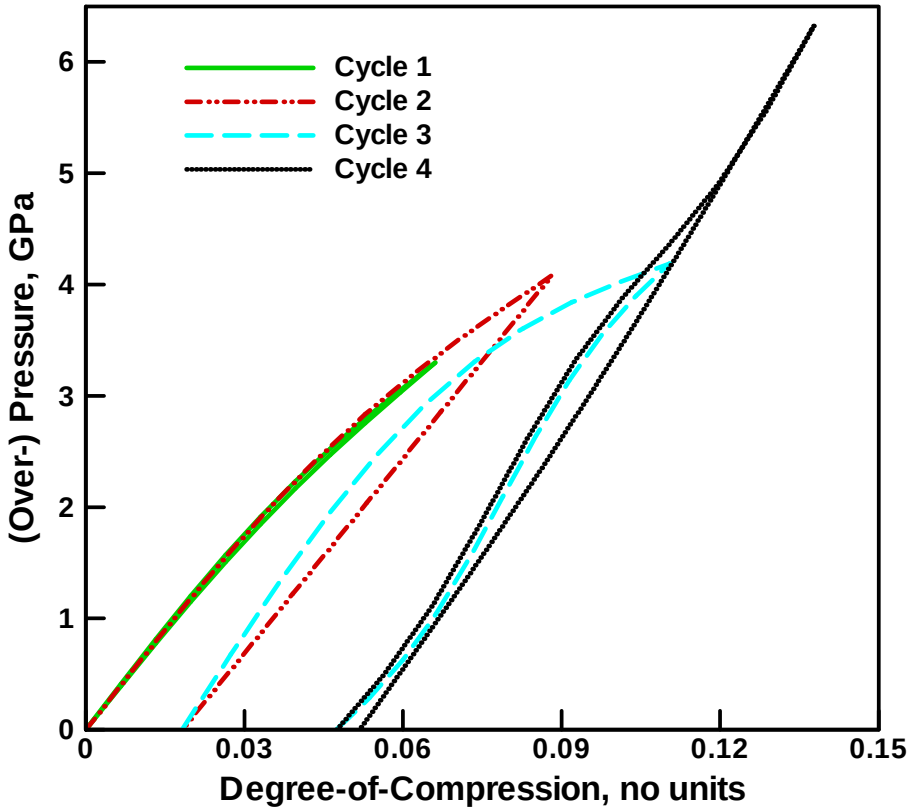

Figure 4.5: Typical pressure vs. degree-of-compression results obtained in the present molecular-level analysis of repeated pressurization/depressurization simulations. In each loading cycle, pressurization was carried out to a higher peak pressure followed by a complete depressurization (i.e. to the atmospheric pressure).

It should be noted that the aforementioned findings (a) and (c) were found not to be very sensitive to the random selection of the initial molecular-level configuration of glass. On the other hand, the extent of irreversible densification was found to vary in a 3-7% range depending on the choice of this configuration. This observation suggests that the volumetric response of the soda-lime glass in its pre- and post-irreversible compaction states as well as the pressure at which irreversible compaction initiates/proceeds are functions of the global/assembly level thermodynamic state of the material while the extent of the irreversible densification is more sensitive to the local-details of the material microstructural state.

4.5.1.3 Densification-induced Material Strengthening

As mentioned earlier, molecular level simple-shear tests were carried out in order to assess the extent of irreversible-densification induced strengthening of glass. Toward that end, shearing of the computational cell was carried out in small increments followed by energy minimization with respect to the atomic positions. An example of the typical molecular-level topology evolution accompanying these tests is displayed in Figures 4.6(a)-(d). To help prevent the computational crystal from settling into a nearby metastable higher-energy configuration, a 10,000-step 300K *NVT* molecular dynamics (*equilibration*) run was introduced between the cell shearing and the energy minimization steps. This procedure yielded a plot of the potential energy increase (relative to that in the initial optimized computational cell) versus the shear angle of the computational cell. The shear angle gradient of the potential energy increase divided by the constant unit cell volume is then used to define the material shear strength. This procedure revealed that the shear strength of glass in the irreversibly-compacted state is higher by a factor of ca. 1.5 relative to the strength of glass in the initial state.

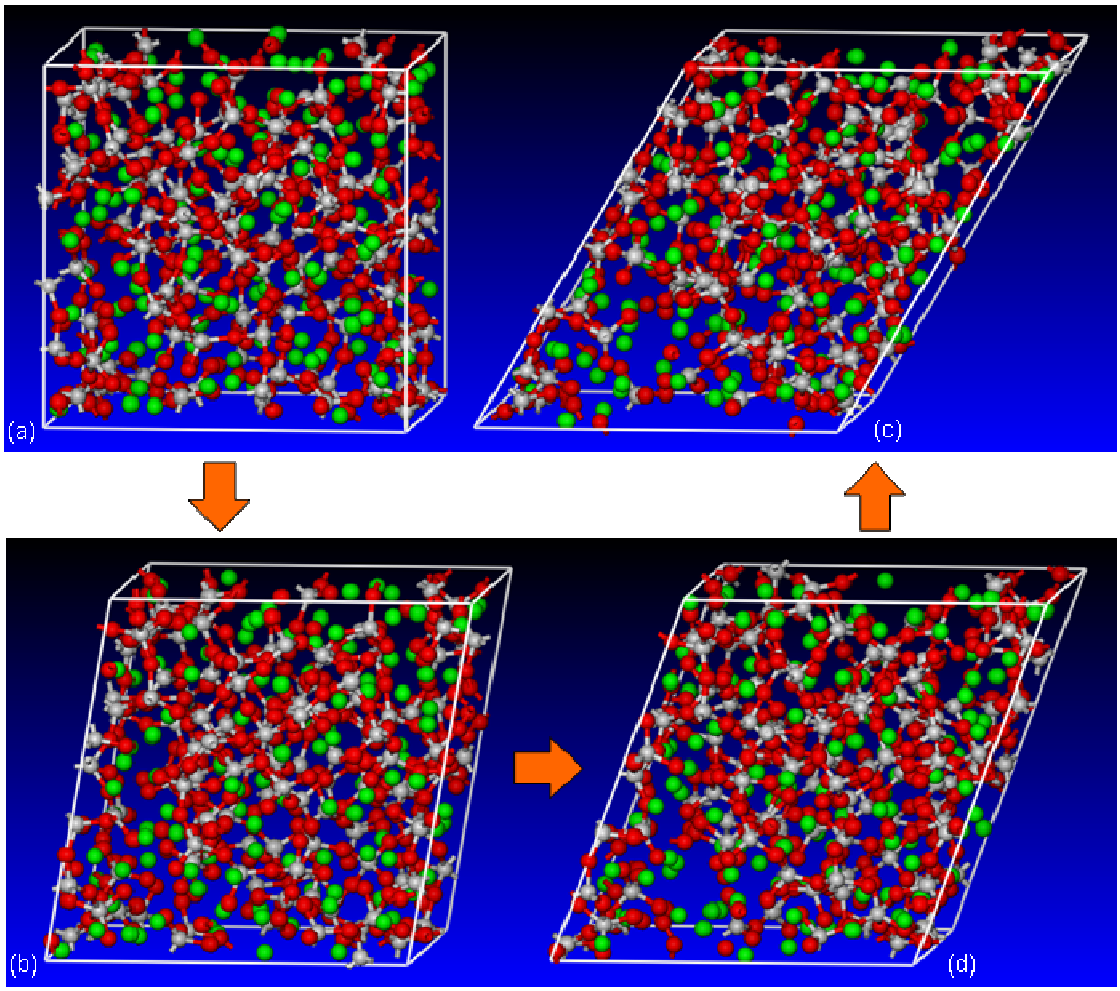

Figure 4.6: An example of molecular-level topology evolution accompanying simple-shear mechanical tests. The tests were used to assess the extent of irreversible-densification induced strengthening of glass.

4.5.1.4 Kinetics/Dynamics of Irreversible-densification Processes

Conventionally, room–temperature is considered to be associated with a low value of the material homologous temperature and, in the case of soda-lime glass, lies several hundreds of degrees below the glass-transition temperature. Hence, it is quite unusual that significant microstructural changes can occur in soda-lime glass at room temperature. However, it should be recognized that, in the present case, the glass is subjected to high levels of pressure which greatly increases the potential energy of this material in its original microstructural state. In other words,

as the pressure is increased other microstructural states of glass become thermodynamically preferred. In the lower range of pressures, while the alternative microstructural states may be thermodynamically preferred, the presence of an activation-energy barrier prevents (except at sufficiently high temperatures) the phase transition of the material from its initial microstructural state to the thermodynamically-preferred microstructural state. In the upper range of these pressures, on the other hand, the activation energy barrier disappears (at least, locally) so that the phase transition and the associated irreversible-densification can take place at very high rates and without any assistance from thermal activation.

4.5.2 JH2 Equation of State and Strength-model Modifications

The molecular-level modeling results attained in the previous section were used to modify the original JH2 EOS and the strength model (as presented in Section 4.4). A brief description of these modifications is given in the remainder of this section.

4.5.2.1 Modifications to the Equation of State

An examination of the polynomial EOS for glass as implemented in the ANSYS/Autodyn material library revealed that the extent of non-linearity is quite small, and hence, the P vs. μ relationship was simplified using a linear EOS. In accordance with the results obtained in the previous section, the following additional simplifications/assumptions were made: (a) the bulk modulus was assumed to take the same (constant) value in both the initial and compacted state of glass, as well as in all intermediate glass states; and (b) irreversible densification of glass is assumed to take place at a constant level of pressure. In accordance with the molecular-level computational results presented in the previous section, this level of pressure was set to a value of 4GPa.

A schematic of the changes made in the *P* vs. μ relationship is given in Figure 4.7. The aforementioned modifications in the JH2 EOS were implemented in the "*MDEOS_USER_1.f90*" material user subroutine which is then linked with ANSYS/Autodyn object code to form a new executable.

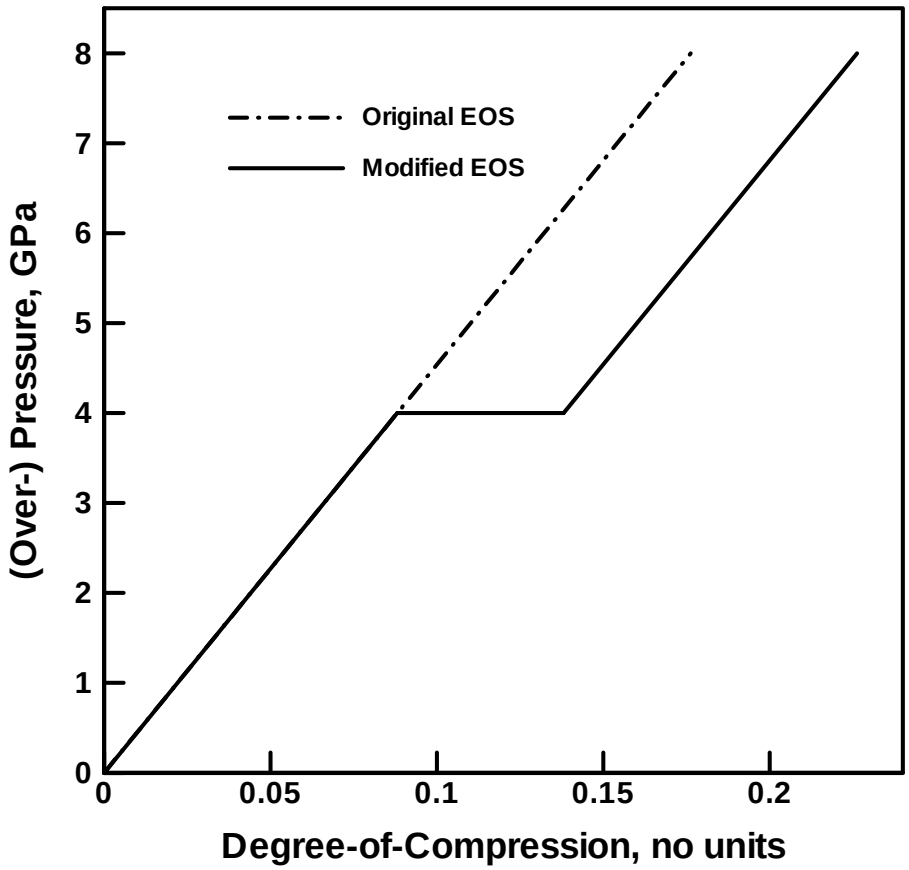

Figure 4.7: A schematic the modifications made in the JH2 (Over-pressure, P vs. Degree-of-Compression, μ) Equation of State in order to account for the effect of high-pressure irreversible densification.

4.5.2.2 Modifications of the Strength Model

Irreversible densification of glass is assumed to increase its strength, both in the damage-free and the fractured states. This assumption is based on the following argument: in the case of the damage-free glass state, irreversible densification is assumed to *repair* molecular-level void-

like regions. In the case of the fractured glass state, irreversible densification is assumed to act as a potent fragment-deformation mechanism resulting in mutually more-conformal fragments. The resulting increase in inter-fragment contact surface areas would then give rise to an increase in the friction-controlled strength of fractured glass. An examination of Eqs. (4.26)-(4.27) revealed that the parameters *A* and *B* control glass strength in the two states, respectively. Following the aforementioned molecular-level findings regarding densification-induced strengthening of the glass, parameters *A* and *B* are increased by a factor of 1.5 for the fully densified glass material. At the intermediate levels of glass densification, parameters *A* and *B* are assumed to be linearly related to the degree of irreversible densification. The aforementioned modifications in the JH2 strength model were implemented in the "*MDSTR_USER_1.f90*" material user subroutine which is then linked with ANSYS/Autodyn object code to form a new executable.

4.5.3 Effect of High-pressure Irreversible-densification on Ballistic-impact Resistance of Glass

In the previous section, the molecular-level computational results regarding high-pressure irreversible-densification of glass were used to modify the EOS and the strength relations within the JH2 continuum model for this material. In this section, a simple transverse impact of a monolithic glass plate by a solid right-circular cylinder (*FSP*) is analyzed computationally in order to assess if the aforementioned modifications in the JH2 model have any significant effect on the temporal evolution and spatial distribution of damage within the glass plate during impact and on the overall glass-plate penetration resistance.

4.5.3.1 Problem Formulation

A schematic of a circular disk-shaped glass-plate (25.0mm-thick, 75.0mm-radius) impacted by an FSP (12.7mm-diameter, 12.7mm-length) problem is provided in Figure 4.8(a). Due to the attendant symmetry of the problem, an axisymmetric 2-D formulation was employed.

An example of the finite-element mesh based on the first-order four-node finite elements is displayed in Figure 4.8(b). It is seen that a finer mesh is used in the FSP and in the region of the glass plate which is most-severely affected during impact/penetration of the plate by the FSP.

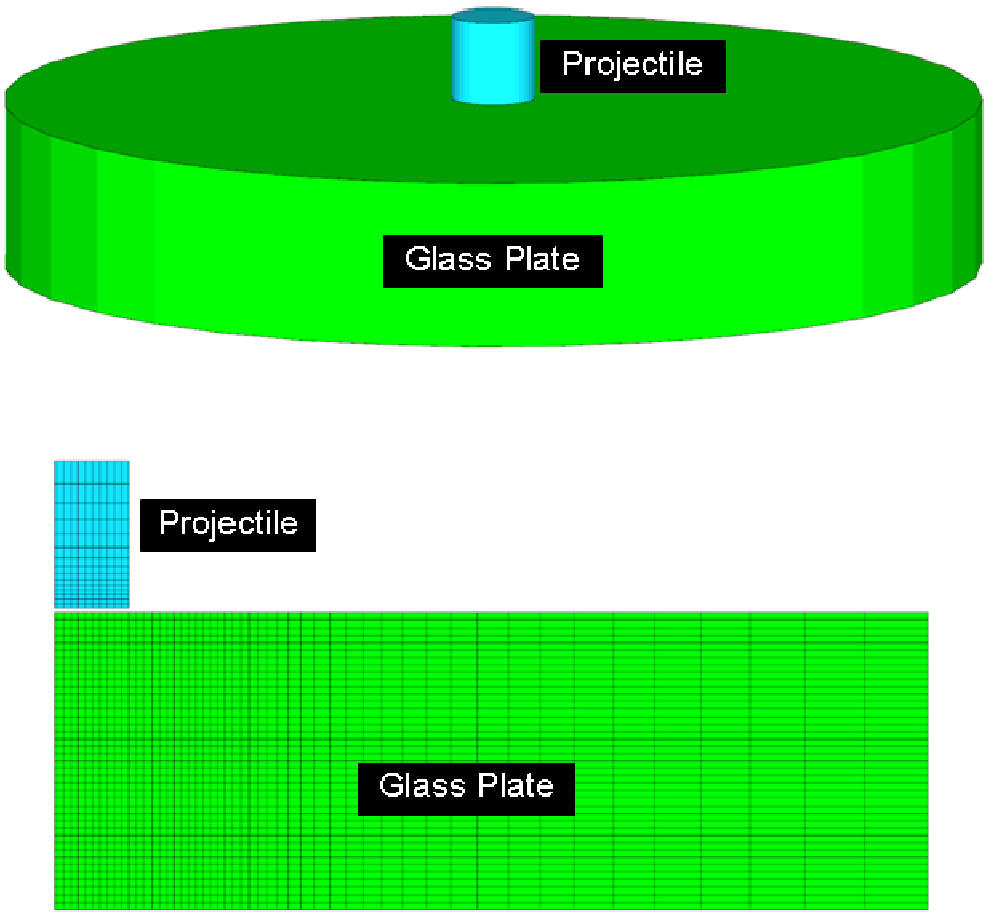

Figure 4.8: (a) A schematic of the glass plate impacted by a right-circular solid cylindrical projectile; and (b) an example of the computational mesh, based on the first-order four-node finite elements, used to model the projectile and the glass plate.

The FSP is assumed to be made of AISI/SAE 4340 steel and this material is modeled using a linear EOS, the Johnson-Cook strength model, the Johnson-Cook failure model and an erosion model based on the equivalent geometrical (i.e. elastic + plastic + crack) instantaneous

strain. The details regarding formulation and parameterization of this model can be found in our previous work [4.28].

All the calculations carried out in the present work were done using ANSYS/Autodyn, a general purpose non-linear dynamics modeling and simulation software [4.24]. A transient non-linear dynamics problem is analyzed within ANSYS/Autodyn by solving simultaneously the governing partial differential equations for the conservation of momentum, mass and energy along with the material-model equations and the equations defining the initial and the boundary conditions. The equations mentioned above are solved numerically using a second-order accurate explicit scheme and one of the two (*Lagrang*e or *Euler*) basic mathematical approaches/processors. The key difference between the two processors is that within the Lagrange processor the numerical grid is attached to and moves along with the material during calculation while within the Euler processor, the numerical grid is fixed in space and the material moves through it. In the present work, both the FSP and the glass plate are modeled using the Lagrange processor. In our recent work [4.28], a brief discussion was given of how the governing differential equations and the material-model relations define a self-consistent system of equations for the dependent variables (nodal displacements, nodal velocities, material-element densities and material-element internal energy densities). In the same reference, a brief overview was provided of the contact/interaction and erosion algorithms implemented in ANSYS/Autodyn.

The initial conditions are defined is such a way that the FSP is assigned a downward velocity while the glass plate is assumed to be stationary. To reduce the effect of reflection of the shock waves at the (outer) hoop surface of the glass plate, the so called *transmit* boundary conditions were applied to all the nodes residing on this surface. The transmit boundary conditions enable propagation of the stress waves across the hoop surface without reflection [4.28].

4.5.3.2 Glass-plate Impact Computational Results

An example of the results pertaining to the temporal evolution and spatial distribution of deformation and damage within the glass-plate and the FSP is displayed in Figures 4.9(a)-(d). Various deformation/failure models are color coded to improve clarity of the results. The results displayed in Figures 4.9(a)-(d) show that shear-induced damage/failure is found mainly in the region underneath the FSP, tensile failure occurs at the glass-plate back-face (and is caused by reflection of the compressive stress wave at this face), and the FSP undergoes extensive plastic deformation (but little or no failure). These findings are fairly common and, hence, will not be discussed any further. It should be noted, however, that the results displayed in Figures 4.9(a)-(d) pertain to an FSP initial velocity of 600m/s and the original (unmodified) JH2 glass-material model.

When the JH2 material model was modified to include the effect of high-pressure irreversible-densification and the FSP initial velocity was maintained at 600m/s, an identical temporal evolution and spatial distribution of the material deformation and failure was found as those in Figures 4.9(a)-(d). This finding was readily rationalized by establishing that the pressure within the glass-plate never reached the level of 4GPa required for the irreversible-densification to commence.

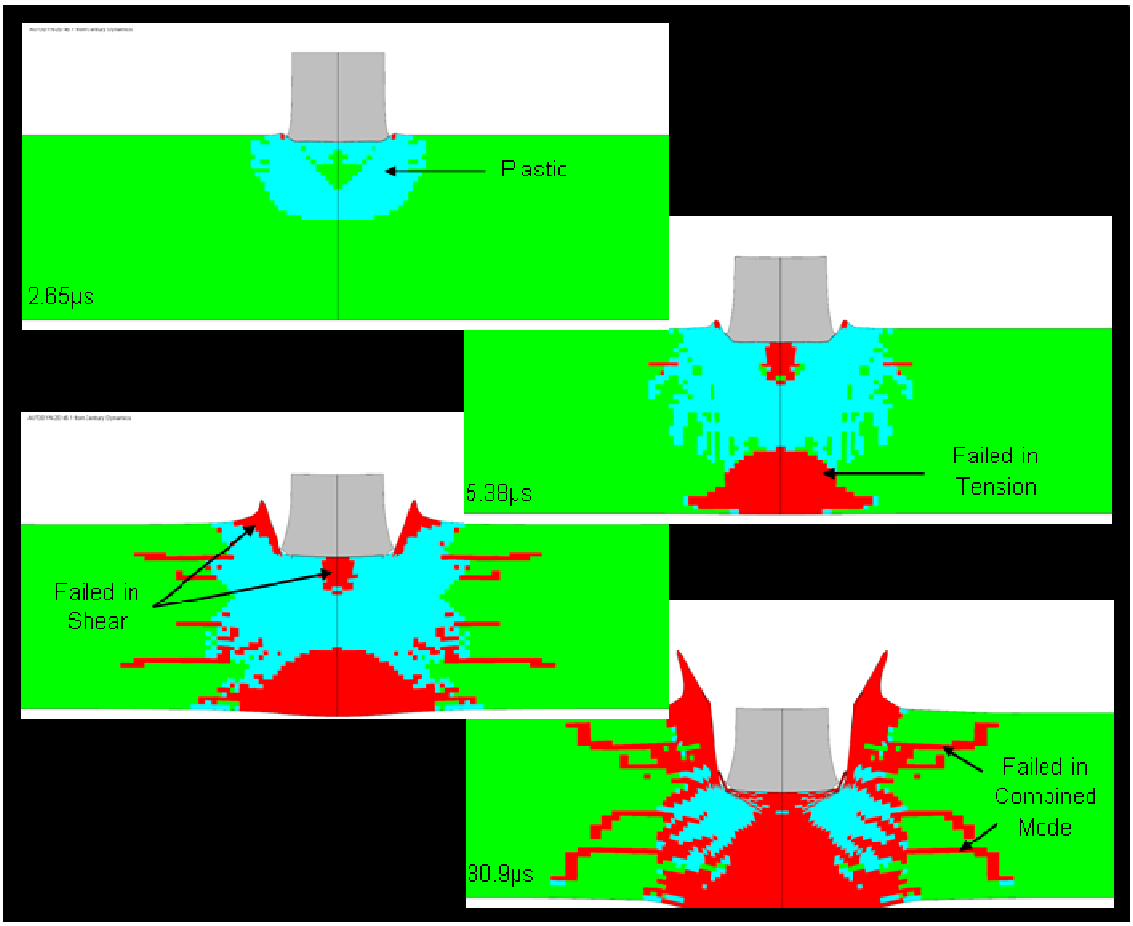

Figure 4.9: An example of the results pertaining to the temporal evolution and spatial distribution of deformation and damage within the glass-plate and the FSP

When the FSP velocity was increased to 1000m/s, the effect of irreversible-densification was observed. An example of this effect is given in Figures 4.10(a)-(b), in which distribution of deformation and damage within the glass-plate and the FSP are given for the cases of original and modified JH2 glass material models, respectively. The results displayed in these figures show that the extent of damage in the FSP increased, while the extent of damage in the glass-plate is reduced for the case of the modified JH2 material model. Also, the FSP exit velocity was found to be reduced from 469.1m/s to 460.2m/s as a result of glass material model modifications. This is a relatively small decrease (ca. 2%) in the FSP residual velocity which may suggest that the

irreversible compaction of glass may not be a potent ballistic-resistance enhancing mechanism in glass.

To further explore the effect of irreversible densification, a parametric study was set up in which the key parameters of this process were varied within physically realistic limits. Specifically, the pressure at which densification starts was varied in a range 1-10GPa range, density increase between 5 and 15% and the densification-induced strengthening extent (i.e. the multiplier of *A* and *B* parameters) in a 1.0-2.0 range. This study revealed that, at an FSP velocity of 1000m/s, the FSP exit velocity can be reduced from 469.1m/s to 346.4m/s (a 26% reduction). The optimal set of irreversible-densification parameters was identified as: densification pressure 1GPa, density increase 5% and a strengthening extent of 2.0. Figure 4.10(c) reveals spatial distribution of deformation/damage for the modified JH2 glass model and the optimal set of irreversible densification parameters. It is seen that there is a significant reduction in damage to the glass material directly under the projectile due to the increased strength of the densified glass. This reduction in failed material under the projectile promotes an increase in the extent of plastic deformation experienced by the projectile which leads to spreading of its material over a larger area. These observed effects combine to allow for a significant decrease in the kinetic energy of the projectile with respect to the non-optimized glass material case.

Additional simulations were next carried out in order to establish if irreversible-compaction of glass (if associated with the aforementioned optimal set of parameters) can improve the ballistic-resistance of glass at lower FSP velocities. It was found that at an FSP initial velocity of 600m/s, the FSP residual velocity was reduced from 240.4m/s to 154.2m/s. Thus, if the irreversible-densification parameters of glass can be set to their optimal values, then the ballistic penetration resistance can be improved for a range of FSP impact velocities.

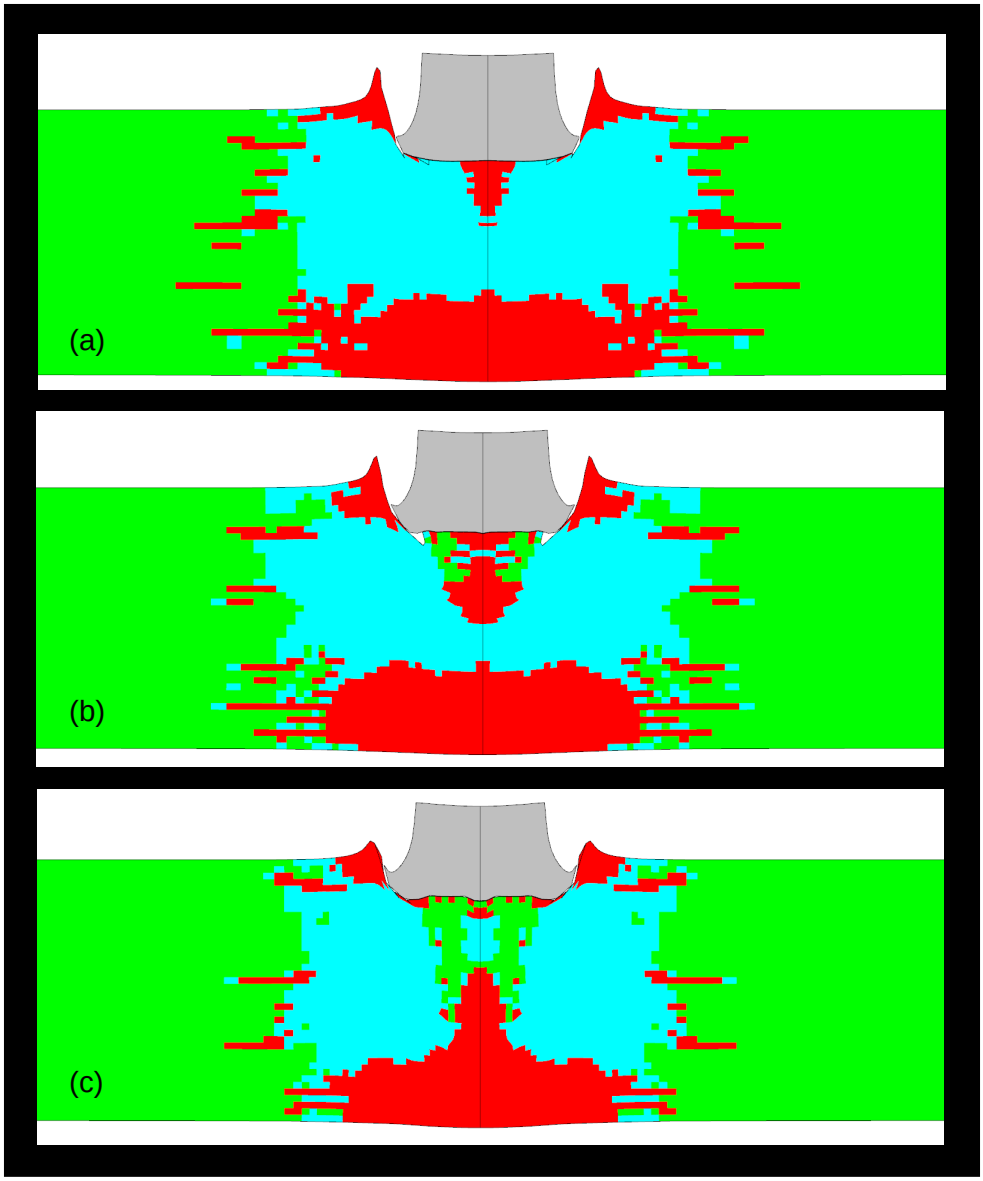

Figure 4.10: The effect of the JH2 material-model modifications on the spatial distribution of damage within a soda-lime glass plate impacted with a 12.7mm-diameter, 12.7mm-height right circular solid cylinder at an initial velocity of 1000m/s: (a) the original model; (b) the model modified using molecular-level finding; and (c) the modified using an optimal set of high-pressure irreversible-densification parameters.

4.5.3.3 Experimental Validation

While there are numerous reports of experimental investigations aimed at assessing the ballistic performance of soda-lime glass [e.g.4.12-15, 4.31], there are no open-literature reports

regarding the operation or the role of irreversible densification in improving the ballistic performance of soda-lime glass. To address this problem, a companion experimental investigation is underway at the Army Research Laboratory, Aberdeen Proving Ground, MD. Preliminary findings obtained in the post-mortem X-ray diffraction studies of glass fragments, carried out as part of this investigation, show the presence of a higher-density soda-lime glass microstructural state and can be found in Ref. [4.32].

4.5.3.4 Materials-by-design Approach

In summary, the results obtained in the present work show that high-pressure irreversible-densification of glass can become a potent ballistic-resistance enhancing mechanism provided (via chemical modifications, and various thermo-mechanical and chemical treatments) the densification parameters can be set to or near optimal values. In our ongoing work, molecular-level modeling is being extensively used to help better define such glass-modifying strategies/procedures. Specifically, within the molecular-level modeling framework, the effect of the glass chemistry and its random-network structure (as characterized by a set of random-network microstructural parameters [4.29,4.30]) on the irreversible-densification characteristics (i.e. the onset pressure and the extent of density change) is being examined. In addition, a link is being established between the molecular-level modeling parameters and the JH2 continuum-level material parameters. Table 4.1 summarizes the JH2 model parameters and lists their typical values for the case of a *non-transforming* soda-lime glass. In the present work, the Equation of State is modified to account for the irreversible densification transition and two strength parameters (parameters A and B) were modified. In our on-going work, an attempt is being made to identify additional JH2-model parameters which require modifications as the soda-lime glass chemistry and the random-network structure are being modified. It is hoped that this will become a fruitful exercise of the so-called *materials-by-design* concept in which component-level

experimental and computational investigations are carried out in order to identify the envelope of optimal material properties. This is then followed by an extensive experimental/computational procedure aimed at designing and synthesizing the materials with the targeted set of properties/performance attributes.

Table 4.1: Johnson-Holmquist 2 Material Model Parameters for Soda-Lime Glass

Parameter	Symbol	Unit	Value
Equation of State: Linear			
Bulk Modulus	K_1	Pa	4.54e10
Strength Model: Johnson-Holmquist 2			
Shear Modulus	G	Pa	3.04e10
Hugoniot Elastic Limit	σ_{HEL}	Pa	5.95e9
Intact Strength Constant	A	N/A	0.93
Intact Strength Exponent	N	N/A	0.77
Strain Rate Constant	C	N/A	0.003
Fractured Strength Constant	B	N/A	0.35
Fractured Strength Exponent	M	N/A	0.40
Max Fracture Strength Ratio	-	N/A	0.50
Failure Model: Johnson-Holmquist 2			
Hydro Tensile Limit	T	Pa	-3.5e7
Damage Constant 1	D_1	N/A	0.053
Damage Constant 2	D_2	N/A	0.85
Bulking Constant	β	N/A	1.0

4.6 Summary and Conclusions

Based on the results obtained in the present work, the following main conclusions can be made:

1. Molecular-level modeling of soda-lime glass revealed the occurrence of an irreversible-densification process when the pressure exceeds ca. 4GPa. Close examination of molecular-level topology revealed that this process is associated with an increase in the average coordination number of the silicon atoms, and the creation of two to fourfold (smaller, high packing-density) Si-O rings.

2. Modifications of the continuum-level material model for glass to include the effect of irreversible-densification resulted in minor improvements in the ballistic-penetration resistance of glass and only for high projectile initial velocities. Also, it is observed that the main threat to a soda-lime glass-based transparent-armor panel during the ballistic impact arises from the normal/tensile and less from deviatoric/shear stresses.

3. A parametric study involving variations of the key irreversible-densification parameters within physically realistic limits revealed that the optimal combination of these parameters can result in substantial improvements in the ballistic-resistance of glass over a wide range of projectile velocities.

4. It is suggested that various chemical-modification and thermo-mechanical treatment strategies should be employed in order to attain this optimal set of irreversible-densification parameters. This is an example of the materials-by-design concept within which an optimal combination of material parameters is identified in order to maximize component-level performance.

4.7 References

4.1 E. Strassburger, P. Patel, W. McCauley and D. W. Templeton, *Visualization of Wave Propagation and Impact Damage in a Polycrystalline Transparent Ceramic- AlON*, Proceedings of the 22nd International Symposium on Ballistics, November 2005, Vancouver, Canada.

4.2 AMPTIAC Quarterly: *Army Materials Research*: *Transforming Land Combat through New Technologies*, 8, no.4, 2004.

4.3 E. Strassburger, P. Patel, J. W. McCauley, C. Kovalchick, K. T. Ramesh and D. W. Templeton, *High-Speed transmission Shadowgraphic and Dynamic Photoelasticity Study of Stress Wave and Impact Damage Propagation in Transparent Materials and Laminates Using The Edge-on Impact Method*, Proceedings of the 23rd International Symposium on Ballistics, Spain, April 2007.

4.4 D. Z. Sun, F. Andreiux, A. Ockewitz, *Modeling of the Failure Behavior of Windscreens and Component Tests*, 4th LS-DYNA Users' Conference, Bamberg, Germany, 2005.

4.5 Woodcock, L. V., Angell, C. A. and Cheeseman, P., *Molecular dynamics studies of the vitreous state: Simple ionic systems and silica*, The Journal Chemical Physics, 65, 1976, 1565–1577.

4.6 R. G. D. Valle, E. Venuti, *High-pressure Densification of Silica Glass: A Molecular-dynamics Simulation*, Physical Review B, 54, 6, 1996, 3809-3816.

4.7 K. Trachenko, M. T. Dove, *Densification of Silica Glass under Pressure*, Journal of Physics: Condensed Matter, 14, 2002, 7449-7459.

4.8 Y. Liang, C. R. Miranda, S. Scandolo, *Mechanical Strength and Coordinate Defects in Compressed Silica Glass: Molecular Dynamics Simulations*, Physical Review B, 75, 024205, 2007.

4.9 B. Nghiem, *PhD thesis*, University of Paris 6, France 1998.

4.10 C. Denoual and F. Hild, *Dynamic Fragmentation of Brittle Solids: A Multi-scale Model*, European Journal of Mechanics of Solids A, 21, 2002, 105-120.

4.11 M. Yazdchi, S. Valliappan and W. Zhang, *A Continuum Model for Dynamic Damage Evolution of Anisotropic Brittle Materials*, International Journal of Numerical Methods in Engineering, 39, 1996, 1555-1583.

4.12 F. Hild, C. Denoual, P. Forquin and X. Brajer, *On the Probabilistic and Deterministic Transition Involved in a Fragmentation Process of Brittle Materials*, Computers and Structures, 81, 2003, 1241-1253.

4.13 M. Grujicic, B. Pandurangan, N. Coutris, B. A. Cheeseman, C. Fountzoulas, P. Patel and E. Strassburger, *A Ballistic Material Model for Starphire®, a Soda-Lime Transparent-Armor Glass*, Materials Science and Engineering-A, 491, 1-2, 2008, 397-411.

4.14 M. Grujicic, B. Pandurangan, W. C. Bell, N. Coutris, B. A. Cheeseman, C. Fountzoulas and P. Patel, *An Improved Mechanical Material Model for Ballistic Soda-Lime Glass*, Journal of Materials Engineering and Performance, 18, 8, 2009, 1012-1028.

4.15 M. Grujicic, B. Pandurangan, N. Coutris, B. A. Cheeseman, C. Fountzoulas and P. Patel, *A Simple Ballistic Material Model for Soda-Lime Glass*, International Journal of Impact Engineering, 36, 2009, 386-401.

4.16 T. J. Holmquist, D. W. Templeton, K. D. Bishnoi, *Constitutive Modeling of Aluminum Nitride for Large Strain High-strain Rate, and High-pressure Applications*, International Journal of Impact Engineering, 25, 2001, 211-231.

4.17 G. T. Camacho and M. Ortiz, *Computational Modeling of Impact Damage in Brittle Materials*, International Journal of Solids and Structures, 33, 20-22, 1996, 2899-2938.

4.18 H. Sun, *COMPASS: An ab Initio Force-Field Optimized for Condensed-Phase Applications Overview with Details on Alkane and Benzene Compounds*, Journal of Physical Chemistry B, 102, 1998, 7338-7364.

4.19 H. Sun, P. Ren, and J. R. Fried, *The COMPASS force field: parameterization and validation for phosphazenes*, Computational and Theoretical Polymer Science, 8, 1/2, 1998, 229-246.

4.20 <http://www.accelrys.com/mstudio/ms modeling/discover.html>.

4.21 <http://www.accelrys.com/mstudio/ms modeling/visualiser.html>.

4.22 <http://www.accelrys.com/mstudio/ms modeling/amorphouscell.html>.

4.23 S. Nose, *A unified formulation of the constant temperature molecular dynamics methods*, The Journal of Chemical Physics, 81, 1984, 511-519.

4.24 AUTODYN-2D and 3D, *Version 6.1, User Documentation*, Century Dynamics Inc., 2006.

4.25 G. R. Johnson and T. J. Holmquist, *An Improved Computational Constitutive Model for Brittle Materials*, High Pressure Science and Technology, 1993. (AIP, New York, 1994).

4.26 T. J. Holmquist, D. W. Templeton, K. D. Bishnoi, *Constitutive Modeling of Aluminum Nitride for Large Strain High-strain Rate, and High-pressure Applications*, International Journal of Impact Engineering, 25, 2001, 211-231.

4.27 M. Grujicic, B. Pandurangan, U. Zecevic, *Ballistic Performance of Alumina/S-2 Glass-reinforced Polymer-matrix Composite Hybrid Lightweight Armor Against Armor Piercing (AP) and Non-AP Projectiles*, Multidiscipline Modeling in Materials and Structures, 3, 2007, 287-312.

4.28 M. Grujicic,B. Pandurangan, C. D. Angstadt, K. L. Koudela, and B. A. Cheeseman, *Ballistic Performance Optimization of a Hybrid Carbon Nanotube/E-glass Reinforced*

Poly-vinyl-ester-epoxy Matrix Composite Armor, Journal of Material Science, 42, 2007, 5347–5349.

4.29 M. Grujicic, W. C. Bell, P. S. Glomski, B. Pandurangan, B. A. Cheeseman, C. Fountzoulas, P. Patel, *Multi-Length Scale Modeling of High-Pressure Induced Phase Transformations In Soda-Lime Glass*, Journal of Materials Engineering and Performance, DOI: 10.1007/s11665-010-9774-2, 2010.

4.30 M. Grujicic, W. C. Bell, B. Pandurangan, B. A. Cheeseman, C. Fountzoulas, P. Patel, *Molecular-Level Simulations of Shock Generation and Propagation in Soda-lime Glass*, Journal of Materials Science, submitted for publication, 2011.

4.31 S. Bless and T. Chen, *Impact Damage in Layered Glass*, International Journal of Fraction, 162, 1-2, 2010, 151-158.

4.32 G. A. Gazonas, J. W. McCauley, I. G. Batyrev, R. C. Becker, P. Patel, B. M. Rice, and N. S. Weingarten, *Multiscale Modeling of Non-crystalline Ceramics (Glass)*, ARL Technical Report, ARL Aberdeen Proving Ground, January 2011.

CHAPTER FIVE

MULTI-LENGTH SCALE MODELING OF HIGH-PRESSURE INDUCED PHASE TRANSFORMATION IN SODA-LIME GLASS

5.1 Abstract

Molecular-level modeling and simulations are employed to study room-temperature micro-structural and mechanical response of soda-lime glass when subjected to high (i.e., several GPa) uniaxial-strain stresses/pressure. The results obtained revealed the occurrence of an irreversible phase-transformation at ca. 4GPa which was associated with a (permanent) 3-7% volume reduction. Close examination of molecular-level topology revealed that the pressure-induced phase transformation in question is associated with an increase in the average coordination number of the silicon atoms, and the creation of two to fourfold (smaller, high packing-density) Si-O rings. The associated loading and unloading axial-stress vs. specific-volume isotherms were next converted into the corresponding loading Hugoniot and unloading isentrope axial-stress vs. specific-volume relations. These were subsequently used to analyze the role of the pressure-induced phase-transformation/irreversible-densification in mitigating the effects of blast and ballistic impact loading onto a prototypical glass plate used in monolithic and laminated transparent armor applications. The results of this part of the work revealed that pressure-induced phase-transformation can provide several beneficial effects such as lowering of the loading/unloading stress-rates and stresses, shock/release-wave dispersion and energy absorption associated with the work of phase-transformation.

5.2 Introduction

Several different materials and design strategies are currently being used in transparent blast/ballistic-impact resistant vehicle structures (e.g. windshields, door windows, viewports,

etc.). Among the most recently introduced transparent materials and technologies, the following have received the most attention: transparent crystalline ceramics (e.g. aluminum-oxinitride spinel, AlON, sapphire [5.1]), new transparent polymer materials (e.g. transparent nylon [5.2]), and new interlayer technologies (e.g. polyurethane bonding layers [5.3]), and new laminate structure designs [e.g. 5.4]. Despite the clear benefits offered by these materials and technologies (e.g. transparent ceramics offer a very attractive combination of high stiffness and high hardness levels, highly ductile transparent polymers provide superior fragment containing capabilities, etc.), ballistic glass remains an important constituent material in a majority of transparent impact resistant structures used today. Among the main reasons for the wide-scale use of glass, the following three are most frequently cited: (a) glass-structure fabrication technologies enable the production of curved, large surface-area, transparent structures with thickness approaching several inches; (b) relatively low material and manufacturing costs; and (c) compositional modifications, chemical strengthening, and controlled crystallization have demonstrated the capability to significantly improve the shock/ballistic impact survivability of glass [e.g. 5.2].

Extensive prototyping and laboratory/field experimental testing is typically required for the development of new glass-based transparent impact resistant structures aimed at reducing the vulnerability of protected vehicle occupants and on-board instrumentation to various blast/ballistic threats. These experimental efforts are critical for ensuring the utility and effectiveness of the transparent impact resistant structures. However, these efforts are generally expensive, time-consuming and involve destructive test procedures. While the role of prototyping/testing programs remains critical, they are increasingly being complemented by the corresponding computation-based modeling and simulation efforts. However, the effectiveness and reliability of the computation-based modeling and simulation approaches is greatly affected by the ability of the associated material models to realistically describe deformation/fracture

response of ballistic glass under high-rate/high-pressure loading conditions encountered during blast/ballistic impact. Therefore, one of the main objectives of the present work is to further advance the application of computational modeling/ simulation-based engineering approaches of transparent impact-resistant structures via the identification and quantification of processes and phenomena occurring in glass under high-pressure/high-strain rate loading conditions as encountered during blast/ballistic impact.

A comprehensive literature review carried out as part of the present work revealed that the mechanical behavior of glass is modeled predominantly using three distinct approaches: (a) molecular-modeling methods; (b) continuum-material approximations, and (c) models based on explicit crack representation. A brief overview and the main findings for each of these three approaches are given below.

Within the molecular modeling methods, glass is treated as an assembly of discrete particles (atoms and ions) which interact with each other via the so-called *inter-atomic (or force field)* potentials. By employing different mechanics and dynamics schemes, these models can provide a fairly accurate assessment of various glass properties such as elastic constants, strength, chemical and thermal diffusivities, surface energies, etc. Of interest to the present work, a great number of researchers have investigated, using molecular modeling techniques, the propensity of various types of glass (of different chemistries and microstructures) to undergo phase transformations when subjected to high hydrostatic pressures on the order of several GPa's [e.g. 5.5-8]. The emphasis in these investigations was placed on elucidating the predominant atomic-level mechanisms and processes (e.g. increased coordination number, often referred to as *coordination defects*, creation of new metastable chemical bonds, etc.) associated with the phase transformations in glass. In the present work, on the other hand, molecular-modeling investigations of high-pressure micro-structure and behavior of soda-lime glass are carried out in

order to predict the continuum-level mechanical response of this material when subjected to blast/ballistic impact loading conditions. Specifically, the potential of the observed high-pressure phase-transformation/ irreversible densification for blast/ballistic impact mitigation is analyzed.

Within the continuum-level glass models [e.g. 5.9-15], glass is treated as a continuum material whose stiffness and strength properties may become degraded by nucleation, growth, and coalescence of cracks. The fundamental assumption in these models is that the elastic-stiffness and strength degradations are the result of inelastic deformation caused by micron and sub-micron size cracks, and that this degradation can be quantified using a so-called *damage tensor* whose evolution during loading can be formulated using generalized Griffith-type crack initiation and propagation criteria for brittle materials. In addition, some continuum models account for the interactions between the cracks, their coalescence, friction between fragments, competition between micro-cracking leading to fine-scale fragmentation of glass and macro-cracking giving rise to coarse fragmentation, etc. [5.16].

Within the explicit crack representation material model framework, glass is treated as a linear elastic material, and its fracture is considered to take place via nucleation, propagation and coalescence of discrete (rather than smeared-out/homogenized) cracks during impact [e.g. 5.17]. In other words, while within the continuum modeling framework the stiffness/strength-degrading effect of smeared-out cracks is included only implicitly, in the explicit crack representation cracks are considered as discrete entities and their effect on material stiffness/strength is accounted for explicitly. When the latter-type of glass models are implemented into a finite element computational framework, crack nucleation and propagation are handled by duplicating nodes at the crack tip/front. Adaptive re-meshing is used to provide a rich enough set of possible fracture paths around the crack tip. As a crack grows, forces at newly cracked (free) surfaces are brought to zero in accordance with the Griffith criterion to account for crack growth induced unloading.

This procedure enables explicit modeling of the crack coalescence processes which can lead to the formation of fragments. The major disadvantage of the discrete models is their propensity to become extremely computationally expensive and become intractable as the number of cracks increases. That is, in order to capture all possible crack nucleating sites, meshes with micron-size elements are ultimately required. This is the main reason that this type of model is used mainly to study various deformation and fracture processes in glass but are rarely utilized in the computer aided engineering efforts aimed at developing transparent structures with superior blast/ballistic-impact survivability.

As demonstrated above, molecular-level, continuum-level and discrete modeling are maturing areas of glass research which are capable of revealing complex intrinsic mechanisms and phenomena associated with deformation and fracture in glass. However, these modeling approaches are typically concerned only with the effect of the observed processes/mechanisms on the behavior of glass at their respective length scales, and practically no reports were found where the knowledge about glass behavior at one length scale was used to improve glass models at other length scale(s). Therefore, the main objectives of the present work are: (a) to investigate and quantify (using molecular-level modeling and simulation techniques) the high pressure–induced phase transformations in soda-lime glass and the accompanied (irreversible) densification; (b) to use the pressure vs. specific-volume loading/unloading isotherms obtained in (a) in order to construct the corresponding pressure vs. specific-volume loading Hugoniots and un-loading isentropes; and (c) to use the Hugoniots and isentropes obtained in (b) in order to analyze shock propagation within soda-lime glass and the potential of pressure-induced phase-transformation/irreversible densification in mitigating the effects of blast/ballistic impact.

The organization of the paper is as follows: A brief description of the molecular-level microstructure of glass including its random-network representation is presented in Section 5.3.

Details regarding computational model, the inter-atomic force field potentials, the computational method and the key results relating to the molecular-level modeling and simulation portion of the present work are presented in Section 5.4. The procedures used for the conversion of the molecular-level derived loading/unloading isotherms into the corresponding loading Hugoniots and unloading isentropes and the associated results are presented in Section 5.5. Examination of the potential of the pressure-induced phase transformation/irreversible-densification in mitigating the effects of blast/ballistic impact is discussed in Section 5.6. The key conclusions resulting from the present study are summarized in Section 5.6.

5.3 Molecular-level Microstructure of Glass

Due to the lack of long range order, glass is referred to as an amorphous material. The molecular microstructure in glass reveals a random distribution of the basic constituents which is quite different than the regular microstructure found in the crystalline materials. The former molecular-level microstructure is typically described using the so-called *random network model* [5.18] which defines glass as a three dimensional network of oxygen polyhedra (a cation surrounded by three or four oxygen ions) mutually connected through sharing of the vertex oxygen atoms. In the case of silicate-based glasses like soda-lime glass, the polyhedra are mainly SiO_4^{4-} tetrahedra. Elements like silicon, which reside in the center of the polyhedra, are typically referred to as *network-formers* and their valence/coordination-number (four, in the case of silicon) defines the geometry of the polyhedra (tetrahedron, in the case of silicon).

When alkali (or alkaline earth) oxides are added to a pure silicate glass, the added oxygen ions become incorporated into the silicate network while the metallic cations remain close-by to provide local charge neutrality. For the added oxygen ions to attach to the silicate network, some of the Si-O bonds within the network must be broken. Accommodation of these additional oxygen ions within the network as well as the metallic cations necessitates that the network must become

more open. Since alkali (or alkaline earth) based oxides modify the basic silicate network in glass, they are typically referred to as *network modifiers*. Soda-lime glass, which is the subject of the present investigation, contains about 14wt.% Na_2O and 9wt.% CaO with both of these oxides acting as network modifiers. In contrast to network modifiers, more-covalent oxides like B_2O_3 donate metallic cations which are directly incorporated into the glass network and that is the reason that these oxides are generally considered as network formers. It should be noted however that due to a lower valence (three, in the case of boron) the nature of the network polyhedra changes locally from silicate tetrahedra to boron-centered triangles. This type of glass network is found in borosilicate glass which is the subject of our on-going investigation.

Within the random network model, it is often convenient to describe the structure of the network in terms of the average number of oxygen ions per network forming ion, typically denoted as *R*. For single component glasses, such as fused silica (pure SiO_2), *R* takes on the value of 2.0. In the case of soda-lime glass, the presence of additional oxygen ions in the glass network increases the *R* value to ca. 2.41. As a general rule of thumb, higher values of *R* reflect the presence a larger number of oxygen ions per glass forming ion and lead to a more open, weaker structure. On the other hand, smaller values of *R* indicate the presence of network formers with a lower coordination number. Depending on the network former coordination number, its concentration, and the strength of its bond with oxygen, varying effects on the morphology of glass network may be observed. In addition to the *R* parameter, a glass network is often also described in terms of the *X* and *Y* parameters which respectively define the average number of non-bridging (connected to one glass forming ion) and bridging (connected to two glass forming ions) oxygen ions per network polyhedron. In fused silica, *X*=4.0 and *Y*=4.0 since this glass contains only bridging oxygen atoms. On the other hand, since soda-lime glass contains

additional non-bridging oxygen ions, *X* takes on a non-zero value (ca. 0.81) while *Y* drops below 4.0 (ca. 3.19).

In addition to the aforementioned changes in the morphology of glass network which are brought about by changes in glass chemistry, similar changes can be induced mechanically (typically requiring several GPa pressure levels). Specifically, at high pressures, the coordination number of the network formers can change resulting in a phase transformation characterized by changes in the geometry of the network polyhedra. The phase transformations in question could be, either, of the first order resulting in the formation of distinct high-pressure phases at a nominally constant pressure or of the second order characterized by gradual evolution of the low-pressure phase to the high-pressure phase over a range of pressures. These phase transformations can be associated with significant volume changes and, since phase-transformation induced energy absorption is a well-documented phenomenon responsible for high toughness levels in TRIP steels and partially stabilized crystalline ceramics, it is of interest to the present study. It should be noted, however, that the phase-transformations analyzed in the present work occur in a pressure-range (ca. 3-5 GPa) consistent with those encountered in typical blast/ballistic impact scenarios or situations and are associated with relatively modest (3-7% volume changes). These phase-transformations should not be confused with the ones taking place at substantially higher pressures (ca. >20GPa), which are associated with substantially larger volume reductions and with the formation of stishovite, an octahedrally coordinated glass phase.

5.4 Molecular-level ANALYSIS of soda-lime Glass

5.4.1 Computational Analysis

Formulation of a molecular-level simulation problem requires, at a minimum, specification of the following three aspects: (a) a molecular-level computational model consisting

of atoms, ions, functional groups and/or molecules; (b) a set of interaction potentials (commonly referred to as force fields) which describe accurately various bonding and non-bonding interaction forces between the constituents of the molecular model; and (c) a computational method(s) to be used in the simulation. Further details of these three aspects of the molecular modeling analysis of soda-lime glass are provided below.

5.4.1.1 Computational Model

At the molecular level, soda-lime glass is modeled as a discrete material consisting of: (a) silicon (Si) and oxygen (O) atoms mutually bonded via a single covalent bond and forming a connected, non-structured/amorphous network of silica (SiO_4^{4-}) tetrahedra; (b) oxygen anions (O^{2-}) attached as terminal functional-groups to the fragmented silica tetrahedra network; and (c) sodium cations (Na^+) dispersed between fragmented silica tetrahedra networks and ionically bonded to the oxygen anions.

While glass is an amorphous material and does not possess any long-range regularity in its atomic/molecular structure, modeling of bulk behavior of glass is typically done at the molecular level by assuming the existence of a larger (amorphous) unit cell. Repetition of this cell in the three orthogonal directions (the process also known as application of the *periodic boundary conditions*) results in the formation of an infinitely-large bulk-type material. This procedure was adopted in the present work.

The cube-shaped computational cell used in the present work contained 2916 particles with an overall chemical composition of $(Na_2O)_{0.15}$ $(SiO_2)_{0.85}$. The unit cell edge-length was set to 3.347nm yielding a soda-lime glass nominal density of 2.613g/cm^3. The three edges (*a*, *b* and *c*) of the cell were aligned respectively with the three coordinate axes (*x*, *y* and *z*).

To create the initial particle configuration in the unit cell, the Visualizer [5.19] program from Accelrys was first used to construct a short silica-chain fragment. The fragment was then

grown by a duplicate-and-attach process using the same program. The resulting silica network (along with additional sodium cations and oxygen anions) was next used within the Amorphous Cell program [5.20] from Accelrys to randomly populate the computational cell while ensuring that the target material density of 2.613g/cm^3 was attained. An example of a typical molecular-level topology within a single unit cell is displayed in Figure 5.1.

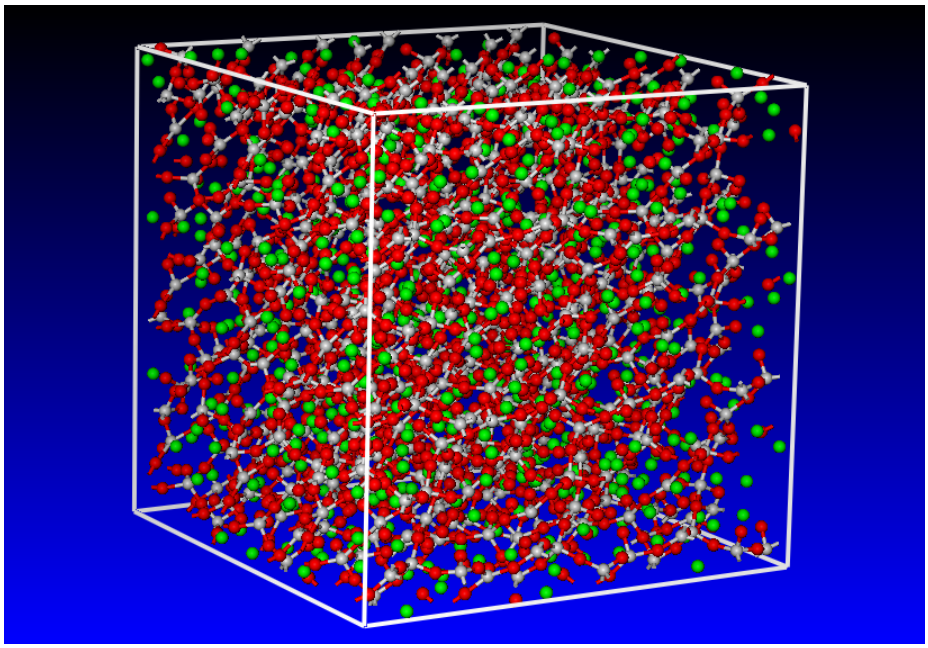

Figure 5.1: The computational unit cell for soda-lime glass molecular-level simulations used in the present work.

5.4.1.2 Force-fields

To fully account for the bonding and non-bonding types of interactions between the atoms/ions/molecules described in the previous section, one must define the respective interaction-potential functions/force-fields, as well as the associated atomic-polar and ionic charges. The knowledge of such force fields enables determination of the potential energy of a molecular-level system in a given configuration. In general, the potential energy of a system of interacting particles can be expressed as a sum of the valence (or bond), $E_{valence}$, cross-term, E_{cross-}

$_{term}$, and non-bond, $E_{non\text{-}bond}$, interaction energies as:

$$E_{total} = E_{valence} + E_{cross-term} + E_{non-bond} \tag{5.1}$$

The valence energy generally includes a bond stretching term, E_{bond}, a two-bond angle term, E_{angle}, a dihedral bond-torsion term, $E_{torsion}$, an inversion (or an out-of-plane interaction) term, E_{oop}, and a Urey-Bradlay term (which involves interactions between two particles bonded to a common particle), E_{UB}, as:

$$E_{valence} = E_{bond} + E_{angle} + E_{torsion} + E_{oop} + E_{UB} \tag{5.2}$$

A schematic explanation of the first four types of valence atomic interactions is given in Figure 5.2.

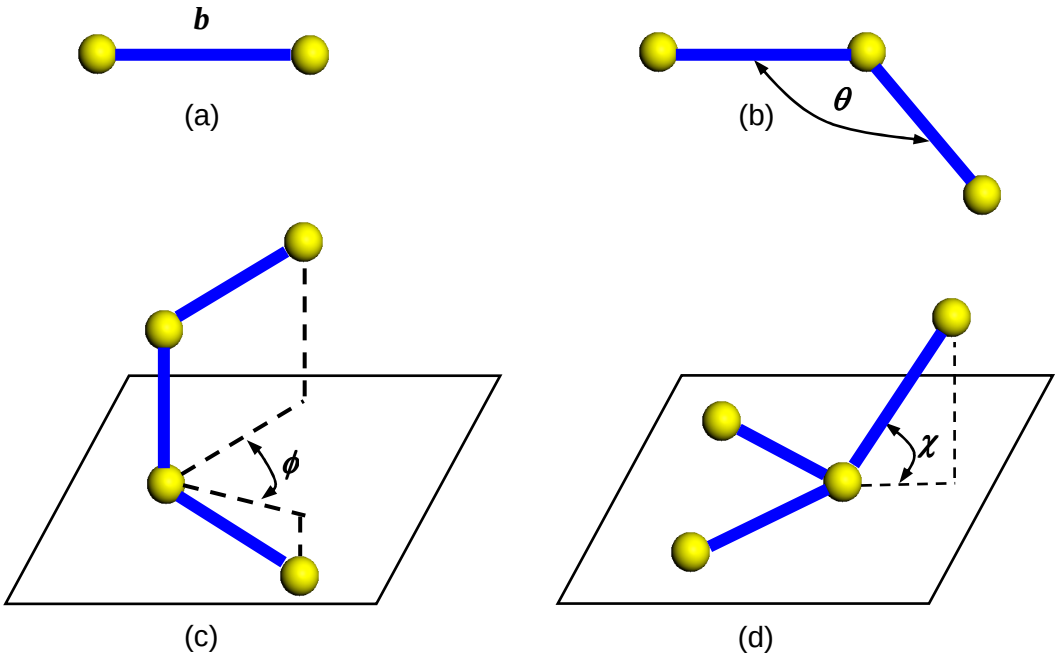

Figure 5.2: A schematic of the: (a) stretch; (b) angle; (c) torsion; and (d) inversion valence atomic interactions.

The cross-term interacting energy, $E_{cross\text{-}term}$, accounts for the effects such as bond length and angle changes caused by the surrounding atoms and generally includes: stretch-stretch

interactions between two adjacent bonds, $E_{bond\text{-}bond}$, stretch-bend interactions between a two-bond angle and one of its bonds, $E_{bond\text{-}angle}$, bend-bend interactions between two valence angles associated with a common vertex particle, $E_{angle\text{-}angle}$, stretch-torsion interactions between a dihedral angle and one of its end bonds, $E_{end\_bond\text{-}torsion}$, stretch-torsion interactions between a dihedral angle and its middle bond, $E_{middle\_bond\text{-}torsion}$, bend-torsion interactions between a dihedral angle and one of its valence angles, $E_{angle\text{-}torsion}$, and bend-bend-torsion interactions between a dihedral angle and its two valence angles, $E_{angle\text{-}angle\text{-}torsion}$, terms as:

$$E_{cross-term} = E_{bond-bond} + E_{angle-angle} + E_{bond-angle} + E_{end\_bond-torsion} + E_{middle\_bond-torsion} + E_{angle-torsion} + E_{angle-angle-torsion} \quad (5.3)$$

The non-bond interaction term, $E_{non\text{-}bond}$, accounts for the interactions between non-bonded particles and includes the van der Waals energy E_{vdW} and the Coulomb electrostatic energy, $E_{Coulomb}$, as:

$$E_{non-bond} = E_{vdW} + E_{Coulomb} \quad (5.4)$$

In the present molecular-level analysis of soda-lime glass COMPASS (Condensed-phased Optimized Molecular Potential for Atomistic Simulation Studies) [5.21, 5.22] functional forms and parameterizations were used for various bond and non-bond interaction energies appearing in Eqs. (5.1)-(5.4). COMPASS is a set of force field potentials which were derived through the use of *ab initio* quantum mechanical calculations and has proven to be highly accurate and reliable in starting various organic/inorganic condensed matter problems. A summary of the COMPASS force-field functions can be found in our previous work [5.23].

5.4.1.3 Computational Method

Molecular-level simulations typically rely on one of the following two techniques: (a) molecular statics, the technique within which the potential energy of the molecular structure in question is minimized with respect to the position of the constituent atoms and ions in the unit

cell as well as with respect to the size and shape of the unit cell; and (b) molecular dynamics, a technique within which the Newton's equations of motion are solved, as a function of time, for all interacting atoms and ions in the system and the appropriate ensemble averages are used to assess/quantify various molecular-level material properties. Both molecular statics and molecular dynamics methods were employed in the present work.

High-pressure induced phase transformations and the associated densification in soda-lime glass were studied in the present work using a conventional *NPT* dynamics method within the Discover program [5.24] from Accelrys, where *N* (the number of particles), *P* (pressure), and *T* (temperature) are the system states that are held constant or ramped in a controlled manner during compression-simulation runs. The equations of motion were integrated using the velocity Verlet algorithm with a time step of 1.0fs. To comply with typical blast/ballistic-impact loading conditions, pressure was ramped linearly at a rate of 0.3GPa/ps. Pressure ramping was accomplished by 0.1GPa discrete increments in pressure followed by 10.0ps equilibration times at a given pressure level. Temperature, on the other hand was held constant at a value of 298K using a Nosé Thermostat [5.26]. Molecular-level microstructure of the soda-lime glass was monitored at different pressure levels as a function of time in order to detect the onset and quantify the progress of phase transformations.

At the end of equilibration at each pressure level, the average material density (inverse of specific-volume) was computed from the corresponding pair-correlation functions. This procedure yielded the pressure vs. specific-volume isothermal relations (*isotherms* in the following) for the pressurization portion of a loading/unloading cycle. To determine the corresponding pressure vs. specific-volume relation during the depressurization portion of a loading/unloading cycle, pressure was decreased in a similar manner as discussed above. Differences in the pressure vs. specific-volume relations for the pressurization and

depressurization portions of the loading cycle are then used to quantify the extent of high-pressure irreversible densification of soda-lime glass.

As will be shown later, high-pressure induced phase transformations in soda-lime glass can affect the strength of this material. Too assess the extent of such strengthening, molecular-level simple-shear tests were carried out. These tests were conducted through the use of a Discover input file which was written in a Basic Tool Command Language (BTCL). This enabled the use of a scripting engine that provides very precise control of simulation runs, e.g. a cell deformation to be carried out in small steps each followed by a molecular dynamics equilibration step and, in turn, by an energy minimization step. The minimization portion of the molecular-level simple shear tests was carried out using a combination of three (Steepest Descent, Conjugate Gradient, and Newton's) potential-energy minimization algorithms within Discover [5.24]. These algorithms are automatically activated/deactivated as the molecular-level configuration approaches its energy minimum (i.e. the Steepest Descent method is activated at the beginning of the energy-minimization procedure, while the Newton's method is utilized in the last stages of the simulation).

To determine the strength of soda-lime glass in its virgin (untransformed) and (pressure-induced) fully transformed conditions, the corresponding computational cells are subjected to a sequence of simple-shear deformation modes. The procedure used in our previous work [5.25] which relates the (minimum) energy to the first and second invariants of the left Cauchy deformation tensor, evolution of the stress state (including the equivalent stress) during deformation is determined. The observed equivalent-stress plateau is then identified as the material strength.

5.4.2 Results and Discussion

In this section, a brief summary of the molecular-level computational results pertaining to the response of soda-lime glass subjected to high pressures is provided. While this portion of the work yielded numerous results, only the ones directly related to the potential effect of phase transformations on the continuum-level material model in the high-rate, high-pressure loading regime are presented and discussed in greater detail. A more comprehensive account of the results obtained will be provided in a future communication.

5.4.2.1 Molecular-level Topology

A detailed examination of the molecular-level topology after subjecting the unit-cell to high pressures revealed distinct differences depending on whether the maximum pressure was below or above ca. 4GPa.

Pressures below ~4GPa

Molecular modeling of glass pressurization/depressurization revealed that when glass is exposed to pressures not exceeding ca. 4GPa, no detectable irreversible changes generally take place in its molecular topology. Closer examination of the atomic structure at different pressure levels between 0GPa and 4GPa revealed:

(a) The presence of *active regions* within which atoms may occasionally undergo large displacements/jumps (ca. 0.1nm). These atomic displacements (the results not shown for brevity) were found to involve coordinated motion of at least a dozen atoms and to be accompanied by abrupt changes in the average potential energy;

(b) In most cases, atomic rearrangement described in (a) appears to be associated with low-frequency transition of the active regions between two distinct *equilibrium* states (of comparable potential energy). These findings are in complete agreement with those found by

Trachenko and Dove [5.27] who termed this phenomenon as Double Well Potential (DWP) and the associated low-frequency transition/ vibrational mode as the *floppy mode*; and

(c) While pressurization up to 4GPa did not yield any permanent changes in the molecular topology, the locations of the active regions were found to change with pressure. That is, the regions active at one pressure level may become inactive at another pressure level while, at the same time other previously inactive regions would become active.

Pressures above ~4GPa

When the computational cell is subjected to pressures exceeding ca. 4GPa and subsequently depressurized to zero pressure, permanent changes in the glass molecular topology were normally observed. These molecular topology changes were accompanied by a permanent density increase on the order of 3–7%. An example of typical results obtained in this portion of the work is given in Figures 5.3(a)-(d), where oxygen atoms/anions are displayed in red and silicon atoms are shown in gray (as well green, pink and yellow highlighting), while sodium cations are omitted for clarity. To aid in visualization/interpretation of the topological changes experienced by glass during high pressure loading/unloading cycles, only a 30-40 atom examplary region of computational cell was monitored in Figures 5.3(a)-(d). The molecular level topologies displayed in these figures pertain respectively to: (a) high-pressure state, Figure 5.3(a); high pressure state after a prolonged (20ps) relaxation period, Figure 5.3(b); (c) ambient pressure state resulting from depressurization of state (a), Figure 5.3(c); and (d) ambient pressure state resulting from depressurization of state (b), Figure 5.3(d). It should be noted that the results displayed in Figure 5.3(c) are essentially identical to those in the initial configuration prior to loading. A closer examination of the molecular-level topology results displayed in these figures revealed that:

(a) Pressurization alters not only molecular-level topology, but also changes the bonding structure and increases the average coordination number (of mainly Si atoms). This can be seen by comparing the results displayed in Figures 5.3(a) and (c). It should be noted here, that the results displayed in Figure 5.3(c) are used in place of the initial molecular-level topology results. In these figures, it is seen that silicon atoms labeled *A* and *B* change their fourfold coordination to fivefold coordination upon pressurization.

(b) As implied earlier, if the depressurization is carried out without allowing the material to relax at high pressures, the molecular level configuration obtained at the ambient pressure is effectively identical to the initial configuration, Figure 5.3(c). Thus, in the resultant ambient-pressure configuration, most silicon atoms regain their fourfold coordination;

(c) Increased duration of the exposure of glass to high pressure, results in continued changes in the molecular-level topology and bond structure. This can be seen by comparing the results displayed in Figures 5.3(a) and (b). These figures show that relaxation of glass leads to the *C*-labeled silicon atom acquiring a fivefold coordination while, at the same time smaller size Si-O rings are being formed. For example, a twofold ring is formed involving the *A* and *C* silicon atoms, while a threefold ring involving the *C*, *D* and *E*-labeled Si atoms also appears, Figure 5.3(b). These changes in the molecular-level topology of glass are a manifestation of its relaxation to a material state that is energetically-preferred at high pressures; and

(d) Upon depressurization of glass which was relaxed at high pressures, some changes in the molecular-level topology and the bonding structure are observed. However, the initial material state is not restored. That is, the material has undergone permanent changes in its molecular level topology, bond structure, and density. This can be seen by comparing results displayed in Figures 5.3(c) and (d). These figures show that while *A* and *B*-label silicon atoms regain their fourfold coordination upon depressurization to ambient pressure, the *C*-labeled silicon atom retains its

fivefold coordination, Figures 5.3(b) and (d). Thus, the average coordination number of silicon atoms in the relaxed-then-depressurized state, Figure 5.3(d), is higher than that in the initial configuration, Figure 5.3(c). Furthermore, while the aforementioned twofold Si-O ring was broken upon depressurization, the threefold ring involving the *C*, *D* and *E*-labeled silicon atoms survived this process. In addition, a new fourfold ring involving the Si atoms labeled *F*, *G*, *H* and *I* was formed. The threefold and fourfold rings were not present in the initial molecular-level configuration, Figure 5.3(c).

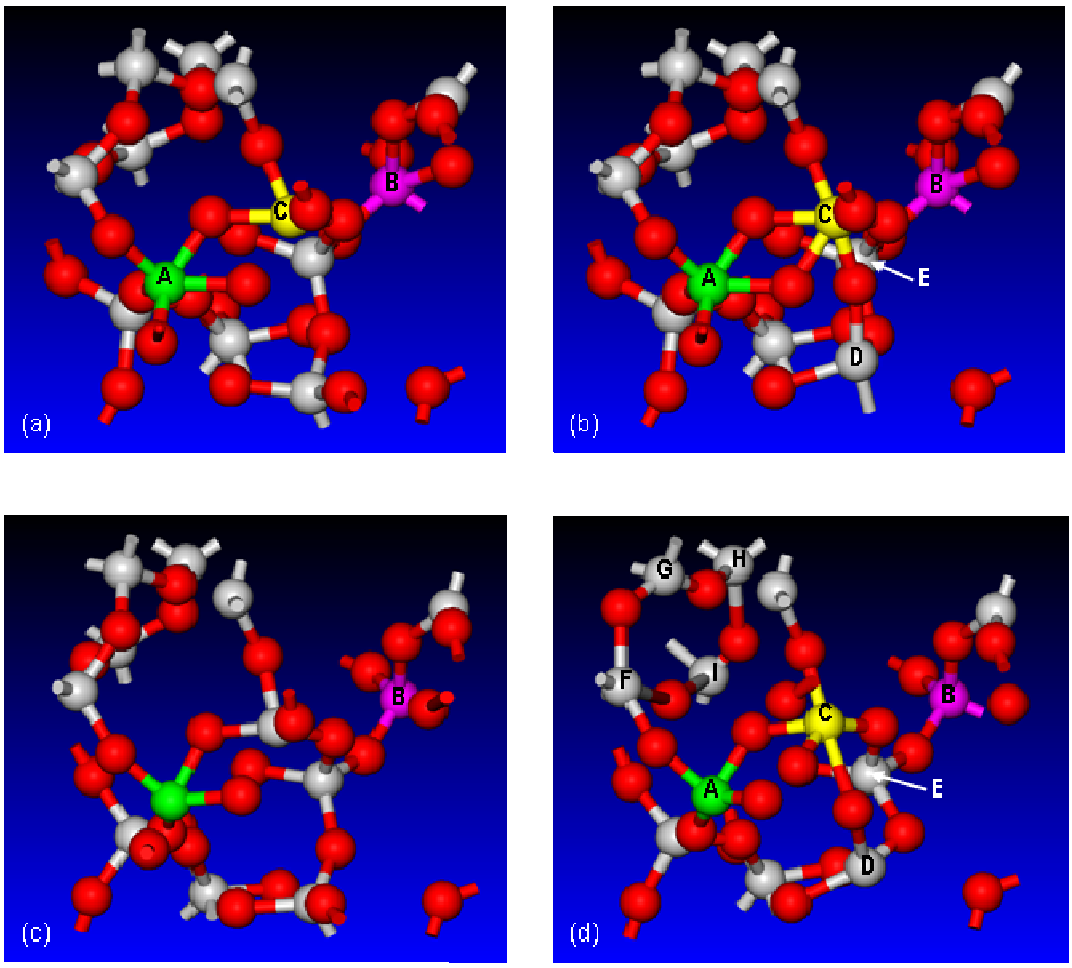

Figure 5.3: The molecular level topologies pertaining to: (a) high-pressure state; (b) high pressure state after a prolonged (20ps) relaxation period; (c) ambient pressure state resulting from depressurization of state (a); and (d) ambient pressure state resulting from depressurization of state (b). See text for explanation.

5.4.2.2 Pressure vs. Specific-volume Isotherm

An example of the typical pressure, *p* vs. specific-volume, *v* (298K isothermal) results obtained in the present molecular-level analysis of high-pressure irreversible densification of glass is displayed in Figure 5.4. The results in Figure 5.4 show four loading pressurization/depressurization cycles. The first cycle does not result in any irreversible densification of glass since the maximum pressure attained is not high enough. The second and

third cycles yield irreversible densification and reveal that this process is associated with a nearly constant ca. 4GPa pressure level. During the last cycle, irreversible densification is completed so that glass behaves as a perfectly elastic material when subjected to any further loading.

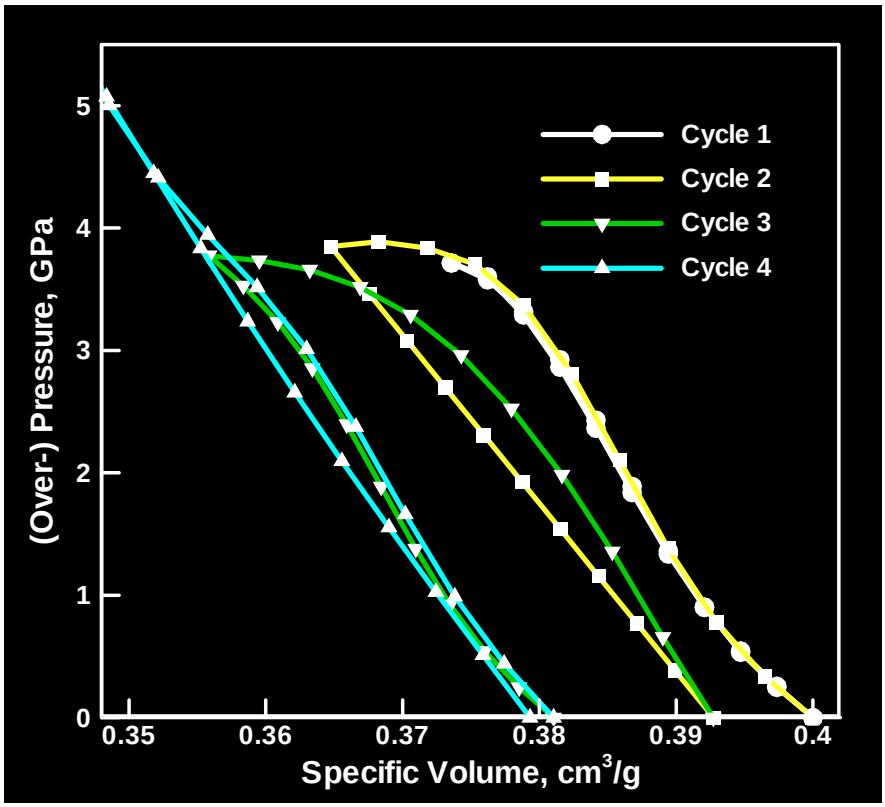

Figure 5.4: Typical pressure vs. specific-volume (298K) loading/un-loading isotherms obtained in the present molecular-level analysis of repeated pressurization/depressurization simulations. In each loading cycle, pressurization was carried out to a higher peak pressure followed by a complete depressurization (i.e. to the atmospheric pressure).

To summarize the aforementioned observations, the examination of the results displayed in Figure 5.4 revealed the following three important findings: (a) irreversible densification begins at a pressure level of ~4GPa and proceeds to full densification at a nominally constant pressure; (b) irreversible densification is associated with a density increase of ca. 3-7%; and (c) the average rate of change of pressure with density (which scales with the material bulk modulus) is not significantly different (and will be assumed equal) in the pre- and post-densification glass states.

It should be noted that the aforementioned findings (a) and (c) were found not to be very sensitive to the random selection of the initial molecular-level configuration of glass. On the other hand, the extent of irreversible densification was found to vary in a 3-7% range depending on the choice of this configuration.

An indirect experimental evidence of the occurrence of phase-transformation/irreversible-densification of soda-lime glass under shock loading in a pressure range around 4GPa was obtained in the work of Grady and Chhabildas [5.28,5.32]. Specifically, Grady and Chhabildas [5.28] observed an unexpectedly low measured particle velocity which they attributed to the interplay of permanent densification or inelastic shear. By carrying out a simple quantitative analysis of the shock wave reflection from the soda-lime interface at which the particle velocity was measured, these authors concluded that the underlying inelastic deformation process would result in a 1.5-2% volume reduction. These findings are in general agreement with those obtained computationally in the present work.

As will be shown in the next section, conversion of the pressure vs. specific-volume isotherms into the corresponding pressure vs. specific-volume Hugoniots and isentropes, requires also the knowledge of the internal energy density, $\boldsymbol{\varepsilon}$, vs. specific volume (loading and unloading) isotherms. While, as will be shown in the next section, $\boldsymbol{\varepsilon}$ vs. $\boldsymbol{v}$ isotherm can be derived from the $\boldsymbol{p}$ vs. $\boldsymbol{v}$ isotherm using a procedure based on the first two laws of thermodynamics and on the Maxwell's equations, the former isotherm was obtained along with the $\boldsymbol{p}$ vs. $\boldsymbol{v}$ isotherms using the same molecular-level computational analysis. A plot of the $\boldsymbol{\varepsilon}$ vs. $\boldsymbol{v}$ isotherms is displayed in Figure 5.5. The results displayed in Figures 5.4 and 5.5 are associated with the same set of molecular-dynamics pressurization/de-pressurization runs.

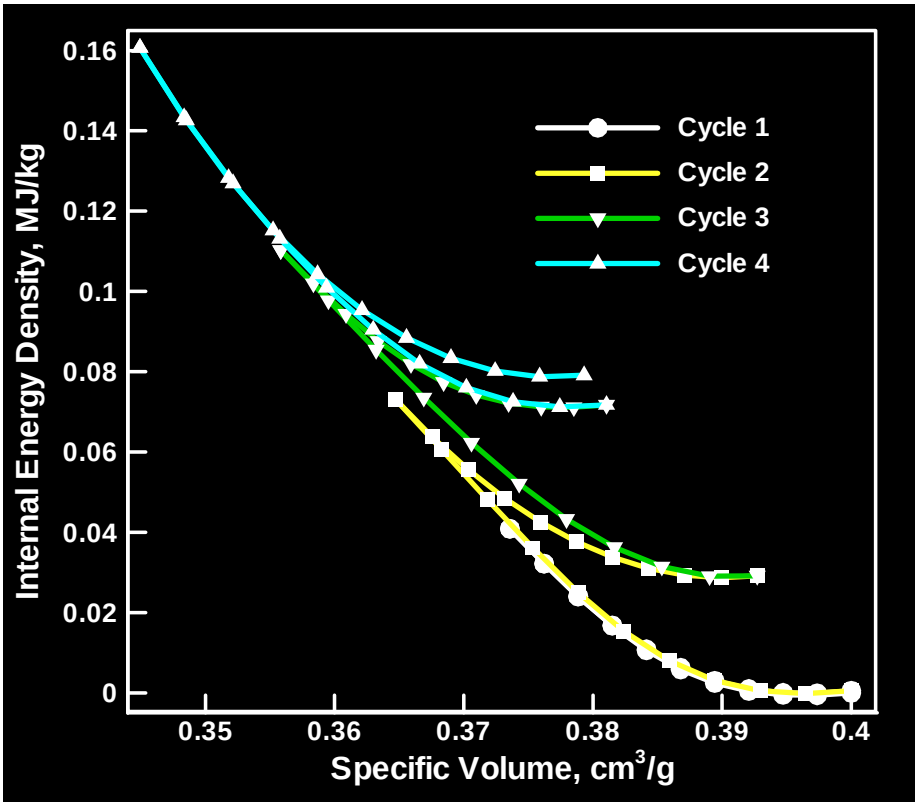

Figure 5.5: Typical internal energy density vs. specific-volume (298K) loading/un-loading isotherms obtained in the present molecular-level analysis of repeated pressurization/depressurization simulations. In each loading cycle, pressurization was carried out to a higher peak pressure followed by a complete depressurization (i.e. to the atmospheric pressure).

5.4.2.3 Transformation/Densification-induced Strengthening

As discussed in Section 5.4.1.3, simple shear computational mechanical tests are used to assess soda-lime glass strength. An example of the typical molecular-level topology evolution accompanying these tests is displayed in Figures 5.6(a)-(b). The computational procedure described in Section 5.4.1.3 established that, depending on the initial structure of the computational cell, the strength of fully-transformed soda-lime glass is higher by 30-50% than that of the virgin material.

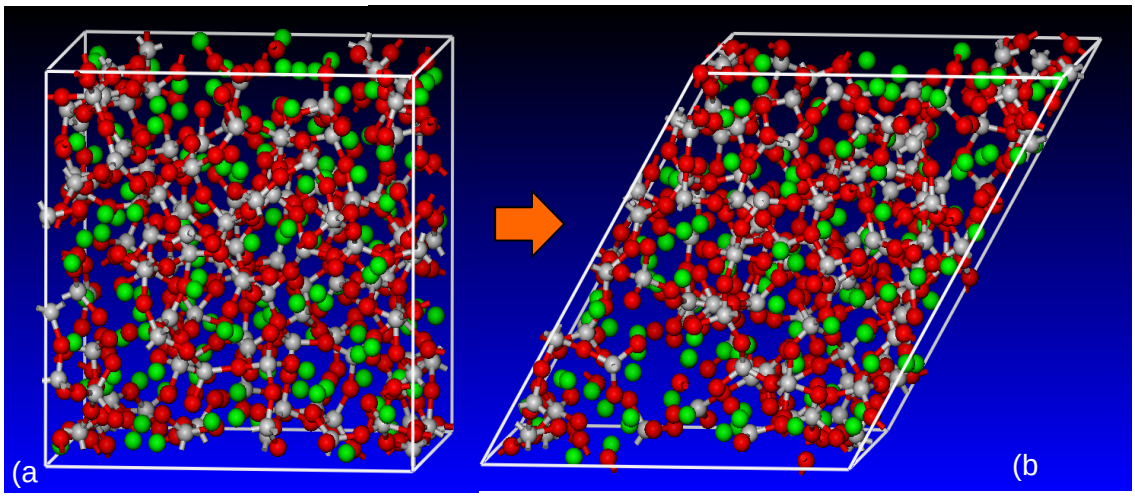

Figure 5.6: An example of molecular-level topology evolution accompanying simple-shear mechanical tests.

5.5 Isotherm to Hugoniot/Isentrope Conversion

As mentioned earlier, one of the main objectives of the present work is to examine the potential of pressure-induced phase-transformation/irreversible-densification in mitigating the effects of shock in ballistic impact. A shock wave (or simply a shock) is a wave which propagates through a medium at a speed higher than the sound speed and its passage causes an abrupt and discontinuous change in the material state variables (e.g., temperature, pressure, density, and internal energy). The magnitude of the state-variable changes and the shock speed increase with the strength of the shock. While acoustic waves give rise to isentropic changes in the material state variables, passage of a shock is typically associated with irreversible (entropy-increasing) changes in the same variables. The reason behind this difference is that shock involves very high strain rates that bring energy-dissipative viscous effects into prominence. As will be shown below, the irreversible nature of the material-state changes brought about by shock passage precludes the p vs. v and ε vs. v isotherms (obtained in the previous section) from being directly used in the shock propagation/interaction analysis (carried out later in the present work).

Before proceeding with the conversion of the loading/unloading isotherms obtained in the previous section into their corresponding Hugoniots and isotherms, it should be noted that the internal energy density has two main contributions: (a) potential-energy contribution associated with bonding and non-bonding interactions between the atomic-scale constituents of the system; and (b) the thermal component which is associated with the vibrational energy of the same constituents. Clearly, specific-volume controls the potential energy part while temperature has a dominant effect on the thermal part. At non-zero absolute temperatures, both the specific-volume (change) and the internal energy density contribute to the internal pressure in the material. A function which relates pressure, p, specific-volume, v, and the internal energy density, ε, is commonly referred to as an *Equation of State* (*EOS*). The EOS is a critical part of a material model for use in (continuum-level) computational investigations of the response of structures to shock loading. In situations in which one is interested only in the problem of shock propagation/interaction in plate-like structures in the presence of uni-axial strain deformation states (as is the present case), a complete definition of the EOS is not required. Instead, a locus of t_{11} vs. v vs. ε (vs. $\dot{x}$-particle velocity vs. U_s-shock speed) shocked-material states commonly referred to as a *Hugoniot* is sufficient where t_{11} is the axial stress, and the only non-zero component of strain (the axial strain) is related to the specific-volume. Likewise, to analyze the propagation/interaction of release (decompression) waves under the same geometrical/deformation state conditions, it is sufficient to define the corresponding t_{11} vs. v vs. ε isentropes.

As a first step towards creating the foregoing Hugoniot/isentrope relations, molecular-scale modeling was employed to obtain $t_{11}^{(\theta)}$ vs. v and $\varepsilon^{(\theta)}$ vs. v (loading and unloading) isotherms, where superscript θ is used to denote a constant temperature condition. However, these relations define the locus of equilibrium material states under isothermal deformation conditions

and could not be directly used in the analysis of shock/release wave propagation/interaction. The main reasons for this limitation are: (a) shock loading is an irreversible process which results in energy dissipation (causing an increase in the shocked-material thermal energy); and (b) shock loading/unloading imparts a significant momentum to the material particles which requires overcoming particle inertial effects. Consequently, at the same level of the compressed-material volume, shocked-material states are associated with higher levels of stress/pressure and internal energy density than their isothermal counterparts. Hence, before the molecular-level isothermal compression relations obtained in the previous section can be used in the analysis of shock propagation/interaction, they must be converted into their respective shock-based Hugoniots/isentropes. Details of this conversion are presented in the remainder of this section. Separate consideration is given to the isotherm conversion to Hugoniots and isentropes.

5.5.1 Determination of Shock-loading Hugoniot

The isotherm-to-Hugoniot conversion procedure employed in the present work follows closely the one outlined in Ref. [5.29]. The first step in this procedure is to separate $t_{11}^{(\theta)} = -p^{(\theta)} + 4\tau_{\max}^{(\theta)}/3$ vs. v into $p^{(\theta)}$ vs. v and $\tau_{\max}^{(\theta)}$ vs. v relations, where $\tau_{\max}^{(\theta)}$ is the maximum shear stress. The next step is to handle the conversion of the latter two isotherms into the corresponding Hugoniots/isentropes separately.

Conversion of the $p^{(\theta)}$ vs. v isotherm into the corresponding Hugoniot is rooted in the assumption that the known isotherm and the sought Hugoniot are associated with the same pressure vs. density vs. internal energy Mie-Gruneisen EOS. If, for a given range of specific-volumes, v, the isotherm in question defines $p^{(\theta)}(v)$ and $\varepsilon^{(\theta)}(v)$ (θ-temperature) set of material states on the EOS surface, then the Hugoniot centered on the initial state $p^{(H)}=0$, $\varepsilon^{(H)}=\varepsilon_R$ and $v=v_R$ is defined, over the same range of v as:

$$p^{(H)}(v) = p^{(\theta)}(v,\theta_0) + \frac{\gamma(v)}{v}\left[\varepsilon^{(H)}(v) - \varepsilon^{(\theta)}(v,\theta_0)\right] \tag{5.5}$$

where $\gamma = \left.\frac{\partial p}{\partial \varepsilon}\right|_v v$ is the Gruneisen gamma. It should be noted that states $\boldsymbol{p^{(H)}}$ and $\boldsymbol{\varepsilon^{(H)}}$ in Eq. (5.5) are mutually related through the Rankine-Hugoniot equation as:

$$\varepsilon^{(H)} - \varepsilon_R = \frac{1}{2}\left(-p^{(H)}\right)\left(-v + v_R\right) \tag{5.6}$$

As far as the $\boldsymbol{\varepsilon^{(\theta)}}$ vs. $\boldsymbol{v}$ isotherm is concerned, it was shown (in Figure 5.5) that this relation can be obtained directly using the molecular-level computations discussed in the previous section. Alternatively, this relationship can be derived from the $\boldsymbol{p^{(\theta)}}$ vs. $\boldsymbol{v}$ isotherm by applying the following two step procedure: (a) to account for the fact that the internal energy density is a function of specific-volume and entropy (while entropy depends on the specific-volume and temperature), $\frac{\partial \varepsilon^{(\theta)}(v,\eta(v,\theta))}{\partial v}$ is first derived using the chain rule as:

$$\left.\frac{\partial \varepsilon^{(\theta)}}{\partial v}\right|_\theta = \left.\frac{\partial \varepsilon^{(\theta)}}{\partial v}\right|_\eta + \left.\frac{\partial \varepsilon^{(\theta)}}{\partial \eta}\right|_v \left.\frac{\partial \eta}{\partial v}\right|_\theta = -p^{(\theta)} + \theta\left(\frac{\gamma}{v}C^v\right) \tag{5.7}$$

where η is the entropy density. $p^{(\theta)} = -\left.\frac{\partial \varepsilon^{(\theta)}}{\partial v}\right|_\eta$ and $\theta = \left.\frac{\partial \varepsilon^{(\theta)}}{\partial \eta}\right|_v$ relations originate from the combined statement of the first and second laws of thermodynamics $d\varepsilon^{(\theta)} = \theta d\eta - p^{(\theta)} dv$, while $\frac{\gamma}{v}C^v = \left.\frac{\partial \eta}{\partial v}\right|_\theta$ is obtained through the use of Maxwell's equations; and (b) Eq. (5.7) is next integrated between the initial specific-volume, v_0, and current specific-volume, v, as:

$$\varepsilon^{(\theta)}(v,\theta_0) = \varepsilon_0 - \int_{v_0}^{v} p^{(\theta)}(v';\theta_0)dv' + \frac{\gamma_R}{v_R}C_R^v\theta_0(v - v_0) \tag{5.8}$$

where $\varepsilon_0 = \varepsilon^{(\theta)}\left(v_0, \eta\left(v_0, \theta_0\right)\right)$, $C^v = \left.\frac{\partial \varepsilon}{\partial \theta}\right|_v$ is the constant-volume specific-heat, and θ_0 is the temperature associated with the isotherm in question. By combining Eqs. (5.5), (5.6) and (5.8) and solving the resulting equation for $p^{(H)}$, one obtains the sought Hugoniot as:

$$p^{(H)}(v) = \frac{p^{(\theta)}(v, \theta_0) + \frac{\gamma_R}{v_R}\left[\varepsilon_R - \varepsilon_0 + \int_{v_0}^{v} p^{(\theta)}(v', \theta_0) dv' - \theta_0 \frac{\gamma_R}{v_R} C_R^v (v - v_0)\right]}{1 - \frac{\gamma_R}{2v_R}(v_0 - v)} \tag{5.9}$$

It should be noted that in Eq. (5.9), it was assumed that $\frac{\gamma}{v}\left(= \frac{\gamma_R}{v_R}\right)$ and C_R^v remain unchanged during shock loading. These assumptions are commonly made in the case of the so-called *Gruneisen materials* in which gamma is only a function of *v*. Eq. (5.9) shows that for a given $p^{(\theta)}(v)$ isotherm associated with the initial material states ε_0, θ_0 and v_0 (and defined over a range of *v*), the corresponding $p^{(H)}(v)$ Hugoniot centered at the initial state (ε_R , v_R) can be obtained (over the same range of *v*) provided material parameters γ_R and C_R^v are known. In the present work, these two parameters are assigned the following values: γ_R=0.63 [5.30] and C_R^v =900 J/kgK [5.31]. These values correspond to the ambient temperature and pressure conditions of glass chosen as the reference state of this material. Eq. (5.9) also shows that it is convenient to make the initial isothermal state of the material and the reference state of the shocked material identical. In this case, $\varepsilon_R = \varepsilon_0$ and Eq. (5.9) becomes somewhat simpler.

As far as the conversion of the $\tau_{\max}^{(\theta)}$ vs. ***v*** relations to $\tau_{\max}^{(H)}$ vs. ***v*** relations, it was assumed that the shock-loading would primarily influence the hydrostatic portion of the stress field. Hence, no conversion of the deviatoric part of the axial stress was carried out. Consequently, $t_{11}^{(H)}(v)$ was obtained by simply adding the $4\tau_{\max}^{(H)}(v)/3$ isotherm to the $-p^{(H)}(v)$ Hugoniot.

5.5.2 Determination of the Release-wave Unloading Isentrope

The analysis presented above allows the conversion of a loading isotherm to the corresponding loading Hugoniot. Following the procedure described by Davison [5.29], it can be readily shown that high-rate unloading associated with the propagation of release/rarefaction waves is an adiabatic/isentropic process. Hence, to analyze propagation of these waves in plate-like structures associated with uni-axial strain deformation, one must convert unloading isotherms (obtained via the molecular-level simulations) into the corresponding isentropes. The conversion procedure used here is quite similar to the foregoing isotherm-to-Hugoniot conversion procedure and involves the following steps:

(a) an equation analogous to Eq. (5.5) is first constructed in which the Hugoniot quantities are replaced with their isentropic counterparts, $p^{(\eta)}$ and $\varepsilon^{(\eta)}$;

(b) in this equation, $\varepsilon^{(\theta)}(v)$ is again expressed using Eq. (5.8); and

(c) $\varepsilon^{(\eta)}(v)$ is obtained using a procedure analogous to that employed during the derivation of Eq. (5.8) to yield:

$$\varepsilon^{(\eta)}\left(v;\eta_R^{(\eta)}\right)=\varepsilon_R^{(\eta)}-\int_{v_R^{(\eta)}}^{v} p^{(\eta)}\left(v';\eta_R^{(\eta)}\right)dv' \tag{5.10}$$

where $\eta_R^{(\eta)}$ is the constant/reference value of the entropy density along the isentrope. Since Eq. (5.10) contains the unknown function $p^{(\eta)}\left(v;\eta_R^{(\eta)}\right)$, the equation mentioned in (a) cannot be used to simply compute $p^{(\eta)}$ by evaluating the right-hand side of this equation. To overcome this problem, this equation is differentiated with respect to $\boldsymbol{v}$ to yield the following linear, first order, ordinary differential equation with constant coefficients:

$$\frac{\partial p^{(\eta)}}{\partial v}+\frac{\gamma_R}{v_R}p^{(\eta)}=\frac{\partial p^{(\theta)}}{\partial v}+\frac{\gamma_R}{v_R}p^{(\theta)}-\left(\frac{\gamma_R}{v_R}\right)^2 C_R^v\theta_R^{(\theta)} \tag{5.11}$$

This equation can be readily integrated numerically to yield $p^{(\eta)}(v)$. However, it should be noted that the unloading isotherm associated with the same temperature, θ_0 , as the loading isotherm cannot be used here. The reason for this is that shock is accompanied with energy dissipation so that the shocked-material temperature is normally higher than the temperature in the material's reference state. Hence, isothermal unloading would take place along a $\theta_R^{(\eta)} > \theta_0$ isotherm. This isotherm can be obtained using the known θ_0 unloading isotherm (generated using the molecular level simulations) and by integrating $\left.\frac{\partial p}{\partial \theta}\right|_v = \frac{\gamma_R}{v_R} C_R^v$ to obtain:

$$p^{(\theta)}\left(v;\theta_R^{(\eta)}\right) = p^{(\theta)}\left(v;\theta_0\right) + \frac{\gamma_R}{v_R} C_R^v\left(\theta_R^{(\eta)} - \theta_0\right) \tag{5.12}$$

The foregoing procedure yields a $p^{(\eta)}\left(v;\eta_R^{(\eta)}\right)$ isentrope. To obtain the corresponding $t_{11}^{(\eta)}\left(v;\eta_R^{(\eta)}\right)$ relation, a procedure analogous to the one used in the case of shock-loading Hugoniot was used.

5.5.3 Results and Discussion

By employing the procedures described in the previous two sections, the axial stress vs. specific-volume isotherms obtained via the use of molecular-level simulations are converted into the respective hugoniots and isentropes. The results obtained are summarized in Figure 5.7(a). Since $t_{11}^{(H)}$ vs. ***x*** Hugoniots are generally quite beneficial in the analysis of shock reflection/transmission, these relations are also generated by combining the $t_{11}^{(H)}$ vs. ***v*** Hugoniots with the corresponding jump equations. The results of this procedure are depicted in Figure 5.7(b). As will be shown in the next section, changes in the soda-lime glass hugoniots brought

about by the pressure-induced phase-transformations/irreversible-densifications may significantly affect the shock–mitigation ability of this material.

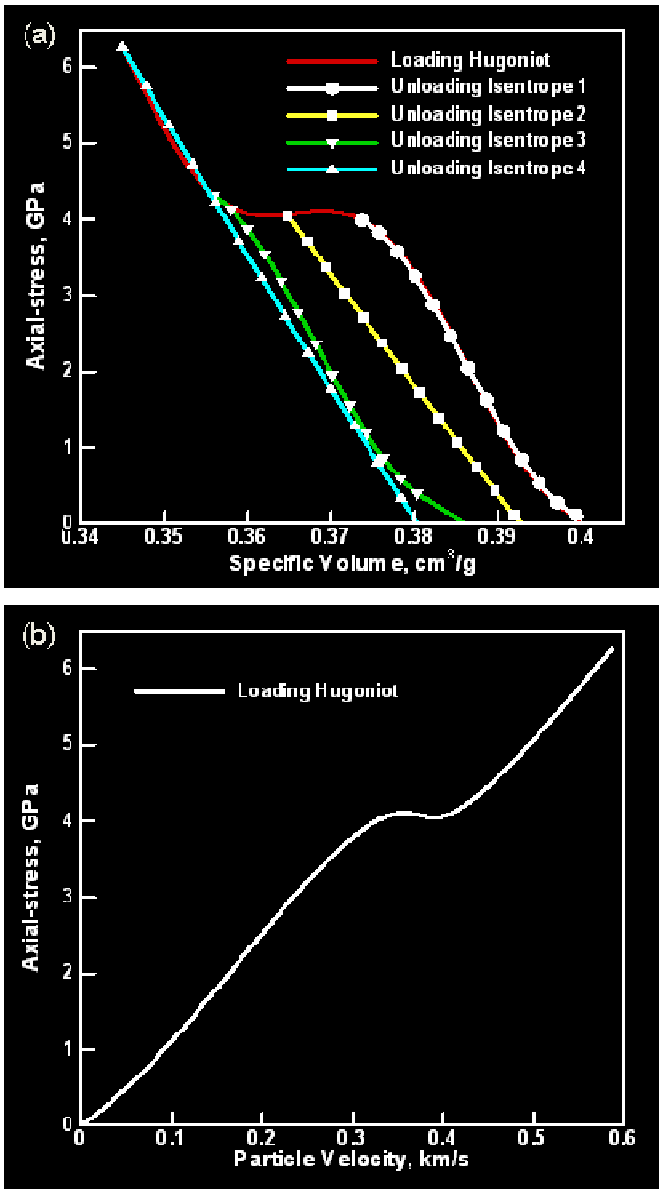

Figure 5.7: (a) Axial-stress vs. specific-volume; and (b) axial-stress vs. particle-velocity Hugoniot and isentrope relationships for soda-lime glass undergoing pressure-induced phase-transformation/irreversible-densification.

5.6 Analysis of Shock Mitigation in Soda-lime Glass

In this section, an attempt is made to assess (and, wherever possible, quantify) the effect of ca. 4GPa pressure-induced phase-transformation/irreversible-densification in soda-lime glass on its ability to mitigate the effects of shock loading. Specifically, in addition to analyzing how irreversible densification affects the strength/speed of shocks, the effect of the same phenomenon on the propagation/interaction of release waves is also analyzed. These waves are typically generated as a result of shock reflection at material interfaces (e.g. glass/polycarbonate interface in laminated transparent-armor systems) and free surfaces. Furthermore, the ability of pressure-induced phase-transformation/irreversible-densification to absorb/dissipate (kinetic) energy accompanying shock loading is also discussed in this section.

5.6.1 Shock Propagation in Soda-lime Glass

In many respects, the occurrence of pressure-induced phase transformations in soda-lime glass at sufficiently high levels of pressure is analogous to the occurrence of plasticity in metals under sufficiently high levels of equivalent (deviatoric) stress. Consequently, some similarities relative to the propagation, transmission/reflection and interaction of shocks and release waves should be expected in the two cases. To facilitate the present analysis of shock propagation/interaction in soda-lime glass, a schematic of the $p^{(H)}$ vs. v Hugoniot for soda-lime glass is provided in Figure 6.8(a). For comparison, the Hugoniot of a hypothetical *non-transforming* soda-lime glass is also depicted in this figure. The initial (*down-stream*) state of material is denoted as point *A*.

The first similarity between shock-induced plasticity and shock-induced irreversible densification is that, shocks propagate not as single waves (which would produce a single upstream material states such as the one denoted by point *B* in Figure 5.8(a)) but rather in pairs.

The leading shock, the so-called "*elastic precursor*", shocks the material to the state at which the conditions for the onset of phase-transformation are met (point *C* in Figure 5.8(a)). The trailing shock, the so-called "*plastic shock*", then gives rise to the transformed/densified material state (point *D* in Figure 5.8(a)).

Since the *plastic shock* travels at a substantially lower speed, the accompanying stress rates are significantly reduced relative to the case of a *purely elastic* single shock (the shock speeds scale with the magnitude of the slope of the corresponding (*AB*, *AC* and *CD*) Rayleigh lines in Figure 5.8(a)). This helps the material maintain its structural integrity (i.e. the probability of cracking is significantly reduced) and ensures functional performance (optical clarity) of the transparent-armor structure. A schematic is provided in Figure 5.8(b) in order to depict the observed differences in shock wave propagation through *non-transforming* and *transforming* soda-lime glass.

It should be noted that the analysis presented above was carried out under the assumption that shock loading is associated with the same *up-stream* pressure-level in both the *transforming* and *non-transforming* soda-lime glass. However, due to differences in the Hugoniots of these two materials, this assumption may not be generally valid. To determine differences in the *up-stream* pressure-levels for the two materials (under the constant blast-loading conditions), a schematic of the $p^{(H)}$ vs. $\dot{x}$ Hugoniot is depicted in Figure 5.8(c). In addition, the Hugoniot of air is also depicted in this figure and point *A* is used to denote the air-borne shock state. By employing the so-called *impedance matching* method (which involves mirroring the air Hugoniot about a vertical line through the shock state *A* and finding the points of intersection between the mirrored Hugoniot and the two soda-lime glass Hugoniots), the *transmitted* shock states within soda-lime glass can be determined. These states are denoted, in Figure 5.8(c), using points *B* and *C* for the *non-transforming* and *transforming* soda-lime glass, respectively. It is seen that somewhat lower

up-stream pressure accompanies shock loading of the *transformed* soda-lime glass. This finding points towards yet another potential way in which pressure-induced phase-transformations in soda-lime glass can help mitigate the effects of shock loading.

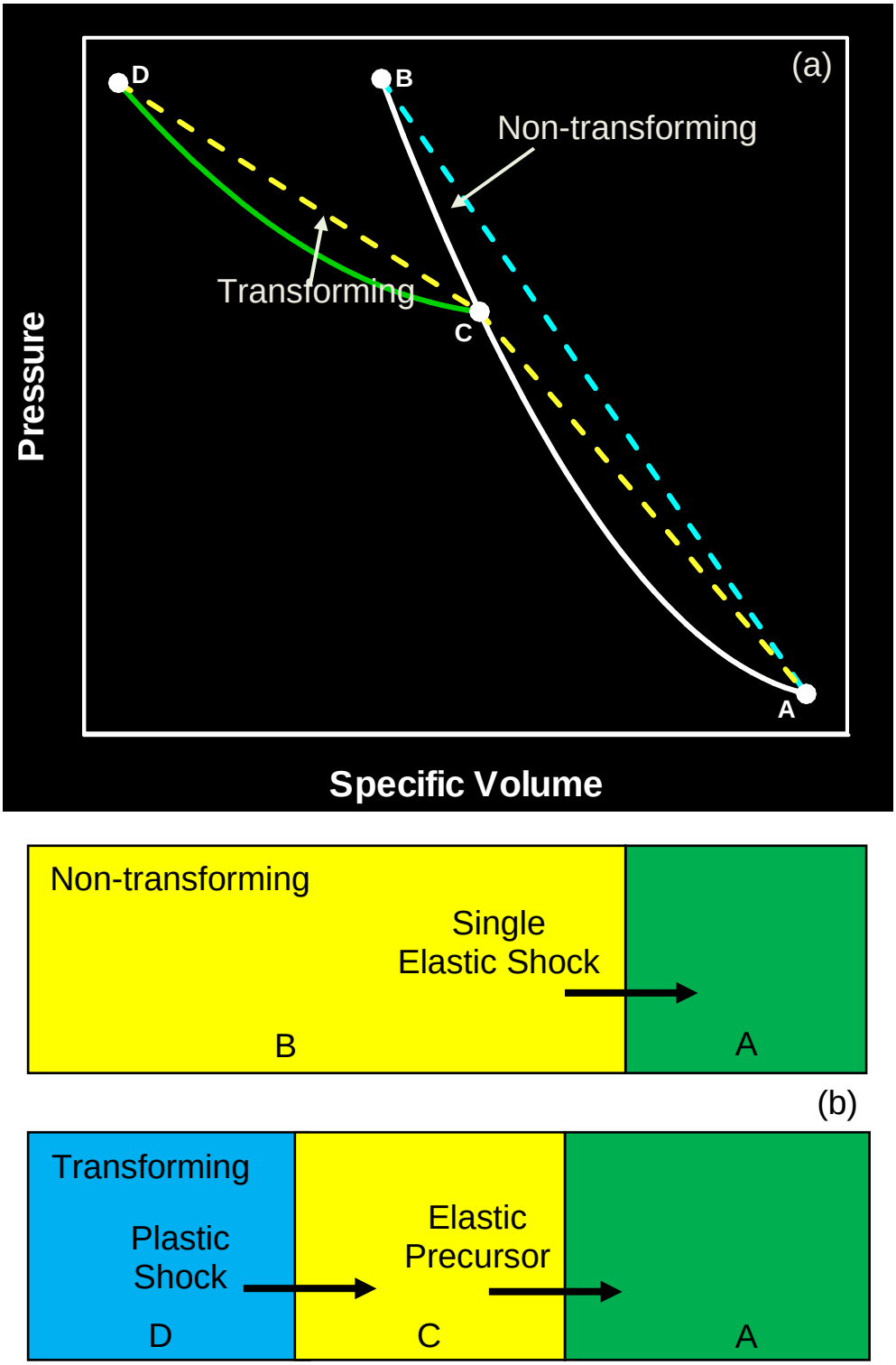

Figure 5.8: Various hugoniots and characteristic plots used in the analysis of shock and release wave propagation through a non-transforming and a transforming soda-lime glass.

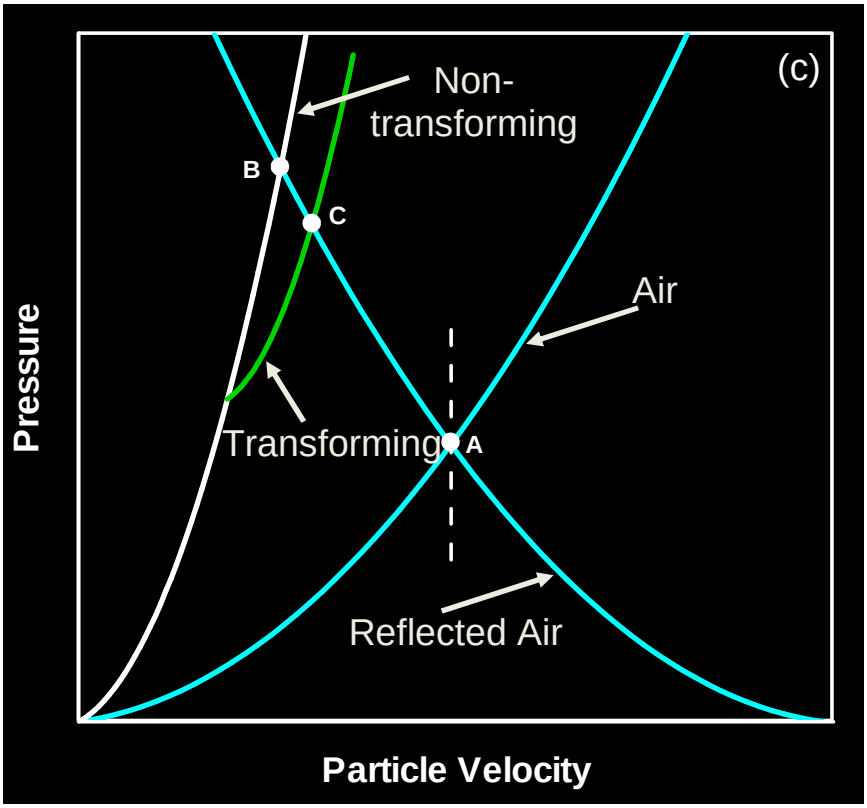

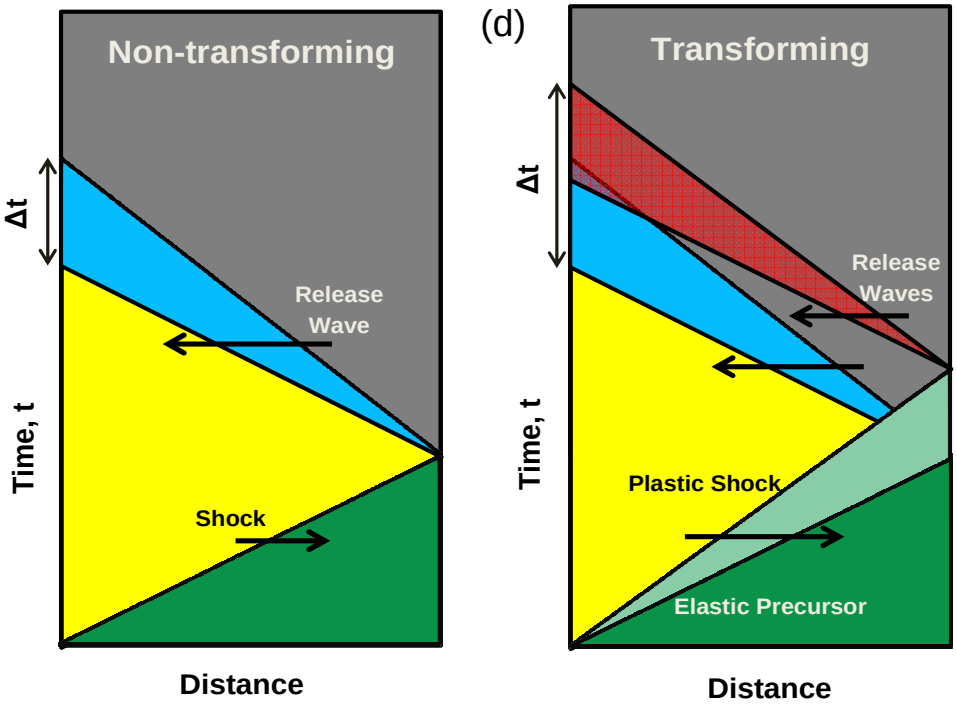

Figure 5.8: Continued.

5.6.2 Release-wave Propagation in Soda-lime Glass

In laminated (multi-layer) transparent armor structures, initial shock loading results, through multiple wave reflection/transmission/interaction, in a number of shock and release waves propagating at any instant of time in any of the armor laminae. When two approaching release waves intersect, the material bounded by the two resulting release waves travelling away from each other may be subjected to tension. If the attendant tensile stresses exceed the material fracture strength, fracture/spall may take place causing a loss in optical clarity/functional performance of the transparent armor structure.

As discussed in Section 5.4, molecular-level simulation results of soda-lime glass shear response under pressure revealed that pressure-induced phase-transformations/irreversible-densification increases the shear strength of the material. While fracture of glass could not be modeled directly using the present molecular-level computational approach, it is anticipated that an increase in shear strength of the soda-lime glass due to pressure-induced irreversible-densification will result in a similar increase in the material fracture strength. This is another potential way in which pressure-induced phase-transformation/irreversible-densification can improve shock mitigation performance of soda-lime glass.

Another potential mechanism for reduction of the fracture/spall propensity in shock-loaded glass is associated with greater dispersion (i.e. increased profile width) of the reflected release waves. In simple terms, if two intersecting release waves are more dispersed, lower values of the peak tensile stress and/or lower volume of the material subjected to the peak tensile stresses are expected. To determine if pressure-induced phase–transformations in soda-lime glass promote release wave dispersion, schematics of the time vs. distance (characteristic analysis) plots are depicted in Figure 5.8(d) for the two cases of soda-lime glass. In the *non-transforming* soda-lime case, a single shock originating at the left surface of the glass panel at zero time traverses the

panel and reflects from the right panel surface as a release wave. The difference in the arrival times of the trailing and the leading characteristics of this wave to the left panel surface can then be used as a measure of the release wave dispersion. In the case of a *transforming* soda-lime glass, a pair of shocks is generated at the left panel surface and each shock generates a separate release wave upon reflection from the panel right surface. Clearly, the width of the combined rarefaction wave (defined now as the difference in the arrival time of the *plastic shock* release wave trailing edge and the *elastic precursor* release wave leading edge) is greater suggesting another potential mechanism by which high-pressure densification of soda-lime glass may mitigate shock loading effects.

5.6.3 Energy-absorption Capacity of Soda-lime Glass

Simple examination of the pressure vs. specific-volume Hugoniot displayed in Figure 5.7(a) suggests that ca. 4GPa pressure-induced phase-transformation/irreversible-densification may yield additional important benefits with respect to mitigating the effects of shock loading. While analyzing Figure 5.7(a), it should be recalled that shock-loading takes place along the Rayleigh line(s) connecting the material initial and shocked states, while release-wave unloading takes place along an isentrope. Hence, the area bounded by the Rayleigh line(s), the corresponding isentrope and the $\boldsymbol{v}$ axis, defines the energy absorbed/dissipated in the material which was initially loaded by the passage of a shock and subsequently unloaded by the passage of a release wave. To provide a semi-quantitative assessment of the enhanced energy absorption/dissipation potential of soda-lime glass undergoing pressure-induced phase-transformation/irreversible-densification, a hypothetical Hugoniot and the corresponding isentropes are considered for the non-transforming soda-lime glass. These hypothetical curves are not drawn in Figure 5.7(a) in order to preserve clarity. Nevertheless, it is obvious that the energy absorption/dissipation capacity of the *transforming* soda-lime glass is substantially higher than

that of its hypothetical *non-transforming* counterpart. By comparing the corresponding areas between the Rayleigh line(s) and the isentropes for the fully-transformed and *non-transforming* soda-lime glass in Figure 5.7(a), it was estimated that phase-transformation can increase energy absorption capacity of soda-lime glass by 6-7 times. This is clearly a finding which warrants closer examination in our future work since it may lead to substantial improvements in shock-mitigation performance of transparent armor systems.

5.6.4 Structure/Component-performance Driven Material Design

The work overviewed in the present manuscript clearly revealed that (ca. 4GPa) pressure-induced phase-transformations and the accompanying irreversible- densification can have a beneficial role in regard to mitigating the effects of ballistic/blast-impact-induced shocks in soda-lime based transparent armor structures. Since similar phase-transformations and irreversible-densification phenomena were not found in either fused-silica or borosilicate glass (a part of the ongoing work based on the use of the same molecular-level computational method), it is clear that glass chemistry and microstructure play an important role in the behavior of SiO_2-based amorphous materials under high pressures. A possible explanation for the observed differences in the high-pressure behavior of soda-lime, fused-silica and borosilicate glass can be attributed to expected differences in the nature of their random network of SiO_4^{4-}tetrahedra. As discussed in Section 5.3, soda-lime glass is associated with a more-open random network due to the presence of network modifiers (Na_2O and CaO). The results obtained in the present work then suggest that, under relatively modest pressures of ca. 4GPa, material (irreversible) densification can take place resulting in the formation of a material with a more compacted random network. In the case of fused-silica and borosilicate glass, zero-pressure random network is already quite compacted so that no measurable densification takes place at ca. 4GPa pressure level. In these glasses (as well as in soda-lime glass), densification takes place at substantially higher pressures and involves not

simple bonding changes in the SiO_4^{4-} glass network, but the generation of a stishovite phase composed of SiO_6^{6-} octahedrons.

Returning to the problem of ca. 4GPa pressure-induced phase-transformation/irreversible-densification in soda-lime glass, it should be noted that while the presence of the more open random network may be beneficial from the shock-mitigation point of view, this effect must be balanced against the accompanying reduction in the virgin material fracture strength. The latter effect may lead to spall/cracking-resistance loss in soda-lime glass and the associated loss of optical clarity (an example of the functional failure of a transparent-armor structure). In other words, as potential modifications in soda-lime glass are being considered in an attempt to maximize its shock-mitigation potential, one must monitor the effect of these modifications on the material fracture strength. This is a prototypical example of the *materials-by-design* approach within which structure/component performance assessment is used to guide the design (and processing/synthesis) of materials which maximize such performance. It should be noted that the virgin material fracture strength is not of major importance in the case of blast-loaded glass panels in which tensile loading is normally preceded by compressive shock loading (which as shown here), gives rise to the material-densification induced strengthening. On the other hand in the case of ballistic impact, radial tensile shocks are often induced which may cause the formation of so-called *ring cracks*. In this case, the virgin material fracture strength is an important material selection parameter which controls the initial ballistic-penetration resistance.

5.7 Summary and Conclusions

Based on the results obtained in the present work, the following summary remarks and main conclusions can be made:

1. Molecular-level modeling of soda-lime glass revealed the occurrence of an irreversible-densification process when the pressure exceeds ca. 4GPa. Close examination of molecular-level topology revealed that this process is associated with an increase in the average coordination number of the silicon atoms, and the creation of two to fourfold (smaller, high packing-density) Si-O rings.

2. A series of loading/unloading/reloading computational experiments is carried out in order to generate the appropriate 298K pressure vs. specific-volume isotherms.

3. These isotherms are next converted into the corresponding (pressure vs. specific-volume and pressure vs. particle velocity) loading Hugoniots and unloading isentropes.

4. The obtained Hugoniot and isentrope relations are used to semi-quantitatively assess the potential of pressure-induced phase transformation in soda-lime glass for mitigating shock-loading effects. This procedure identified several beneficial effects of the pressure-induced phase transformation in soda-lime glass such as lowering of the loading/unloading stress-rates and stresses, shock/release-wave dispersion and energy absorption associated with the work of phase-transformation.

5.8 References

5.1 E. Strassburger, P. Patel, W. McCauley and D. W. Templeton, *Visualization of Wave Propagation and Impact Damage in a Polycrystalline Transparent Ceramic- AlON*, Proceedings of the 22nd International Symposium on Ballistics, November 2005, Vancouver, Canada.

5.2 AMPTIAC Quarterly: *Army Materials Research*: *Transforming Land Combat Through New Technologies*, 8, no.4, 2004.

5.3 E. Strassburger, P. Patel, J. W. McCauley, C. Kovalchick, K. T. Ramesh and D. W. Templeton, *High-Speed transmission Shadowgraphic and Dynamic Photoelasticity Study of Stress Wave and Impact Damage Propagation in Transparent Materials and Laminates Using The Edge-on Impact Method*, Proceedings of the 23rd International Symposium on Ballistics, Spain, April 2007.

5.4 D. Z. Sun, F. Andreiux, A. Ockewitz, *Modeling of the Failure Behavior of Windscreens and Component Tests*, 4th LS-DYNA Users' Conference, Bamberg, Germany, 2005.

5.5 L. V. Woodcock, C. A. Angell and P. Cheeseman, *Molecular dynamics studies of the vitreous state: Simple ionic systems and silica*, The Journal Chemical Physics, 65, 1976, 1565–1577.

5.6 R. G. D. Valle, E. Venuti, *High-pressure Densification of Silica Glass: A Molecular-dynamics Simulation*, Physical Review B, 54, 6, 1996, 3809-3816.

5.7 K. Trachenko, M. T. Dove, *Densification of Silica Glass under Pressure*, Journal of Physics: Condensed Matter, 14, 2002, 7449-7459.

5.8 Y. Liang, C. R. Miranda, S. Scandolo, *Mechanical Strength and Coordinate Defects in Compressed Silica Glass: Molecular Dynamics Simulations*, Physical Review B, 75, 024205, 2007.

5.9 B. Nghiem, *PhD thesis*, University of Paris 6, France 1998.

5.10 C. Denoual and F. Hild, *Dynamic Fragmentation of Brittle Solids: A Multi-scale Model*, European Journal of Mechanics of Solids A, 21, 2002, 105-120.

5.11 M. Yazdchi, S. Valliappan and W. Zhang, "*A Continuum Model for Dynamic Damage Evolution of Anisotropic Brittle Materials*," International Journal of Numerical Methods in Engineering, 39, 1996, 1555-1583.

5.12 F. Hild, C. Denoual, P. Forquin and X. Brajer, "*On the Probabilistic and Deterministic Transition Involved in a Fragmentation Process of Brittle Materials*," Computers and Structures, 81, 2003, 1241-1253.

5.13 M. Grujicic, B. Pandurangan, N. Coutris, B. A. Cheeseman, C. Fountzoulas, P. Patel and E. Strassburger, *A Ballistic Material Model for Starphire®, A Soda-lime Transparent Armor Glass*, Materials Science and Engineering A, 492, 1, 2008, 397-411.

5.14 M. Grujicic, B. Pandurangan, W. C. Bell, N. Coutris, B. A. Cheeseman, C. Fountzoulas and P. Patel, *An Improved Mechanical Material Model for Ballistic Soda-Lime Glass*, Journal of Materials Engineering and Performance, 18, 8, 2009, 1012-1028.

5.15 M. Grujicic, B. Pandurangan, N. Coutris, B. A. Cheeseman, C. Fountzoulas and P. Patel, *A Simple Ballistic Material Model for Soda-Lime Glass*, International Journal of Impact Engineering, 36, 2009, 386-401.

5.16 T. J. Holmquist, D. W. Templeton, K. D. Bishnoi, "*Constitutive Modeling of Aluminum Nitride for Large Strain High-strain Rate, and High-pressure Applications*," International Journal of Impact Engineering, 25, 2001, 211-231.

5.17 G. T. Camacho and M. Ortiz, *Computational Modeling of Impact Damage in Brittle Materials*, International Journal of Solids and Structures, 33, 20-22, 2899-2938, 1996.

5.18 W. D. Kingery, H. K. Bowen and D. R. Uhlmann, *Introduction to Ceramics*, 2nd ed., John Wiley & Sons: New York, 1976, 91-124.

5.19 <http://www.accelrys.com/mstudio/ms modeling/visualiser.html>.

5.20 <http://www.accelrys.com/mstudio/ms modeling/amorphouscell.html>.

5.21 H. Sun, *COMPASS: An ab Initio Force-Field Optimized for Condensed-Phase Applications Overview with Details on Alkane and Benzene Compounds*, Journal of Physical Chemistry B, 102, 1998, 7338-7364.

5.22 H. Sun, P. Ren, and J. R. Fried, *The COMPASS force field: parameterization and validation for phosphazenes*, Computational and Theoretical Polymer Science, 8, 1/2, 1998, 229-246.

5.23 M. Grujicic, Y-P. Sun and K. Koudela, *The Effect of Covalent Functionalization of Carbon Nanotube Reinforcements on the Atomic-Level Mechanical Properties of Poly-Vinyl-Ester-Epoxy*, Applied Surface Science, 253, 2007, 3009-3021.

5.24 <http://www.accelrys.com/mstudio/ms modeling/discover.html>.

5.25 M. Grujicic, B. Pandurangan, C. D. Angstadt, K. L. Koudela, and B. A. Cheeseman, *Ballistic performance optimization of a hybrid carbon nanotube/E-glass reinforced poly-vinyl-ester-epoxy matrix composite armor*, Journal of Material Science, 42, 2007, 5347–5349.

5.26 S. Nose, *A unified formulation of the constant temperature molecular dynamics methods*, The Journal of Chemical Physics, 81, 1984, 511-519.

5.27 K. Trachenko, M. T. Dove, *Densification of Silica Glass under Pressure*, Journal of Physics: Condensed Matter, 14, 2002, 7449-7459.

5.28 D. E. Grady and L. C. Chhabildas, *Shock-wave Properties of Soda-lime Glass*, Report No: SAND96-2571C, 1996.

5.29 L. Davison, *Fundamentals of Shock-wave Propagation in Solids*, Shock-wave and High Pressure Phenomena, Springer-Verlag, Berlin, Heidelberg, 2008.

5.30 Y. Sato and O. L. Anderson, *A Comparison of the Acoustic and Thermal Gruneisen Parameters for Three Glasses at Elevated Pressure*, Journal of Physics and Chemistry of Solids, 41, 4, 1980, 401-410.

5.31 *Cambridge Engineering Selector*, <http://www.grantadesign.com>.

5.32 C. S. Alexander, L. C. Chhabildas, W. D. Reinhart, D.W. Templeton, *Changes to the Shock Response of Fused Quartz due to Glass Modification*, International Journal of Impact Engineering, 35, 2008, 1376-1385.

CHAPTER SIX

MOLECULAR-LEVEL ANALYSIS OF SHOCK-WAVE PHYSICS AND DERIVATION OF THE HUGONIOT RELATIONS FOR SODA-LIME GLASS

6.1 Abstract

Non-equilibrium and equilibrium molecular dynamics simulations are employed in order to study the mechanical response of soda-lime glass (a material commonly used in transparent armor applications) when subjected to the loading conditions associated with the generation and propagation of planar shock waves. Particular attention is given to the identification and characterization of various (inelastic-deformation and energy-dissipation) molecular-level phenomena and processes taking place at the shock front. The results obtained revealed that the shock loading causes a 2-4% (shock strength-dependent) density increase. In addition, an increase in the average coordination number of the silicon atoms is observed along with the creation of smaller Si-O rings. These processes are associated with significant energy absorption and dissipation and are believed to control the blast/ballistic impact mitigation potential of soda-lime glass.

The present work was also aimed at the determination (via purely computational means) of the shock Hugoniot (i.e. a set of axial stress vs. density/specific-volume vs. internal energy vs. particle velocity vs. temperature) material states obtained in soda-lime glass after the passage of a shock wave of a given strength and on the comparison of the computed results with their experimental counterparts. The availability of a shock Hugoniot is critical for construction of a high deformation-rate, large-strain, high pressure material model which can be used within a continuum-level computational analysis to capture the response of a soda-lime glass based

laminated transparent armor structure (e.g. a military vehicle windshield, door window etc.) to blast/ballistic impact loading.

6.2 Introduction

While novel transparent ceramics and transparent polymeric materials are being increasingly used in various blast/ballistic-impact resistant vehicle transparent structures (e.g. windshields, door windows, viewports, etc.), ballistic glass remains an important material component in these structures [6.1,6.2]. The main reasons for this have been discussed in great detail in our recent work [6.3-6].

Typically, the development of new glass-based transparent impact resistant structures involves extensive prototyping and laboratory/field experimental testing. While these experimental efforts are critical for ultimate validation of the transparent impact resistant structures, they are generally expensive, time-consuming and involve destructive test procedures. In addition, it is well-established (e.g. [6.3-6]), that the effectiveness and reliability of the computation-based modeling and simulation approaches is strongly correlated with the fidelity of the associated material models. In other words, it is critical that these models realistically describe deformation/fracture response of the subject material (ballistic glass, in the present case) under high-rate, large-strain, high-pressure loading conditions encountered during blast/ballistic impact. Therefore, one of the main objectives of the present work is to explore the possibility for using molecular-level computational simulations in order to improve fidelity of the models representing the material under consideration. Specifically, phenomena and processes accompanying the formation and propagation of shock-waves within soda-lime glass will be investigated in order to derive the associated functional relations between different material state variables.

A comprehensive literature review carried out as part of our prior work [6.6] revealed that the mechanical behavior of glass is modeled predominantly using three distinct approaches: (a) molecular-modeling methods [6.7-10]; (b) continuum-material approximations [6.3-6, 6.11-14]; and (c) models based on explicit crack representation [6.15,6.16]. In addition, this review established that only the molecular-level models are capable of identifying nanometer length scale phenomena and the associated microstructure evolution processes accompanying high-rate deformation of soda-lime glass. This is the main reason that molecular-level methods and tools are employed in the present work.

As mentioned above, the main objective of the present work is to investigate various shock-wave related phenomena using molecular-level computational methods. A shock wave (or simply a shock) is a wave which propagates through a medium at a speed higher than the sound speed and its passage causes an abrupt and discontinuous change in the material state variables (e.g., pressure, internal energy, density, temperature and particle velocity). The magnitude of the state-variable changes and the shock speed increase with the strength of the shock. In reality, since no material can support a discontinuity in its state variables, shocks manifest themselves as continuous (structured) waves with a steep and narrow wave front. While acoustic waves give rise to isentropic changes in the material state variables, passage of a shock is typically associated with irreversible (entropy-increasing) changes in the same variables. The reason behind this difference is that shock involves very high strain rates that bring energy-dissipative viscous effects into prominence.

Based on an open-literature review, conducted as part of the present work, it was established that molecular-level computational methods were first employed to study shocks more than 30 years ago [6.17-20]. While the initial focused on shock phenomena in dense fluids, subsequent analyses were extended to single-crystalline solids. The key findings related to the

generation and propagation of shocks in the single-crystalline solids investigated can be summarized as follows: (a) shock wave phenomena are inherently more complex in solids than in fluids, because solids, in addition to the lattice parameter, introduce a new length scale (i.e. the size/spacing of defects) which tends to control the nature/extent of inelastic-deformation processes (mainly responsible for energy dissipation at the shock front); (b) initial (un-steady) shock waves tend to become steady (time-invariant) as they propagate and this process is facilitated by the transverse displacement of atoms which produce inelastic deformations. These deformation involves concerted slippage of atoms over each other and is not dominated by viscous flow as in the case of shocks in fluids; and (c) in order to eliminate free-surface effects and model bulk-material behavior, molecular-level modeling of shock is typically carried out using computational systems with periodic boundary conditions (at least in directions transverse to the shock-wave propagation direction). As a consequence of the use of the periodic boundary conditions within shock wave molecular-level simulations, a single shock (or often a pair of converging shocks) is associated with each computational cell. To attain steady wave conditions of the shock, computational domains sufficiently long in the direction of shock wave propagation have to be employed. For a typical 5000-7000m/s range of the shock speed and a typical 20ps computation time the minimum computational-cell length required is of the order of 100-150nm. It should be also noted that, lateral dimensions of the computational domain have to be also sufficiently large to avoid spurious effects associated with the use of the periodic boundary conditions. Consequently, computational domains involving several tens of thousands of atoms have to be employed in shock wave simulations requiring prolonged wall-clock simulation times. Furthermore, since weak and moderate shocks in single crystalline solids can have width on the order of 100-500nm they could not be readily modeled using the molecular-level methods. However, as will be shown in the present work, when the energy dissipative mechanisms are not

very potent (as is the case in soda-lime glass), moderate shocks are associated with significantly smaller width and they could be studied using molecular-level methods.

As mentioned earlier, a preliminary molecular-level computational study of shock generation/propagation in soda-lime glass is carried out in the present work. The study has the following two main objectives:

(a) To determine the shock Hugoniot (centered on the initial stress-free quiescent state) of soda-lime glass. A Hugoniot is the locus of axial stress vs. specific volume vs. energy density (vs. particle velocity vs. shock speed) shocked (*upstream*) material states. The Hugoniot is often used in the derivation of the continuum-level material models of the type employed in transient non-linear dynamics analyses of the response of structures to shock loading. In situations in which one is interested only in the problem of planar shock propagation/interaction (in the presence of uni-axial strain deformation states), a complete definition of the continuum-level material model is not required. Instead, the knowledge of the corresponding Hugoniots (i.e. Hugoniot functional relations) is sufficient; and

(b) The Hugoniot relations mentioned in (a) provide a global statement of mass, momentum, and energy conservation accompanying shock-induced material transition from a given initial (*downstream*) equilibrium state to all possible final (*upstream*) equilibrium states for steady planar shock waves (of different strengths). However, these relations provide no information about the structure of the shock front or the nature of the dissipative structural rearrangement mechanisms that lead to the formation of a steady shock wave. Hence, the second objective of the present work is to carry out a detailed examination of the downstream, shock-front and upstream material states (as represented by the local stresses, strains, densities/specific volumes, temperatures etc.) and molecular-level morphology in order to identify and characterize these processes.

The organization of the paper is as follows: A brief description of the molecular-level microstructure of glass including its random-network representation is presented in Section 6.3. A brief overview of the molecular-level computational procedure including the computational cell construction, force field identification, computational method(s) selection, shock-wave generation and the problem definition are respectively presented in Sections 6.4.1-6.4.5. The key results obtained in the present work are presented and discussed in Section 6.5. A summary of the work carried out and the key results/conclusions are given in Section 6.6.

6.3 Molecular-level Microstructure of Glass

One of the basic properties of all glass-like materials is their lack of long-range atomic order which classifies them as amorphous materials. For instance, the atomic arrangement in pure silicate glass (i.e. fused silica) is highly random relative to the crystalline Si-O modifications like quartz or cristobalite. To describe the random atomic arrangement within glass the so-called *random network model* [6.21] is typically employed. Such a model represents amorphous materials as a three-dimensional linked network of polyhedra with central cations of various coordinations depending on the character of the atomic constituents. In the case of silicate-based glasses like fused silica and soda-lime glass, the polyhedral central cation is silicon. In this case, each silicon is surrounded by four oxygen anions and forms a SiO_4^{4-} tetrahedron, whereby each oxygen is bonded to (or bridges) two silicon atoms. Other polyhedra may exist in the network depending on the valence of the added polyhedral-center cations.

Ceramic glasses like soda-lime glass investigated in the present work, are generally a mixture of various oxides. Oxide constituents of the ceramic glasses are generally classified as: (a) *Network Formers*: Oxides (e.g., SiO_2, B_2O_3, GeO_2) falling into this category have the tendency to form a continuous network with "*bridging*" oxygen atoms; and (b) *Network Modifiers*: Oxides falling into this category are typically based on alkali (e.g. Na, K etc.) and

alkaline earth (e.g. Ca, Mg etc.) metals. In the specific case of soda-lime glass, investigated in the present work, the 14wt.% Na_2O and 9wt.% CaO additions pure SiO_2 glass both act as network modifiers. When alkali/alkaline earth metal-based oxides are added to pure SiO_2 glass, excess oxygen which results from the ionic dissociation of these oxides is incorporated into the glass network. This process disrupts network continuity since it replaces single continuity-forming bridging oxygen atom with two (network-breaking) singly-charged non-bridging oxygen ions. The latter oxygen ions are the result of charge transfer from the initially double charged oxygen ions (produced during dissociation of alkali/alkaline earth metal-based oxides) to the initially neutral bridging oxygen atoms. The metallic cations formed during dissociation tend to hover around the non-bridging oxygen ions for local charge neutrality.

Within the random network model, the microstructure of glass is described using several network state parameters. Among these, the most frequently used are: (a) the so-called *R* parameter, defined as the average number of oxygen ions per network forming cation. In a glass of a given chemistry, this parameter is effectively microstructure-insensitive since its value depends solely on the chemical composition of glass. For example, in the case of fused silica, in which there are two oxygen anions for every network forming silicon cation, the *R* value is 2.0. On the other hand, in the case of soda-lime glass, the introduction of additional oxygen ions (without the introduction of additional network forming cations) causes the *R* value to increase to ca. 2.41. In accordance with the earlier discussion regarding the role of glass modifiers, it is apparent that a larger value of the *R* parameter implies a more open, weaker glass network. The effect of network formers on the *R* parameter is more complicated and depends on the network former coordination number as well as its concentration. Overall the *R* parameter is a measure of the maximum extent of connectivity that can be achieved within a glass of a given chemistry. It should be noted that since shock loading is assumed to only produce physical/microstructural

changes in glass, the *R* value is not expected to change during shock loading; (b) the so-called "*X*" parameter which defines the average number of non-bridging (connected to only a single network forming cation) oxygen atoms per network polyhedron. The equilibrium value of this parameter can again be calculated using the known chemical composition of glass. For example, this parameter takes on a zero equilibrium value in the case of fused silica since all oxygen ions are of a bridging type. However, in the case of soda-lime glass for the reasons mentioned above, the equilibrium value of this parameter is ca. 0.81. It should be noted that shock loading-induced damage in glass will generally increase the number of non-bridging oxygen ions (through Si-O bend breaking), resulting in an increase of the *X* parameter beyond its equilibrium value and; (c) the so-called "*Y*" parameter which defines the average number of bridging (connected to two network forming cations) oxygen atoms per network polyhedron. The equilibrium values for this parameter in fused silica and soda-lime glass are 4.0 and 3.19, respectively. Shock loading will generally lower the value of this parameter below the equilibrium value.

In addition to chemical modifications of glass, changes in the microstructure of this material can be brought about by mechanical loading/deformation (typically requiring several GPa pressure levels). Specifically, high pressure may result in a reorganization of the atomic network (phase change) in the form of changes to the coordination of the network forming cations. These phase changes can be of first order, which are characterized by the formation of a distinct high-pressure phase at a nominally constant pressure, or they may be of second order which are phase changes which involve a continuous morphing of the original phase into the final high-pressure phase over a range of pressures. These phase transformations may be associated with significant volume changes and, since phase-transformation induced energy absorption is a well-documented phenomenon responsible for high toughness levels in TRIP steels and partially stabilized crystalline ceramics, it is of interest to the present study.

The phase transformations of glass which are investigated in the present work occur in the range of 3 to 5 GPa. The phase transformations in question have not been fully investigated or characterized in terms of the random network model or using other microstructural parameters. However, the presence of these transformations has been inferred indirectly through the changes in the shock Hugoniot relations for soda-lime glass [6.32]. These changes typically result in an anomalous stiffness-decreasing response of the material during loading. This pressure range was chosen for the current investigation as it is consistent with the levels seen in glass structures subject to ballistic/blast loading and is associated with relatively modest (3-7%) volume changes. These phase-transformations should not be confused with those seen to take place at substantially higher pressures (ca. >20GPa), which are considered to be of second order and associated with substantially larger volume reductions and with the formation of stishovite, an octahedrally coordinated glass phase.

6.4 Molecular-level Analysis of soda-lime Glass

As mentioned earlier, molecular-level computational methods have been employed in the present work in order to investigate shock formation and propagation in soda-lime glass. Within these methods, all atoms, ions and bonds are explicitly accounted for and molecular mechanics, dynamics or Monte Carlo algorithms are used to quantify the behavior of the material under investigation.

While *ab-initio* quantum mechanics methods have the advantage over the molecular-level methods since they do not require parameterization, they have a serious short-coming. Namely, due to prohibitively high computational cost, they can be currently employed only for systems containing no more than a few hundred atoms/particles. As will be shown below, while ab-initio quantum-mechanics calculations are not directly used in the present work, some of the computational ab-initio quantum mechanics results are used in the parameterization of the

material model at the molecular length/time scale. Utility of the molecular-level computational results is greatly dependent on accuracy and fidelity of the employed force field (the mathematical expressions which describe various bonding and non-bonding interaction forces between the constituents of the molecular-level model). In the present work, the so-called *COMPASS* (Condensed-phase Optimized Molecular Potentials for Atomistic Simulation Studies) force field is used [6.22,6.23]. This highly accurate force field is of an ab-initio type since most of its parameters were determined by matching the predictions made by the ab-initio quantum mechanics calculations to the condensed-matter experimental data. Hence, it should be recognized that the COMPASS force field is a prime example of how the highly accurate results obtained on one length/time scale (quantum mechanic/electronic, in the present case) and the experimental data can be combined to parameterize material models used at coarser length/time scale (the molecular length/time scale, in the present case).

Formulation of a molecular-level simulation problem requires, at a minimum, specification of the following three aspects: (a) a molecular-level computational model consisting of atoms, ions, functional groups and/or molecules; (b) a set of force field functions; and (c) a computational method(s) to be used in the simulation. More details of these three aspects of the molecular-level modeling and simulation of soda-lime glass are provided below.

6.4.1 Computational Model

At the molecular level, soda-lime glass is modeled as a discrete material consisting of: (a) silicon (Si) and oxygen (O) atoms mutually bonded via a single covalent bond and forming a connected, non-structured/amorphous network of silica (SiO_4^{4-}) tetrahedra; (b) oxygen anions (O^{2-}) attached as terminal functional-groups to the fragmented silica tetrahedra network; and (c) sodium cations (Na^{+}) dispersed between fragmented silica tetrahedra networks and ionically bonded to the oxygen anions.

While glass is an amorphous material and does not possess any long-range regularity in its atomic/molecular structure, modeling of bulk behavior of glass is typically done at the molecular level by assuming the existence of a larger (amorphous) unit cell. Repetition of this cell in the three orthogonal directions (the process also known as application of the *periodic boundary conditions*) results in the formation of an infinitely-large bulk-type material. This procedure was adopted in the present work.

The parallelopiped-shaped computational cell used in the present work contained 2304 particles (Si-512, Na^+-512, O^--256 and O-1024). The computational cell edge-lengths were initially set to a=7.471nm and b=c=1.868nm, yielding a soda-lime glass initial nominal density of 2.613g/cm^3. The three edges (*a*, *b* and *c*) of the cell were aligned respectively with the three coordinate axes (*x*, *y* and *z*).

To create the initial particle configuration in the unit cell, the Visualizer [6.24] program from Accelrys was first used to construct a short silica-chain fragment. The fragment was then *grown* by a duplicate-and-attach process using the same program. The resulting silica network (along with additional sodium cations and oxygen anions) was next used within the Amorphous Cell program [6.25] from Accelrys to randomly populate the computational cell while ensuring that the target material density of 2.613g/cm^3 was attained. An example of a typical molecular-level topology within a single unit cell is displayed in Figure 6.1.

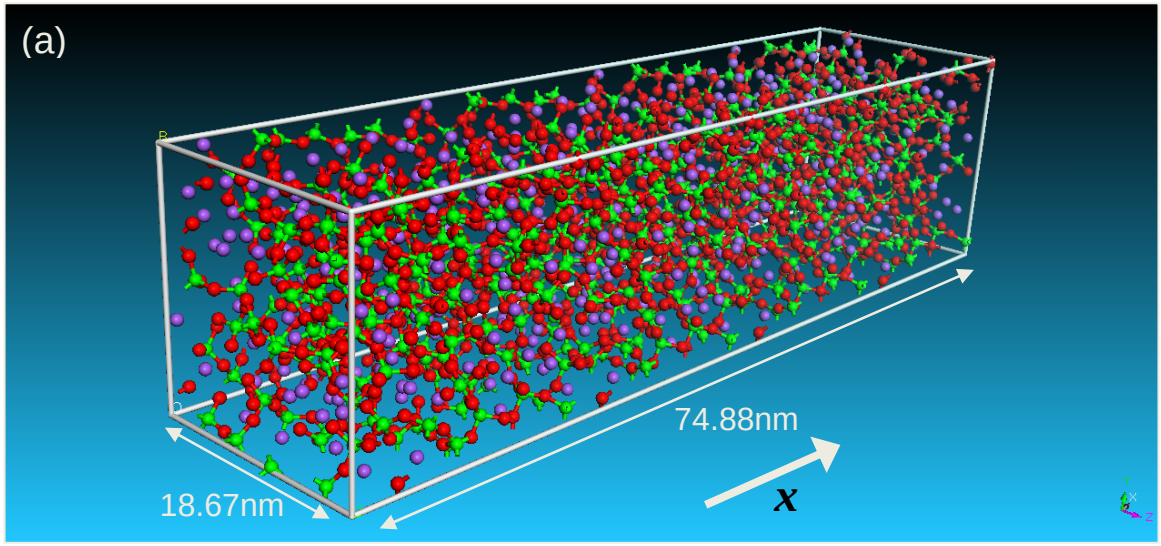

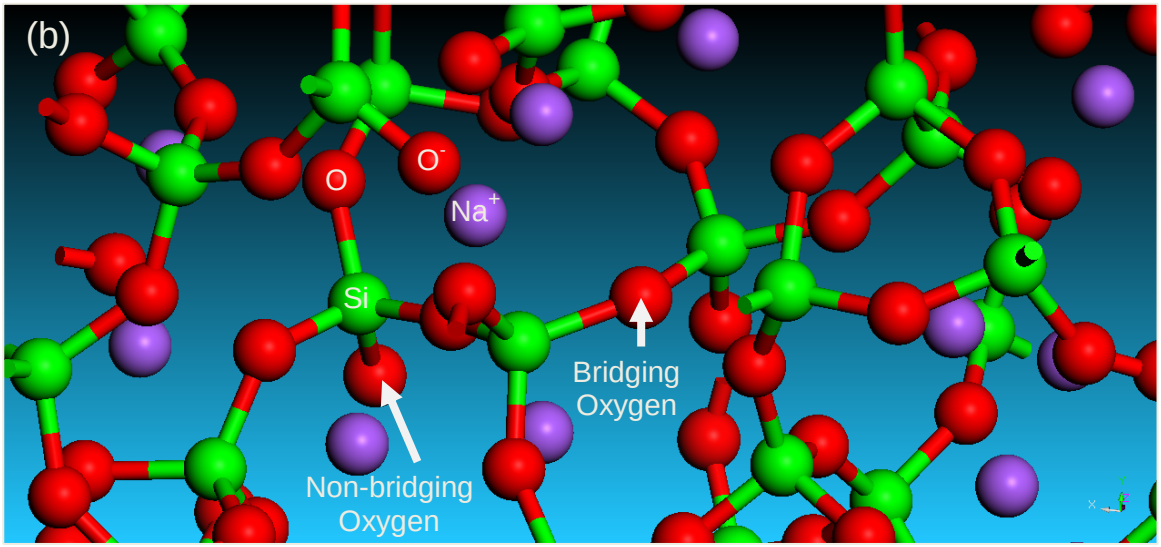

Figure 6.1: (a) The computational unit cell for soda-lime glass molecular-level simulations used in the present work; and (b) an example of the local atomic structure.

6.4.2 Force-fields

As stated above, the behavior of a material system at the molecular-level is governed by the appropriate force-fields which describe, in an approximate manner, the potential energy hyper-surface on which the atomic nuclei move. In other words, the knowledge of force-fields enables determination of the potential energy of a system in a given configuration. In general, the

potential energy of a system of interacting particles can be expressed as a sum of the valence (or bond), cross-term and non-bond interaction energies. Each of these energy components, in turn, contains a number of subcomponents. For example, the valence energy contains the contributions from single bond stretching, two-bond angle changes, three-bond dihedral bond angle changes, etc. The cross energy term includes the contributions from the interactions of the subcomponents of the valence terms (e.g. stretch/stretch interaction, stretch/bond-angle change interaction, etc.). The non-bond interaction term, accounts for the interactions between non-bonded atoms and includes the van der Waals energy and the Coulomb electrostatic energy.

As mentioned earlier, the present molecular-level analysis of soda-lime glass employs the COMPASS [6.22, 6.23] force-field for various bond and non-bond interaction energies. A summary of the COMPASS force-field functions can be found in our previous work [6.26]."

6.4.3 Computational Method

Both molecular statics and molecular dynamics simulations were employed in the present work. Within the molecular statics approach, the unit-cell potential energy is minimized with respect to the position of the constituent particles/atoms. The potential energy minimization within Discover [6.27] (the atomic simulation program from Accelrys used in the present work) is carried out by combining the Steepest Descent, Conjugate Gradient and the Newton's minimization algorithms. These algorithms are automatically inactivated/activated as the atomic configuration is approaching its energy minimum (i.e. the Steepest Descent method is activated at the beginning of the energy minimization procedure while the Newton's method is utilized in the final stages of this procedure).

As will be discussed in greater detail in Section 6.5, molecular statics is employed to determine the state of the material swept by a shock. As will be shown, this procedure is based

on the use of (bonding and non-bonding) potential energy components and neglects shock-induced changes in the (configurational) entropy of the system. To assess the consequence of this simplification, the approach described in Ref. [6.28] was considered. This approach defines a dimensionless parameter and states that when this parameter is significantly smaller than unity, entropy effects can be neglected. Unfortunately, detailed temperature and pressure dependencies of the material mechanical response of soda-lime glass needed to evaluate this parameter were not available with sufficient fidelity. Hence, the results obtained by the application of this procedure, which suggest that the entropy effects may not be highly critical, cannot be accepted with a high level of confidence.

Within the molecular dynamics approach, gradient of the potential energy with respect to the particle positions is first used to generate forces acting on the particles and, then, the associated Newton's equations of motion (for all particles) are integrated numerically in order to track the temporal evolution of the particle positions. Both the equilibrium and non-equilibrium molecular dynamics methods are employed in the present work. Within the equilibrium molecular-dynamics methods, the system under consideration is coupled to an (external) environment (e.g. constant pressure piston, constant temperature reservoir, etc.) which ensures that the system remains in equilibrium (i.e. the system is not subjected to any thermodynamic fluxes). As will be discussed in next section, NVT (where N is the (fixed) number of atoms, V, the computational cell volume (also fixed), and T(=298K) is the temperature) equilibrium molecular dynamics is employed in the first stage of the shock generation procedure. In addition, as will be discussed in Section 6.5, *NVE* (E is the total energy) equilibrium molecular dynamics is also employed during determination of the shock Hugoniot. Within non-equilibrium molecular dynamics, the system is subjected to large perturbations (finite changes in the axial parameter of the computational cell, in the present case) which create a thermodynamic flux (i.e. the flux of

energy and momentum, in the present case). More details regarding the use of Discover to carry out molecular statics and molecular dynamics analyses can be found in our prior work [6.6].

6.4.4 Shock-wave Generation

To generate a planar shock (or more precisely a pair of planar shocks) within the computational cell, the following procedure is employed:

(a) At the beginning of the analysis, a *sufficiently long* NVT molecular dynamics simulation is carried out in order to equilibrate the system/material.

(b) The shock is then initiated (and driven) by continuously contracting the computational cell x-direction lattice parameter a as:

$$a(t) = a(t=0) - 2u_p t \tag{6.1}$$

where t denotes time, u_p is the so-called *piston* velocity (or equivalently the particles upstream velocity) in the x-direction. u_p is varied over a range between 187.5 and 1500m/s in order to simulate the generation and propagation of shock of various strengths. Meanwhile, computational-cell transverse lattice parameters $\boldsymbol{b}$ and $\boldsymbol{c}$ are kept constant in order to obtain planar (uniaxial-strain) shock conditions. In this process, the computational cell faces normal to the shock propagation-direction behave very similarly to the impact-surface of a plate-like target subjected to a so-called symmetric *flyer-plate* impact test [6.29]. The procedure employed here generates a pair of shock waves which propagate, at a shock speed $\boldsymbol{U}_s$, from the cell boundaries toward its center. It should be noted that while the procedure employed involved contraction of the unit-cell at only one of its faces, due to the use of the periodic boundary conditions, a pair of shocks was generated. In other words, it was not possible to generate a single shock while maintaining material continuity (i.e., satisfying the periodic boundary condition). As schematically shown in Figure 6.2, these shock waves leave behind a *shocked* material state

characterized by a higher material density (as well as internal energy, temperature, stress, particle velocity, and entropy).

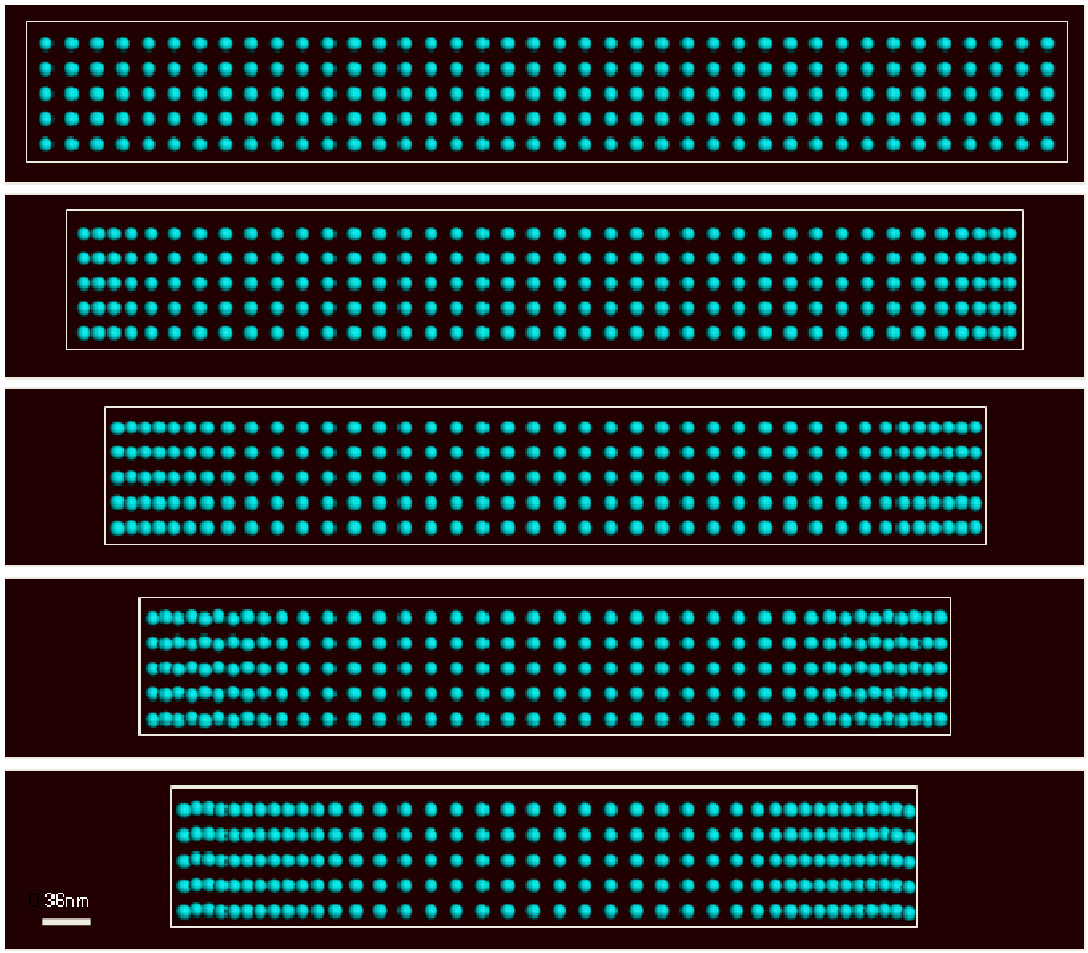

Figure 6.2: A schematic of the generation of a pair of shocks in a molecular-level system via the process of computational-cell parameter contraction.

The aforementioned procedure for shock-wave generation and the subsequent molecular statics/dynamics analyses are carried out through the use of a Discover input file [6.27] which is written in a BTCL (Basic Tool Command Language) language. This enabled the use of a scripting engine that provides very precise control of simulation jobs, e.g. a cell deformation to be carried out in small steps each followed by a combined energy-minimization/molecular-dynamics simulation run.

6.4.5 Problem Formulation

The problem addressed in the present work involved generation of shock waves of different strengths (using the aforementioned computational cell parameter contraction method), determination of the associated shock-Hugoniot relations and identification and elucidation of the main molecular-level inelastic-deformation/energy dissipation processes taking place at or in the vicinity of the shock front. The procedure for shock wave generation was presented in the previous section.

As far as the shock Hugoniot determination is concerned, it entailed the knowledge of the shock-wave profiles (and their temporal evolution) for the axial stress, material density, particle velocity, internal energy and temperature. The latter are obtained by lumping particles/atoms and their (bond and non-bond) potential and kinetic energy contribution, into fixed-width bins, in the order of their axial coordinates. As will be shown in the next section, two types of bins are used: (a) a Lagrangian-type which is fixed to the initial/reference state of the computational cell and (b) a moving-type which is attached to the advancing shock front.

Identification of the molecular-level inelastic-deformation/energy dissipation processes entailed a close examination of the changes in a material bond structure and topology caused by the passage of the shock.

6.5 Results and Discussion

6.5.1 Shock-wave Observation and Structure Characterization

An example of the typical results, obtained in the present work, pertaining to material molecular-level microstructure/topology evolution caused by a continuous axial contraction of the computational cell is displayed in Figures 6.3(a)-(d). The results displayed in these figures clearly reveal the generation of a pair of planar shock waves at the two opposing ***y-z*** faces of the

computational cell, Figure 6.3(a), and their subsequent propagation toward the center of the cell, Figures 6.3(b)-(d). An approximate location of the center-point of the two shocks is indicated using arrowheads in Figures 6.3(a)-(d). The results displayed in Figures 6.3(a)-(d) show that the shock waves remain fairly planar during their motion. The analysis of shock-wave propagation was terminated at a time which is shorter than the two-shock collision time. However, the analysis can be extended throughout the shock-interaction, which will be done in our future work.

While the results displayed in Figures 6.3(a)-(d) provide clear evidence for the formation and propagation of a pair of opposing planar shock waves, they do not offer any information about the structure/shape of the shock-wave front or about the state of the (upstream) material swept by the shock. The latter aspects of shock-wave generation and propagation within soda-lime glass are addressed in the remainder of this section and in the subsequent sections.

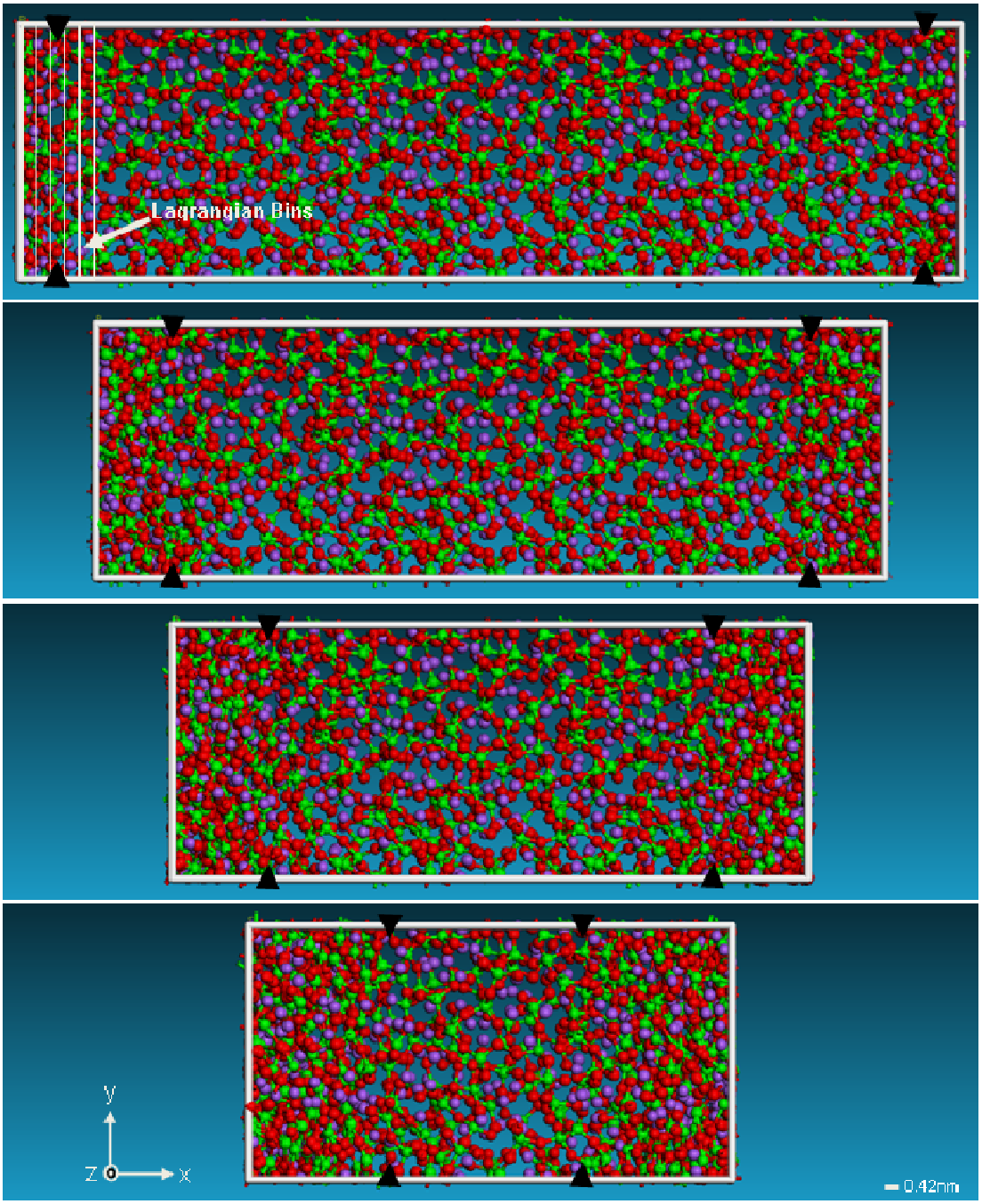

Figure 6.3: Temporal evolution of the molecular level material microstructure accompanying generation and propagation of a pair of planar shocks is soda-lime glass.

To reveal the structure/shape of the shock wave, the method of (Lagrangian) bins described in Section 6.4.5 is employed. In this case, the bins are stationary since they are fixed to

in the (initial) reference atomic configuration of the computational cell. Consequently, the same atoms are associated with a given bin throughout the entire molecular dynamics simulation. These bins (with an increased thickness, for clarity) are depicted in Figure 6.3 top part, the initial configuration. Examples of the typical results obtained through the use of this method are displayed in Figures 6.4(a)-(b). The results displayed in these figures are obtained under identical conditions except for the rate of axial contraction of the computational cell which is 100% higher in the case of Figure 6.4(b) (750m/s) relative to Figure 6.4(a) (375m/s). In these figures, particle velocities at different simulation (i.e. post shock wave generation) times, 1=60fs, 2=120fs, 3=180fs, etc. are plotted against the Lagrangian bin center ***x***-location (for the shock propagating to the right, only). Brief examination of the results displayed in Figures 6.4(a)-(b) reveals that:

(a) two shock waves are generated (only the right-propagating shock is shown though) at the computational cell faces normal to the ***x***-direction. These shocks subsequently propagate

(b) after a brief transient period, the shocks appear to attain steady wave profiles (i.e. a nearly time-invariant profile within a reference frame which is attached to, and moves with, the shock front). This is demonstrated for the weaker shock case in Figure 6.4(c) in which the shock profile for the curves labeled 3 and 4 in Figure 6.4(a) are redrawn within a moving frame attached to the inflection point of the shock profile; and

(c) both the particle velocity and the shock speed increase with the computational-cell contraction rate. It should be noted that the curves bearing the same numerical label in Figures 6.4(a)-(b) correspond to the same simulation time.

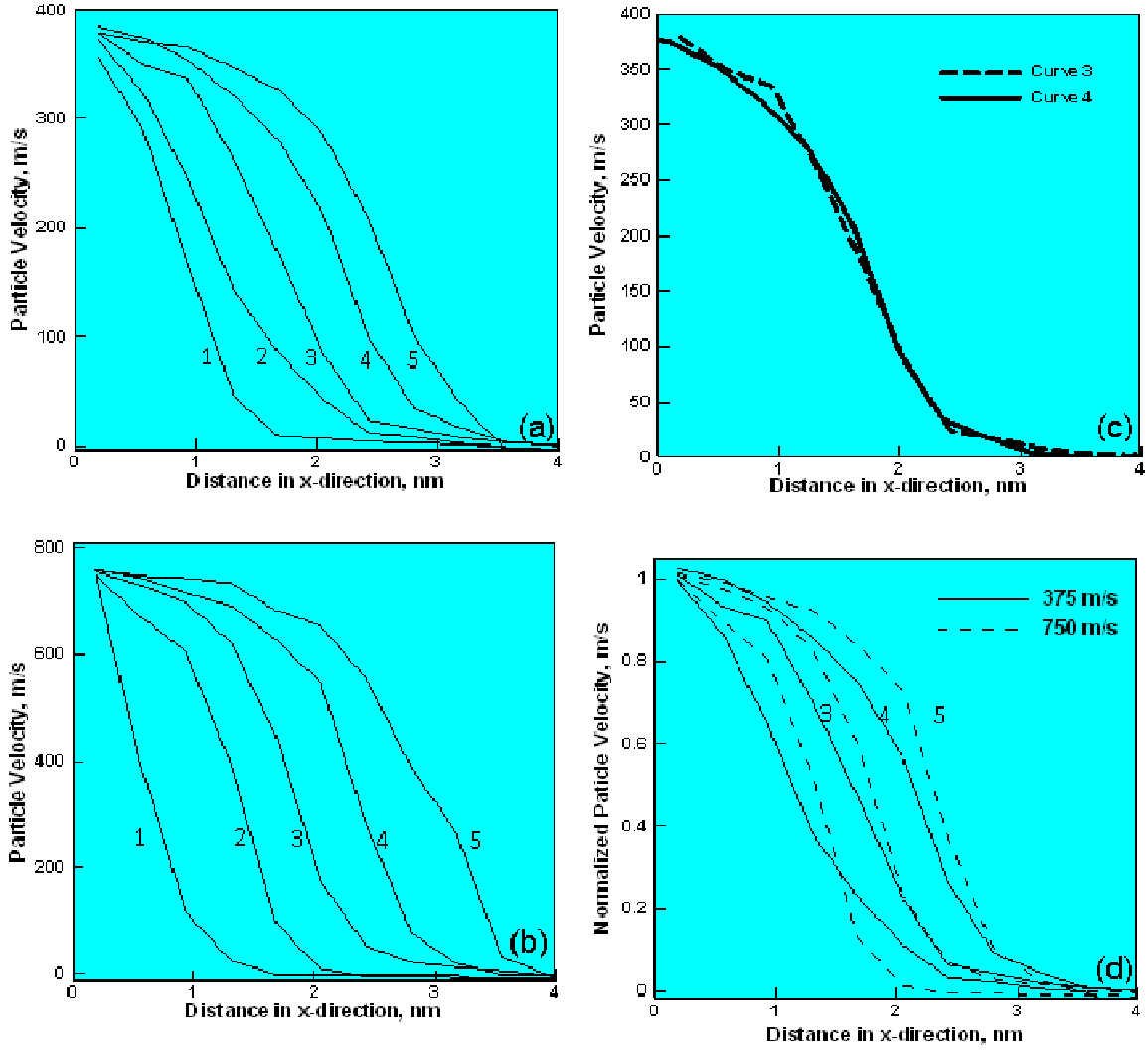

Figure 6.4: Temporal evolution of the particle velocity associated with the propagation of two approaching shock waves under the imposed computational cell contraction rate of (a) 375m/s; and (b) 750m/s. The simulation time associated with each of the curves is equal to the curve number label multiplied by 60fs; (c) superposition of the curves 3 and 4 from part (a) suggesting steady nature of the shock wave; and (d) superposition of the curves 3, 4 and 5 from parts (a) and (b) demonstrating that the shock width decreases while shock speed increases with an increase in shock strength. Note that the particle velocities are normalized with respect to the respective maximum value.

It should also be noted that no thermostat was used in the present non-equilibrium molecular dynamics simulations, so that the steady-wave shock profile is a natural consequence of a balance between the continuous supply of momentum to the system (through the continuous

computational cell axial contraction) and the observed lateral motion of the atoms in the continuously enlarged upstream material domain swept by the shock. It should be noted that, due to the use of periodic boundary conditions in the lateral directions, despite the fact that the unit cell was constrained in these directions, atoms are free to pass through the computational cell lateral boundaries. In general, the use of a thermostat modifies the ($F=ma$ Newtonian-type) equations of motion solved within the molecular dynamics simulations by the introduction of a (velocity-proportional) viscous-dissipation term. It is well-established that, when shock formation and propagation is analyzed within a continuum framework, the use of a viscous-dissipation term is mandatory for the attainment of a steady-wave shock profile. This fact has often been used as a justification for the use of a (local or global) thermostat within molecular-level simulations of shock-wave formation/propagation. While such practices greatly facilitate the attainment of a steady shock, they cannot be readily defended since shock formation and propagation is generally considered to be an adiabatic (no system/surrounding energy exchange) process due to the near-instantaneous material transition to the shocked state. In addition, shock generation/propagation is a non-isentropic process due to the attendance of various energy dissipation mechanisms. These were the determining factors in the decision to not use a thermostat in the present work. Due to the lack of a thermostat, the molecular dynamics simulations employed in the present work can be characterized as being of a non-equilibrium type. It is interesting to point out that despite the fact that no viscous-dissipation term was added to the Newton's equations of motion, the results displayed in Figures 6.4(a)-(b) show some of the defining features of shock-waves when they are analyzed in the continuum-level simulations (in the presence of viscous dissipation). Specifically, a steady shock is generated and the shock width decreases with an increase in the shock strength. This point has been demonstrated in Figure 6.4(d) in which curves labeled 3,4 and 5 from Figure 6.4(a)-(b) have been re-plotted.

The examination of the results displayed in Figures 6.4(a)-(d) further reveals that in the weak-to-intermediate shock strength range examined, the observed shock-width is quite small (ca. 2-3nm). This finding suggests that the dominant energy dissipation processes captured by the molecular-level simulations are quite weak. As will be shown later, these processes involve changes in the soda-lime glass atomic coordination and in the size of the smallest Si-O rings. In other words, as pointed out by one of the reviewers of the present manuscript, viscous dissipation processes with characteristic times at the microsecond time scale are not active in the present simulations. This, in general, only affects the width of the shock profile but not the values of the shocked-material state variables.

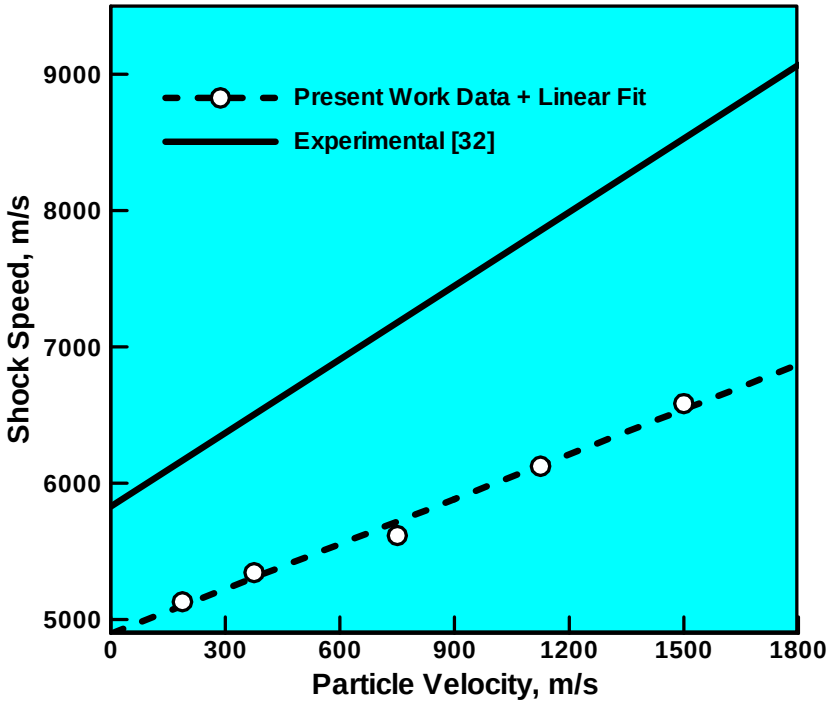

Figure 6.5: The Hugoniot relation pertaining to the particle velocity dependence of the shock speed.

6.5.2 Determination of Shock-Hugoniot Relations

The results presented in Figures 6.4(a)-(b) reveal the steady-shock profile and can be used to find a functional relation between the shock speed, U_s, and the particle velocity, u_p. This was done in the present work and the results obtained (depicted using discrete symbols) along with their least-square linear fit (depicted as a straight line) are displayed in Figure 6.5. Also displayed in Figure 6.5 is a linear fit to the corresponding experimental data (adjusted to the correct value of the acoustic wave speed) reported in Ref. [6.32]. While the agreement between the present computational data and their experimental counterparts displayed in Figure 6.5 appears to be only fair, it should be recognized that the experimental data were associated with a large scatter and that many measured shock speed data points substantially below a typical value (5830m/s) of the sound speed in soda-lime glass. The U_s vs. u_p relation is one of the so-called shock Hugoniot relations. The U_s vs. u_p relation mentioned above is a simple projection of the Hugoniot to the U_s - u_p plane. In the case of planar shocks, of interest in the present work, the other commonly used Hugoniot relations include: axial stress, t_{11}, vs. density, ρ (or specific volume, $v=1/\rho$); (mass-based) internal energy density, e, vs. ρ (or v);t_{11} vs. u_p and temperature T vs. ρ (or v). These relations were determined in the present work using two distinct methods:

(a) The first method is based on the three so-called *jump equations* which are defined as [6.29]:

$$\rho^{-}U_s = \rho^{+}\left(U_s - u_p\right) \tag{6.2}$$

$$t_{11}^{-} + \rho^{-}U_s^2 = t_{11}^{+} + \rho^{+}\left(U_s - u_p\right)^2 \tag{6.3}$$

$$e^{-} + \frac{t_{11}^{-}}{\rho^{-}} + 0.5U_s^2 = e^{+} + \frac{t_{11}^{+}}{\rho^{+}} + 0.5\left(U_s - u_p\right)^2 \tag{6.4}$$

These equations relate the known downstream material states (denoted by a superscript "–") and the unknown upstream material states (denoted by a superscript "+") associated with the shock of

a given strength (as quantified by the shock speed or the downstream-to-upstream particle velocity jump). These equations are next combined with the previously determined U_s vs. u_p relation and the prescribed (shock-strength defining quantity) U_s or u_p to solve for the unknown upstream material states. It should be noted that this method enables determination of only material mechanical state variables (t_{11}, e, $v(=1/\rho)$, U_s and u_p). To obtain temperature, a separate set of equilibrium *NVE* (*E*-total energy of the system) molecular dynamics simulations is carried out. In each case, a local computational sub-cell is defined containing only the upstream (shocked) material. The number of particles, the volume of the sub-cell and its total internal energy are all maintained constant. The associated *equilibrium* temperature is then calculated using the time-averages of the atomic velocities (see Eq. (6.6) below); and

(b) Time averages of the atomic positions, $\boldsymbol{r_i}$, velocities, $\boldsymbol{v_i}$, and interaction forces, $\boldsymbol{f_i}$ ($\boldsymbol{i}$ is the atomic label) are used to compute the unknown, local (bin-based) thermo-mechanical quantities using the following standard statistical thermodynamic relations:

$$\rho = \frac{1}{V_{bin}}\left[\left(\sum_{i=1}^{N_{bin}} m_i\right)_{avg}\right] \tag{6.5}$$

$$T = \left(\frac{1}{3N_{bin}k_b}\left[\sum_{i=1}^{N_{bin}} m_i v_i.v_i\right]\right)_{avg} \tag{6.6}$$

$$t_{11} = \frac{1}{V_{bin}}\left(N_{bin}k_bT + \sum_{i=1}^{N_{bin}} r_i \otimes f_i\right)_{avg} \tag{6.7}$$

$$E = \left(E_{Total} + \frac{1}{2}\left(\sum_{i=1}^{N_{bin}} m_i v_i.v_i\right)\right)_{avg} \tag{6.8}$$

where subscript *avg* denotes time averaging, N_{bin} and V_{bin} the number of atoms within and the volume of the bin, respectively, k_b is the Boltzmann's constant, E_{Total} is the potential energy of a system in a given configuration, while "$\cdot$" and "$\otimes$" indicate dot product and tensorial product

operators, respectively. It should be noted that the stress relation, Eq. (6.7) is a particular representation of the standard virial-based stress equation [6.33].

It should be noted that, in this case, the bins were defined within a reference frame which is attached to (and moves with) the steady-shock front. Clearly, in this case different atoms may reside within a given bin at different simulation times. On the other hand, the bins correctly collect the information about the atoms (temporarily) residing in a given segment of the steady-shock profile. In other words, time averages are calculated not for a fixed assembly of atoms, but rather for a transient set of atoms associated with a given moving bin. It should be also noted that since one of the main objectives of the present work was determination of the Hugoniot relations, only the data pertaining to the bins located in the fully-shocked upstream region are collected and analyzed (for different shock-strength conditions). In other words, the data collected by the bins located within the shock profile and downstream of the shock are ignored.

The results of these two procedures are displayed in Figures 6.6(a)-(d). In each of these figures, two cases are shown and labeled as *Method (a)* or *Method (b)* in order to indicate the method used for generation of the corresponding results. The results displayed in these figures show that, in the weak-shock regime, method(a) consistently over predicts (by as much as 100%) the values of the material state variables relative to method(b). This relative difference continuously diminishes with shock strength so that in the strong-shock regime the predictions of the two methods are different by less than 10%.

The Hugoniot relations displayed in Figure 6.5 and Figures 6.6(a)-(d) are typically used within a continuum-level computational analysis of shock-wave generation/ propagation in two ways:

(a) They are directly used in the analysis of shock-wave propagation under uniaxial strain conditions [6.31]; and

(b) Alternatively, they can be used to derive a continuum-level material model which is consistent with the material mechanical response under high-rate, large-strain, high-pressure conditions. Such a model is subsequently used in general three-dimensional, non-linear dynamics computational analyses [6.32].

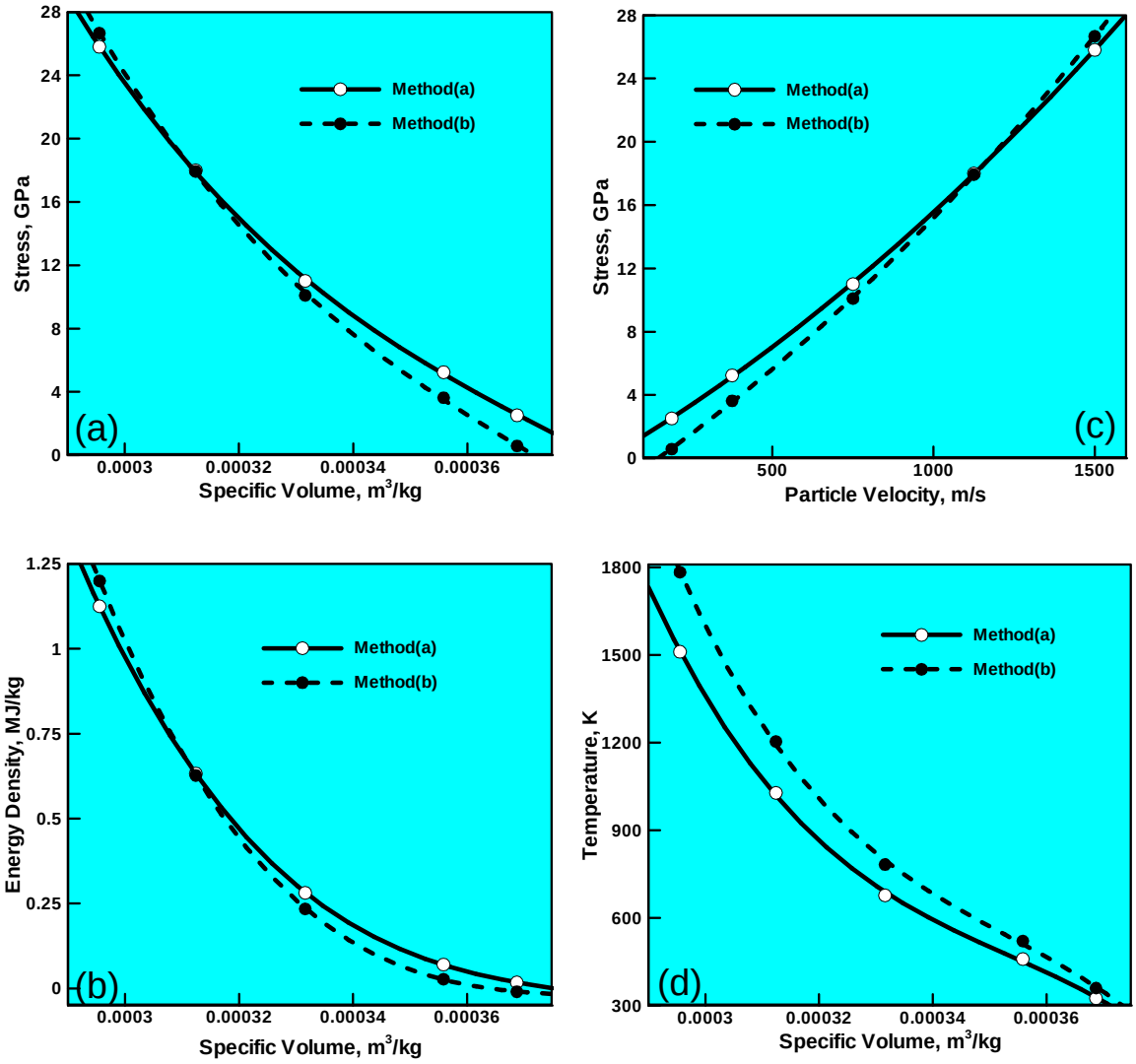

Figure 6.6: (a) Axial stress vs. specific volume; (b) energy vs. specific volume; (c) axial stress vs. particle velocity; and (d) temperature vs. specific volume Hugoniot relations. Please see text for explanation of the *Method (a)* and *Method (b)*.

In our recent work [6.6], it was shown that the Hugoniot relations can be generated by converting the corresponding isotherms (obtained via quasi-static, molecular-level mechanical

tests). This procedure was found to be associated with a number of challenges (e.g. a particular form of the equation of state had to be assumed, several material properties/relations had to be assessed independently, etc.). Most of these challenges were not encountered in the present work since the Hugoniot relations are derived more directly from the molecular-level computational results.

6.5.3 Shock-induced Material-state Changes

The results presented and discussed in the previous sections clearly revealed the formation and propagation of planar shocks in soda-lime glass and enabled formulation of the appropriate shock-Hugoniot relations. In the present section, a more detailed investigation is carried out of the molecular-level material microstructure in the wake of a propagating planar shock.

It should be first realized that the analysis of material microstructure and its evolution due to shock loading in soda-lime glass is quite challenging due to the absence of a crystal structure in this material. Namely, when molecular-level simulations of shock generation/propagation are carried out in (nearly perfect) single crystal solids [6.17,6.20], the presence of a crystal lattice greatly facilitates the investigation of deviations from the long range order (i.e. formation of various point, line and planar defects) and the nature of the associated inelastic deformation processes. Soda-lime glass is, on the other hand, an amorphous material in its initial condition and remains so after being subjected to shock loading. To address the challenge of material microstructure characterization and its changes resulting from shock loading, the following microstructural parameters were monitored: (a) the random network ***X*** parameter. The R parameter was not monitored since it is microstructure insensitive while Y parameter was not monitored since X+Y =4.0 in pure silicate glasses (like soda lime glass); (b) the ***Si***-atom average

coordination number(i.e. bonding structure); (c) the size of the smallest Si-O ring; and (d) the material's average density.

In the case of single-crystalline solids, previous molecular-level shock-wave formation/calculation work (e.g. [6.17,6.20]) established that the steady-wave condition is attained not as a result of (velocity-dependent) viscous dissipation (as is the case for shocks in fluids), but rather as a result of inelastic deformation (permanent slippage of crystal planes and the formation of crystal defects) and phase transformation processes. The microstructural parameters identified above are used to characterize the type and the extent of these processes.

6.5.3.1 X Parameter Evaluation

In general, changes in the *X* parameter are the result of competition between Si-O bond breaking processes (increases the average number of non-bridging oxygens per un-shocked material polyhedron) and the processes which lead to an increase in Si-atom coordination number (decrease the *X* parameter value). Since the instances of Si-atom coordination-number increase are found to greatly out-number the Si-O bond-breaking instances, the value of the *X* parameter has been found to decrease by 5 to 10% from its equilibrium value (=0.81).

6.5.3.2 Si-atom Average Coordination Number

Examination of the material microstructure in the shock wake revealed that the Si-atom average coordination number increases from its initial value of 4.0 by 2-3 percent. An example of the shock-loading induced increase in Si-atom coordination number is depicted in Figure 6.7(a)-(d). To aid in visualization/interpretation of the microstructural/topological changes experienced by soda-lime glass during shock loading, only a 20-30 atom exemplary region of the upstream material is analyzed in these figures. In addition, sodium cations are not displayed.

In Figures 6.7(a) and 6.7(c), ***x-y*** and ***y-z*** projections are given of the material region under consideration in its initial state. The corresponding projections for the same material region after the passing of a shock are displayed in Figures 6.7(b) and 6.7(d). For improved clarity, three silicon atoms are highlighted in green. To make apparent the Si-atom coordination-number increase, one of the Si atoms is labeled as "*Si*" along with the oxygen atoms bonded to it. It is clear that the silicon atom in question was initially four-fold coordinated and it became five-fold coordinated upon the passage of the shock.

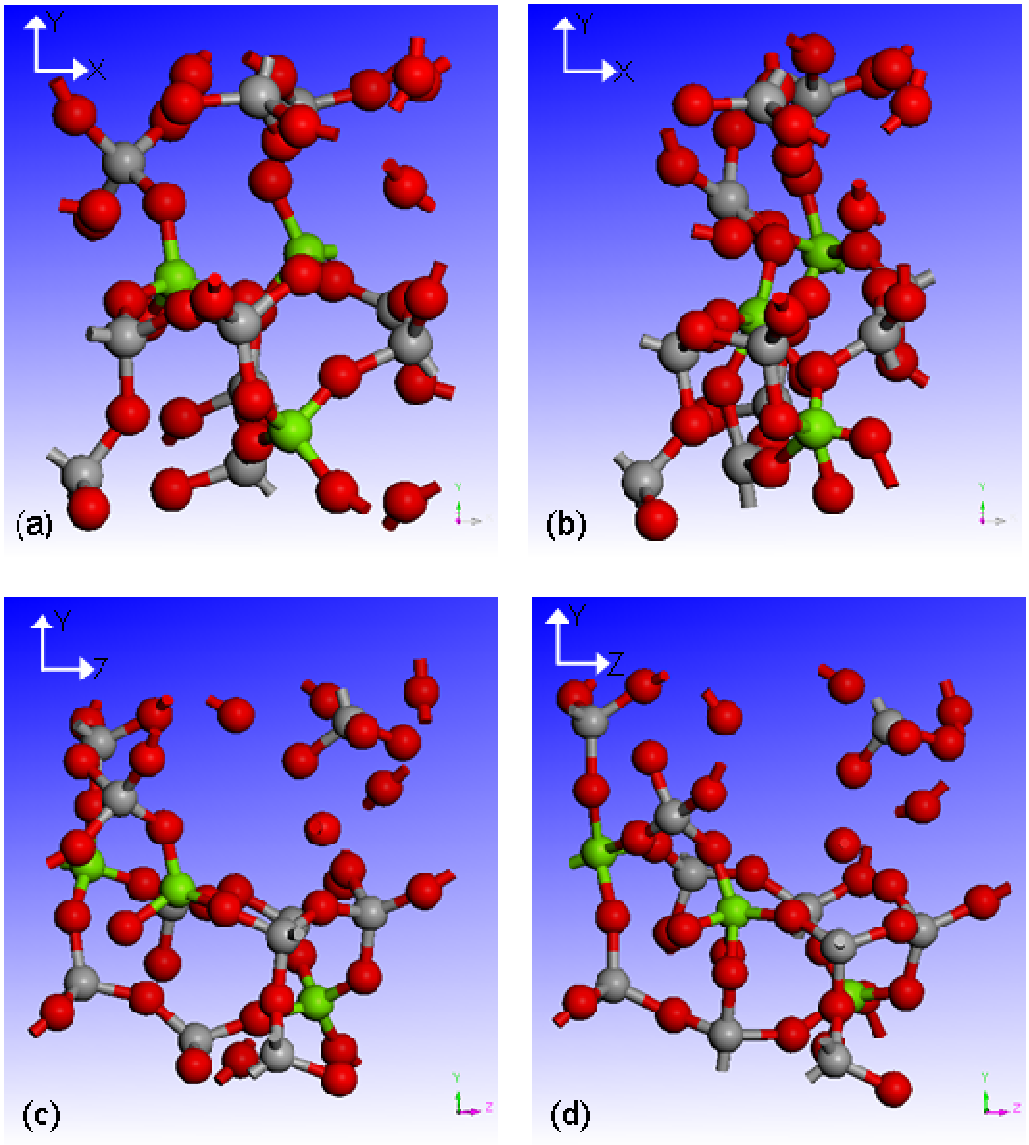

Figure 6.7: Development of five-fold coordinated silicon atoms in soda-lime glass under shock loading: (a) material initial state, x-y projection; (b) post-shock state of the same material region as in (a); (c) and (d) correspond respectively to the y-z projection of (a) and (b).

It should be noted that the molecular-level microstructural changes described above are a manifestation of the transition of soda-lime glass to a state that is energetically-favored at high shock-induced stresses (large densities). This finding is consistent with the experimental observation of Alexander et al. [6.32] who reported the formation of stishovite-like domains

containing six-fold coordinated silicon atoms in soda-lime glass at ca. 30GPa shock-induced axial stress levels.

6.5.3.3 Si-O Ring Minimum Size

It should be first noted that a comprehensive statistics-based Si-O ring minimum-size analysis is quite complicated and is beyond the scope of the present work. Such an analysis will be carried out in our future work. Instead, only a qualitative analysis of the molecular-level shocked material microstructure is carried out here in order to obtain evidence for the potential reduction in the minimum size of the Si-O rings. An example of two Si-O rings each containing five silicon atoms found in the as-shocked material is shown in Figure 6.8. For improved clarity, these rings are highlighted in purple and yellow. Similar rings were not observed in the initial un-shocked material. This finding was reconfirmed using different (yet, all equilibrium) initial molecular structures. Thus, the present work suggests that shock loading causes a reduction in the minimum Si-O ring size.

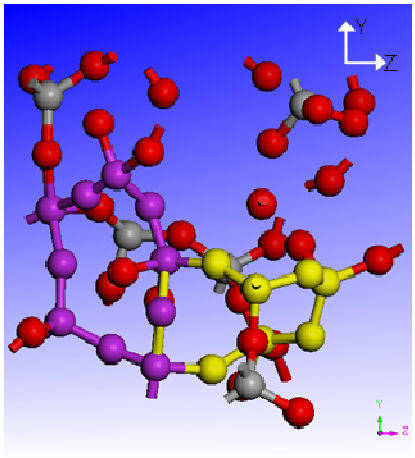

Figure 6.8: Observations of smaller Si-O rings (containing five Si atoms) in the as-shocked soda-lime glass. Similar small-size rings Si-O rings were not observed in the initial/un-shocked material state. The rings in question have been highlighted for clarity.

6.5.3.4 Material's Average Density

It should be also recognized that shock loading leads to a permanent 2-4% (shock strength-dependent) increase in the material density. This material densification process along with the aforementioned processes leading to an increase in the silicon-atom coordination and smaller Si-O ring formation are all associated with energy absorption/dissipation and, hence, are expected to play an important role in the blast/ballistic impact mitigation potential of soda-lime glass.

6.5.4 Final Remarks

Within the present work, molecular-level computational methods are employed to study various phenomena accompanying shock-wave generation and propagation in soda-lime glass. It should be noted that the present work does not suggest that molecular-level analyses of shock generation and propagation should replace the corresponding continuum-level (hydrodynamic) analyses. The latter are far better suited (and feasible) for studying the behavior of real-life engineering systems (e.g. vehicle windshield subjected to blast impact). Rather, the present approach is highly beneficial relative to the identification and characterization of the nanoscale phenomena/processes taking place at the shock front. Once these phenomena/processes are well understood and characterized (a formidable task) the knowledge gained can be used to formulate (and parameterize) more physically-based material models suitable for use in continuum-level analyses.

6.6 Summary and Conclusions

Based on the results obtained in the present work, the following summary remarks and main conclusions can be drawn:

1. Various phenomena accompanying the formation and propagation of a planar shock-wave within soda-lime glass, a material commonly used in transparent armor applications, are investigated using molecular-level computational methods.

2. The results obtained show that even without the use of a viscous-dissipation-based thermostat a steady-wave planar shock profile can readily be established in this material.

3. The time-averaged results pertaining to the atomic positions, velocities and interaction forces are used to construct the appropriate shock Hugoniot relations, the relations which define the locus of stress, energy density, mass density, temperature and particle velocity in soda-lime glass swept by a shock propagating at a given speed.

4. Detailed examination of the molecular-level microstructure evolution in the shock-wave wake is carried out in order to identify the nature of energy-absorbing and shock-wave spreading mechanisms. The results revealed that shock loading causes extensive changes in atomic coordination and the bond structure as well as a 2-4% (shock strength-dependent) density increase. Specifically, the atomic coordination of many silicon atoms has been found to increase from four to five and numerous smaller Si-O rings are observed. These processes are associated with substantial energy absorption and dissipation and are believed to greatly influence the blast/ballistic impact mitigation potential of soda-lime glass.

6.7 References

6.1 E. Strassburger, P. Patel, W. McCauley and D. W. Templeton, *Visualization of Wave Propagation and Impact Damage in a Polycrystalline Transparent Ceramic- AlON*, Proceedings of the 22nd International Symposium on Ballistics, November 2005, Vancouver, Canada.

6.2 AMPTIAC Quarterly: *Army Materials Research*: *Transforming Land Combat Through New Technologies*, 8, no.4, 2004.

6.3 M. Grujicic, B. Pandurangan, N. Coutris, B. A. Cheeseman, C. Fountzoulas, P. Patel and E. Strassburger, *A Ballistic Material Model for Starphire®, A Soda-lime Transparent Armor Glass*, Materials Science and Engineering A, 492, 1, 2008, 397-411.

6.4 M. Grujicic, B. Pandurangan, W. C. Bell, N. Coutris, B. A. Cheeseman, C. Fountzoulas and P. Patel, *An Improved Mechanical Material Model for Ballistic Soda-Lime Glass*, Journal of Materials Engineering and Performance, 18, 8, 2009, 1012-1028.

6.5 M. Grujicic, B. Pandurangan, N. Coutris, B. A. Cheeseman, C. Fountzoulas and P. Patel, *A Simple Ballistic Material Model for Soda-Lime Glass*, International Journal of Impact Engineering, 36, 2009, 386-401.

6.6 M. Grujicic, W. C. Bell, P. S. Glomski, B. Pandurangan, B. A. Cheeseman, C. Fountzoulas and P. Patel, *Multi-length Scale Modeling of High-pressure Induced Phase Transformations in Soda-lime Glass*, Journal of Materials Engineering and Performance, DOI: 10.1007/s11665-010-9774-2, 2010.

6.7 L. V. Woodcock, C. A. Angell and P. Cheeseman, *Molecular dynamics studies of the vitreous state: Simple ionic systems and silica*, The Journal Chemical Physics, 65, 1976, 1565–1577.

6.8 R. G. D. Valle, E. Venuti, *High-pressure Densification of Silica Glass: A Molecular-dynamics Simulation*, Physical Review B, 54, 6, 1996, 3809-3816.

6.9 K. Trachenko, M. T. Dove, *Densification of Silica Glass under Pressure*, Journal of Physics: Condensed Matter, 14, 2002, 7449-7459.

6.10 Y. Liang, C. R. Miranda, S. Scandolo, *Mechanical Strength and Coordinate Defects in Compressed Silica Glass: Molecular Dynamics Simulations*, Physical Review B, 75, 024205, 2007.

6.11 B. Nghiem, *PhD thesis*, University of Paris 6, France 1998.

6.12 C. Denoual and F. Hild, *Dynamic Fragmentation of Brittle Solids: A Multi-scale Model*, European Journal of Mechanics of Solids A, 21, 2002, 105-120.

6.13 M. Yazdchi, S. Valliappan and W. Zhang, *A Continuum Model for Dynamic Damage Evolution of Anisotropic Brittle Materials*, International Journal of Numerical Methods in Engineering, 39, 1996, 1555-1583.

6.14 F. Hild, C. Denoual, P. Forquin and X. Brajer, *On the Probabilistic and Deterministic Transition Involved in a Fragmentation Process of Brittle Materials*,"Computers and Structures, 81, 2003, 1241-1253.

6.15 T. J. Holmquist, D. W. Templeton, K. D. Bishnoi, *Constitutive Modeling of Aluminum Nitride for Large Strain High-strain Rate, and High-pressure Applications*, International Journal of Impact Engineering, 25, 2001, 211-231.

6.16 G. T. Camacho and M. Ortiz, *Computational Modeling of Impact Damage in Brittle Materials*, International Journal of Solids and Structures, 33, 20-22, 1996, 2899-2938.

6.17 B. L. Holian and G. K. Straub, *Molecular Dynamics of Shock Waves in Three-Dimensional Solids: Transition from Nonsteady to Steady Waves in Perfect Crystals and Implications for the Rankine-Hugoniot Conditions*, Phys. Rev. Lett., 43, 1979, 1598.

6.18 G. K. Straub, S. K. Schiferl and D. C. Wallace, *Thermodynamic Properties of Fluid Sodium from Molecular Dynamics*, Phys. Rev. B, 28, 1983, 312-316.

6.19 V. Y. Klimenko and A. N. Dremin, in *Detonatsiya, Chernogolovka*, O. N. Breusov et al., Eds., AkademiiNauk, Moscow, 1978, 79.

6.20 B. L. Holian, W. G. Hoover, B. Moran and G. K. Straub, *Shock-wave Structure via Non-equilibrium Molecular Dynamics and Navier-Stokes Continuum Mechanics*, Phys. Rev. A, 22, 1980, 2498.

6.21 W. D. Kingery, H. K. Bowen and D. R. Uhlmann, *Introduction to Ceramics*, 2nd ed., John Wiley & Sons: New York, 1976, 91-124.

6.22 H. Sun, *COMPASS: An ab Initio Force-Field Optimized for Condensed-Phase Applications Overview with Details on Alkane and Benzene Compounds*, Journal of Physical Chemistry B, 102, 1998, 7338-7364.

6.23 H. Sun, P. Ren, and J. R. Fried, *The COMPASS force field: parameterization and validation for phosphazenes*, Computational and Theoretical Polymer Science, 8, 1/2, 1998, 229-246.

6.24 <http://www.accelrys.com/mstudio/ms modeling/visualiser.html>.

6.25 <http://www.accelrys.com/mstudio/ms modeling/amorphouscell.html>.

6.26 M. Grujicic, Y. P. Sun and K. L. Koudela, *The Effect of Covalent Functionalization of Carbon Nanotube Reinforcements on the Atomic-level Mechanical Properties of Poly-Vinyl-Ester-Epoxy*, Applied Surface Science, 253, 2007, 3009.

6.27 <http://www.accelrys.com/mstudio/ms modeling/discover.html>.

6.28 D. N. Theodorou and U. W. Suter, *Atomistic Modeling of Mechanical Properties of Polymeric Glasses*, Macromolecules, 19, 1986, 139-154.

6.29 L. Davison, *Fundamentals of Shock Wave Propagation in Solids*, Springer-Verlag, Berlin, Heidelberg, Germany, 2008.

6.30 M. Grujicic, W. C. Bell, B. Pandurangan and T. He, *Blast-wave Impact Mitigation of Polyurea When used as a Helmet Suspension-pad Material*, Materials and Design, 31, 9, 2010, 4050-4065.

6.31 M. Grujicic, W. C. Bell, B. Pandurangan and P. S. Glomski, *Fluid/Structure Interaction Computational Investigation of the Blast-wave Mitigation Efficiency of the Advanced Combat Helmet*, Journal of Materials Engineering and Performance, DOI: 10.1007/s11665-010-9724-z, July 2010.

6.32 C. S. Alexander, L. C. Chhabildas, W. D. Reinhart and D. W. Templeton, *Changes to the Shock Response of Fused Quartz due to Glass Modification*, Int. J. Impact Engineering, 35, 2008, 1376-85.

6.33 M. P. Allen and D. J. Tildesley, *Computer Simulations of Liquids*, Clarendon Press, 1994.

CHAPTER SEVEN

CONCLUSIONS AND FUTURE WORK

7.1 General Discussion and Concluding Remarks

As will be recalled, the overall objective of the present dissertation was to advance the field of glass material modeling and the accompanying computational analysis procedures. It is believed that the research contained herein has achieved this in the following ways:

1. The continuum-level glass material model developed in the ongoing work of the author's research group and the computational procedure employed proved capable of capturing the predominate features of multi-hit ballistic impact scenarios relative to: laminate impact-resistance performance loss upon subsequent impacts, glass fragment containment by polycarbonate lamina, and comparisons with experimental outcomes. This research provides confidence that the employed material model and computational approach may be extended to investigate other novel glass laminates for impact performance assessment.

2. Experimental and computational analyses of the ballistic impact performance of a simple borofloat glass-based laminate lead to the conclusion that air-side and tin-side float glass strike-face orientations resulted in equivalent laminate damage response and impact performance. The two main achievements of this investigation were: (i) demonstration of the borofloat glass material model's (and the computational approach employed) ability to recreate the experimentally observed damage behavior and laminate impact resistance performance, and (ii) revealing the lack of a performance enhancement achieved by orienting the borofloat plate air-side as the laminate strike face within the specific laminate structure tested. This research, again, served as evidence of the glass material model efficacy, as well as highlighted the capability of the computational approach employed.

3. The initial investigations into the molecular-level modeling demonstrated (computationally) the (previously experimentally observed) irreversible densification of glass when subjected to pressures in excess of ca. 4GPa. This finding served as a guide for soda-lime-glass-specific modifications to the well-established Johnson-Holmquist 2 material model to account for the densification phenomenon in continuum-level finite-element glass impact simulations. This research served as a gage for the potential impact performance enhancements that can be attributed to this densification process.

4. Further molecular-level investigations resulted in the computational determination of the soda-lime glass pressure versus specific-volume compression isotherm. From this isotherm, the glass Hugoniot and isentrope relations were determined and subsequently employed to semi-quantitatively assess the potential of pressure-induced phase transformation in soda-lime glass for mitigating shock-loading effects such as those experienced during blast and ballistic impact. The utility of this procedure was demonstrated through the identification of several potentially beneficial blast/ballistic mitigating effects of the pressure-induced phase transformation in soda-lime glass.

5. Finally, non-equilibrium molecular dynamics simulations were carried out in order to model shock formation and propagation within glass. The resulting shock had a steady profile whose propagation speed and associated particle velocity were used to explicitly determine the material shock hugoniot (which defines the locus of post-shock stress, energy density, mass-density, temperature, and particle velocity equilibrium states). Additional investigation of the molecular-level results revealed a 2-4% (shock strength-dependent) density increase and the accompanying densification mechanisms. These results help elucidate some of the energy-absorbing and non-viscous energy dissipation mechanisms that must be considered when developing a continuum-level finite element material model for highly dynamic impact scenarios.

7.2 Suggestions for Future Work

The majority of the glass material modeling in the present work has been carried out using model parameterization from publically available literature. The experimental simulations used for validation of the model have also been from open literature, but typically not from the same source as the model parameters. It would be desirable to have these both from the same sources due to the unavoidable variability in float glass processing history of the samples used for characterization vs. the experimental impact testing.

An additional component of the continuum-level material model that deserves consideration is the separate handling of the hydrodynamic and deviatoric response of soda-lime glass. A separate equation of state to model the hydrodynamic (pressure controlled) response of the material allows for the incorporation of volumetric nonlinearity and inelasticity resulting from phase changes, irreversible densification, etc. The deviatoric response can then be modified based on shear-induced micro-cracking, plasticity, and other potential material shear strength-limiting phenomena. At the time of writing of this dissertation, investigations are underway to determine to what degree these nonlinear and inelastic material response phenomena contribute the overall dynamic/impact response of glass, in addition to their incorporation into our continuum-level material model for glass through an equation of state and strength model. The results of this investigation, that the present author is involved in, will be presented in a future journal publication.

APPENDICES

Appendix A

Additional High Speed Photographs of Laminate Impact, Chapter 3

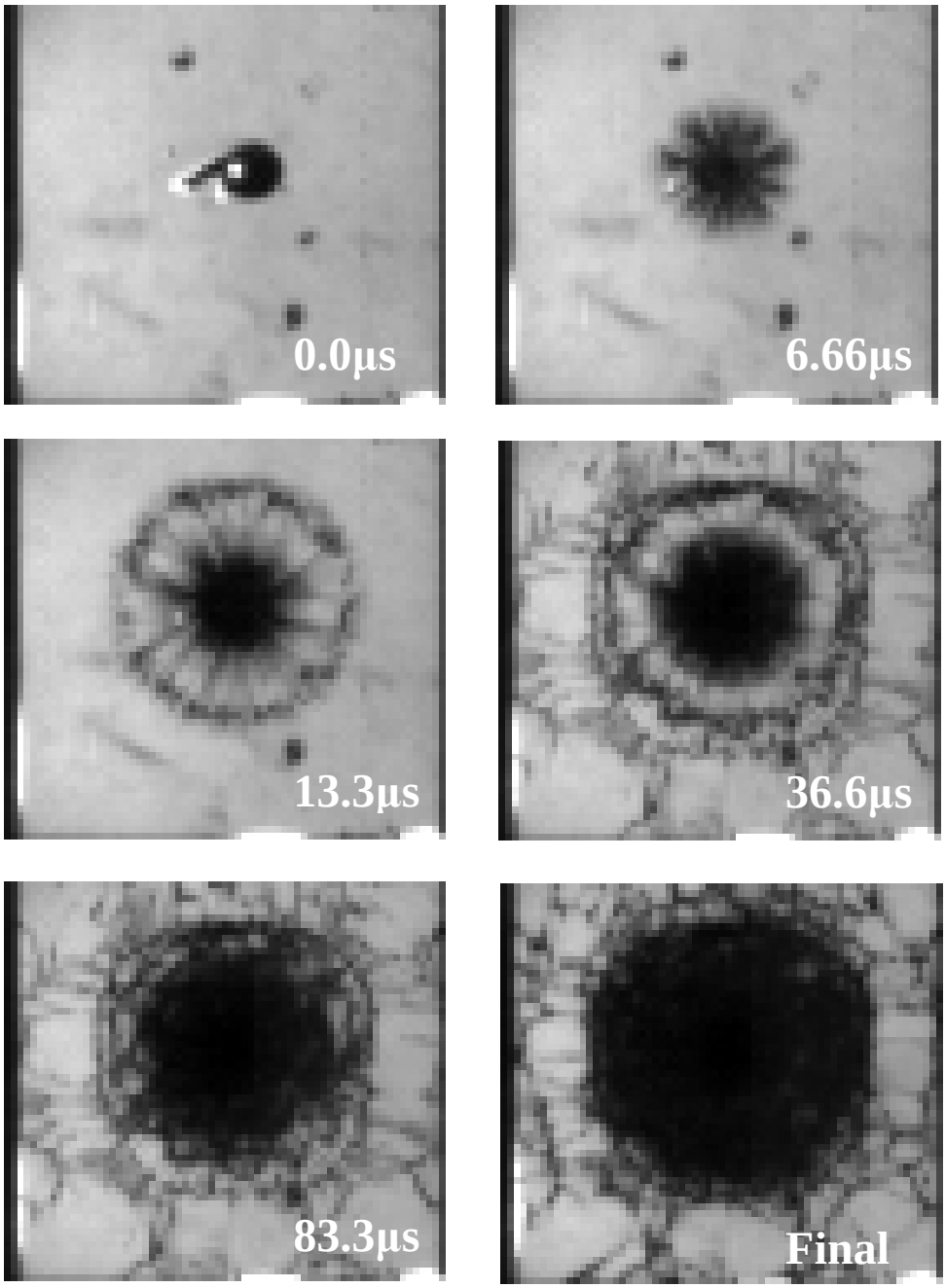

Figure A.1: Temporal evolution of damage in a 3.18mm-thick borofloat glass plate bonded to a 3.18mm-thick polycarbonate plate using a 2.54mm-thick polyurethane interlayer. Projectile: 5.53mm-diameter steel BB, Velocity = 470m/s, Strike -face = tin-side

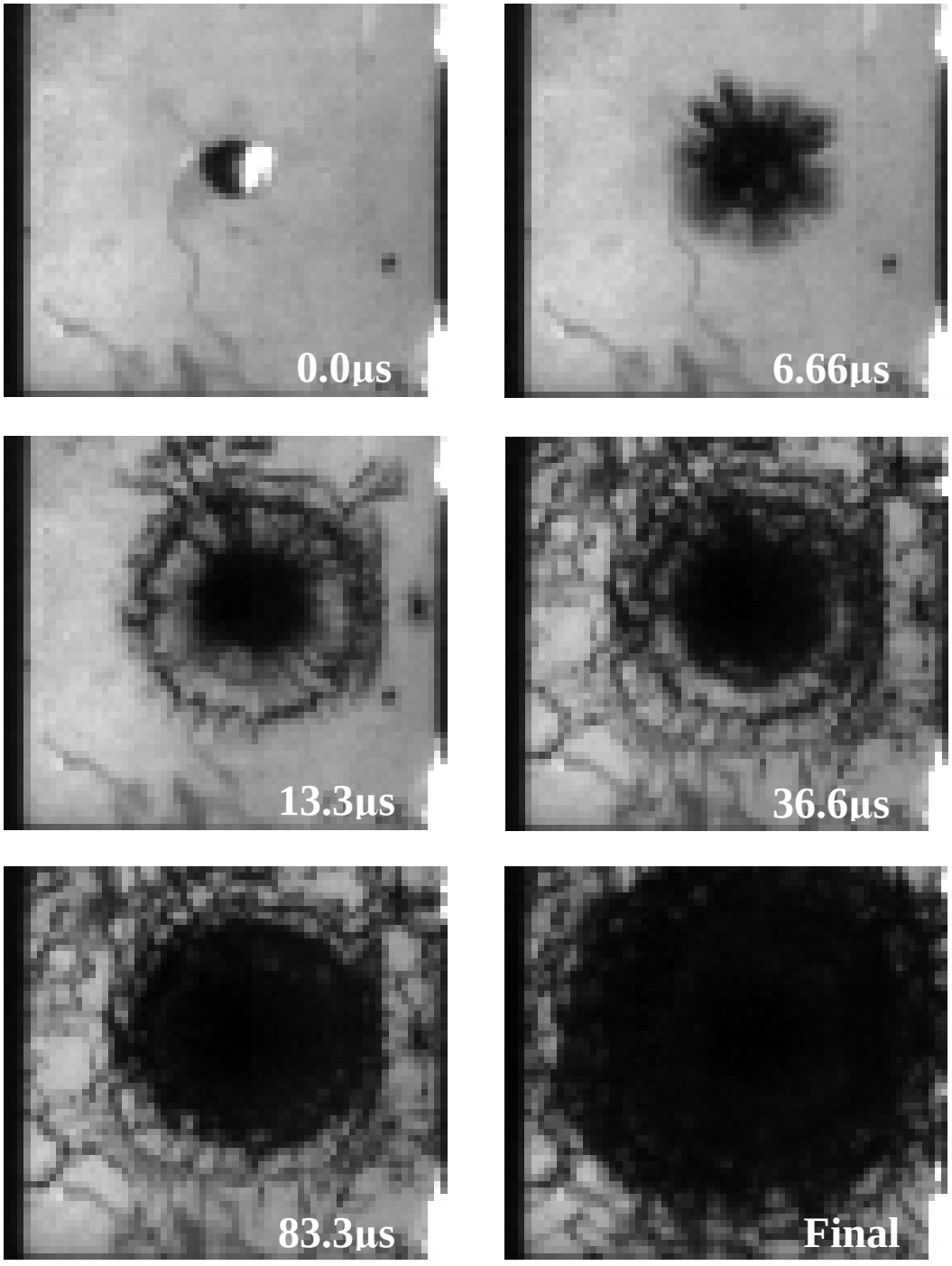

Figure A.2: Temporal evolution of damage in a 3.18mm-thick borofloat glass plate bonded to a 3.18mm-thick polycarbonate plate using a 2.54mm-thick polyurethane interlayer. Projectile: 5.51mm by 5.51mm steel RCC, Velocity = 493m/s, Strike -face = air-side

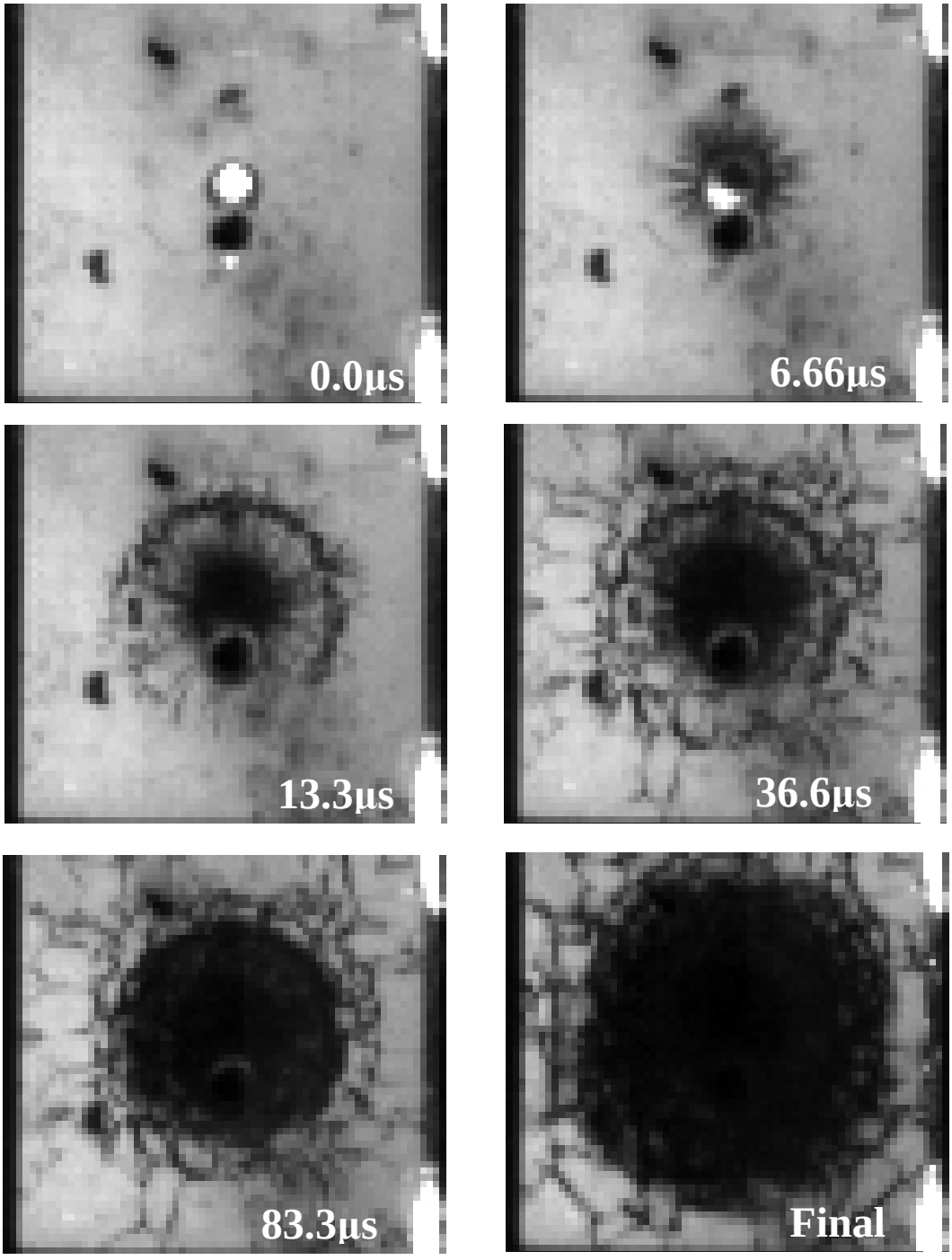

Figure A.3: Temporal evolution of damage in a 3.18mm-thick borofloat glass plate bonded to a 3.18mm-thick polycarbonate plate using a 2.54mm-thick polyurethane interlayer. Projectile: 5.51mm by 5.51mm steel RCC, Velocity = 493m/s, Strike -face = tin-side

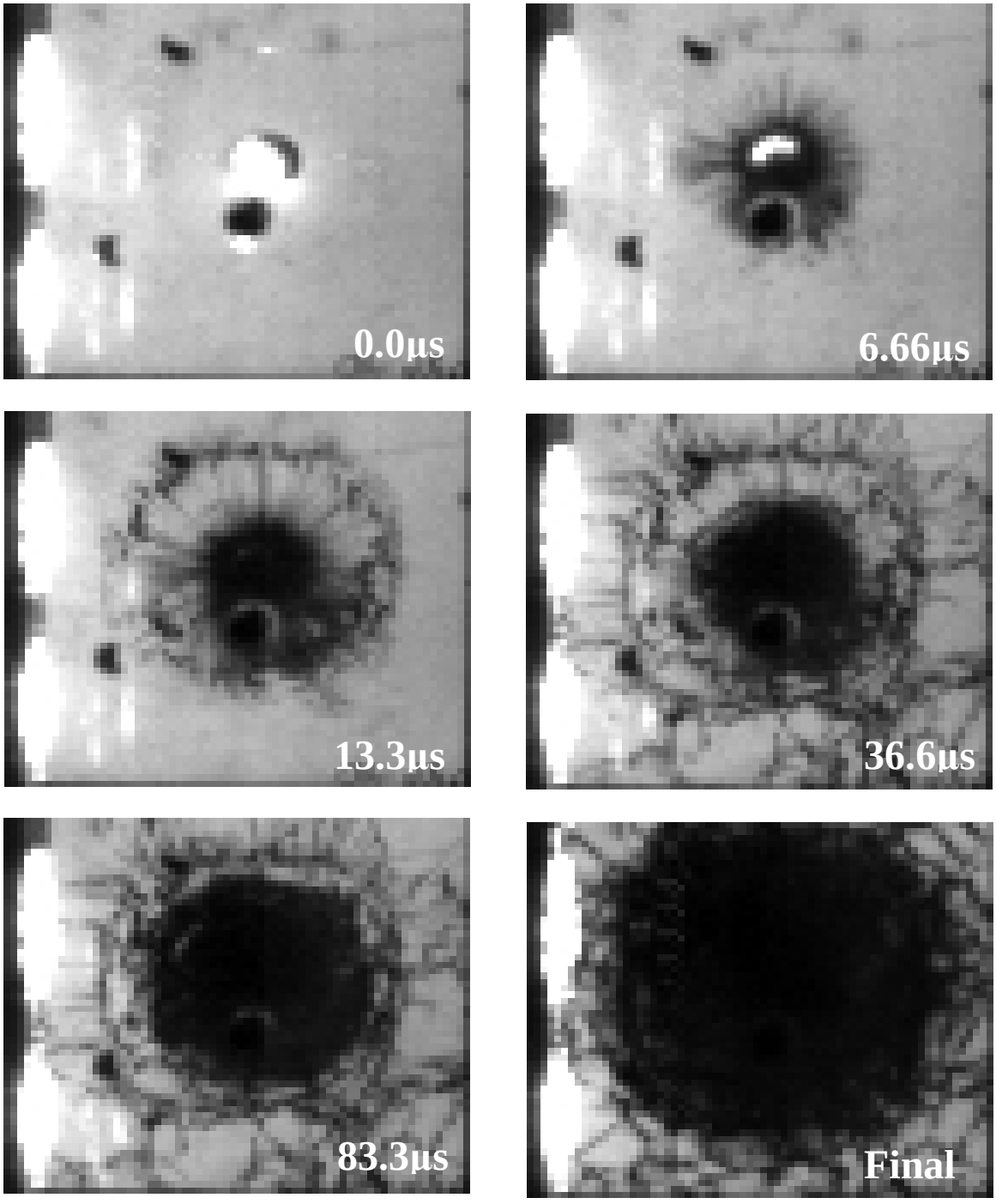

Figure A.4: Temporal evolution of damage in a 3.18mm-thick borofloat glass plate bonded to a 3.18mm-thick polycarbonate plate using a 2.54mm-thick polyurethane interlayer. Projectile: 5.51mm by 5.51mm steel RCC, Velocity = 540m/s, Strike -face = air-side

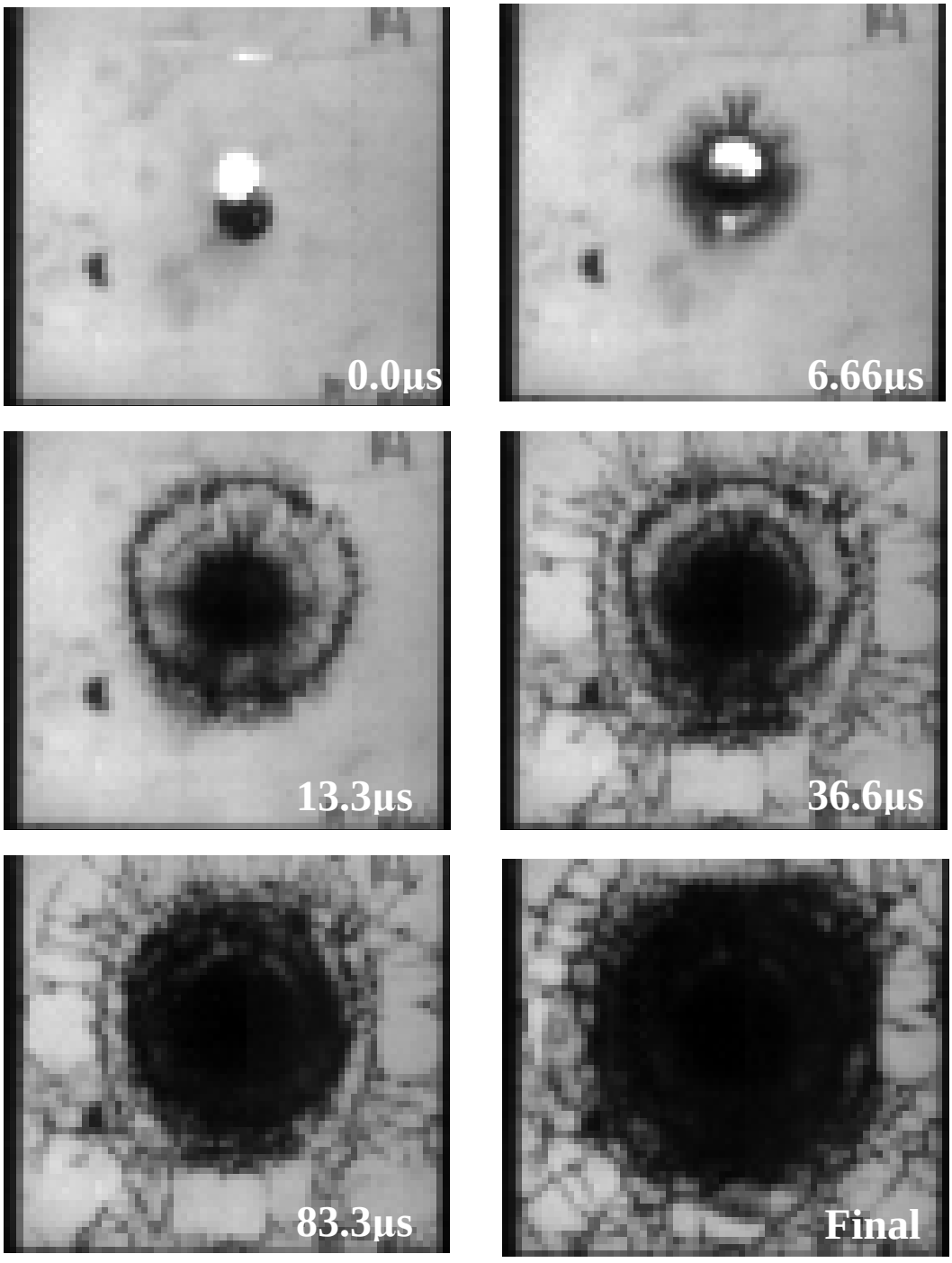

Figure A.5: Temporal evolution of damage in a 3.18mm-thick borofloat glass plate bonded to a 3.18mm-thick polycarbonate plate using a 2.54mm-thick polyurethane interlayer. Projectile: 5.51mm by 5.51mm steel RCC, Velocity = 596m/s, Strike -face = tin-side

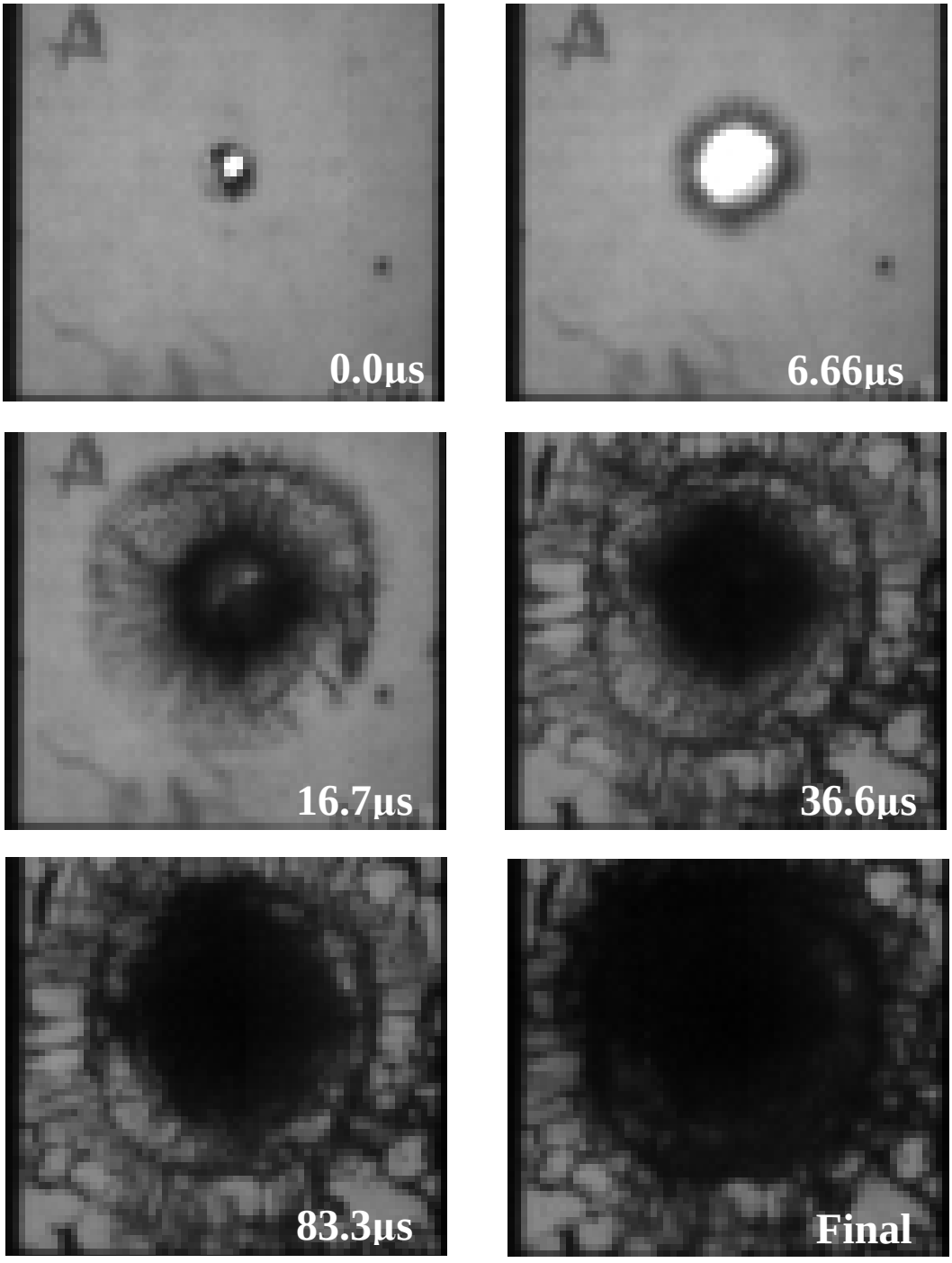

Figure A.6: Temporal evolution of damage in a 6.35mm-thick borofloat glass plate bonded to a 3.18mm-thick polycarbonate plate using a 2.54mm-thick polyurethane interlayer. Projectile: 5.51mm by 5.51mm steel RCC, Velocity = 532m/s, Strike -face = air-side

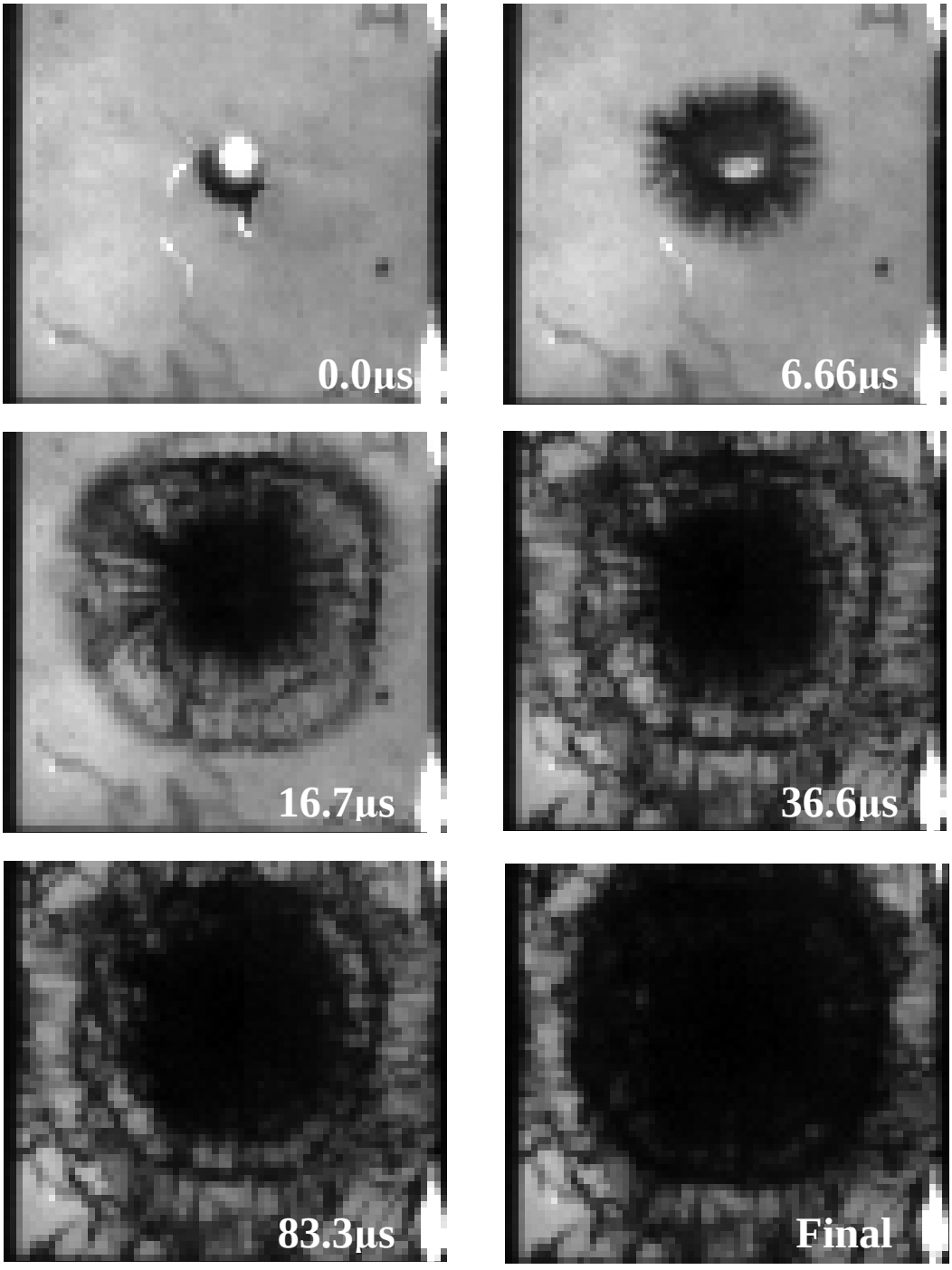

Figure A.7: Temporal evolution of damage in a 6.35mm-thick borofloat glass plate bonded to a 3.18mm-thick polycarbonate plate using a 2.54mm-thick polyurethane interlayer. Projectile: 5.51mm by 5.51mm steel RCC, Velocity = 540m/s, Strike face = tin-side